A STUDY OF THE DISTRIBUTION OF CARBON IN THE NEARBY UNIVERSE

Inaugural-Dissertation

zur

Erlangung des Doktorgrades

der Mathematisch-Naturwisschenschaftlichen Fakultät

der Universität zu Köln

vorgelegt von

Christian Björn Glück

aus Bochum

Köln

2017

Berichterstatter:	Prof. Dr. Jürgen Stutzki
	Prof. Dr. Joachim Hemberger
Tag der mündlichen Prüfung:	29. Juni 2016

für Theresa

Abstract

The composition and the evolution of the interstellar medium (ISM) is a major topic in the current research debate. The present thesis aims to gain a wider perspective of the distribution and composition of C^+, C^0, CO and H_2 in the Milky Way and in the nearby spiral galaxy M33. [CII], [CI](1–0), $^{12/13}$CO(1–0), ^{12}CO(2–1) and ^{12}CO(4–3) emission spectra are primarily used to trace and characterise the physical and chemical conditions within the ISM and to study its evolution. Three major samples were analysed, each providing an insight into different aspects of the ISM.

First, the nature and composition of clouds along the line of sight towards the quasars B0355+508 and B0212+735 is investigated. These clouds were identified as warm non–LTE diffuse clouds with a temperature of T~30 K and subthermal excited CO lines for roughly two decades. If the clouds were indeed diffuse, [CII] emission lines with an integrated line intensity of few K km/s were expected. SOFIA/GREAT [CII] observations, carried out within this thesis, do not show such [CII] lines. It is shown that the observations are not compatible with the scenario of warm diffuse clouds. The clouds towards B0355+508 and B0212+735 can not be diffuse. Furthermore, it is shown that all the observational data is fully consistent with an ensemble of cold dense clumps, that have volume densities of $n(\mathrm{H})\sim10^{3.5}$ cm^{-3} to 10^4 cm^{-3} and core temperatures of T~15 K.

Secondly, the latitudinal and radial distribution of carbon in the fourth quadrant of the Milky Way, is studied. The study is based on the analysis of spectrally resolved latitudinal observations of $^{12/13}$CO(1–0), CO(2–1), CO(4–3) and [CI](1–0). These lines were observed between b=±2° at eight galactic longitudes between l=306° to 354 °. I have determined and analysed the latitudinal and radial distribution of the different transitions. The study shows that the most of the [CI](1–0) emission can not be observed in the absence of low–J CO lines. This indicates that C^0 primarily arises from the surface of the CO photodissociation layer. The observed latitudinal profiles of CO and [CI](1–0) have a asymmetrical shape and can not be described by a single Gaussian. The scale height of the different transitions is determined at different distances to the Galactic Centre. It is found that the radial distribution of the scaleheight can be fitted with a power law, $\propto\sqrt{R_{\mathrm{GC}}}$. The profiles have a similar shape as synthetic [CII] profiles carried out within the SILCC–project. That might indicate that the local structure of the Milky Way is triggered to a large degree by supernovae.

The distribution and composition of carbon and hydrogen are investigated in the case study of five giant molecular clouds (GMCs) in the nearby galaxy M33. M33 is of interest as it has a half solar metallicity. I present [CI](1–0) observations of these GMCs. With the use of comple-

mentary [CII], $^{12/13}$CO(1–0), CO(2–1), HI and [NII]122μm data, I am able to determine the column densities of all major carbon species, CO, $C^0$and $C^+$and the column densities of neutral atomic hydrogen. The amount of H_2 is directly determined via the carbon column densities in the molecular phase. In addition, the fraction of CO dark H_2 is derived. Furthermore, I discuss the radial and spectral distribution of the different gas species. H_2 conversion factors for the observed line transitions are calculated. Finally, the individual positions are discussed in detail. The results indicate that the CO dark H_2 fraction is presumably higher towards lower metallicities. Probably up to $\sim$2/3 of the H_2 is CO dark in M33. The majority of this CO dark H_2 is traced by [CII], not by [CI](1–0). I also discuss the effect of different assumed [CII] excitation temperatures. It is shown that the assumed [CII] excitation temperature deeply affects the estimated amount of carbon and hydrogen, in particular the amount of CO dark H_2.

Zusammenfassung

Die Zusamensetzung und die Entwicklung des interstellaren Mediums (ISM) ist eine bedeutendes Thema der aktuellen Forschung. Die vorliegende Arbeit soll ein tieferes Verständnis für die Verteilung sowie die Zusammensetzung von C^+, C^0, CO, sowie von H_2 in der Milchstraße und deren Nachbargalaxie M33 vermitteln. Hierzu wurden hauptsächlich Spektren von [CII], [CI](1–0), $^{12/13}$CO(1–0), ^{12}CO(2–1) und ^{12}CO(4–3) analysiert. Die Daten erlauben einen Einblick in die physikalischen und chemischen Bedingungen des ISM und ermöglichen es seine Evolution zu erforschen. Die vorliegende Arbeit basiert hauptsächlich auf der Analyse dreier unterschiedlicher Beispiele, die diverse Aspekte des ISM beleuchten.

Ich untersuche hierzu zuerst die Zusammensetzung von Wolken entlang der Sichtlinie zu den Quasaren B0355+508 und B0212+735. Diese Wolken werden seit gut zwei Jahrzehnten für warme diffuse Wolke gehalten ($T{\sim}30$ K), in welchen sich das CO in einem subthermal angeregten Zustand befindet. Sollten die Wolken tatsächlich diffus sein, müssten in ihnen [CII] Linien mit einer integrierten Linienintensität von einigen K km/s beobachtbar sein. Die [CII] Beobachtungen, welche mit SOFIA/GREAT durchgeführt wurden, zeigen diese Linien jedoch nicht. Im Rahmen dieser Arbeit wird gezeigt, dass diese Beobachtungen unvereinbar mit warmen diffusen Wolken sind. Des Weiteren wird dargestellt, dass alle Beobachtungen durch ein Ensemble kalter, dichter Klumpen, mit Volumendichten von $n(\mathrm{H}){\sim}10^{3.5}$ cm^{-3} bis 10^4 cm^{-3} und Kerntemperaturen von etwa $T{\sim}15$ K, erklärt werden können.

Anhand von $^{12/13}$CO(1–0), CO(2–1), CO(4–3) und [CI](1–0) Beobachtungen betrachte ich die radiale und vertikale Verteilung von Kohlenstoff im vierten Quadranten der Milchstraße. Die spektral aufgelösten Daten wurden bei acht unterschiedlichen galaktischen Längengraden zwischen l=306° und l=354° Länge, in einem Bereich zwischen den galaktischen Breitengraden b=±2°beobachtet. Die Analyse zeigt, dass der größte Teil von [CI](1–0) nicht in der Abwesenheit von niedrigen CO Rotationslinien beobachtet werden kann. Dies impliziert, dass [CI](1–0) wahrscheinlich von der CO–Photodissoziationsschicht emittiert wird. Die vertikalen Profile, senkrecht zu der galaktischen Ebene, von [CI](1–0) und den CO Übergängen haben eine asymmetrische Form und können nicht durch eine einzige Gaußkurve beschrieben werden. Ebenso wurde die Skalenhöhe der einzelnen vertikalen Verteilungen bei unterschiedlichen Entfernungen zum galaktischen Zentrum bestimmt. Deren radiale Verteilung kann mittels eines Potenzgesetzes ($\propto\sqrt{R_{\mathrm{GC}}}$) beschrieben werden. Des Weiteren weisen die beobachteten Profile starke Ähnlichkeiten zu synthetischen [CII] Profilen auf, welche im Rahmen des SILCC-Projekts simuliert wurden. Dies könnte darauf hinweisen, dass die lokalen Strukturen der Milchstraße zum großem Teil durch Supernova–Explosionen bestimmt wird.

Am Beispiel von fünf Riesenmolekülwolken (GMCs) analysiere ich die Verteilung und die Zusammensetzung von Kohlenstoff und Wasserstoff in M33. Diese fünf GMCs befinden sich auf der Hauptachse dieser Galaxie. M33 ist von großer Bedeutung für diese Arbeit, da ihre Metallizität nur halb so groß ist wie die der Milchstraße. Ich präsentiere [CI](1–0) Beobachtungen von diesen GMCs und kombiniere diese mit komplementären [CII], $^{12/13}$CO(1–0), CO(2–1), HI und [NII]122μm Daten. Diese Daten erlauben die Bestimmung der Säulendichten von CO, C^0 und C^+ sowie der des neutralen atomaren Wasserstoffs. Die Menge von H_2 wird aus den Kohlenstoffsäulendichten der molekularen Phase bestimmt. Der Anteil des H_2, der nicht durch CO–Linienübergänge bestimmt werden kann (CO dunkles H_2), wird ebenfalls bestimmt. Ich diskutiere außerdem die radiale und die spektrale Verteilung der einzelnen Gasarten. Zuletzt werden die einzelnen GMCs nochmals im Detail besprochen. Die Ergebnisse deutet darauf hin, dass der Anteil des CO dunklen H_2bei einer niedrigeren Metallizität erhöht ist. Ungefähr $\sim$2/3 des H_2in M33 ist nicht mit CO assoziiert. Die Mehrzahl des molekularen Wasserstoffs kann wahrscheinlich durch [CII] ausfindig gemacht werden, nicht jedoch durch die [CI](1–0) Linie. Der Einfluss von unterschiedlicher Anregungstemperaturen von [CII] wird ebenfalls diskutiert. Ich zeige, dass die angenommene [CII] Anregungstemperatur einen großen Einfluss auf die Berechnungen der Gesamtmenge von Kohlenstoff und Wasserstoff besitzt, insbesondere auf den Anteil von CO dunklem H_2.

Contents

Part I

INTRODUCTION & MOTIVATION

Chapter 1

Introduction

The overall goal of this thesis is to create a wider perspective of the distribution and composition of the *interstellar medium* (ISM) in the nearby universe. This study is focused on the analysis of ionised (C^+) and neutral atomic (C^0) carbon as well as on carbon monoxide (especially its low rotational transitions between J=1–0, 2–1 & 4–3) emission spectra in the Milky Way and in the nearby galaxy M33. This thesis uses these lines to trace and characterize the physical and chemical conditions within the ISM and to study its evolution. Of particular interest is the distribution and the fraction of molecular hydrogen.

The following section will give a brief introduction of the ISM and explain the motivation as well as the goals of this thesis.

Since Jansky (1933) detected *'Electrical Phenomena that apparently are of Interstellar Origin'* in 1933, the interstellar medium has been studied. Since then astronomers have studied the composition of the ISM, its role and impact on the formation of stars and galaxies as well as their evolution. The composition of the ISM is not uniform. It consists of different gas *phases*. Each phase represents gas at specific, different temperatures and densities, such as hot diffuse ions and cold dense molecular clouds with a complex chemistry and molecules (cf.chapter 2). The mass of the ISM is dominated by hydrogen (∼74%). The majority of the remaining mass is helium (∼23%; cf. Alfaro & Delgado 2011). The remaining mass is comprised by the heavier elements.

Hydrogen occurs in its ionised (H^+), neutral (H^0) and/or molecular form (H_2) in the ISM. H^+ dominates the hot phase of the ISM and H^0 the warm and cold neutral phase. Molecular hydrogen dominates the mass in the dense cold regions of the ISM. The emission of H^+ and H^0 [i] can be easily observed from ground based observatories, while molecular hydrogen is almost invisible for the observer[ii], even though it is the most abundant molecule in the universe (e.g. Field, Somerville & Dressler 1966, cf. chapter 4). Therefore, H_2 is commonly studied indirectly via tracers. Common tracers for H_2 are low rotational transitions of carbon monoxide (cf. e.g Young & Scoville 1982; Liszt 1982; Bloemen et al. 1986; Scoville & Sanders 1987; Wilson & Scoville 1989; Bolatto et al. 2013) and the

i Single ionised hydrogen can be observed at a wavelength of 656.3 nm. Neutral atomic carbon is commonly observed via its ground state hyper-fine transition at 21 cm. The physic of line transition is explained in detail in section 4.1.

ii H_2 is a symmetrical molecule. It has no permanent dipole moment. Therefore rotational transitions are forbidden and no radio transitions can be observed. For details see Section 4.1

emission of dust (e.g. Hollenbach & Salpeter 1971; Jura 1975; Hollenbach & Tielens 1999; Röllig et al. 2013). Not all H_2 is traced by CO transitions. It is assumed that about one third of the molecular mass in molecular clouds in the Milky Way is located in H_2 regions where the carbon is exclusively ionised (C^+) or/and neutral atomic (C^0) in the absence of CO (Hollenbach & Tielens 1999; Wolfire et al. 2010). This molecular hydrogen is often denoted as *'dark gas'* (Grenier et al. 2005) and *'CO dark H_2 gas'* (Leroy et al. 2011). Therefore, it is of great interest to study the transitions of C^+ and C^0. Furthermore, the transition of single ionised carbon is almost ubiquitous in the ISM, and it is a dominant coolant for major phases. It is further assumed that neural atomic carbon is associated with diffuse interstellar clouds (in formation) (e.g. Bergin et al. 2004; Beuther et al. 2014) as well.

The key to study the ISM and to gain an almost complete overview of its composition is the combination of spatially and spectrally resolved observations of different lines which trace the different processes and phases. The study of different lines provides information about the physical and chemical conditions of the ISM. The comparison of different line transitions allow for instance to estimate the densities and temperatures within the source of interest. Spatially resolved data show the line intensities at the projected two dimensional sky. Spectral data provides an additional velocity dimension. Spectrally resolved data is thus in particular suitable to the study of the ISM. The spectral information provide a direct insite into the kinematics within molecular clouds. They allow to distinguish between different possible velocity components along the line of sight, as they hav differnt central velocities. The line-shape supplies information about the physical conditions within the observed sources as well. The comparison of different line profiles delivers further information about the physical and chemical conditions in molecular clouds in three dimensions. A central point of thesis will be the comparison of CO and the transitions of neutral atomic and ionised carbon. This allows *inter alia* to allocate the distribution of CO-dark H2 in molecular clouds.

The examination of spectral lines of ionised, neutral and molecular carbon (especially carbon monoxide) is predestined for this task. The observation and combination of different carbon transitions allow to gain thus an almost full picture of the ISM as each transition is tracing a designated phase of the ISM (cf. section 2.1).

These carbon transitions have frequencies within the the sub–millimetre and millimetre regime, which corresponds to frequencies of a few 10^2 Gigahertz (GHz) to a few Terahertz (THz). The observation of these frequencies (especially THz frequencies) is a technically demanding challenge. State of the art receivers[iii] and telescopes allow to study GHz and THz frequencies with the required spatial <u>and</u> spectral resolution ($\lesssim 1'$ and $\lesssim 10^{-1}$ km/s) within the last years. The observations require a dry atmosphere[iv], as these frequencies are easily absorbed by water vapour. Therefore, (sub–)millimetre telescopes are commonly located at high al-

iii Often heterodyne receivers are used to observe spectra with a high spectral resolution. For details see the Appendix B.

iv As thumb rule: Higher frequencies require a dryer atmosphere. By experience it can be said that [CI](1–0) (492 GHZ) requires a precipitable water vapor (pwv) of $\lesssim$0.7 mm. [CII] observations (1900 GHZ) require a pwv<0.1mm. I recommend Guan (2013) concerning the effect of the atmosphere for sub-millimeter observations.

Figure 1.1: The Stratospheric Terahertz Observatory (STO) shortly before the launch at the 12th January 2012 near the McMurdo station in Antarctica.
Credit: Left: Antony A. Stark;
Right: Screen-shot from the Operation Video of the Columbia Scientific Balloon Facility (CSBF)/NASA few second before the launch of STO.

titudes, such as the Mauna Kea (Hawaii, ~4000m), the Pampa la Bola (Atacama desert, ~5000m), the Antarctic plateau[v], in air planes or in space.

Facilities that are particularly worth mentioning in this context are the Herschel space observatory (Pilbratt et al. 2010) with the HIFI (de Graauw et al. 2010), PACS (Poglitsch et al. 2010) and SPIRE receivers (Griffin et al. 2006; 2010)[vi] as well as the air borne submillimeter telescope SOFIA (e.g. Becklin et al. 2007; Becklin 2015) with the GREAT, and upGREAT–receiver (Heyminck et al. 2012; Risacher et al. 2015) allowing observations of ionised carbon.

The transitions of neutral atomic carbon can be observed by the Caltech Submillimeter Observatory (CSO, Phillips 1996; Kooi 2009; Kooi et al. 2010), APEX with the APEX-3-receiver (Güsten et al. 2006; Vassilev et al. 2008), AST/RO (Balm 1996; Stark et al. 2001) and Nanten2/SMART (Kawamura et al. 2005; Graf et al. 2002; 2008). Prominent observatories for low J–transitions of carbon monoxide are Mopra (Moorey et al. 1997; Burton et al. 2013a), IRAM-30m (Brunswig 1993; Mauersberger 2003) and the Plateau de Bure interferometer (PdB; Blondel et al. 1996; Karastergiou & Neri 2006).

Recently, a small number of studies have investigated the ISM by use of all the different carbon transitions. These studies are preliminary focused on individual objects. Examples can be found in the studies by Beuther et al. (2015) of infrared dark clouds, García et al. (2014) of the warm ISM in the region around Sgr A*, the N159 star-forming region in the Large Magellanic Cloud by Okada et al. (2015), the S109 region by Schneider et al. (2003) and the study of M17 SW by Pérez-Beaupuits et al. (2015).

v The South Pole for example is located 'only' at an altitude of ~2800 m. Nevertheless the atmosphere is very dry, pwv~0.25mm, due to the low atmospheric pressure (~700 millibar) and the low temperatures. The driest atmosphere for ground based observations can be found at the Dome A (~4000 m), located at the summit of the Antarctic plateau (Kulesa et al. 2008; Burton et al. 2014)

vi HIFI is a heterodyne spectrometer with a spectral resolution of $\lesssim$1 MHz. PACS and SPIRE are bolometers. Bolometers provide no, or only low resolved (by using filters), spectral information. I would like to refer to Appendix B, for further details.

The Herschel space observatory key program GOT C^+ studied the distribution of [CII] in the Milky Way at the galactic latitude b=0° [vii] (Pineda et al. 2013; Langer et al. 2014b; Pineda et al. 2014).

A full sample of all the carbon lines at galactic scales has not been performed so far. An attempt to gain such a full sample of major parts of the Milky Way was the *Mopra–STO–Nanten2 Atomic and Molecular Gas Survey* (Burton et al. 2012). This survey had planned to map the C^+, C^0 and CO distribution within the the fourth quadrant [viii] of the Milky Way with an overall spatial resolution of $\Delta\delta \lesssim 1'$ and $\Delta v \lesssim 0.1$ km/s. $^{12/13}C^{16/17/18}O(1–0)$ observations of this region are performed within the Mopra Southern Galactic Plane CO Survey. The balloon-born *Stratospheric Terahertz Observatory* (*STO*; Walker et al. 2008; 2010; Walker 2012; cf. Fig. 1.1) tried to map the [CII] emission within b=±0.5° the galactic latitude. After the launch on January 12th 2012 near the McMuro station, STO circumnavigated the Antarctic continent for 14 days at an altitude of almost ∼40 km. Technical problems with the cryostat which appeared shortly after the launch, and problems with the star-camera, prevented a [CII]–mapping of the Milky Way. Therefore, no [CII] data is provided within this project. STO was the major motivation to map the distribution of C^0 and CO transitions in the fourth quadrant of the Milky Way. The $^{12/13}C^{16/17/18}O(1–0)$ transitions are mapped between 350°≤ l ≤=310° and -0.5°≤ b ≤0.5° (Burton et al. 2013a; Braiding et al. 2015). The vertical distribution of [CI](1–0), CO(2–1), CO(4–3) and $^{12/13}C^{16/17/18}O(1–0)$ was mapped between -2°≤ b ≤2° [ix] at selected galactic longitudes by observations with AST/RO and Morpa (cf. Fig. 1.2). It is planned to provide complementary [CII] observations for the b–strips with SOFIA/upGREAT. Complementary HI data of this quadrant is available from the *Southern Galactic Plane Survey* (SGPS; McClure-Griffiths et al. 2005) obtained by the Australia Telescope Compact Array (ATCA) and the Parkes radio observatory with a dish–diameter of 64 m.

An other attempt to gain a full sample of all the carbon lines in a galaxy is the Herschel open time key project HERM33ES (Kramer et al. 2010). A goal of the HERM33ES is to gain an almost complete overview of the ISM of M33, with respect to the galactic radius. M33 was intensively studied by all three instruments on-board Herschel; HIFI, PACS, SPIRE. SPIRE observed the 250μm, 360μm and 520μm emission of the almost entire galaxy. PACS and HIFI observed i.a. [CII] in selected regions along the major axis. Complementary CO and HI data was observed within the HERM33ES-project as well.

This thesis studies the distribution of carbon within the ISM. To a large extent this study is based on data that is provided within the Mopra–STO–Nanten2 Atomic and Molecular Gas Survey and the HERM33ES project. In order to achieve this goal, this thesis combines data of the CO, C^0 and C^+ transitions in the Milky Way and M33. Some missing line transitions are complemented by own observations, that are published in this thesis. This thesis was also intended to analyse the STO [CII]–observations and

vii The project observed the [CII] transition, using Herschel/HIFI, at b=0°via a systematic sparse sampling of the Galactic disk, with a longitudinal spacing of 0.87° to 4.5°.

viii The fourth quadrant of the Milky Way is given by the galactic longitudes 360°≤ l ≤ 270°

ix These strips are denoted as b–strips in the following

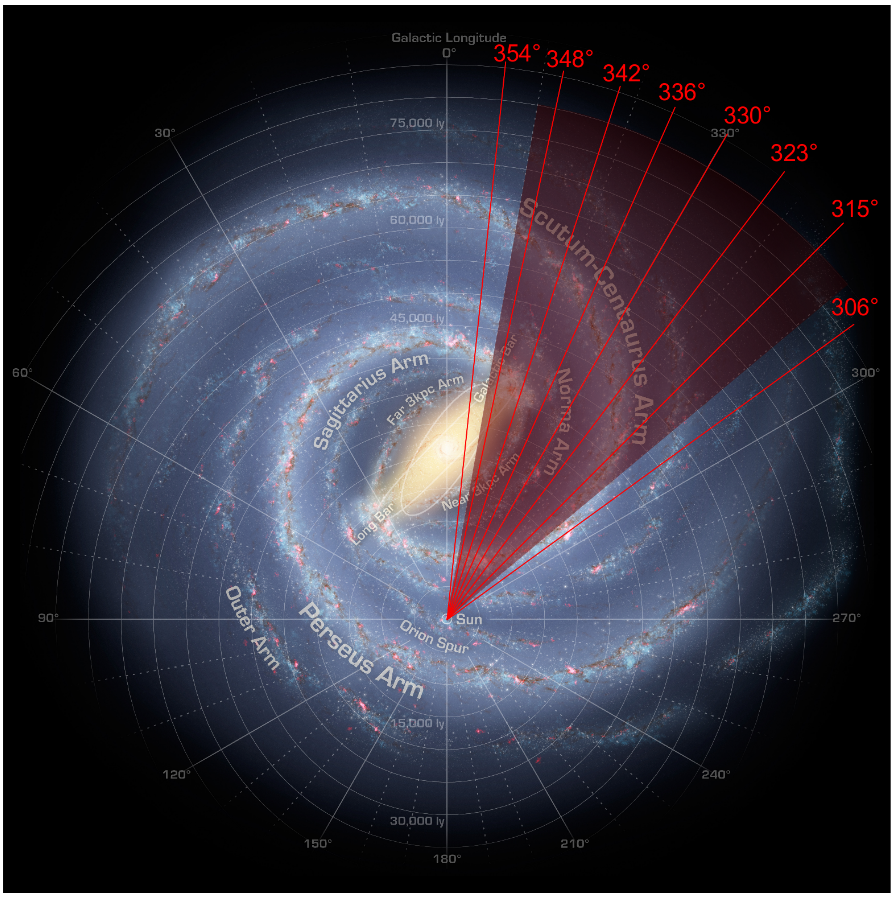

Figure 1.2: Artist illustration of the Milky Way. The red stripes mark the line of sight of the b-stripes observed with AST/RO. The filled transparent red area show the regions that were planed to be mapped by STO.
Credit: R. Hurt, NASA/JPL-Caltech

to compare the observations with complementary CO and C^0 data. The technical problems of STO prevented this study.

The study is led by the overall question:

What is distribution of carbon in the ISM and what conclusions can be drawn for the ISM in general?

This major question is divided and accompanied by the following question:

I *What are the composition and nature of clouds that are identified as diffuse CO clouds?*

The nature and composition of diffuse clouds are not well known. Diffuse clouds are commonly identified by the absorption of mm–waves in front of a bright foreground source. Liszt & Lucas (1998) succeeded in detecting CO (J=1–0)and CO (J=2–1) emission, identified to be associated with the diffuse clouds in a representative sample of mm–wave absorption towards the lines-of-sight to quasars. Pety et al. (2008b) identified these clouds as warm non-LTE[x] diffuse clouds with a temperature of $T \gtrsim 30$ K and subthermal excited CO lines. Liszt &

x Local Thermal Equilibrium (LTE)

Pety (2012) was able to map the CO (1–0) emission with a few arcmin extent around these positions. Small scale CO variations were interpreted as variations within the chemistry, not as density or column–density variations in the clouds.
The hypothesis is tested at the example of two nearby clouds from Liszt & Pety (2012) by SOFIA /GREAT [CII] observations. This question is tackled in chapter 5.

II *What is the radial and vertical distribution of C^0 and CO in the Milky Way?*

The distribution of the C^0 transitions in the ISM is not well studied. The distribution of C^+ and CO(1–0) in the galactic plane was investigated in recent studies. The GOT C^+ project has studied the distribution of ionised carbon along the galactic plane at b=0° (Pineda et al. 2013; Langer et al. 2014b; Pineda et al. 2014). The Mopra Southern Galactic Plane CO Survey (Burton et al. 2011; 2013a; Braiding et al. 2015) investigates the distribution of $^{12/13}C^{16/17/18}O$(1–0) in the southern galactic plane between $b=\pm0.5°$ galactic latitude. This thesis tries to fill the carbon gap between these surveys by analysing [CI](1–0) observations.
In chapter 6 I analyse spectral resolved $^{12/13}$CO(1–0), CO(2–1) and CO(4–3) and [CI](1–0) strip–data between the galactic latitudes $b=\pm2$ (so called b–strips) at different galactic longitudes, provided by observations with AST/RO and Mopra. The radial and the vertical distribution of these transitions is determined as well as the average width of the gas perpendicular to the galactic disc (*'scale height'*). Further the data is analysed regards the question whether there are differences in the distribution of the CO transitions and [CI](1–0).

III *Which processes drive the large scale structure of the ISM within the Milky Way?*

The comparison of the vertical distribution of CO and [CI](1–0) with simulated [CII] maps (Walch et al. 2015; Franeck et al. submitted) allows conclusions about the dominant processes that drive the evolution of the ISM (chapter 6)

IV *How does the metallicity affect the distribution of carbon and the fraction of 'CO-dark H_2 gas'?*
The affect of a half solar metallicity onto the distribution of carbon is studied at the example of the nearby galaxy M33 in chapter 7. The fraction of CO dark H_2 in M33 is studied as well. It is assumed that the fraction of CO dark H_2 is increased towards lower metallicities.
In this thesis, I present spectral resolved [CI](1–0) observations of five giant molecular clouds (GMCs) along the major axis of M33. The observations were performed with the APEX, CSO and Nanten2 telescopes. The data is combined with complementary HI, [CII] and low J–CO observations provided within the framework of the HERSCHEL open key time project HERM33ES (Kramer et al. 2010). The combination of these data allows to determine the distribution of C^+, C^0 and CO in the M33. Based on these calculations I determine the fraction and the (radial and spectral) distribution of H_2 that is

traced by the different carbon species. The fraction of CO dark H_2 is calculated and is compared with theoretical predictions by Wolfire, Hollenbach & McKee (2010).
Based on the derived H_2 column densities and the integrated line intensities I will calculate H_2 conversion factors for the integrated [CII], [CI](1–0) and CO(2–1) line intensities. These conversion factors are intended to be a simple and workable method to estimate the amount of H_2 in molecular clouds. The calculated conversion factors will be to compared established conversion factors in the Milky Way and with theoretical predictions for environments with a lower metallicity.

Part II

SCIENTIFIC BACKGROUND

Chapter 2

The interstellar medium

The following chapter provides a general introduction into the structure and composition of the ISM.

2.1 OVERVIEW OF THE INTERSTELLAR MEDIUM

In general, the term *interstellar medium* refers to all the baryonical matter located between the stars [i]. The majority of the baryonic mass within the Milky Way is bound in stars or stellar remnants (Draine 2011). The fraction of the ISM to the total baryonic mass within the Milky Way is ∼10% to ∼15%. (Draine 2011). Nevertheless, the ISM is of tremendous importance for galaxies, despite its relatively small mass fraction. The ISM itself consists mainly of hydrogen (∼70% by mass and ∼91% by atoms) and helium (∼28% of the mass and ∼9% by the number of atoms). Heavier elements contribute in total to ∼1.5% to its mass (∼0.1% of the atoms) (Ferrière 2001).

The ISM consists of a wide range of different *phases*. Each phase represents gas and dust within a range of specific temperatures and densities. The description of the following section is mainly based on the categorisation of Tielens (2010) and Ferrière (2001).

HOT IONIZED MEDIUM: The *hot ionized medium* (HIM) consisting of hot gas with typical high temperature of $T \sim 10^{5.5-6}$ K, heated by supernova shock (Aschenbach 1988; McCammon & Sanders 1990), and low volume densities of $n \sim 10^{-3}$ cm^{-3}. The HIM represents ∼30-70% of the gas volume within the galaxy (Ferrière 2001).

HII REGIONS: The *H*II *regions* are named after their dominant gas form, ionized hydrogen. HII -regions are commonly located nearby hot young O and B–type stars[ii]. Their UV radiation pentrates the gas and photo-ionizes the hydrogen. The temperatures of HII regions are $\sim 10^4$ K (Spitzer 1947; Mallik 1975; Draine 2011). The densities

i Besides the baryonical matter the universe consists of dark matter and the dark energy. Baryons have a mass fraction of ≈4.8% to the total energy of the modern universe. The fraction of dark matter is ≈25.8%. The majority of energy in the universe consists of dark energy (Planck Collaboration et al. 2014a;b)

ii Johnson & Morgan (1953) classify stars by their spectral type into seven main types: O, B, A, F, G, K, M, the so-called Morgan-Keenan spectral classifications. Within this classification system, the blue O-type stars have the highest mass and temperature. The red M-type stars have the lowest mass and temperatures.

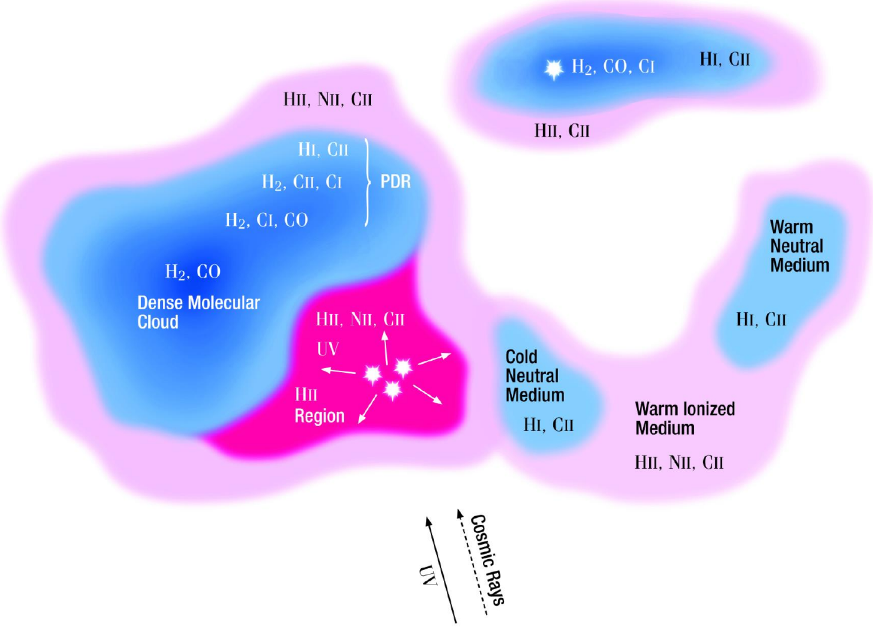

Figure 2.1: Sketch of the different phases of the ISM.
Credit: Jorge Pineda

within these regions vary between $n{\sim}10^{-1}\mathrm{cm}^{-3}$ to 10^4 cm^{-3}. This phase is predominantly cooled by the forbidden line transitions[iii] such as ionized nitrogen ([NII]205μm and [NII]122μm) and oxygen ([OII] and [OIII]), but also by the transition of single ionized carbon, [CII].

WARM IONIZED MEDIUM: Low dense HII gas ($n \sim 10^{-1}$ cm^{-3}) (Struve & Elvey 1938) is also denoted as the *warm ionized medium* (WIM). A significant fraction of the hydrogen mass, ~23%, and of the volume, ~10-20%, of the ISM can be assigned to the WIM.

NEUTRAL ATOMIC GAS: The neutral atomic gas can be divided into the following two phases (Ferrière 2001): the *warm neutral medium* (WIM) and the *cold neutral medium* (CNM). Both phases have in common that they mainly consist of neutral atomic hydrogen. The dominant coolant in both phases is the [CII] fine structure transition.

The warm neutral medium is characterised by broad emission lines. Typically, it has kinetic gas temperatures of $T \sim 5000$ K and volume densities of $n \sim 0.6$ cm^{-3}. This gas phase is widely distributed in the galaxy with a volume fraction of ~40%.

The cold neutral medium is characterised by narrow lines with widths of a few km/s, that are observed in emission or absorption. The CNM mainly consists of cold clouds with temperatures of $T \simeq 50$-200 K and densities from $n \sim 10^1$ cm^{-3} to 10^2 cm^{-3}. The CMN contributes ~1 to 5 % to the total volume fraction of the ISM in the Milky Way. Nevertheless, it contains a non-negligible amount of its baryonical mass which amounts to ~1/3.

MOLECULAR GAS: The densest and coldest phase of the ISM is formed by *molecular gas* , $T \sim 10^1$ K to 10^2, which is commonly assembled

iii The physic of these transitions is explained in detail in section 4.1

in gravitationally bound molecular clouds. Compared to the other phases, they are relatively compact and dense. The typical volume densities can be measured on a scale of $n \sim 10^{3-6}$ cm^{-3} and fill ~5% of the ISM volume. In comparison to its modest volume fraction, this molecular gas contains about ~20% a rather big percentage of the total mass of the ISM. In this context, the star formation occurs in the densest and coldest regions of this phase. Molecular clouds are commonly traced by low J–CO transitions or dust emission, but neutral and ionized carbon are also associated with these clouds.

DUST: Despite its rather small percentage of ~1% to the total mass of the ISM, *dust* plays an important role in galaxies (e.g. Parkin et al. 2012; Zavala et al. 2015). The dust in the ISM is mainly composed of graphite (Mathis et al. 1977; Draine & Lee 1984; Jones 2009), (amorphous) olivine[iv] and water ice (e.g. van Dishoeck et al. 1998). The distribution of the dust grain-sizes can be described by a power law (Mathis et al. 1977). The diameter of the dust particles ranges from ~1 to 10^{-3} μm with an open passage to the *Polycyclic Aromatic Hydrocarbons* (*PAHs*) (Gillett, Forrest & Merrill 1973; Leger & Puget 1984; Allamandola, Tielens & Barker 1985) at the lower end[v].

The dust grains in the ISM absorb a substantial fraction of the incoming radiation of stars (on average 1/3; Shull & Beckwith 1982; Kennicutt 2008; Draine 2011). Therefore, they contribute significantly to the shielding and the cooling of molecular clouds. The temperatures of the dust grains range from $\sim 10^1$ to 10^2 K. These low temperatures enable the gravitational bounding of molecular gas. Furthermore, dust grains are crucial for the formation of many molecules. The dust shields molecules from the penetrating UV radiation. Furthermore, the surface of icy dust grains serves as a catalyst to the formation of H_2 and therefore they are crucial for the bulk of the molecular mass in the ISM [vi]. The continuum emission of dust correlates well with the line emissions that are associated with molecular clouds and the CNM (e.g. Bohlin 1975; Hollenbach & Tielens 1999; Planck Collaboration et al. 2014a).

There are no sharp boundaries amongst the different phases of the ISM. In fact, the different phases interact in a highly dynamic way as they are commonly assembled at relatively small scales of a few 10^1pc to a few 10^2pc. These regions are commonly denoted as *Giant Molecular Clouds* (*GMCs*).

For a general overview of the allocation of the different phases see Figure 2.1.

The amount of dust and PAHs along the path of the photons is commonly expressed by the extinction of photons with a wavelength of λ=550

iv Olivine is assigned to the group of silicate minerals. Olivine particles of interstellar origin are collected by the 'Stardust' spacecraft (Westphal et al. 2014). The olivine particles of interstellar origin are thus the first to be examined in a laboratory. Presumably 36 interstellar dust grains, analysed by the Cosmic Dust Analyzer (Srama et al. 1996) of the Cassini space-craft, consist of olivine as well (Altobelli et al. 2016)

v For a detailed review of the interstellar dust I recommend Henning (2010)

vi The formation processes of molecular hydrogen are described in section 2.3

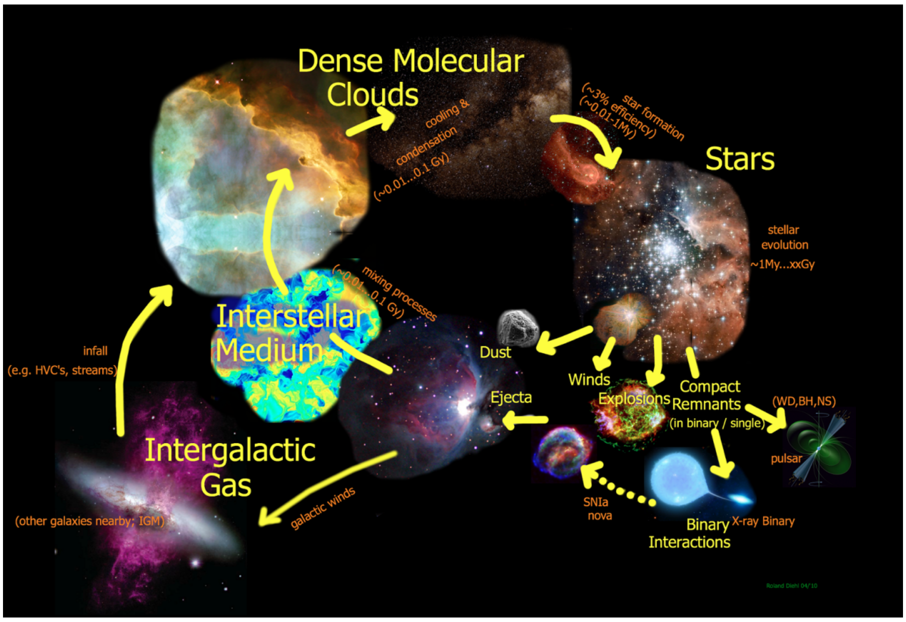

Figure 2.2: Schematic illustration of the 'life cycle of matter' in a modern spiral galaxy.
Credit: Roland Diehl, Max Planck Institut für extraterrestrische Physik

nm (green light). The extinction is described via $I(V) = I(0) \times 10^{\frac{A_\mathrm{V}}{2.5}}$, with A_v being the so-called *optical extinction* at 550 nm in the magnitudes unit (mag) and $I(V)$ being the visual intensity at a given A_v. If the ratio of dust to gas is constant, the optical extinction can be linearly correlated to the number of hydrogen nuclei along the path of the photons. In that case, the column density of hydrogen nuclei can be described via $N(\mathrm{H}) \approx 2{\times}10^{21}\ A_\mathrm{v}\ \mathrm{cm}^{-2}\ \mathrm{mag}^{-1}$. Interstellar clouds are often classified by their optical extinction, into diffuse, translucent and dense clouds (cf. e.g. Snow & McCall 2006). Diffuse clouds have a typical column density of $N(\mathrm{H}) < 2{\times}10^{21}\ \mathrm{cm}^{-2}$ (A_v<1 mag), dense (and dark) clouds have a typical column density of $N(\mathrm{H}) \sim 10^{22}\ \mathrm{cm}^{-2}$ (A_v>4 mag), while the column densities of translucent clouds are somewhere in between.

The different gas phases represent the different stages in the '*life cycle of matter in galaxies*' (Knapp 1995). The interaction between the stars, the ISM and the recycling of matter determines the physical and chemical composition of the ISM as well as the stars and thus the evolution of galaxies. Stars are formed by and consist of the matter of the ISM. In turn, the ISM consists (at least partially) of the repository of stellar ejecta (Tielens 2010)..

The diffuse phases of the ISM, such as the HIM, WIM and CNM, can be compressed to dense cold molecular regions (cf. Elmegreen 1996; Burton et al. 2013b), either triggered by a self-gravitational collapse of the clouds (Ostriker & Kim 2004), a collision of clouds (Kwan & Valdes 1987), converging flows in a turbulent medium (Hennebelle & Pérault 2000), by stellar winds and outflows[vii] and/or shocks induced by supernovae (McCray & Kafatos 1987). Currently it is a topic of research which of these processes are dominant. These dense molecular clouds can be considered as the birthplace of stars. The stars interact with the ISM via their ra-

vii I highly recommend Storey (1984) with regard to the physics of Protostellar outflows

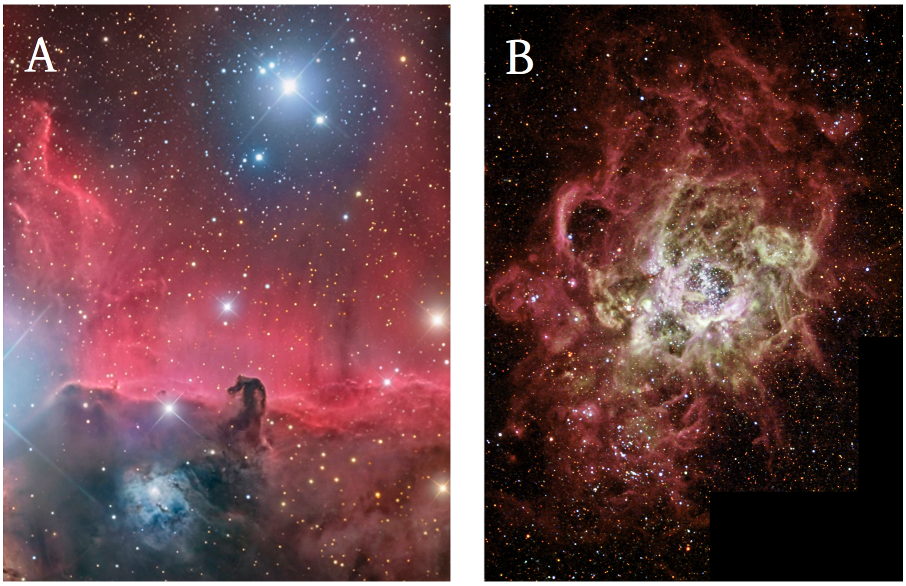

Figure 2.3: PDRs at the example of the Horsehead Nebula (alias Barnard 33, image A) and NGC 604 (image B).
Image A: The red glow around the Horsehead Nebula shows the Hα emission of the emission nebula IC 434. The UV radiation, penetrating the cloud, arises from the star cluster σ Ori at the top of the image. The stars cluster consists of stars with the spectral types O, B and A. **Credit:** M. Burali, T. Capecchi, M. Mancini (Osservatorio MTM)
Image B: NGC 604 is located in the nearby galaxy M33 (section 3.3). It is the second most massive HII region the Local Group after 30 Doradus. It hosts ~200 O and B stars (Hunter et al. 1996). Their UV radiation penetrates approximately half a dozen giant molecular clouds (e.g. Wilson & Scoville 1992; Churchwell & Goss 1999).
Credit: NASA and The Hubble Heritage Team (AURA/STScI)

diation, stellar winds or other ejected gas (e.g. as helium flash) or/and supernovae. These processes enrich the ISM with heavier elements which are synthesised inside the stars. Furthermore, they heat and disrupt the dense clouds [viii] which finally leads to the diffuse ISM again. Alternatively, these processes can compress the ISM and trigger new star formation[ix]. An atom roughly needs ~50-100 $\times 10^6$ years to cyclee through this loop in the solar neighbourhood ones (Molinari et al. 2014).

2.2 PHOTON-DOMINATED REGIONS

The following section focuses on the physical and chemical properties of *photon-dominated regions*, PDRs [x]. PDRs are almost ubiquitous in the ISM. They represent ~90% of its total molecular mass (Hollenbach & Tielens 1999). Therefore, it comes as no surprise that the majority of the sources studied in this thesis are photon-dominated regions as well.

This section is intended to provide a basic overview of PDRs. This is based on contributions made in Hollenbach, Takahashi & Tielens (1991), Sternberg & Dalgarno (1995), Hollenbach & Tielens (1999), Tielens (2010), Wolfire, McKee, Hollenbach & Tielens (2003), Wolfire, Hollenbach & Mc-

viii Typically, GMCs are disrupted when ~2-20% of the GMC-mass is transformed to stars (Molinari et al. 2014)
ix This 'life cycle of matter in galaxies' is illustrated in Figure 2.2
x The term 'photon-dominated regions' is coined by Sternberg & Dalgarno (1995). Photon-dominated regions are often denoted as *photo-dissociation regions* (likewise abbreviated as PDRs) Hollenbach & Tielens (1999),

Kee (2010), Röllig et al. (2006), Röllig et al. (2013).

The physics, chemistry and structure of major parts of the ISM is driven and defined by the penetrating UV radiation. The main source to the UV photons are O- and B-type stars. Ultraviolet photons with energies $h\nu$>13.6 eV ionize the hydrogen around these stars. These photons create HII-regions known as *Strömgren spheres*. Ultraviolet photons with energies between 6eV<$h\nu$<13.6eV[xi] are denoted as *Far Ultraviolet photons (FUV)*. These photons do not ionize hydrogen, but they do have enough energy to ionize other atoms and ions, as carbon for example, to photo-dissociate molecules (e.g. H_2 and CO) and to heat the dust. The connection between PDRs and O and B stars is not exclusive. PDRs can be produced by the average interstellar radiation field (ISFR) as well. Its strength is briefly discussed in the following section.

The strength of the penetrating FUV field is commonly expressed in multiples of the average ISFR near the sun and measured in *Habing units*[xii].

2.2.1 STRUCTURE OF A PDR

FUV photons interact with the ions, atoms, molecules and dust/PAHs particles in the molecular clouds in multiple ways. The FUV photons ionize atoms, photo-dissociate molecules and are absorbed by dust grains and PAHs. The strength of the FUV field is thus declining deeper into the cloud and the ISM is heated by the energy input of the penetrating FUV radiation.

The strength of the incident FUV fields influences many import aspects of the PDRs, such as its chemical compositions, the abundance of molecules, atoms and ions, the amount of free electrons and the temperature and densities. Therefore, a large number of chemical reactions in PDRs are triggered by the FUV radiation. For example, CO is photo-dissociated by FUV photons and C^0 is ionized to C^+. C^+ can capture an electron and recombine to C^0. C^0 can react with OH to CO (cf. Fig. 2.5).

PDRs possess different distinguished chemical zones for different A_v, each have specific prioritised chemical reactions. The abundance of the different molecules, atoms and ions can be roughly assigned to specific optical excitations. At specific FUV fields intensities, the destruction rate of a gas species is equal to its formation rate, forming a transition layer between the specific gas species.

The chemical transition zones of hydrogen, $H^+ \rightarrow H^0$ and $H^0 \rightarrow H_2$, as well as the transition zones of carbon, C^+, C^0 and CO, are commonly used to describe the structure within a PDR (cf. Fig. 2.4). The next paragraph will describe these layers and their transition zones. The de-

xi 6eV<$h\nu$<13.6eV; the lower limit is determined by the ionisation potential of dust/PAHs. The upper limit is given by the ionization energy of hydrogen.

xii Habing (1968) estimated the strengths of the IFRS to be 1.2×10^{-4} erg cm^{-2} sr^{-1}. This strength is commonly denoted as a '*Habing field*' in his honour. Draine (1978) showed that the strength of the average local ISFR is ~1.7 times higher than originally calculated, G_0= 1.7 Habing $\sim 2 \times 10^{-4}$ erg cm^{-2} sr^{-1}. The average local average interstellar radiation field of 1.7 Habing is often denoted as a '*Draine-field*', χ, in honour of Bruce T. Draine

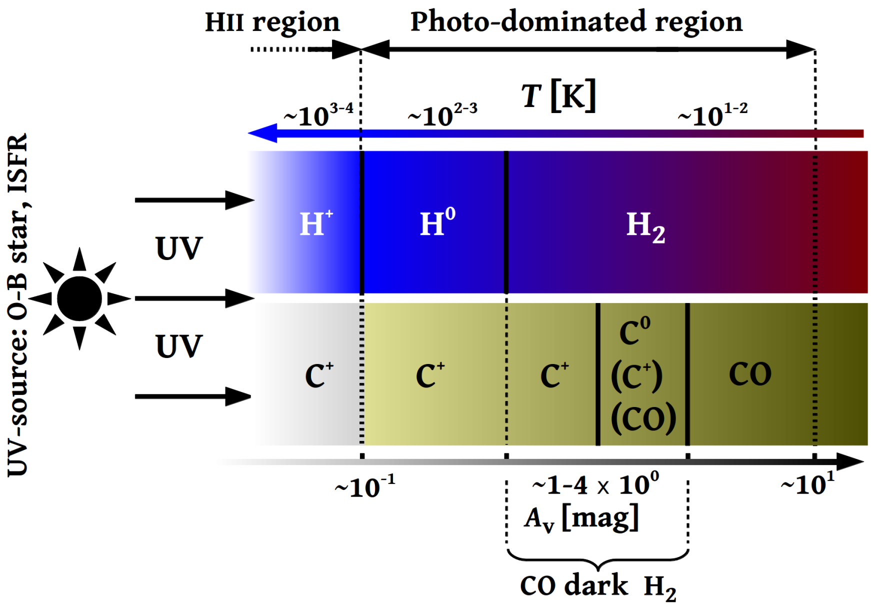

Figure 2.4: Schematic illustration of the hydrogen (upper panel) and carbon layers (lower panel) of a cloud, which is penetrated by UV-radiation from the left side. The region that is dominated by FUV radiation (Photo-dominated region) is marked by solid arrows at the top of the illustration. The visual extinction and total hydrogen column density is illustrated at the lower x-axis with increasing values towards higher distances from the surface of the PDR. The gas temperature rises towards the PDR-surface which is illustrated by the upper x-axis. C^+ is associated with the phases where the hydrogen is in its ionized, neutral atomic and molecular form. C^0 and CO is associated with H_2. The dotted line at the right shows a position where the cloud is stopped to be dominated by photons. At a higher A_v , CO starts to freeze out onto dust grains.

scription starts at the surface of the PDR and continues towards higher A_v.

The surface of a PDR is defined by the transition layer between H^+ and H^0. It is determined by an average FUV energy of 13.6 eV. That corresponds to an A_v~0.1 mag. Due to the high extinction rate, which is caused by the FUV radiation, only a few dust particles are present within the transition zone. Atomic ionized carbon is present at both sides of this layer. The next transition layer is the transition layer between H^0 and H_2. It is located at an $A_v \approx$1-2 mag. This transition zone is mainly controlled by 'self shielding' of H_2. Due to the large amount of molecular hydrogen in PDRs, H_2 can become optically thick ($N(H_2) \sim 10^{14} cm^{-2}$) and block all the photons which can photo-dissociate H_2 at larger cloud depths. Therefore, these photons are not present towards larger cloud depths. The self-shielding entails the effect that the H^0/H_2 transition layer is located at lower A_v than expected from the pure dissociation energy of the H_2 molecule of 4.48 eV. CO, for example, has a higher dissociation energy of 11.09 eV, while its transition layer is associated with higher cloud depths of A_v~2-4 mag (see below).

The transition layers between C^+, C^0 and CO are located between an A_v of ~2 to 4 mag, accordingly they are associated with a higher optical extinction than the H^0/H_2 transition layer. Carbon has an ionisation energy of 11.60 eV while CO is photo-dissociated at 11.09 eV. C^0 is expected to be within these boundaries. The transition layers of the photo-dissociation

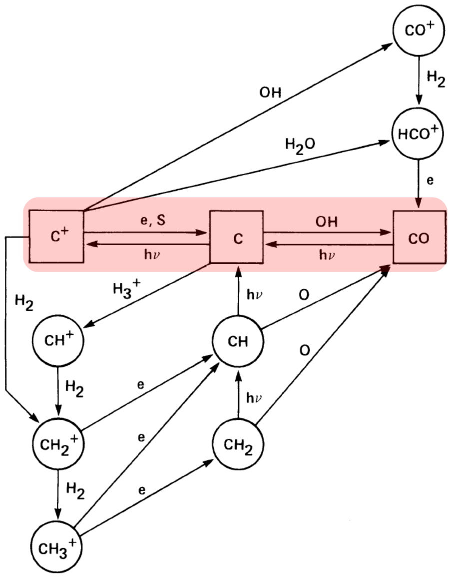

Figure 2.5: Simplified chemical network of major carbon bearing components in diffuse clouds and PDRs. The network between C^+, C^0 and CO is highlight by the red box. This chemical network is of high relevance in the context of this thesis.
Credit: Hollenbach et al. (1991)

of CO and C^+ can be moved to lower A_v by self-absorption[xiii]. The precise position of these transition layers are difficult to estimate and are still discussed in the current research debate. Various studies propose a $C^+/C^0/CO$ transition layer in which C^0 cannot be observed in the absence of C^+ and CO (e.g. Tielens & Hollenbach 1985a;b; Sternberg & Dalgarno 1989). Hollenbach, Takahashi & Tielens (1991), Wolfire et al. (2003) and Wolfire et al. (2010) propose an additional gas phase dominated by neutral atomic carbon[xiv]. These transition layers are of great relevance for this thesis.

Note that C^+ is associated with ionized, neutral atomic and molecular hydrogen, whereas C^0 and CO are associated exclusively with H_2. Molecular hydrogen, that is not directly associated with CO, is denoted as '*CO dark* H_2'[xv] (Leroy et al. 2011). The position of CO dark H_2 in a PDR is schematically illustrated in Figure 2.4.

The gas within the ISM has a no homogeneous distribution. It has a fractal structure (e.g. Elmegreen 1996). This fractal structure can be described by an ensemble of clumps. The distribution of the clump-masses as well as the relation of the clump size and mass, is described by a power law relation (Stutzki et al. 1998; Andree-Labsch et al. 2014).

2.2.2 HEATING AND COOLING PROCESSES

The following section describes the energy balance in PDRs. Various heating and cooling processes determine the energy balance of a PDR which finally determine the chemical and physical structure of PDRs as well. Different gas heating and gas cooling scenarios are shown exemplified in Fig 2.6, in this case referring to a plane-parallel PDR.

xiii [CII] self-absorption, for example, is observed towards NGC 2024 (Stutzki et al. 2013).
xiv Observations in M17 SW (Pérez-Beaupuits et al. 2015) as well as observations in M33 presented in this thesis, have found C^0 in the absence of CO
xv for further details see section 2.2.4

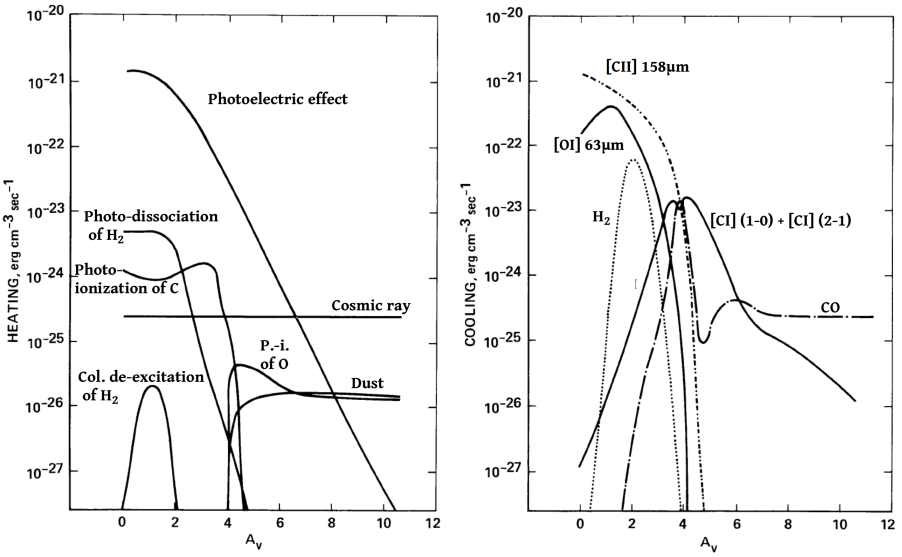

Figure 2.6: The image shows different gas heating (left) and gas cooling terms (right) A_{V} in a plan-parallel PDR (Hollenbach, Takahashi & Tielens 1991). The PDR has a constant density of n=10^3 cm^{-3} and an incident FUV flux of 10^3 Habing. CO illustrates the total cooling
Credit: Fig. 1 and 2 in Hollenbach, Takahashi & Tielens (1991)

2.2.2.1 Heating

The heating of a PDR is mainly dominated by the deposit of energy via FUV photons that interact with gas and dust particles within the clumps. FUV photons interact via multiple processes with these particles. Major heating processes are described in the following:

PHOTOELECTRIC EFFECT AND PHOTO IONIZATION The heating of PDRs is dominated by the photoelectric effect. When a FUV photon is absorbed by a dust grain or PAH, its energy is transformed into the kinetic energy of an electron. The electron is injected into the gas phase if the kinetic energy of the electron exceeds the coulomb potential and the work function of the grain. The excess of the kinetic energy is transferred to the kinetic energy of the other particles in the ISM via collisions which consequently heat the ISM.

The efficiency of the photo electric heating is at its maximum with a density of $\lesssim$3 $\times$ 10^3 cm^{-3} and a kinetic gas temperature of $T\lesssim$ 100 K. The heating amounts to about $\Gamma \simeq 5 \times 10^{-26}\, G_0$ erg (H-Atom)$^{-1}$ s^{-1}.

The ionization of carbon via FUV photons is an additional heating source of PDRs. These ejected electrons also are the major source of free electrons in PDRs.

COLLISIONAL DE-EXCITATION OF VIBRATIONAL EXCITED H_2 is an important heating process in these PDR-layers in which the hydrogen is mainly neutral atomic ($A_{\mathrm{V}}\lesssim$2 mag). Line absorbed FUV photons vibrational excite the H_2-molecules. At low densities (n $\lesssim$10^{-4} cm^{-2}) the excited states are de-excited to the ground vibrational state via a cascade of emitted infrared photons.

PHOTO-DISSOCIATION OF H_2 The photo-dissociation of $H_2$is another heating source. The surplus energy of the resulting two single hydrogen atoms is re-partitioned to the other particles of the ISM.

FORMATION OF H_2 ON DUST GRAINS This heating mechanism is of relevance for the inner regions of PDRs. H_2 is formed on dust grains[xvi]. The formation of a H_2 molecule releases a binding energy of 4.48 eV. This energy is used to release the molecule from the dust grain into the gas phase to rotationally excite the molecule and to increase its kinetic energy. If it is assumed that the energy is equally partitioned, 1.5 eV can be used to heat the gas (Röllig et al. 2013).

COSMIC RAY HEATING The cosmic ray heating is a major heating source at large clouds depths ($A_\mathrm{v}\gtrsim 6$ mag). At these A_v the FUV radiation is almost extinct, while the cosmic ray particles can also penetrate higher cloud depths ($A_\mathrm{v}\sim 100$ mag). The energy of the injected electrons is collisionally re-partitioned to the other gas components which heat the gas.

The penetrating cosmic ray heating amounts to $\sim 3 \times 10^{-27}$ erg (H-Atom)$^{-1}$ s^{-1}.

GAS-DUST GRAIN COLLISIONS AND TURBULENCE The collisions of gas particles and dust grains as well as the turbulent dissipation are other heating mechanisms.

2.2.2.2 Cooling

PDRs are cooled via the emission of continuum IR radiation of dust grains ($\sim$90%) and the emission of far infrared photons produced by fine-structure and rotational transitions ($\sim$10%). The necessary condition for the cooling via dust IR continuum radiation are collisions of dust grains, which are the case in the dense regions of the clouds[xvii]. In that case the temperatures of the dust and gas are coupled.

Due to the low number of dust grain collisions at low densities and high temperatures (diffuse gas), the cooling of the diffuse phases is dominated by the fine-structure transitions of ions. In this context the [CII] transition is worth mentioning, as it is *inter alia* the major coolant for diffuse H_2. The cooling via line transitions has a maximal efficiency in optically thin gas as the photons can leave the PDRs. If the gas is optically thick, the emitted photons can be reabsorbed. Thus, the dwell time of the energy within the clumps is increased.

The observation of line transitions is of great interest in all the different regions of the ISM, as these lines provide information about the kinematics within the sources. That is not the case for IR continuum emission from dust. The physic of fine structure and rotational transitions is described in section 4.1.

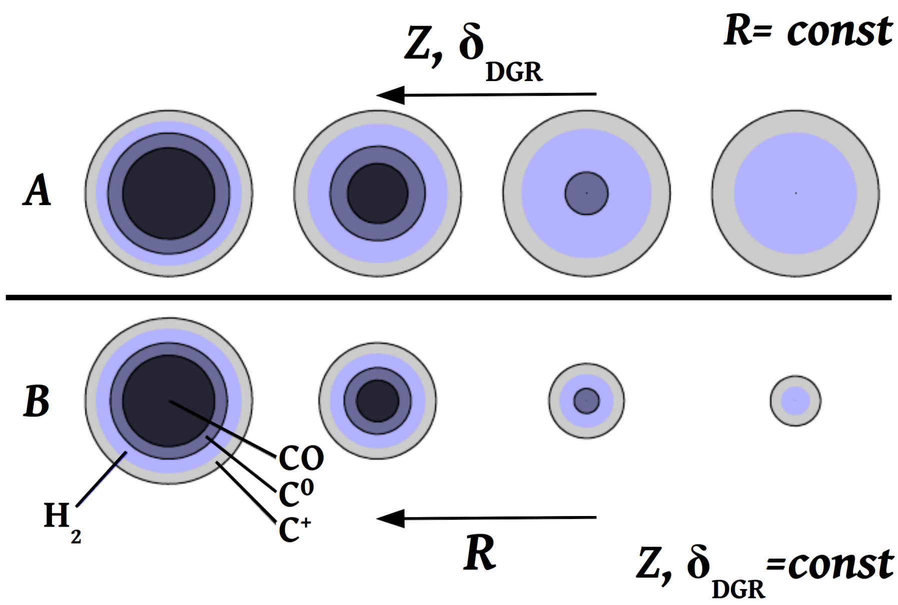

Figure 2.7: The image shows the effects of different metallicities, Z and the dust to gas ratios, δ_{DGR} (image A) as well as the effect of the clump size (image B) on the distribution of H_2 (blue), C^+ (grey), C^0 (blue-grey) and CO (dark blue-grey) on spherical clumps in an uniform radiation field. The radius of the clumps stays constant in image A, while the metallicity increases from the right to the left side to the image. Image B shows the effect of different clump sizes at a constant Z and δ_{DGR}.
Credit: Based on Fig. 8 in Bolatto, Wolfire & Leroy (2013)

2.2.3 METALLICITY EFFECTS AND DEFFECTS OF DIFFERNT CLUMP SIZES

The metallicity is of great importance for the structure and the composition of PDRs. Environments with a low metallicity have a lower dust to gas ratio compared to those with a high metallicity. In a low metallicity environment the average UV field generally has higher energies. In addition, the FUV radiation is less excited and can hence penetrate gas at larger clump depths. For example, in dwarf galaxies with a low metallicity ($Z{\sim}0.1\ Z_{\odot}$) almost ~10% of the incoming FUV radiation is absorbed by dust grains and re-emitted in the infrared. This value rises to more than 99% in the circumnuclear regions of many infrared-luminous galaxies (Kennicutt 2008). The FUV photons can hence ionize atoms and photo-dissociate molecules in larger clouds depths at low metallicities. The transition layers between the different chemical regions are consequently moved to higher distances from the cloud surface.

The width of the chemical layers, D, are effected by the metallicity as well. At low metallicities C^+ and C^0 fill a larger fraction of the volume within the PDRs, while the fraction of CO decreases. The width of the C^+ and C^0 layer are thus expected to increase, while the width of the CO zone decreases. The width of the C^+ layer is approximately inversely proportional to the metallicity, $D_{C^+} \propto Z^{-1.1}$ (Röllig et al. 2006). Under certain conditions, such as a strong UV-field, small clump sizes, low densities and low metallicities, all CO can be photo-dissociated. At low metallicities and at low clump masses the fraction of CO dark H_2 increases compared

xvi see section 2.3
xvii $n \gtrsim$ few $10^3 \mathrm{cm}^{-3}$, I like to refer to section 4.2 for further details

to clumps with a high metallicity and mass. At metallicities $Z \lesssim 0.1\ Z_\odot$ CO is only marginally observed in PDRs.

The effect of different metallicities on the distribution of C^+, C^0 and CO to clumps with a constant size in an uniform radiation field is illustrated in Figure 2.7. C^+ and C^0 transitions are assumed to be reliable tracers for H_2 at low metallicities.

The fraction of CO dark H_2 is affected by the size of the clumps, as well. Its fraction increases towards smaller clump sizes (therefore smaller mass surface densities as well) compared to larger clumps. In a constant radiation field, the widths of the CO core decreases towards smaller clump sizes and towards smaller clumps sizes, while the widths of the C^+ and C^0 layers remain constant, Therefore, the fraction of H_2 traced by C^+ and C^0 increases towards smaller clump sizes as well. The effect is illustrated in Figure 2.7.

2.2.4 FRACTION OF CO DARK H_2 IN PDRS

The following section discusses a method to estimate the fraction of CO dark H_2 as function of the metallicity and clump diameter. Wolfire et al. (2010) estimated the fraction of CO dark H_2 in a spherical GMC as function of the the metallicity, cloud density (measured in A_v), FUV field. Equation (A9) in Wolfire et al. (2010) derived the relative CO dark H_2 fraction via

$$\mathfrak{f}(\mathrm{DG})_{\mathrm{W10}} = 1 - \left[1 + \left(\frac{k_{æ} - 1}{3 - k_{æ}}\right) \frac{0.76\,\Delta A_{\mathrm{V,DG}}}{Z' N_{22}(\mathrm{H})}\right]^{-\frac{3-k_{æ}}{k_{æ}-1}} \tag{2.1}$$

with $k_{æ}$ being the power-law gradient of the mean density in the GMC, Z the metallicity in fractions of $Z_\odot$, $N_{22}(\mathrm{H})$=$N(\mathrm{H})_{\mathrm{tot}} \times 10^{-22}$, and $\Delta A_{V,DG}$ the extinction of the CO dark gas layer in the GMC.

Figure 2.8 shows the fraction of CO dark H_2 for different column densities and metallicities for constant $\Delta A_{V,DG}$ and $k_{æ}$. In the Milky Way roughly 1/3 of the H_2 is CO dark (Wolfire et al. 2010). This fraction increases to ~ 0.5 for a half solar metallicity.

2.3 H_2 FORMATION

H_2 is the most abundant molecule in the universe. H_2 is involved in a number of chemical processes. The formation of H_2 is thus of great interest. This section is mainly based on Tielens (2010) and Röllig et al. (2013).

H_2 is formed predominantly on the surface of dust grains, but can also be formed in the gas phase.

The formation of H_2 in the gas phase is generally of subordinate importance in the present universe, as these formation processes are slow. Excited molecular hydrogen, $H_2{}^*$[xviii] can be formed in the gas phase via the reaction of two H atoms ($H + H \rightarrow H_2{}^*$). Radiative transitions are strongly forbidden in H_2 (cf. section 4.1). The surplus energy has thus a long dwell time in the molecule, and the reaction occurs at a slow rate of $\lesssim 10^{-23}\ \mathrm{cm}^{-3}\ \mathrm{s}^{-1}$.

xviii The '*' indicates that the molecule is excited.

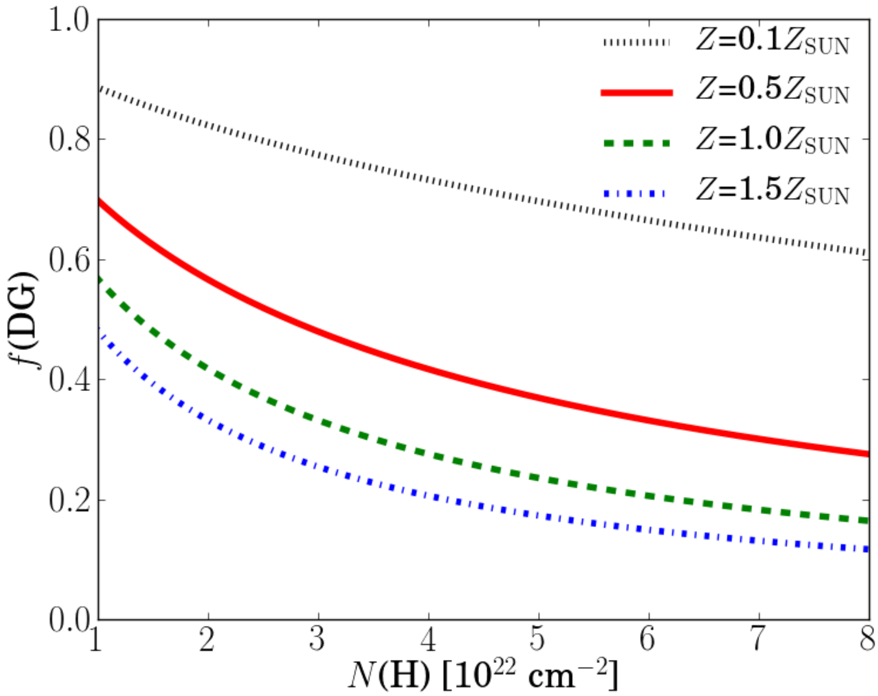

Figure 2.8: Fractions of CO dark H_2 as function the total hydrogen column density for metallicities of Z=0.1, 0.5 ,1.0 and 1.5 $Z_\odot$. The CO dark H_2fractions shown in this figure are calculated via equation 2.1 for a $\Delta A_{\rm V,DG}$ 2.2 and $k_{æ}$ = 2.2

Another H_2 formation process in the gas phase is the reaction of a H^- ion with H ($H^- + H \rightarrow H_2{}^* + e^-$). Due to the short life time of H^- in molecular clouds, this process is very slow as well[xix].

The formation of H_2 in the modern universe occurs predominantly on the surface of dust grains. Hydrogen atoms can stick to the grain surface via chemisorption and physisorption[xx]. The hydrogen atoms can move on the surface via tunnelling and thermal diffusion. At low temperatures ($T \lesssim 100$ K) the moving of physisorbed atoms via tunnelling-processes dominates, and vice versa the thermal diffusion of chemisorbed atoms at high temperatures ($T \gtrsim 100$ K). Excited H_2 is formed when a hydrogen atom meets a recombination partner. The surplus energy of the excited H_2 is largely absorbed by the dust-grain. A fraction of this surplus energy can been transformed into the kinetic energy of the H_2 molecules, which is needed to release the molecule into the gas phase.

A detailed description of the H_2–formation on dust grains can be found in Röllig et al. (2013).

xix This formation processes may have been of importance in the early universe (red-shift z $\gtrsim$ 6.5), before dust has been formed (Lepp & Shull 1984; Sobral et al. 2015).

xx Chemisorption designates the strong covalent bond between the atom and the grain surface. Physisorption denotes a weak bind interaction between the grain surface an the atom via the Van der Waals force.

Chapter 3

The Milky Way and M33

This thesis is based on observations in the Milky Way and the nearby galaxy M33. This section provides the reader with a short description of the these two galaxies. I will describe their morphology and basic physical parameters. First I will allocate these galaxies within the nearby universe.

3.1 THE LOCAL GROUP

Galaxies are assembled in groups and clusters. The Milky Way and M33 are members of the so called *Local Group*, which is a subgroup of the Virgo supercluster. The local group is a small group of galaxies of more than 50 galaxies (van den Bergh 2000a). Its most massive members are the spiral galaxies M31[i] (alias the Andromeda Galaxy), the Milky Way and M33 (alias Triangulum Galaxy[ii]). The other galaxies are small irregular dwarf galaxies. Most of them are satellites of M31 and the Milky Way. The Large Magellanic Cloud (LMC) and the Small Magellanic Cloud (SMC) are prominent satellites of the Milky Way. M33 might be a companion of M31[iii].

3.2 THE MILKY WAY

The Milky Way (MW) is a barred spiral galaxy (Chen et al. 1996), classified as SBbc (Benjamin et al. 2005) in the *de Vaucouleurs system* (de Vaucouleurs 1959). The diameter of the Milky Way is still discussed in current research debate. Its diameter is declared to be between ∼30 kpc Draine 2011) to ∼50 kpc (Xu et al. 2015). The Milky Way has a total baryonical mass of $\sim 5{\times}10^{11} M_\odot$ (Draine 2011).

The majority of the gas and dust in the Milky Way is assembled in its spiral arms. The structure of the Milky Way is not trivial to determine, as the solar system is located within the galactic disc. Although the first suggestion of a spiral arm structure of the Milky Way is dated back to the year 1852 (Alexander 1852) its exact composition is still disputed.

i M31 is the most massive galaxy in the Local group, with a mass of $\sim 1.5 \times 10^{12}$ $M_\odot$, followed by the Milky Way with a mass of $\sim 5{\times}10^{11} M_\odot$ and M33 with a total mass of 5×10^{10} $M_\odot$.

ii M33 is observed in the constellation Triangulum

iii see section 3.3

Four logarithmic main spiral arms (*Scutum–Crux(Centaurus)*, *Sagittarius–Carina*, *Perseus* and the *Norma* or *Cygnus/Outer* arm, respectively)[iv] have their origin at or near the outer edges of the bar(s) (Vallée 2008; Churchwell et al. 2009; Steiman-Cameron et al. 2010) at distances of $\sim$3 kpc from the galactic centre (Rodriguez-Fernandez & Combes 2008; Rodríguez-Fernández 2011). Note that resent estimations give a total bar half-length of up to $\sim$ 5 kpc (Wegg, Gerhard & Portail 2015). The existance of an elongated second bar is discussed (Nishiyama et al. 2005; Wegg, Gerhard & Portail 2015). The outer edges of the bars are connected by the two so called *3-kpc (expending) arms* (Rougoor & Oort 1960; Rodríguez-Fernández 2011). The Scutum-Centaurus and the Perseus arms are in general brighter and more massive than the Norma and Sagitarius arms. A kneed shape of the main spirals at distances $\gtrsim$9 kpc is suggested (Efremov 2010). Furthermore, the Milky Way consists of several spurs and bridges located between the main spirals. The solar system is located in the so called *Orion-Cygnus* spur. The precise distance between the galactic centre and the sun is still controversially discussed in current research debates, as the established standard methods have different problems and lead to different distances [v]. Recent studies set the distance to $R_{\mathrm{GC}}\sim$ 7 to 9 kpc (e.g. Bica et al. 2006; Vanhollebeke, Groenewegen & Girardi 2009). The present study uses the current IAU recommendation of R_{GC}=8.5 kpc (e.g. McClure-Griffiths & Dickey 2007). A schematically illustration of MW is shown in figure 1.2.

The main spiral arms of the Milky Way can be described by logarithmic spirals (von der Pahlen 1911; Danver 1942; Roberts, Roberts & Shu 1975; Vallée 2008; Steiman-Cameron et al. 2010)[vi] The spiral arms form a relativity thin warped disc (Kalberla & Kerp 2009). The thickness of the disc depends on the discussed gas phase[vii]. The molecular gas, for example, is assembled in a relative thin disc with a total width of $\sim$ 100 pc, while the WIM has an average thickness of $\sim$500 pc.

The metallicity within the Milky Way has a gradient along the galactic radius (e.g. Shaver et al. 1983; Ferrini et al. 1994; Peeters et al. 2002; Rudolph et al. 2006; Maciel & Costa 2010; Magrini et al. 2015)[viii]. Within the inner regions of the galaxies $R_{\mathrm{GC}}\lesssim$10 kpc the metallicity decreases from 12+log(O/H)$\approx$9 to 8.5 with a power slope of $\sim$-0.06 dex/kpc(Rudolph et al. 2006; Maciel & Costa 2010). The metallicity at the location of the

iv The designation of the spirals is ambiguous. Due to historical reasons the names of the spiral arms depend on their location at the sky, cf Fig 1.2.

v The distance to the galactic centre is commonly estimated via RR Lyr variables in the galactic bulge, the optical extinction at dust, and observations of globular clusters in the galactic halo, and the measurement of the trigonometric parallaxes of stars near the galactic centre using VLBI (e.g. Reid 1993; Bica et al. 2006; Groenewegen, Udalski & Bono 2008; Vanhollebeke, Groenewegen & Girardi 2009; Majaess 2010, Reid et al. 2014).

vi von der Pahlen (1911) showed for the first time that the spiral arms of M33, M51 and M74 can be described by logarithmic spirals. Danver (1942) concludes that the spiral of galaxies can be fitted by logarithmic spirals. The theoretical work by Roberts, Roberts & Shu (1975) showed that density waves within axisymmetric galaxies are described by logarithmic spirals as well. For further details see section 6.3.3.

vii The widths of the different gas layers, as well as the underlying physics, is discussed in detail in chapter 6.

viii The gradient was observed for the first time by Shaver et al. (1983). Rudolph et al. (2006); Maciel & Costa (2010); Magrini et al. (2015), who give current estimates of this gradient sun is 12+log(O/H) $\approx$ 8.7. Note that the slope of the gradient is less steep for $R_{\mathrm{GC}} \gtrsim$10 kpc. The metallicity decreases $\sim$-0.01 dex/kpc (Maciel & Costa 2010; Magrini et al. 2015). A metallicity gradient perpendicular to the galactic disc is observed as well (Ivezić et al. 2008; Schlesinger et al. 2012).

3.3 M33

The following section is dedicated to the spiral galaxy M33. I recommend the work by Hodge (2012) and Buchbender (2013) for further details.

The late type spiral galaxy M33 is classified as a SA(s)cd galaxy in the Vaucouleurs scheme. M33 is the third most massive galaxy in our Local Group, with a total mass of $\sim 5 \times 10^{10}$ $\mathrm{M}_{\odot}$ (Corbelli 2003). M33 is located at a distance of $\sim$840 kpc from the sun (Freedman, Wilson & Madore 1991)[ix]. An angle of $1''$ at the sky corresponds thus to $\sim$4.1 pc in M33. M33 is seen at a low inclination of $\sim$56° (Regan & Vogel 1994). The combination of the distance and the low inclination angle allows to study individual sources in an extragalactic source even with single dish telescopes, with a low depth along the line-of-sight.

M33 is a chemical young galaxy (Druard et al. 2014). The metallicity of M33 is about half solar and is roughly independent of galactic radius, R_{M33}. The oxygen-hydrogen abundance can be fitted by 12+log(O/H) $\approx$ 8.42 -0.03 R_{M33} (Magrini et al. 2009). Its metallicity is thus similar to those of the Large Magellanic Cloud (LMC; Pagel et al. 1978; Hunter et al. 2007). The fraction of the dust to the gas is relatively high, compared to the Milky Way. The dust to gas ratio is $\sim$170 to 290 (Buchbender 2013), while the Milky Way has a gas-to-dust ratio of $\sim$100 to 150 (Draine 2011) Roughly $\sim$6% of its total mass is gas, $\sim 3 \times 10^9$ (H^0, H_2, He) (Corbelli 2003).

The major axis of M33 has a length of $\sim$20 kpc ($\sim$84$'$) in the optical (Holmberg 1958) and a length of $\sim$30 kpc ($\sim$135$'$) in HI (van den Bergh 2000b). M33 has no perfect global spiral structure. The spiral structure is often described as 'flocculent' (Elmegreen et al. 2003; Hodge 2012; Buchbender 2013). The precise arm structure is still controversially debated, although this galaxy was one of the first cases where the spiral structure was examined (Danver 1942). Two distinctive spiral arms are observed in M33, a northern and a southern arm. These arms are pronounced in HII, as well in the submillimetre regime (e.g. Hermelo et al. 2016). The souther spiral can be described by a smooth logarithmic spiral, while the northern arm has a kneed structure[x]. The northern arm hosts a number of prominent GMCs and HII-region, i.a. NGC604, the second most massive HII-region in the local group[xi], with $\sim$200 O and B stars (Hunter et al. 1996). Besides these two spirals the ISM is relatively fractionated. Further fainter spiral arms are for example identified by Humphreys & Sandage (1980) and Regan & Vogel (1994). The current study examines individual GMCs on the northern and southern spiral and sources in the centre and a source north of the northern spiral arm.

ix The distance is determined via the photometry of Cepheid in M33
x The kneed structure of the northern spiral is discussed in section 7.6.2
xi The most massive HII-region in the local group is 30 Doradus, located in the Large Magellanic Cloud

The centre of M33 hosts no super massive black hole. The upper limit for a possible central black hole is $<2\times10^4$ $M_\odot$ (Lauer et al. 1998). The lack of a central massive black hole is suggested to explain the high star formation efficiency in M33, as a momentum to stabilize the structure is missing (Kormendy & McClure 1993; Lauer et al. 1998). Nevertheless, a source in its centre is worth to mention. The centre of M33 contains the most luminous steady X-ray source in the local group, M33-X8[xii].

M33 is thought to be closely associated with M31. These galaxies have a distance of $\sim$200 kpc (e.g. Galleti et al. 2004). A HI stream between both galaxies is observed (Braun & Thilker 2004). The stream is possibly formed by a close encounter of both galaxies 1 to 3 GYr ago (Braun & Thilker 2004; Putman et al. 2009). Tidal interactions between both galaxies are used to explain the warped outer disc of M33 (Corbelli, Schneider & Salpeter 1989; Putman et al. 2009). A halo of dwarf galaxies around M33 is not observed, which is uncommon for a spiral galaxy (e.g. Martin et al. 2009)[xiii]. Therefore M33 cannot be seen as an isolated galaxy.

M33 is denoted as a stepping stone between irregular objects, as the LMC and SMC, and late-type galaxy as the Milky Way or M31 (e.g. Druard et al. 2014), based on its spiral structure, relatively low metallicity and mass, the high dust to gas ratio, the high star formation efficiency and the missing halo of dwarf galaxies.

M33 is extensively studied within the frame work of the Herschel open time key project HERM33ES (Kramer et al. 2010; Boquien et al. 2011; Gratier et al. 2010; Mookerjea et al. 2012; Xilouris et al. 2012; Buchbender et al. 2013; Buchbender 2013; Druard et al. 2014; Mookerjea et al. 2016).

xii M33-X8 is formed by binary system of a star with $\sim$10 $M_\odot$ and a black hole with $\sim$70 $M_\odot$. It has a luminosity of $\simeq 2.2\times10^{39}$ erg/s (Peres et al. 1989; Takano et al. 1994; Lauer et al. 1998; Weng et al. 2009).

xiii The Milky Way and M31 have a halo of $\sim$20 to 30 dwarf galaxies (e.g. Martin et al. 2009; Belokurov et al. 2014).

Figure 3.1: Optical image of M33 observed with the VLT Survey Telescope (VST). *Credit*: ESO

Chapter 4

Studying the ISM with spectral line measurements

The interstellar medium includes a large number of molecules, atoms and ions. The Cologne Database for Molecular Spectroscopy[i] (CDMS) lists almost 800 entries for molecules and ions of astrophysical interest (Müller et al. 2001; 2005; 2008). All the different molecules, atoms and ions have different physical and chemical properties and origins. The understanding of their creation and destruction can shed light on the physical and chemical conditions of their environment. Of particular interest for this study are the (hyper-)fine structure and rotational transitions of H^0, C^+, $C^0$and CO. These transitions have low excitation energies. They are observed at (sub-)millimetre wavelengths. These transitions are excited even at low temperatures and are observed in the cold regions regions of the ISM. Thus, they provide an insight into the regions where stars are formed.

The following chapter describes methods that allow to derive physical parameters from observed lines. The special focus lies on methods to determine the column and volume density as well as temperature and pressure in the ISM. The described methods will be used within this thesis. In a first step, it is necessary to recapitulate the physics of electro-magnetic line transitions in molecules, atoms and ions.

Section 4.1 will briefly summarise the physics of line transitions, the excitation of molecules and atoms and the population of energy levels. Section 4.2 describes in which way the number of atoms in the line of sight (column density), can be derived from the observed line intensity. Methods to deduce the optical depths of a line, the pressure in the ISM and the strengths of the ambient UV field will be described in the following sections.

4.1 FINE STRUCTURE, HYPER-FINE STRUCTURE AND ROTATIONAL TRANSITIONS

This thesis is largely based on the observation and the analysis of the hyperfine transition HI, the fine structure transitions of ionised and neutral atomic carbon, and the rotational transition of carbon monoxide. The following thesis assumes that the reader is familiar with the physics of (hyper-)fine structure and rotational transitions. A good description of their physics can be found in Häsel & Neumann (1995) and Draine (2011). For the physics of ISM-related hyper-fine structure transitions, I also highly

i https://www.astro.uni-koeln.de/cdms/

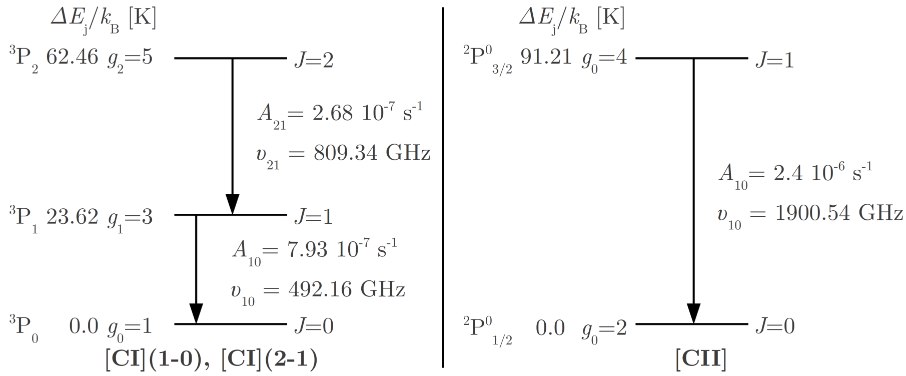

Figure 4.1: Fine structure transitions of the ground state of neutral atomic and single ionised carbon. g is the degeneracy of the energy level, $g = 2J{+}1$. $A_{\rm ul}$ is the Einstein A-coefficient of the specific transition. The energy difference between the energy levels, $\Delta E/{\rm k_B}$ and the frequency, ν, of the transition is shown as well. The figure is adapted from Draine (2011).

recommend the review by Bowen (1936).

Fine structure transitions are commonly denoted as *forbidden transitions*. In spectroscopic notation, these forbidden transitions are marked by squared brackets, '[ ]'. At this point, I would like to briefly shed light on the historical reasons where the term 'forbidden transitions' actually comes from. This aspect is commonly not elaborated in the literature.

Commonly fine structure transitions have low probabilities ($<10^{-3}$ s^{-1}; e.g. Eddington 1927; Bowen 1936 and CDMS). For a long time these transitions were not detected at normal lab conditions (e.g., Takamine & Fukuda 1924, Rayleigh 1927)[ii]. The fine structure energy levels are easily deexcited by collisions and, therefore, were not observed in laboratories. Due to the low densities within the diffuse ISM (few 10^{-1} to few 10^3 cm^{-3}), their excited states are not collisionally deexcited and, therefore, are observable in space. The first fine structure transition that was observed in space was the $^3P_1$ and $^3P_2$ transition of OIII in the chief nebular (Bowen 1927a;b). Therefore, transitions with a low probability are denoted as *forbidden transitions*. The term first appears in the astrophysical context in Foote et al. (1925) and Fowler (1927). In the meantime, forbidden transitions have been observed in laboratories as well. Examples are the transitions of single ionised carbon, [CII], (Cooksy et al. 1986)[iii] and the ground state fine structure transitions of neutral atomic carbon [CI](1–0) (Yamamoto & Saito 1991) and [CI](2–1) (Klein et al. 1998).

As already mentioned, the transitions of H^0, C^+, $C^0$and CO are of a great importance for this thesis. I will briefly discuss these transitions in the following. The transitions of molecular hydrogen and other symmetrical molecules will be discussed as well.

ii Takamine & Fukuda (1924) and Rayleigh (1927) searched for fine structure transitions in Mercury without success.

iii [CII] was detected in space for the first time by Russell et al. (1980) at a frequency of 1.91 THz. Its precise frequency (1.90 THz) was determined by Cooksy et al. (1986).

4.1.1 FINE STRUCTURE TRANSITION OF C^+

Single ionised carbon has the ground state configurations ${}^2P^0_{1/2}$ and ${}^2P^0_{3/2}$. The only possible fine structure transitions of the ground state, ${}^2P^0_{1/2} \rightarrow {}^2P^0_{3/2}$, has an energy difference of $\Delta E/k_\mathrm{B}$=91.3 K, resulting in line transition at $\Delta E/h$=ν=1.901 THz (λ=157.7 μm) (cf. Figure 4.1). In spectroscopic notation, this transition is denoted as [CII].

[CII] is the major cooling line in significant parts of the ISM. Carbon is singly ionised at 11.26 eV. This is below the ionisation energy of hydrogen of 13.60 eV. The ionisation energy of other elements is above the one of hydrogen. For example, nitrogen and oxygen possess ionisation energies of 13.62 eV and 14.53 eV. The [CII] line is thus, the dominant and almost ubiquitous present coolant for major phases of the neutral ISM (Dalgarno & McCray 1972; de Jong, Dalgarno & Boland 1980; Tielens & Hollenbach 1985a;b).

4.1.2 FINE STRUCTURE TRANSITIONS OF C^0

The ground configuration of neutral atomic carbon, ${}^3P$, is split into three fine structure levels: ${}^3P_0$,${}^3P_1$ and ${}^3P_2$. Therefore, two fine structure transitions are possible: ${}^3P_1 \rightarrow {}^3P_0$ and ${}^3P_2 \rightarrow {}^3P_1$. These transitions have energies of $\Delta E/k_\mathrm{B}$=23.6 K and $\Delta E/k_\mathrm{B}$=62.5 K and are observable at ν= 492.16 GHz and 809.34 GHz (cf. Figure 4.1). These transitions are denoted as [CI](1–0) and [CI](2–1).

4.1.3 HYPER-FINE TRANSITION OF NEUTRAL ATOMIC HYDROGEN, HI

The spins of the electron and proton in neutral atomic hydrogen are parallel or antiparallel. The energy difference between the antiparallel spin configuration and the parallel configuration (with a slightly higher energy) in the ground state is 5.87 $\times 10^{-6}$ eV $\equiv$6.82$\times 10^{-3}$K. This corresponds to the famous wavelengths of λ=21.1 cm respectively ν=1420.4 MHz[iv]. Due to the low energy needed, the excitation of the energy levels can be induced by the Cosmic Microwave Background ground radiation (CMB). In spectroscopic notation, this transition is denoted as HI. For historical reasons, HI is denoted without squared brackets, whereas the transition is 'forbidden'[v].

4.1.4 RATIONAL TRANSITIONS OF CO

Carbon monoxide is the second abundant molecule in space and the 'working horse' to study the dense cold regions in molecular clouds. Ground-state CO has a dissociation energy of 11.09 eV (e.g. Visser, van Dishoeck & Black 2009).

The energy difference between J=1 to J=0 is 5.53 K for ^{12}CO. Due to this low energy difference, CO excites even in the cold region of molecular clouds. This energy corresponds to a frequency of $\Delta E/h$=115.271 GHz.

iv van de Hulst 1945; Ewen & Purcell 1951; Muller & Oort 1951
v A_{10}(HI)=2.87 $\times 10^{-15}$ s^{-1}, c.f. Table 4.1

	ν [GHz]	A_{ul} [s^{-1}]	$E_{\mathrm{u}}/\mathrm{k_B}$ [K]
HI	0.142	2.877×10^{-15}	6.8×10^{-3}
^{12}CO(1–0)	115.271	7.20×10^{-8}	5.53
^{13}CO(1–0)	110.201	6.33×10^{-8}	5.29
^{12}CO(2–1)	230.538	6.91×10^{-7}	11.06
^{12}CO(4–3)	456.842	6.13×10^{-6}	21.92
[CI](1–0)	492.161	7.99×10^{-7}	23.62
[CI](2–1)	809.341	2.67×10^{-7}	62.46
[CII]	1900.537	2.32×10^{-6}	91.21

Table 4.1: Frequency, Einstein A coefficient and energy of transitions used in this thesis. The values are obtained from the CDMS.

The transition is commonly denoted as CO(1–0). Further CO transitions that are of relevance for this thesis are ^{13}CO(1–0), ^{12}CO(2–1) and ^{12}CO(4–3). The frequencies of CO transitions used in this thesis are listed in Table 4.1.

4.2 CALCULATING THE COLUMN DENSITIES IN LOCAL THERMAL EQUILIBRIUM

The following section is about a method that allows to determine the column density of a gas species from the observed line intensity in an assumed local thermal equilibrium (LTE). The argumentation is mainly based on Mangum & Shirley (2015).

In LTE, the energy levels of a system are in a statistical equilibrium. The level population of a multiple level system with the levels i and j can be determined by a matrix equation, in which the probabilities of the spontaneous and stimulated emission, absorption and collision between the energy levels are in balance. The probabilities of the spontaneous and stimulated emission, as well as of the absorption, are described by the *Einstein rate coefficients* A_{ij}, B_{ij} and Bji.

In thermal equilibrium, the upwards and downwards transitions within the system are in balance. The resulting relative population of the energy levels are described by the Boltzmann distribution,

$$\frac{n_u}{n_l} = \frac{g_u}{g_l} e^{-\frac{h\,\nu_{ul}}{k_{\mathrm{B}}\,T_{\mathrm{ex}}}} \tag{4.1}$$

with T_{ex} being the excitation temperature. The excitation temperature of a system is given by the mean of the kinetic gas temperature, T_{kin}, and radiation temperatures, T_{rad}, weighted with the relative radiative and collisional rate coefficients. At high densities, the population of the energy levels is dominated by collisions with other gas particles. The density in which the spontaneous emission is in equilibrium with the de-excitation by collisions is the so–called *critical density*. The critical density is given by (e.g. Goldsmith et al. 2012)

$$n_{\mathrm{crit}} = \frac{1-e^{-\tau}}{\tau} \frac{A_{\mathrm{ul}}}{C_{\mathrm{ul}}} \tag{4.2}$$

with τ being the optical depth of a cloud. The optical depth corresponds to the maximal path lengths in which a photon can travel before it is scattered or absorbed. The term (1-e$^{-\tau}$)/τ in Equation (4.2) describes the escape probability of a photon out of the cloud, the so-called opacity. At low optical depths ($\tau_\nu \ll$1), the medium is transparent and the whole volume of the medium is observable. At high optical depths ($\tau_\nu \gg$1), only photons from the surface of the medium are observed. At high densities, n$\gg n_{\rm crit}$, the $T_{\rm ex}$ is equal to the kinetic temperature of the gas. In this case the population of the energy levels is described by the Boltzmann distribution, and the gas is called *thermalised*. If n$\ll n_{\rm crit}$, $T_{\rm ex}$ is equal to the radiation temperature and the energy levels of the gas are *sub–thermally* excited.

The path of a photon through a medium is described by the radiative transfer equation. It equates the absorption and emission of the photons along the path. For further details I recommend Mangum & Shirley (2015).

The lines discussed in this thesis, have wavelengths of $\lesssim$10^{-3}m, and thus $h\,\nu \ll k_{\rm B}\,T$. Therefore, the Rayleigh–Jeans approximation can be used in the following. The radiative transfer equation in terms of the main beam radiation temperature of a source, $T_{\rm mb}$, in LTE for an assumed constant excitation temperature, is expressed by

$$T_{\rm mb} = \left(\mathcal{J}_\nu(T_{\rm ex}) - \mathcal{J}_\nu(T_{\rm BG})\right)\left(1 - e^{-\tau_\nu}\right)\varPhi_{\rm B} \tag{4.3}$$

with $\varPhi_{\rm B}$being the so–called beam filling factor and

$$\mathcal{J}_\nu(T) = \frac{h\nu}{k_{\rm B}}\left[e^{\frac{h\nu}{k_{\rm B}T}} - 1\right]^{-1}. \tag{4.4}$$

The beam filling factor is defined as the spatial fraction of a source within the beam. The term $\mathcal{J}_\nu(T_{\rm BG})$ subtracts possible background radiation from the observational data. For example, dust emission is an important background source. The Cosmic Microwave Background radiation (CMB) at $T_{\rm CMB}$≈2.73 K (Penzias & Wilson 1965; Planck Collaboration et al. 2014a)[vi] has to be considered for CO(1–0).

In the optically thin case $(1-e^{-\tau})\rightarrow\tau$. Using this approximation, Equation (4.3) can be transformed to

$$\tau = \frac{T_{\rm mb}}{\mathcal{J}_\nu(T_{\rm ex}) - \mathcal{J}_\nu(T_{\rm BG})\varPhi_{\rm B}}. \tag{4.5}$$

The Equations (4.4) and (4.3) allow to express the excitation temperature via $T_{\rm mb}$ and τ_ν

$$T_{\rm ex} = \frac{h\nu}{k_{\rm B}} \times \left[\ln\left((1-e^{-\tau})\varPhi_{\rm B}\frac{h\nu}{k_{\rm B}}\frac{1}{T_{\rm mb} + \mathcal{J}(T_{\rm CMB})} + 1\right)\right]^{-1}. \tag{4.6}$$

Vice versa Equation (4.6) can be solved for τ

$$\tau = -\ln\left(1 - \frac{k_{\rm B}}{\varPhi_{\rm B} h\nu}\left(T_{\rm mb} + \mathcal{J}(T_{\rm CMB})\right)e^{\frac{h\nu}{k_{\rm B}T_{\rm ex}}-1}\right). \tag{4.7}$$

vi First detection of the CMB by Penzias & Wilson (1965). The actual precise value is determined by Planck Collaboration et al. (2014a).

Both equations are used in chapter 7.

The column density of a molecule in the upper energy level u is defined as the integral of the number of molecules n along the pathlength s

$$N_u \equiv \int n_u \mathrm{d}s. \tag{4.8}$$

The number of molecules along the path is directly related to the optical depths τ_ν via

$$N_u = \frac{8\pi\nu^2}{c^2} \frac{1}{e^{\frac{h\nu}{k_\mathrm{B}T_{ex}}} - 1} \frac{1}{A_{ul}} \int \tau_\nu \mathrm{d}\nu. \tag{4.9}$$

To estimate the total number of molecules, N_tot, N_u has to be related to the population of all energy levels. The relation is given by

$$\frac{N}{N_u} = \frac{Q}{g_u} e^{\frac{E_u}{k_\mathrm{B}T_{ex}}} \tag{4.10}$$

with Q being the so–called partition function. The partition function gives the weighted sum over all energy levels. The partition function is given by

$$Q = \sum_u g_u e^{\frac{E_u}{k_\mathrm{B}T_\mathrm{ex}}}. \tag{4.11}$$

The combination of the Equations (4.10) and (4.9) gives the total column density

$$N_\mathrm{tot} = \frac{8\pi\nu^3}{c^3} \frac{Q}{g_u} \frac{1}{A_{ul}} \frac{e^{\frac{h\nu}{k_\mathrm{B}T}}}{\left(1 - e^{-\frac{h\nu}{k_\mathrm{B}T_\mathrm{mb}}}\right)} \int \tau_v \mathrm{d}v \tag{4.12}$$

where the relation $\mathrm{d}\nu = \frac{\nu}{c}\mathrm{d}v$ is used. This relation converts the integration over the frequencies to an integration over velocities.

The optical depth τ_ν is not directly measured. It is, therefore, of interest to express Equation (4.12) via the brightness temperature. The combination of the Equations (4.5) and (4.12) gives the total column density in the optically thin limit

$$\boxed{N_\mathrm{thin} = \frac{8\pi\nu^3}{c^3} \frac{Q}{g_u} \frac{1}{A_{ul}} \frac{e^{\frac{h\nu}{k_\mathrm{B}T}}}{\left(1 - e^{-\frac{h\nu}{k_\mathrm{B}T_\mathrm{mb}}}\right)} \frac{1}{\mathcal{J}_\nu(T_\mathrm{ex}) - \mathcal{J}_\nu(T_\mathrm{BG})\Phi_\mathrm{B}} \int T_\mathrm{mb} \mathrm{d}v}. \tag{4.13}$$

The total column density is given by

$$\boxed{N_\mathrm{tot} = \frac{\tau}{1 - e^{-\tau}} \times N_\mathrm{thin}} \tag{4.14}$$

with $\tau/(1 - e^{-\tau})$ being the correction term for the opacity.

The Einstein A coefficients used in this thesis are listed in Table 4.1.

For the sake of simplicity, concrete total column density equations for the CO transitions, as well as for [CI](1–0), [CII] and HI, are listed in Apendix A.

4.3 OPTICAL DEPTHS VIA ISOTOPE LINE RATIOS

The optical depth τ of a transition can be calculated numerically via the observed peak temperature of two isotopes $T_{\rm mb}$ and the relative isotope ratio. In the following, I discuss the examples of ^{13}CO and ^{12}CO. The relation of the ^{13}CO and ^{12}CO peak temperature and their optical depths τ_{12} and τ_{13} is given by

$$\begin{aligned} \frac{T_{\rm mb}\left(^{12}{\rm CO}(J_{\rm u}-J_{\rm l})\right)}{T_{\rm mb}\left(^{13}{\rm CO}(J_{\rm u}-J_{\rm l})\right)} &= \frac{1-e^{-\tau_{12}}}{1-e^{-\tau_{13}}} \\ \Leftrightarrow \frac{T_{\rm mb}\left(^{12}{\rm CO}(J_{\rm u}-J_{\rm l})\right)}{T_{\rm mb}\left(^{13}{\rm CO}(J_{\rm u}-J_{\rm l})\right)} &= \frac{1-e^{-x_{\frac{12}{13}}\times\tau_{13}}}{1-e^{-\tau_{13}}} \end{aligned} \tag{4.15}$$

with $x_{\frac{12}{13}}$ being the isotope ratio ^{12}C/^{13}C.

The isotope ratios are commonly determined via the intensity ratio of optically thin line transitions. Within the uncertainties of ~20%, the local interstellar medium has a $x_{\frac{12}{13}} \approx 70$ (e.g. Milam et al. 2005; Casassus et al. 2005). This ratio is no global constant. The ^{12}C/^{13}C ratio depends on the age of the gas. In particular, type II supernovae enrich the ISM with ^{12}C. This leads to a decrease of $x_{\frac{12}{13}}$ in regions with a higher supernovae rate. In consequence, ^{12}C/^{13}C ratio shows a radial gradient within the Milky Way with a lower $x_{\frac{12}{13}}$ towards the Galactic Centre. The isotope ratio can be approximated by $x_{\frac{12}{13}} \approx 6.2 \times R_{\rm GC} + 18.7$ with $R_{\rm GC}$ being the distance from the Galactic Centre in kpc (Milam et al. 2005).

4.4 CONVERSION BETWEEN VELOCITY INTEGRATED INTENSITIES AND LINE FLUXES

This section discusses the conversion between velocity (and frequency) integrated intensities I and fluxes $\mathcal{I}$. The velocity integrated intensities give the main beam brightness temperatures that are integrated over the width of a line. The flux of a line shows directly the energy that is received at the telescope. Two different lines with identical integrated intensity have different fluxes as the emitted energy is a function of the frequency. The flux $\mathcal{I}$ in the units erg cm^{-2} s^{-1} of a transition with a frequency ν can be calculated from the observed velocity integrated line intensity $\int T_{\rm mb}\,{\rm d}v$ = I(line) in K km s^{-1} via

$$\mathcal{I}(\text{line}) = \frac{2k_B\nu_i^3}{c^3} \times 10^5 \int T_{\rm mb}\,{\rm d}v = \mathcal{K}_{\rm line} \times\ I(\text{line}) \tag{4.16}$$

with $\mathcal{K}$ being a constant conversion factor for different line transitions. Conversion factors for important line transitions are listed in Table 4.2.

4.5 THERMAL INFRARED LUMINOSITY AND FAR UV FLUX

The following discusses a relation between the emitted thermal infrared luminosity, $L_{\rm TIR}$, and the penetrating far ultraviolet flux, FUV.

Far ultraviolet radiation is a major heating source of the ISM. In a first approximation, it can be be assumed that all incoming FUV radiation is

Transition	ν [GHz]	$\mathcal{K}$ [erg K^{-1} cm^{-3}]
HI	0.14	2.937×10^{-33}
^{12}CO(1–0)	115.3	1.570×10^{-9}
^{12}CO(2–1)	230.5	1.256×10^{-8}
[CI](1–0)	492.2	1.222×10^{-7}
[CII]	1900	7.035×10^{-6}
[NII]122μm	2459	3.196×10^{-6}

Table 4.2: Conversion factor, $\mathcal{K}$, for different line transitions, used to convert velocity integrated intensities, I, and fluxes,$\mathcal{I}$; $\mathcal{I} = \mathcal{K} \times \int T_{\rm mb}\,{\rm d}v$.

absorbed by the dust surface of a PDR. The dust cools via the emission of far infrared photons. The penetrating FUV flux is linear related to the $L_{\rm TIR}$ via (e.g. Mookerjea et al. 2012; Buchbender 2013)

$$G_0 = 4\pi 0.5 L_{\rm TIR} \tag{4.17}$$

with G_0 being the strength of the penetrating FUV field in units of Habing field (1.6×10^{-3} erg s^{-1} cm^{2}). $L_{\rm TIR}$ is in the units erg s^{-1} cm^{-2} sr^{-1}.

4.6 VOLUME DENSITY FROM THERMAL PRESSURE

The following section is about a method that estimates the hydrogen volume density based on the thermal pressure at the surface of a PDR.

The thermal pressure $P_{\rm therm}$ is directly proportional to the thermal energy of the gas particles $k_{\rm B}T$ and their density, n (e.g. Wolfire et al. 2003).

$$P_{\rm therm} \equiv 1.1 n \times k_{\rm B} T \tag{4.18}$$

If the heating is dominated by FUV radiation, as it is the case on the surface of a PDR (Section 2.2), it is possible to equate the penetrating FUV radiation and the thermal pressure within a cloud. Wolfire et al. (2003) gives the thermal pressure as function of the penetrating FUV Field G_0'=G_0/1.7 (in Habing units, 1.3×10^{-4} ergs s^{-1} cm^{-2} sr^{-1}), the dust / PAH abundance $Z_{\rm d}'$=$Z_{\rm d}/10^{-4}$, the gas-metal abundance $Z_{\rm g}'$=$Z_{\rm g}/10^{-4}$ and the total gas ionisation rate $\zeta_{\rm t}'$=$\zeta_{\rm t}/10^{-16}$ via

$$P_{\rm therm} = \frac{8500\, k_{\rm B}\, G_0' \frac{Z_{\rm d}'}{Z_{\rm g}'}}{\left(1 + 3.1 \left(G_0' \frac{Z_{\rm g}'}{\zeta_{\rm t}'}\right)^{0.365}\right)} \tag{4.19}$$

The volume density as function of the ambient FUV field is given by the combination of the Equations (4.18) and (4.19).

$$n \equiv \frac{P_{\rm therm}}{1.1\, k_{\rm B}\, T} \tag{4.20}$$

$$\simeq \frac{8500\, G_0' \frac{Z_{\rm d}'}{Z_{\rm g}'}}{\left(1 + 3.1 \left(G_0' \frac{Z_{\rm g}'}{\zeta_{\rm t}'}\right)^{0.365}\right) \times 1.1\, T} \left[{\rm cm}^{-3}\right] \tag{4.21}$$

This formula is valid for clouds in which the gas is in thermal balance, $T \lesssim$1000 K and the cooling of the gas is dominated by [CII] and [OII].

4.7 OPTICAL EXTINCTION

Bohlin et al. (1978) found a linear correlation between the colour excess $E(B\text{–}V)$ and the mean total hydrogen column density $N(\mathrm{H}) = N(\mathrm{H\,I} + \mathrm{H_2}) = N(\mathrm{H\,I}) + 2 \times N(\mathrm{H_2})$

$$\langle \frac{N(\mathrm{H})}{E(B-V)} \rangle = 5.8 \times 10^{21} \mathrm{cm^{-2} mag^{-1}}. \quad (4.22)$$

The optical extinction is related to the colour excess via (Savage et al. 1977)

$$A_\mathrm{v} = 3.1 \times E(B-V). \quad (4.23)$$

4.8 H_2 CONVERSION FACTORS

An established method to calculate the molecular hydrogen column density in GMCs is the use of carbon monoxide as a proxy for H_2. The molecular hydrogen column densities are commonly estimated by multiplying an H_2 conversion factor with the observed integrated line intensity of a low–J CO transition or [CI](1–0).

A number of studies of molecular clouds in the Milky Way, and in other disk galaxies with a similar metallicity, have found a power–law correlation between the viral mass of clouds and their emitted $^{12}C^{16}O(1\text{–}0)$ luminosity (e.g. cf. Solomon et al. 1987; Dame, Hartmann & Thaddeus 2001; Bolatto, Wolfire & Leroy 2013). This relation can be translated into a linear correlation between the molecular hydrogen column density $N(\mathrm{H_2})$ and the emitted velocity integrated $^{12}CO(1\text{–}0)$ emission $\int T_\mathrm{mb}(CO(1-0))\, \mathrm{d}v = I(\mathrm{CO}(1\text{–}0))$ as elaborated in Solomon et al. (1987). Dickman (1975) proposed to calculate the amount of molecular hydrogen in a cloud by scaling $I(\mathrm{CO}(1\text{–}0))$ with a H_2-CO(1–0) conversion factor X_CO

$$N(\mathrm{H_2}) = X_\mathrm{CO} \times I(\mathrm{CO}(1-0)). \quad (4.24)$$

$N(\mathrm{H_2})$ is in the units $\left[\mathrm{cm^{-2}}\right]$ and the integrated line emission in $\left[\mathrm{K\ km\ s^{-1}}\right]$. Within uncertainties of $\sim$30%, a X_CO=2×10^{20} cm^{-2} K km s^{-1} is established for the $^{12}C^{16}O(1\text{–}0)$ line in the Milky Way (Bolatto, Wolfire & Leroy 2013).

The CO-H_2 conversion factor does not show huge variations within the clouds of galaxies with a similar metallicity as in the Milky Way. This is explained by the relative constants of the cloud properties, such as temperature, surface density and velocity dispersion that determine X_CO (Narayanan & Hopkins 2013; Glover & Clark 2015).

A constant conversion factor described in the previous paragraph, may not be suitable for clouds with a high column density (Glover & Mac Low 2011; Carlhoff et al. 2013), strong UV-radiation (Weiß et al. 2001; Offner et al. 2014; Glover & Clark 2015) and/or low metallicity (Z) (Israel 1997; Gratier et al. 2010; Glover & Clark 2015). In the following, I will discuss the concrete impact of the metallicity on the H_2-CO conversion factor. I will also discuss alternatives to the 'standard' H_2-CO above mentioned as well.

In dense regions, ($A_\mathrm{v} \gtrsim$3-4 mag), ^{12}CO becomes optically thick and, hence, saturates. Conversion factors X_CO based on optically thin CO transitions (e.g. ^{13}CO, C^{18}O) are used in regions with a high A_v, as an alternative for a H_2–^{12}CO(1–0) conversion factor (e.g. Carlhoff et al. 2013).

Studies of Weiß et al. (2001), Offner et al. (2014) and Glover & Clark (2015) have shown that the H_2-CO conversion factor is deeply affected by the penetrating radiation field. In a strong UV field, as found for example in a starburst environment, the rotational levels of CO are populated at higher J than in a low UV field. Low–J are less populated. Hence, the CO emission of high–J CO transitions is higher and the emission of low–J CO lines is lower compared to a faint UV-field. In consequence, a constant H_2–CO conversion could underestimate the amount of H_2 (Weiß et al. 2001; Buchbender 2013). The precise influence on $X_{\rm CO}$ is hard to estimate. Simulations with the ORION adaptive mesh refinement code (Offner et al. 2013) and the PDR-code 3D-PDR (Bisbas et al. 2012) by Offner et al. (2014) and Glover & Clark (2015) show that $X_{\rm CO}$ is sensitive to the penetrating FUV-field. The conversion factor shows high fluctuations for different UV-fields. Offner et al. (2014) and Glover & Clark (2015) propose to use a H_2–[CI](1–0) conversion factor as [CI](1–0) is less affected by the ambient FUV-field (see below).

A large number of studies imply a significantly increased $X_{\rm CO}$ at low metallicities (Wilson 1995; Israel 1997; Madden et al. 1997; Leroy et al. 2009; Gratier et al. 2010; Glover & Mac Low 2011; Druard et al. 2014; Glover & Clark 2015). A lower metallicity results in a lower dust to gas ratio as elaborated in Section 2.2.3. In regions with a low dust to gas ratio dust absorbs less of the incoming UV-radiation. Besides the population of higher J energy levels, CO is easily photodissociated in strong UV fields[vii]. Thus, the fraction of C^0 and C^+ increases towards lower metallicities. The fraction of CO compared to C^0 and C^+ is, hence, lower at low metallicities. To compensate the missing CO, the H_2–CO conversion factor has to be higher at low Z. In first order, $X_{\rm CO}$ can be approximated by an inverse relation of the metallicity Z and the H_2–CO conversion factor (Wilson 1995)

$$X_{{\rm CO}\,Z} = \frac{X_{{\rm CO}-{\rm H}_2\odot}}{Z}. \tag{4.25}$$

Based on observations of low metallicity CO clouds in the LMC, SMC and other irregular galaxies, Israel (1997) establishes a link between the H_2–CO conversion factor and the far infrared luminosity. The correlation of the H_2–CO conversion factor with $L_{\rm TIR}$ can be explained by the relation between the far infrared luminosity and the FUV field (c.f. Section 4.5). For a half solar metallicity the H_2–CO conversion factor is given by (Buchbender 2013)

$$X_{\rm CO} = 1.17 \times 10^{20} \frac{L_{\rm TIR}}{10^6 \times L_\odot} \tag{4.26}$$

whereby $L_{\rm TIR}$ is the far infrared luminosity of the cloud and $L_\odot$ the luminosity of the sun.

Recent studies propose to use a H_2–[CI](1–0) conversion factor to calculate the total amount of H_2 in molecular clouds as an alternative to

vii The photodissociation energy of CO is 11.1 eV (e.g. Visser, van Dishoeck & Black 2009).

the H_2–CO conversion factor (Offner et al. 2014; Lo et al. 2014; Glover et al. 2015; Glover & Clark 2015). Carbon monoxide is not directly associated with all molecular hydrogen in molecular clouds as described above. This is emphasised in an environment with a low metallicity. [CI](1–0) is expected to be a more reliable tracer for H_2 at low metallicities. Furthermore this transition is expected to have an optical depth of $\tau \lesssim 1$ even in massive clouds as opposed to the ^{12}CO transitions. Furthermore, these simulations imply that a H_2–[CI](1–0) conversion factor is relatively invariant towards the penetrating FUV radiation (Offner et al. 2014) in opposite to the X_{CO}. According to these simulations, the H_2–[CI](1–0) conversion factor increases roughly ∼10 to 30% if the incoming FUV flux increases by a factor ten. These values were calculated for a solar metallicity. The increase changes to ∼100% for Z=0.5$Z_\odot$ (Glover & Clark 2015).

Simulations with the ORION adaptive mesh refinement code (Offner et al. 2013) and the PDR-code 3D-PDR (Bisbas et al. 2012) give a H_2-[CI](1–0) conversion factor of $X_{\mathrm{CI\,MW}}$=1.1 × 10^{21} cm^{-2} K^{-1} km^{-1} for the Milky Way (Offner et al. 2014). Adopting this conversion factor with Equation (4.25) gives a conversion factor of $X_{\mathrm{CI}\,0.5Z}$=$X_{\mathrm{CI\,MW}}$ /0.5 = 0.22 × 10^{22} cm^{-2} K^{-1} km^{-1} for a half solar environment. Glover & Clark (2015) calculated a H_2-[CI](1–0) conversion factor of ∼0.16 ×10^{22} s cm^{-2} K^{-1} km^{-1} for a metallicity of Z=0.5 $Z_\odot$ and radiation field strengths of G_0=1, a $X_{\mathrm{CI}\,0.5Z}$∼0.3 ×10^{22} s cm^{-2} K^{-1} km^{-1} for G_0=10 and a $X_{\mathrm{CI}\,0.5Z}$∼0.5 ×10^{22} s cm^{-2} K^{-1} km^{-1} for G_0=100.

After the explanation of the theoretical background, I will now pass to the scientific part of this thesis.

Part III

INVESTIGATING THE DISTRIBUTION OF CARBON IN THE MILKY WAY AND M33

Chapter 5

SOFIA/GREAT [CII] observations in nearby clouds near the lines of sight towards B0355+508 and B0212+735

The following section is dedicated to the composition and the energy balance of clouds which are identified as diffuse clouds, with relatively warm gas. This assumption is tested with [CII] observations at the example of clouds towards the line of sight to the quasars B0355+508 and B0212+735. The results are compared to the expected [CII] line intensities of warm diffuse clouds and in an ensemble of cold dense clumps.

A version of this chapter has been published in Glück et al. (2017).

5.1 INTRODUCTION

Interstellar clouds are classified as diffuse, dense or translucent (cf. e.g. Snow & McCall 2006 and Section 2.1). The composition of diffuse clouds has not been studied well, as these clouds are difficult to observe. Diffuse and translucent clouds have been identified mainly by means of their absorption spectra against bright mm-wave or optical background sources (Sonnentrucker et al. 2007; Burgh, France & McCandliss 2007; Sheffer et al. 2007; Sheffer, Rogers, Federman, Abel, Gredel, Lambert & Shaw 2008) and by optical extinction mapping (Savage et al. 1977). The conditions and composition within these clouds is currently a topic of research.

Liszt & Lucas (1998) succeeded in detecting CO(1–0) and CO(2–1) emission, identified to be associated with diffuse clouds because of their matching velocity characteristics with mm-wave absorption spectra, in a representative sample of mm-wave absorption lines-of-sight against background quasar sources. Liszt & Pety (2012) were able to map the CO (1–0) emission with a few arcminutes extent around these positions. The typical total hydrogen column density $N(\mathrm{H})=N(\mathrm{HI})+ 2\ N(\mathrm{H_2})$ in these clouds was derived to be a few times 10^{21} cm^{-2} with a typical H_2 fraction of $\lesssim 1/3$ (Liszt et al. 2010; Liszt & Pety 2012).

The observations show that the clouds in the sample of Liszt & Pety (2012) presumably located near the edge of the local bubble at distances of about 150 pc from the sun (Liszt & Pety 2012), are surprisingly highly structured with small scale, bright spots in CO, localised both spatially ($\lesssim$1× 10^{-2}pc) and spectrally ($\Delta v \sim$1-2 km/s).

Small scale CO variations were interpreted as variations in the chemistry, rather than density, or column-density variations in the clouds (Pety et al. 2011). The observed high line intensities of CO (1–0), typically I(CO)$\sim$5-20 K km/s, together with the observed, almost uniform, CO (J=2–1)/(J=1–0) integrated intensity ratio of around 0.725 (Liszt & Lucas 1998; Pety, Lucas & Liszt 2008a), were explained as sub–thermal excitation in a diffuse cloud (Goldreich & Kwan 1974; Pety, Lucas & Liszt 2008a) with kinetic temperatures above 30 K, typically $T \approx$40-80 K (Pety, Lucas & Liszt 2008a). Note here that the CO (J=2–1) vs. (J=1–0) line ratios observed in the clouds towards B0355+508 by Pety, Lucas & Liszt (2008a), however, are also consistent with the one expected in cold ($T \approx$ 14 K), dense gas (Pety, Lucas & Liszt 2008a). The CO spectra shown in Liszt & Lucas (1998) imply similar CO (J=2–1)(J=1–0) ratio for the clouds towards B0212+735 and B0355+508. The clouds further show a mean ^{12}CO/^{13}CO brightness temperatures ratio of $T(^{12}\text{CO})/T(^{13}\text{CO})\sim$ 10 to 15 (e.g. Pety et al. 2011). The ratio was explained by chemical fractionation of $^{12/1313}$CO and C^+ in diffuse clouds (Pety, Lucas & Liszt 2008b; Liszt, Pety & Lucas 2010; Pety, Liszt & Lucas 2011). In the diffuse cloud scenario the typical CO column densities are a few times 10^{16}cm^2. The derived hydrogen column densities N(H) in diffuse clouds of a few times 10^{21}cm^2 (cf. Section 5.4) implies that only about $\sim$ 4-7% of the carbon in diffuse clouds is in the form of CO (Sofia et al. 2004; Pety et al. 2011). Therefore, the majority of carbon ($\sim$ 90%) must exist in another form, presumably ionized carbon [CII] (Sofia et al. 2004; Liszt & Lucas 2000). Thus, the [CII] $^2P_{3/2} \rightarrow {}^2P_{1/2}$ fine structure transition at 1.9005369 THz is the major cooling line in the diffuse ISM (Dalgarno & McCray 1972; Tielens & Hollenbach 1985b). For the translucent regime the neutral carbon hyperfine transitions ($^3P_1 \rightarrow {}^3P_0$ and $^3P_2 \rightarrow {}^3P_1$) are expected to contribute up to $\sim$ 30 % of the [CII] cooling amount of the cloud cooling (Juvela et al. 2003).

These predictions provided the motivation to search for the [CII] emission from these clouds using SOFIA/GREAT.

5.2 OBSERVATIONS AND DATA PROCESSING

In November 2013 and February 2014 [CII] was observed in the interstellar clouds near the lines of sight towards B0355+508 and B0212+735 (cf. Table 5.1 and Fig. 5.1) using the dual-channel, single pixel, German REceiver for Astronomy at Terahertz frequencies (GREAT; Graf et al. 2006; Heyminck et al. 2012) onboard the airborne Stratospheric Observatory for Infrared Astronomy (SOFIA; Stutzki 2006; Becklin et al. 2007; Gehrz et al. 2009; Young et al. 2012). A Fourier transform spectrometer (FFTS), with 8192 channels and a bandwidth of 1.5 GHz was used, providing a native resolution of $\sim$0.03 km/s. The observations were performed in single-point total power mode.

Out of a sample of 5 sources, selected for their expected high [CII] brightness from the CO maps by Liszt & Pety (2012), B0355+508 and B0212+735 were selected as they matched the flight plan of SOFIA.

Source	(1) Center Position		(2) CO-peak rel. offsets		(3) CO-void rel. offsets		(4) Off-position rel. offsets	
	Ra (J2000)	Dec (J2000)	Ra ($''$)	Dec ($''$)	Ra ($''$)	Dec ($''$)	Ra ($''$)	Dec ($''$)
B0355+508	03:59:29.73	50:57:50.1	-7	-6	-57	+38	+190	+430
B0212+735	02:17:30.81	73:49:32.6	+47	-64	-187	+86	+607	+33

Table 5.1: Coordinates (J2000) of B0355+508 and B0212+735 (1). The rows (2) and (3) show the relative offsets to the CO-peak and CO-void. The relative offsets of the Off-positions are listed in row (4). Images of the integrated CO emission of the sources are shown in Fig. 5.1.

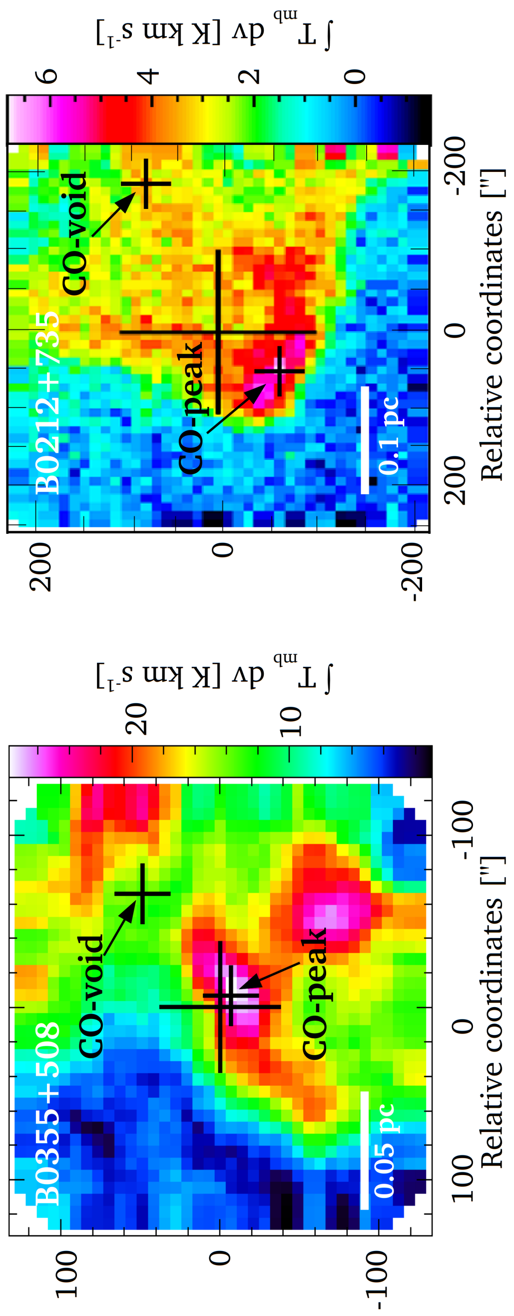

Figure 5.1: Integrated CO (1–0) emission around B0355+508 (Liszt & Pety 2012) and B0212+735 (Pety & Liszt in prep.). Small crosses mark the positions observed in [CII] . The large cross in the middle marks the line of sight towards B0355+508 and B0212+735. The length of the white bar corresponds to 0.05 pc in B0355+508 and 0.1 pc in B0212+735 for an assumed source distance of 150pc (Liszt & Pety 2012).

In each individual source two positions were observed. One position was centred on the brightest CO emission (CO-peak). The second position was pointed towards a region with faint, but clearly detectable, CO emission (CO-void). These positions are marked in Figure 5.1, and their coordinates are given in Table 5.1. This observation strategy was designed to collect information about the C^+ abundance and [CII] cooling in these clouds.

The off-source positions for B0355+508 and B0212+735 (coordinates see Table 5.1) were selected at regions with minimal 100 μm emission (IRAS, Neugebauer et al. 1984) and a minimal A_v (from $E_{\mathrm{B-V}}$ FIRAS/-COBE measurements, Schlegel et al. 1998). Due to their expected low column and volume densities these positions are hence likely to be free of detectable [CII]-emission. Additional CO(1–0) data of the B0212+735 off-position (Pety, priv. comm.) show these positions to be free of CO emission.

The actual allocation of telescopes does not allow any search for neutral carbon neither in B0355+508 and B0212+735, as both sources have a relative high declination in the northern sky [i]. Actually all Telescopes for [CI](1–0) (and [CI](2–1)) observations are located on the southern hemisphere exclusively[ii]. Therefore I searched for possible C^0 in clouds along the line of sight towards the quasar B0528+134 (Ra:05:30:46.41, Dec:12:31:55.1, J2000) as well. This cloud was within the sample of five sources that were proposed for the SOFIA/GREAT observations. This source has similar CO(1–0) and HCO^+ intensities as for the once found for B0355+508 and B0212+735. This source shows similar CO(1–0) and HCO^+ intensities as found in B0355+508 and B0212+735. The [CI](1–0) transition was observed towards this source in October 2014 in a 'footprint' of $110''\times220''$, with the Nanten2 telescope at the Pampa la Bola, Chile. The total on-source integration time was 52 minutes.

The [CI](1–0) observations were performed with the 460–490 GHz channel of the 2×8 pixel SMART receiver (Graf et al. 2002; 2008). The backends of SMART consist of sixteen eXtended bandwidth Fast Fourier Transfer Spectrometer (XFFTS; Klein et al. 2012) with a used bandwidth of 1 GHz and a spectral resolution of 76 kHz.

5.2.1 GREAT AND SMART DATA PROCESSING

The calibration of the SOFIA–data was performed with the standard pipeline for GREAT data (Guan et al. 2012). All spectra were converted to a main beam brightness temperature scale using $T_\mathrm{mb} = T_\mathrm{A}^*/\eta_\mathrm{mb}$, with a main beam efficiency η_mb=0.67 (Heyminck et al. 2012).

i Prominent submillimetre telescopes at the northern hemisphere that allowed [CI](1–0) observations in these sources were the Caltech Submillimetre Observatory (CSO) and the James Clark Maxwell telescope (JCMT, both located on the Mauna Kea on Hawaii). The CSO has closed for external observes in summer 2013 and the JCMT does not have any detector for the C^0 transitions.

ii [CI](1–0) and [CI](2–1) can be observed with the Nanten2 and APEX telescope, both located in the Atacama desert, Chile. Both [CI] transitions are observed from the Antarctica as well, for example with HEAT (Burton et al. 2014).

(1)	(2)	(3)	(4)	(5)
	$v_{\mathrm{LSR\ CO}}$	Δv_{CO}	$I(\mathrm{CO})_{\mathrm{P/V}}$	$I([\mathrm{C\,II}])$
	[km/s]	[km/s]	[K km/s]	[K km/s]
B0212+735				
CO-peak				
A_{P}	-16.9 ± 0.1	2.4 ± 0.1	6.4 ± 0.7	<0.3
B_{P}	-13.8 ± 0.1	1.2 ± 0.4	1.1 ± 0.8	<0.3
C_{P}	-9.8 ± 0.1	1.2 ± 0.1	20.0 ± 2.0	<0.4
CO-void				
A_{V}	-17.6±0.1	1.1±0.1	5.2±0.6	<0.5
B_{V}	-13.8±0.1	1.1±0.1	1.8±0.3	<0.5
C_{V}	-8.9±0.1	1.9±0.1	4.9±0.5	<0.6
B0212+735				
CO-peak				
G_{P}	3.5±0.1	1.4±0.1	8.4±0.9	< 0.5
CO-void				
G_{V}	2.3±0.1	1.8±0.1	5.5±0.6	< 0.4

Table 5.2: Observed upper limits of the integrated [CII] intensities compared to CO lines intensities of separated CO velocity components at the observed positions CO-peak and CO-void in B0355+508 & B0212+735.
(1) Designation of the individual velocity components. The CO-peak and -void positions are marked by the subscripts P and V, respectively.
(2) v_{LSR} of the CO component(s) in the sources.
(3) Width of the CO line.
(4) Integrated CO line intensity in the positions CO-peak and CO-void, labeled by the footnotes P and V
(5) Upper limits for the observed integrated [CII] intensity $I([\mathrm{C\,II}])$. To be able to estimate the upper limit of $I([\mathrm{C\,II}])$ it is assumed that the [CII] line is located at the same v_{LSR} as CO and that the [CII] line-width is equal to Δv_{CO}.

The [CII] and *[CI]* data were processed with the software package *CLASS, version: jan14a* [iii].

A fifth order baseline was subtracted from all spectra. In spectra that showed sinusoidal standing wave patterns, sinusoidal baselines with standing wave periods between 8 and 27 km/s were fitted to the spectra. If the fit improved the RMS by more than 1/5 compared to a linear baseline fit, the fitted sinusoidal pattern was subtracted from the spectrum.

The data for B0212+735 and B0355+508 were smoothed to 0.4 km/s and 0.8 km/s respectively, a factor ∼3 below the CO line widths, for better comparison.

The Nanten2/SMART [CI](1–0) data were average to a single spectra and smoothed to 0.4 km/s (cf. Fig. 5.4).

5.2.2 OBSERVATIONAL RESULTS

- **B0355+508:**
  Sixteen minutes integration time were spent on the CO-peak achieving a RMS of 0.09 K in a velocity bin of 0.8 km/s, corresponding to 1/3 of the line width of the brightest CO line. Two minutes of integration time were spent at the CO-void, achieving a RMS of 0.17 K. In both positions no [CII] emission was detected. The 3σ upper [CII] lines with widths corresponding to those of the CO lines thus are $\lesssim$0.37 K km/s for the CO-peak and $\lesssim$0.71 K km/s for the CO-void.

- **B0212+735:**
  About ten minutes integration time were spent on each position in B0212+735. A RMS of ≈0.21 K is reached in the CO-peak and ≈0.22 K in the CO-void in a velocity bin of 0.4 km/s, corresponding to 1/3 of the line width of the CO line of ∼1.5 km/s. Within the RMS no line could be detected. The 3σ upper limit for the [CII] line thus is $\lesssim$ 0.45 K km/s at both positions.

The listed 3σ limits are upper limits to the integrated [CII] line intensities, derived from the RMS of the velocity bins given. Additional smoothing of the data shows no signs for [CII] lines broader than the CO lines.

The averaged [CI](1–0) data of B0528+134 reached a RMS of 0.22 K in velocity bins of 0.4 km/s. No line could be detected within the RMS (cf. Fig. 5.4).

5.2.3 COMPLEMENTARY OBSERVATIONS

In the following sections three positions per cloud are discussed, the CO-peak (marked as P), CO-void (V), and the line of sight (Q) towards the quasar. CO(1–0) emission spectra are available for all positions. HCO^+ and HI absorption spectra are only available for the LOS towards the quasars.

iii available at http://www.iram.fr/IRAMFR/GILDAS

(1) cloud component	(2) v_{LSR} km/s	(3) Δv km/s	(4) $\int \tau(\mathrm{HCO^+})\, dv$ K km/s	(5) $I(\mathrm{CO})_{\mathrm{Q}}$ K km/s
LOS toward quasar				
B0355+508				
A_{Q}	-17.4	0.8	1.2 ± 0.1	5.1±0.5
B_{Q}	-13.9	1.6	1.3 ± 0.1	<0.2±0.1
C_{Q}	-10.4	0.6	1.3 ± 0.1	15.3±1.5
D_{Q}	-8.5	1.2	1.1 ± 0.1	<0.3±0.1
E_{Q}	-4.1	2.1	1.2 ± 0.1	<0.4±0.1
B0355+508				
F_{Q}	2.5	1.0	0.7 ± 0.1	–
G_{Q}	3.5	0.9	3.0 ± 0.4	11.0±2.4

Table 5.3: HCO^+ absorption and CO emission along the line of sight towards B0355+508 and B0212+735.
(1) Designation of the velocity components
(2) Center velocities of the HCO^+ absorption. For B0355+508 from Liszt & Lucas (2000). For B0212+735 from Lucas & Liszt (1996)
(3) FWHM of the HCO^+ absorption. From Lucas & Liszt (1996)
(4) For B0212+735 from Lucas & Liszt (1996). Some $\int \tau(\mathrm{HCO^+})$ for B0355+508 from Lucas & Liszt (1996) had slightly change in Liszt & Lucas (2000). I list the updated values from Liszt & Lucas (2000)
(5) B0355+508 data from Liszt & Pety (2012). B0212+735 data from Liszt & Lucas (1998)

The CO(2–1) and CO(1–0) emission spectra along the LOS towards the quasars have been observed by Liszt & Lucas (1998) and Liszt & Pety (2012). The CO(1–0) emission spectra towards the CO-peak and -void positions were extracted from maps with a few arcmin extent around the quasars observed by Liszt & Pety (2012) and (Pety & Liszt in prep.). As errors for the CO data standard calibration uncertainties of 15% are assumed.

HCO^+ absorption along the line of sight towards the quasars B0355+508 and B0212+735 have been observed with the Plateau de Bure Interferometer by Lucas & Liszt (1996) and Liszt & Lucas (2000). Complementary HI 21 cm absorption spectra towards the quasars are available from Dickey et al. (1983).

5.3 CO, HCO^+ AND HI IN B0355+508 & B0212+735

The following section describes the individual velocity components as seen in emission and absorption along the line of sight towards the quasars (Section 5.3.1 and 5.3.2). The association of these absorption components with corresponding CO emission components at the CO-peak and CO-void is discussed in Section 5.3.3 and 5.3.4.

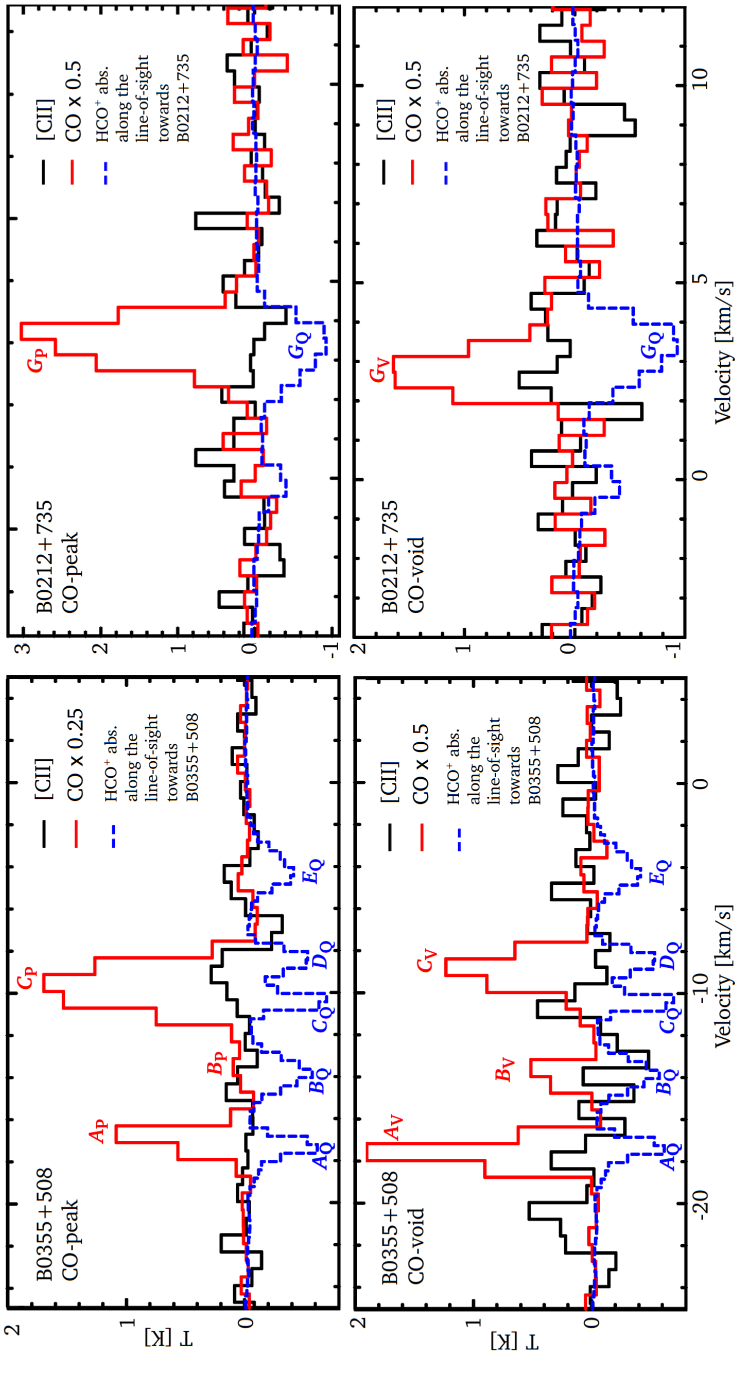

Figure 5.2: [CII] (black) and CO (red; Liszt & Pety 2012) spectra at the positions CO-peak and CO-void in B0355+508 (left) and B0212+735 (right). The spectra of B0355+508 are smoothed to a velocity resolution of Δv=0.8 km/s; B0212+735 spectra are smoothed to Δv=0.4 km/s. The blue dashed line shows the HCO$^+$ absorption spectra along the lines of sight towards the quasars B0355+508 and 0212+735 (Liszt & Lucas 1996; 2000). The red letters mark CO velocity components in the CO-peak and the CO-void, blue letters mark HCO$^+$ absorption components along the line of sight towards the quasar. Identical capital letters mark related velocity components in the three positions. For better clarity the HCO$^+$ absorption component F_Q at v_{LSR}=2.5 km/s in B0212+735 (cf. Table 5.3), which was identified by Lucas & Liszt (1996) is not shown.

5.3.1 THE LINE OF SIGHT TOWARDS B0355+508

B0355+508 is located at a Galactic latitude of b = -1.6°. This low Galactic latitude implies that several diffuse clouds are observed simultaneously along the line of sight.

The HI absorption features in the spectra are very broad. The line-width is ~55 km/s and the absorption is located between v_{LSR}≈-40 km/s and +10 km/s except for the molecular absorption features observed at v_{LSR}=-10 km/s and v_{LSR} = -8 km/s (velocity components C & D in Table 5.3) the HI the molecular lines (cf. Liszt & Pety 2012). This implies that a large amount of HI is in the foreground and background of the source.

The molecular absorption line profiles of CO(1–0) and HCO^+ show a complex structure along the line of sight towards B0355+508 (cf. Liszt & Pety 2012). Five individual HCO^+ components can be distinguished between v_{LSR}≃ -17 km/s and v_{LSR}≃ -5 km/s. Two CO emission components at v_{LSR}≈ -17.2 km/s and -10.3 km/s can be observed. They are associated with the two HCO^+ absorption velocity components A_{Q} and C_{Q} (Table 5.3).

5.3.2 THE LINE OF SIGHT TOWARDS B0212+735

B0212+735 is located at a galactic latitude b~12°. Two prominent HI absorption features can be observed in B0212+735 (cf. Liszt & Pety 2012). The largest amount (~ 80%) of HI v_{LSR} ~ -12 km/s (cf. Liszt & Pety 2012). Roughly 20 % of the totalHI absorption arises from a fainter HI absorption component, located at ~ +4 km/s. Interestingly, all molecular absorption lines and the CO emission line are located in the velocity range of the fainter HI absorption component. No molecular absorption line lies within the strong HI absorption feature. Lucas & Liszt (1996) identified two close-by narrow HCO^+ absorption lines at v_{LSR}=2.5 and 3.5 km/s by using a Gaussian decomposition of the line profile (components F_{Q} and 'G_{Q}' in Table 5.3), whereby the majority of the absorption arises from the component G_{Q}. Due to similar velocities, the CO emission component at this position (Liszt & Lucas 1998) can be associated with the HCO^+ absorption component G_{Q} at 3.5 km/s.

5.3.3 CO-PEAK & CO-VOID OF B0355+508

At the CO-peak of B0355+508 two bright spectral components can be observed in CO (components A_{P}, and C_{P}; cf. Fig. 5.2 and Table 5.2). These components are associated with the components A_{Q} and C_{Q} along the line of sight towards B0355+508 (Table 5.3). A possible third faint CO component (B_{P}) may be associated with the HCO^+ absorption component B_{Q} (cf. Fig. 5.2 and Table 5.2).

Similar to the CO-peak three spectral CO-components can be resolved at the CO-void, A_{V}, B_{V} & C_{V}, which are associated with the CO and HCO^+ components along the line of sight towards the quasar analogous to their counterparts at the CO-peak. (cf. Table 5.2 & 5.3 and Fig 5.2).

5.3.4 CO-PEAK & CO-VOID OF B0212+735

The CO-peak position shows one prominent CO component (G_P) at v_{LSR}=3.5 km/s with a width of $\Delta v \approx$ 1.4 km/s. It is located within the HCO^+ absorption features. The same component appears in the CO-void G_V), although at a slightly lower velocity of v_{LSR}= 2.3 km/s.

In conclusion, all CO emission spectra at the observed positions are associated with HCO^+ absorptions along the lines of sight towards the quasars, while not all HCO^+ absorptions are associated with CO emission velocity components. Liszt & Pety (2012) took this discrepancy as an indication that the ^{12}CO(1–0) spatial distribution maps chemical fluctuations and not the cloud density.

5.4 HYDROGEN DENSITIES

In the following section I discuss the amount of molecular, neutral and total hydrogen in the observed clouds. The calculations of the molecular hydrogen column densities $N(H_2)$ from the HCO^+ absorption and CO emission are based on two different approaches.

- In the interpretation of Liszt & Lucas (2000) the molecular hydrogen densities derived from the HCO^+ absorptions are representative for the densities of the whole cloud. The CO intensity fluctuations in the specific CO-maps were interpreted as local variations in the cloud chemistry, induced by local changes of the ambient physical circumstances, as for instance temporary dissipation of turbulent energy, not as variations of the cloud density (Liszt & Lucas 2000; Liszt & Pety 2012). As a consequence, regions with a low CO abundance should have a higher C^+ abundance than regions with a high CO abundance (Liszt & Lucas 2000, cf. Section 5.5).
- Alternatively, deriving the molecular hydrogen column $N(H_2)$ from the CO line integrated emission is based on the assumption that the CO-maps trace the intrinsic density structure of the source. In that case the position with a high CO emission would have a high column density as well. In consequence also the [CII] emission would be higher in these positions, as I([CII]) is proportinal to the N(H) (cf. Section 5.5 and 5.6).

The following sections estimates the integrated [CII] intensities that are expected in these two scenarios. Alternatives to explain the non-detection of [CII] reported here are also discussed . First I review the different ways that were previously used to estimate the amount of molecular hydrogen in these clouds from HCO^+ absorption and CO emission (Section 5.4.1). Section 5.4.2 discusses the estimated molecular and total hydrogen column densities in the positions. Section 5.5 tests and discusses these two approaches by estimating the expected integrated [CII] intensities. Finally Section 5.6 offers an alternative scenario to explain the observations.

(1)	(2) $N(H_2)_{CO_Q}$ cm^{-2} 10^{20}	(3) $N(H_2)_{HCO^+}$ cm^{-2} 10^{20}	(4) $N(H)_{HCO^+}$ cm^{-2} 10^{21}	(5) $n(H)_{HCO^+}$ cm^{-3} 10^{3}	(6) $N(H_2)_{CO_P}$ cm^{-2} 10^{20}	(7) $N(H)_{CO_P}$ cm^{-2} 10^{21}	(8) $n(H)_{CO_P}$ cm^{-3} 10^{3}	(9) $N(H_2)_{CO_V}$ cm^{-2} 10^{20}	(10) $N(H)_{CO_V}$ cm^{-2} 10^{21}	(11) $n(H)_{CO_V}$ cm^{-3} 10^{3}	(12) $N(\text{HI})_{tot}$ cm^{-2} 10^{20}
		LOS toward quasar				**CO-peak**			**CO-void**		
	B0355+508										
A	10.4±1.1	4.3± 0.7	2.5±0.4	5.3±0.9	13.1±1.4	2.6±0.3	5.7±0.6	10.6±1.1	2.1±0.5	4.6±0.6	**62.8**
B	< 0.4±0.1	4.7 ±0.7	2.7±0.4	5.8±0.9	2.2±1.6	0.4±0.3	1.0±0.7	3.7±0.5	0.7±0.2	1.6±0.4	
C	31.2±3.1	4.7± 0.7	2.7±0.4	5.8±0.9	40.8±4.1	8.2±0.8	17.5±1.8	10.0±1.1	2.0±0.5	4.3±0.4	
D	<0.6±0.1	4.0± 0.7	2.3±0.4	4.9±0.9	–	–	–	–	–	–	
E	<0.8±0.1	4.3± 0.7	2.5±0.4	5.3±0.9	–	–	–	–	–	–	
	B0212+735										
F	–	2.4 ± 0.4	1.4±0.2	1.5±0.2	–	–	–	–	–	–	**16.8**
G	22.5±4.8	10.8 ± 1.4	6.2±0.8	6.7±0.9	17.1±1.8	3.4±0.4	3.7±0.4	11.2±1.3	2.2±0.2	2.4±0.3	

Table 5.4: Molecular, neutral and total hydrogen column densities and volume densities in the positions CO-peak, CO-void and the LOS towards the quasars. Estimated molecular and total hydrogen column densities and volume densities along the line of sight toward the quasars and in the positions CO-peak and CO-void. The footnotes CO and HCO^+ note the underlying method used to derive these values. The CO-footnotes Q, P, V represent the positions LOS towards the quasar, CO-peak and CO-void.
(1) Designation of the assigned velocity components.
(2), (6) & (9) Molecular hydrogen column density derived from the CO emission by the use of Equation (5.4). Liszt et al. (2010) gives a $N(H_2)_{CO}$ of $N(H_2)_{CO} \approx 35\times10^{20}$ cm^{-2} for the LOS towards B0355+508. This value corresponds to the $N(H_2)_{CO}$ derived for the component C along the line of sight towards B0355+508.
(3) Molecular hydrogen column density derived from the HCO^+ absorption along the line toward the quasar by the use of Equation (5.3). The here calculated $N(H_2)_{HCO^+}$ for the components towards B0355+508 are consistent with the $N(H_2)_{HCO^+}$ given by Liszt et al. (2010) of $N(H_2)_{HCO^+} \approx 4.5\times10^{20}$ cm^{-2}.
(4) Total hydrogen column derived from $N(H_2)_{HCO^+}$ and an assumed H_2 fraction of 35%; $N(H)_{HCO^+} = 5.7\times\ N(H_2)_{HCO^+}$
(7) & (10) Lower limits of the total hydrogen column density derived from the CO emission; $N(H)_{CO_{P/V}} = 2\times N(H_2)_{CO_{P/V}}$. The (unknown) contribution of HI to the total amount of hydrogen is not considered
(5), (8) & (11) volume hydrogen densities, derived by dividing $N(H)$ by the assumed cloud diameter d_C for an assumed cloud distance of 150 pc (d_C(B0355+508)=0.15 pc, d_C(B0212+735)=0.3 pc); $n(H)=N(H)/d_C$
(12) Total HI column density of the cold interstellar gas along the lines of sight towards the quasars. From Dickey et al. (1983)

5.4.1 CALCULATING MOLECULAR HYDROGEN DENSITY

The total hydrogen column density can be estimated via the optical extinction $E_{\mathrm{B-V}}$ using equation (4.22)[iv] (Bohlin et al. 1978; Rachford et al. 2009; cf. Section 4.7).

By using this, the molecular hydrogen column density in diffuse clouds can be derived from $\mathrm{HCO^+}$ column densities and using some additional arguments (Liszt & Lucas 1996; Liszt et al. 2010), as follows:

The optical extinction of diffuse clouds shows a correlation to the optical depth of $\mathrm{HCO^+}$ with

$$\int \tau(\mathrm{HCO^+})[\mathrm{Kkm/s}] \simeq 2 \times (E_{\mathrm{B-V}})^{0.7}[\mathrm{mag}] \tag{5.1}$$

This equation is derived from Liszt et al. (2010). The $\mathrm{HCO^+}$ column density $N(\mathrm{HCO^+})$, in turn, can be calculated from the optical depth using the relation.

$$N(\mathrm{HCO^+}) = 1.12 \times 10^{12}\mathrm{cm^{-2}} \int \tau(\mathrm{HCO^+})\mathrm{d}\nu \tag{5.2}$$

Liszt, Pety & Lucas (2010) derived an $\mathrm{H_2}$ fraction of typically $f(\mathrm{H_2})$= 2 $N(\mathrm{H_2})/(2\ N(\mathrm{H_2})\ +\ N(\mathrm{H^0}))$ =0.35 for the clouds, discussed here. The molecular hydrogen column density $N(\mathrm{H_2})$ in diffuse clouds can then be approximated by the combination of Equation (4.22), (5.1) and (5.2) via (Liszt, Pety & Lucas 2010; Liszt & Pety 2012).

$$N(\mathrm{H_2})_{\mathrm{HCO^+}} \approx \frac{N(\mathrm{HCO^+})}{8 \times 10^{-10}\left(2 + \frac{1-f(\mathrm{H_2})}{f(\mathrm{H_2})}\right)} = \frac{N(\mathrm{HCO^+})}{3.1 \times 10^{-9}} \tag{5.3}$$

The last equation refers to an assumed $\mathrm{H_2}$ fraction of $f(\mathrm{H_2})$=0.35. The molecular hydrogen column densities derived from the $\mathrm{HCO^+}$ observations are listed in Table 5.3.

Alternatively, the molecular hydrogen column density in diffuse clouds can be estimated from the integrated CO(1–0) line intensity by use of a $\mathrm{H_2}$–CO conversion factor X_{CO} (c.f. Section 4.8)

$$N(\mathrm{H_2})_{\mathrm{CO}} = X_{\mathrm{CO}} \times I(\mathrm{CO}) \tag{5.4}$$

Liszt et al. (2010) derived a $X_{\mathrm{CO}} = 2.04 \times 10^{20}\ \mathrm{cm^{-2}}$ for diffuse clouds. Note that this value is coincidentally equal to the mean $\mathrm{H_2}$–CO conversion factor measured in the Milky Way (Bolatto, Wolfire & Leroy 2013)[v], which is discussed in Pety, Liszt & Lucas (2011).

5.4.2 NEUTRAL, MOLECULAR AND TOTAL HYDROGEN DENSITIES IN B0355+508 AND B0212+735

Table 5.4 summarizes the molecular hydrogen column densities for the individual velocity components derived with equations 5.3 and 5.4. For almost all CO velocity components in all discussed positions the derived $N(\mathrm{H_2})_{\mathrm{CO}}$ exceeds the $N(\mathrm{H_2})_{\mathrm{HCO^+}}$ of their counterparts along the line of

iv $N(\mathrm{H})$=5.8 × 10^{21} H $\mathrm{cm^{-2}}$ $E_{\mathrm{B-V}}$
v See also Section 4.8

sight to the quasar derived from the HCO^+ absorptions. If the densities in the observed clouds are roughly constant, the CO velocity components would overestimate the expected amount of molecular hydrogen by up to a factor of ~10 (e.g. velocity component C in B0355+508). On the other hand CO would significantly underestimate the amount of molecular hydrogen for HCO^+ velocity components which have no or only faint corresponding counterparts in CO. In that case it can by expected, especially for the velocity components B_P, B_V, E_P, E_V and G_V a relatively bright [CII] emission

If the CO emission traces the intrinsic density structure of the source, the [CII] emission should have a distribution similar to the CO emission.

The total amount of HI in the cold interstellar gas along the lines of sight towards the quasars is listed in Table 5.4 (Dickey et al. 1983). The total amount of hydrogen for the individual velocity components identified is hard to determine as there are no HI absorption measurements available at the CO-peak and CO-void. In addition the HI absorptions lines towards the line of sight to the quasars are relatively broad ($\Delta v(\mathrm{HI}) \gg \Delta v(\mathrm{HCO}^+)$), so that the fractional amount of neutral hydrogen associated with the individual HCO^+ absorption features cannot be easily determined. As the $N(\mathrm{H}_2)_{\mathrm{HCO}^+}$ calculations are based on an H_2 fraction of 35%, resulting in $N(\mathrm{HI}){\approx}3.7\ N(\mathrm{H}_2)$. Therefore, total hydrogen column densities of $N(\mathrm{H})_{\mathrm{HCO}^+}= 2{\times}N(\mathrm{H}_2)_{\mathrm{HCO}^+}{+}N(\mathrm{HI}) = 5.7{\times}N(\mathrm{H}_2)_{\mathrm{HCO}^+}$ based on the HCO^+ absorptions are assumed. As a lower limit for the total hydrogen based on the CO emission it is assumed that all hydrogen is in molecular form; $N(\mathrm{H})_{\mathrm{CO}}{=}2{\times}N(\mathrm{H}_2)_{\mathrm{CO}}$. The thus derived total hydrogen column densities for the individual velocity components are listed in Table 5.4. Note that the derived total hydrogen column densities for the majority of the velocity components are $\gtrsim 2{\times}10^{21}$ cm^{-2}; corresponding to an $A_\mathrm{v}{\gtrsim}1$ mag. These A_v classify the majority of the clouds at the upper limit of the diffuse regime or even in the translucent regime.

With the assumption that the cloud diameter d_C is equal to the depth of the cloud it is possible to estimate the volume hydrogen density $n(\mathrm{H})$ in the individual clouds with $n(\mathrm{H}){=}N(\mathrm{H})/d_\mathrm{C}$. Based on the typical sizes of the structural features in the CO(1–0)-maps (Fig. 5.1), cloud diameter of 0.15 pc (200″) for B0355+508 and 0.3 pc (400″) for B0212+735 based on assumed clouds-distances of 150 pc (Liszt & Pety 2012) are estimated. The cloud diameter (in parsec) is given by $d_\mathrm{C}[\mathrm{pc}]{\approx}4.85{\times}10^{-6}$ $\rho[″]\ d[\mathrm{pc}]$, whereby $\rho[″]$ is the diameter of the cloud in arcsec and d[pc] the cloud-distance in parsec. The thus derived $n(\mathrm{H})$ for the individual velocity components are listed in Table 5.4. The densities derived from $N(\mathrm{H})_{\mathrm{HCO}^+}$ span between ~4000 to 7000 cm^{-3} and between ~2400 to 17000 cm^{-3} derived from $N(\mathrm{H})_{\mathrm{CO}}$. These densities are unusually high for diffuse clouds. Diffuse clouds are normally associated with a $n(\mathrm{H}){\sim}100$ cm^{-3} (cf. Tielens 2010), roughly 20-100 times less than the derived values. These densities are commonly found in translucent and dense molecular clouds.

5.5 EXPECTED DIFFUSE CLOUD [CII] INTENSITIES

I will now discuss the heating (Section 5.5.1) and cooling (Section 5.5.2) in diffuse clouds. With the assumption that the cooling of diffuse clouds is dominated by [CII] the expected lower limit of the integrated [CII] intensity, I([CII]), emitting from the observed positions (Section 5.5.2) are calculated.

5.5.1 HEATING IN DIFFUSE CLOUDS

In diffuse clouds with a visual extinction around unity and an ambient interstellar radiation field of G_0= 1 (Habing 1968) photo-electric heating is expected to be the major heating source. For low density clouds with a density $\lesssim$3 × 10^3 cm^{-3} and a temperature $T\lesssim$ 100 K, the efficiency of photo-electric heating is at its maximum (Tielens 2010), and the heating amounts to about $\Gamma \simeq$5 × 10^{-26} G_0 erg (H-Atom)$^{-1}$ s^{-1} (Bakes & Tielens 1994; Tielens 2010), about 17 times stronger than the penetrating cosmic ray heating of ∼3 × 10^{-27} erg (H-Atom)$^{-1}$ s^{-1} (Tielens 2010). Additional heating may be due to turbulent dissipation, resulting in local hot spots, a mechanism favored to explain the unexpectedly high abundance of some species in diffuse clouds, in particular CH^+ (Falgarone et al. 2010a; Godard et al. 2010; Falgarone et al. 2010b). In addition, the formation of H_2 may contribute some heating to the clouds (Liszt & Lucas 1996). Hence photoelectric heating alone provides a lower limit to the heating. Further heating of the diffuse clouds may be induced by magnetohydrodynamic shocks and C-shocks (Pineau des Forets, Roueff & Flower 1986; Draine & Katz 1986; Gusdorf et al. 2008). Chemical reactions induced by these shocks would increase the C^+ column densities in diffuse gas significantly and could explain the detected HCO^+ (Draine & Katz 1986).

5.5.2 COOLING OF DIFFUSE CLOUDS; EXPECTED I([CII]) IN DIFFUSE CLOUDS

The [CII] 158 μm fine structure line is expected to be the dominant coolant in diffuse clouds (Hollenbach & Tielens 1999). Due to its relatively low critical density (∼ 3× 10^3 cm^{-3}) (Goldsmith et al. 2012) C^+ gets easily excited in diffuse clouds. Oxygen is neutral in diffuse gas, but the [OI] 63 μm ground state fine structure line has a much too high critical density to be significantly excited (Tielens & Hollenbach 1985a; Wolfire, Tielens & Hollenbach 1990); nitrogen will be neutral and hence cannot radiate. Where the carbon is in molecular form (CO), carbon monoxide rotational line cooling should dominate. The above line of reasoning allows to estimate an expected [CII] brightness of the CO-clouds near the lines of sights towards B0355+508 and B0212+735, in case they are indeed diffuse clouds.

The contribution of [CII] cooling does not exceed ∼30 % of the [CII] cooling (Juvela et al. 2003). Therefore it is not considered in the following.

In thermal equilibrium the cloud heating is in balance with the cooling. The expected integrated [CII] line intensity can be estimated by equating the photoelectric heating at a given G_0 with the [CII] cooling function,

$$
\begin{aligned}
I([\mathrm{CII}]) \left[\frac{\mathrm{K}}{\mathrm{km\ s}}\right] &= \frac{1}{4\pi}\frac{c^3}{2k_\mathrm{B}\nu^3}10^{-5}\Gamma\, G_0 N(\mathrm{H}) \\
&= 1.1\times 10^4\ \Gamma\, G_0 N(\mathrm{H}) \qquad (5.5)
\end{aligned}
$$

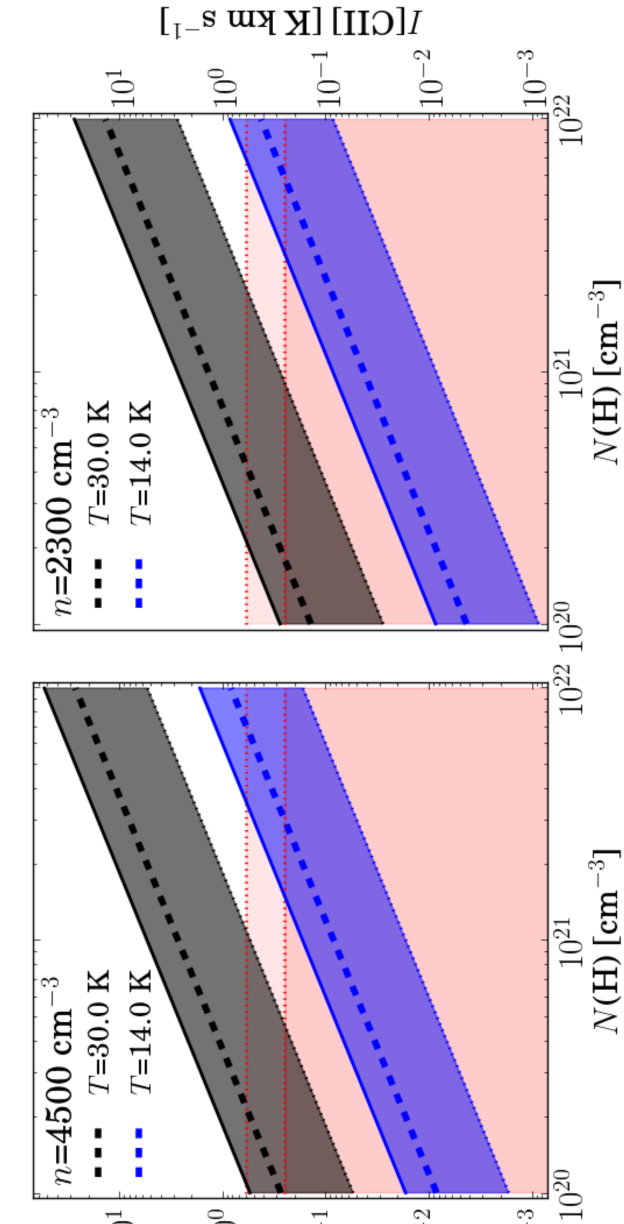

Figure 5.3: Expected $I([\mathrm{C\,II}])$ for $n(\mathrm{H})$=4500 cm^{-3} (left) and $n(\mathrm{H})$= 2300 cm^{-3} (right) at different total hydrogen column densities $N(\mathrm{H})$ and temperatures calculated from equation 5.7. The filled grey areas show the expected $I([\mathrm{C\,II}])$ for a T=30 K. The blue areas show the expected $I[\mathrm{C\,II}]$) for a cold cloud with a kinetic gas temperature of 14 K, as indicated by the CO(2–1)/CO(1–0) ratio. The dashed lines (- - -) represent the $I([\mathrm{C\,II}])$ for a beam filling factor of Φ_b=0.5. The upper and lower edge of the grey and blue filled areas shows the $I([\mathrm{C\,II}])$ for a beam filling factor of Φ_b=1 and Φ_b=0.1. The red areas mark the upper limits of the here presented [CII] observations.

(1)	(2)	(3)	(4)
	$I([\text{CII}])_{\text{HCO}^+}$	$I([\text{CII}])_{\text{CO}_\text{P}}$	$I([\text{CII}])_{\text{CO}_\text{V}}$
	K km s^{-1}	K km s^{-1}	K km s^{-1}
LOS toward quasar		**CO-peak**	**CO-void**
	B0355+508		
A	1.4±0.2	1.5±0.2	1.2±0.1
B	1.5±0.2	0.3±0.2	0.4±0.1
C	1.5±0.2	4.7±0.5	1.1±0.1
D	1.3±0.2	–	–
E	1.4±0.2	–	–
	B0212+735		
F	0.8±0.1	–	–
G	3.5±0.5	1.9±0.2	1.3±0.1

Table 5.5: Lower limits for the expected I([CII]) in diffuse clouds derived from the photo electric heating rate following Equation (5.6).
(1) Designation of the assigned velocity components.
(2) Expected integrated [CII] intensity based on the total hydrogen column $N(\text{H})_{\text{HCO}^+}$ derived from the HCO^+ absorptions and an H_2 fraction of 35%; (3)&(4) Expected integrated [CII] intensities in the positions CO-peak ($I([\text{CII}])_{CO_P}$) and CO-void ($I([\text{CII}])_{CO_V}$) based on molecular hydrogen column densities derived from the CO CO column density. The contribution of HI to the total amount of hydrogen is not considered.

For an assumed photoelectric heating rate of $\Gamma \simeq 5 \times 10^{-26}$ erg (H-Atom)$^{-1}$ s^{-1} and an ambient interstellar field of G_0=1, Equation (5.5) gives an expected integrated [CII] line intensity I([CII]) of

$$I([\text{CII}]) \left[\frac{\text{K}}{\text{km s}}\right] = 5.7 \times 10^{-22} N(\text{H}) \left[\frac{\text{K}}{\text{km s}}\right] \tag{5.6}$$

The expected I([CII]) for the total hydrogen column densities (cf. Table 5.4) of the individual velocity components derived with Equation (5.6) are listed in Table 5.5.

- In the scenario that the spatial variations in the CO-maps are indeed induced by chemical and not by density variations, the expected I([CII]) is based on the total hydrogen column density derived from the HCO+ absorption, $N(\text{H})_{\text{HCO}^+}$. The derived intensities range from I([CII])=1.3 K km/s to 3.5 K km/s, a factor ~3 to 7 above the upper limits for a 3σ [CII] detection in the observed positions.
  Note that these intensities are based on an assumed H_2 fraction of 35%. Neglecting the additional hydrogen column present in HI would still lead to an expected I([CII])≈0.5 K km/s in B0355+508 and 1.2 K km/s in B0212+735. Even in that case [CII] lines >3σ should have been observed for almost all velocity components.

- In the scenario that the CO emission traces the density and not chemical variations, the derived lower limits of the [CII] emission are a factor ~3 to 15 above the upper limits for a 3σ [CII] detection for the majority of the velocity components. The expected I([CII]) spans from ~0.3 (B_P) to 4.7 K km/s (C_P), where the majority of the components have an expected I([CII]) of 1-2 K km/s. Note that

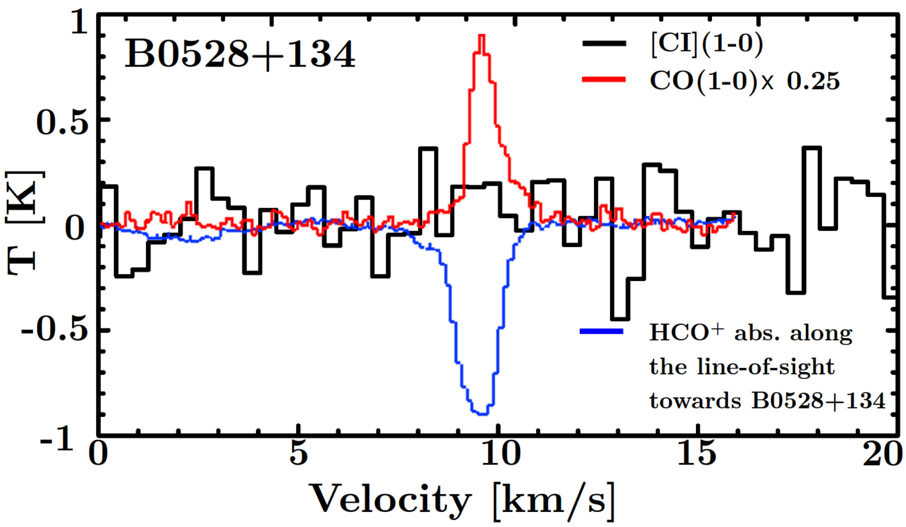

Figure 5.4: [CI](1–0) (black) and CO(1–0)(red) spectra towards B0528+134. The HCO^+ absorption spectra is shown by the blue line. The CO(1–0) and HCO^+ spectra are extracted from Liszt & Pety (2012).

these densities are lower limits; adding the additional (but unknown) HI-column density in these positions would increase the total.

The fraction of neutral carbon is undetermined in these clouds. It cannot be excluded that a fraction of the cloud cooling occurs due to the C^0 hyperfine transitions, thus leading to fainter [CII] emission lines. Using the upper limit for C^0-cooling of ∼30% estimated by (Juvela et al. 2003), the emission should still have been detected. The [CI](1–0) observations in B0528+134 show no [CI](1–0) with the RMS of 0.22K (cf. Fig. 5.4). If the conditions in B0528+134 are similar to those in B0355+508 and B0212+735, these observations indicate that C^0 has a minor significance for the cooling of the clouds, discussed here.

In summary, the balance between heating and cooling calculated for the diffuse cloud case predicts that integrated [CII] intensity are roughly a factor ∼3 up to a factor 15 above the 3σ detection limit for the cloud components identified in CO. This indicates that the underlying assumption of the clouds being diffuse and warm is not adequate: there is no way to hide the [CII] column that complements the detected CO, unless the [CII] is less excited. This can be the case either with lower densities, resulting in a conflict with the sizes and column densities of the clouds or with a lower temperature as discussed below.

5.6 [CII] AND CO EMISSION FROM COLD DENSE CLOUDS

In the following section I show that observed low–J CO line intensities and the upper limits on the integrated [CII] intensities are consistent with the scenario of PDR layers on cold and dense cloud fragments.

Note that the scenario of dense clouds is encouraged by the derived high molecular hydrogen volume and column densities of the individual velocity components (cf. Table 5.4). As described in Section 5.4.2 the derived N(H) correspond to optical extinction of A_v ≈1-4 mag. These A_v classify them as translucent and as dense molecular clouds, which is also consistent with the derived $n(\mathrm{H})$ density of a few times 10^3 cm^{-3}. In translucent clouds the photoelectric heating is less efficient, thus the clouds would be colder and [CII] would be less excited. In such clouds ($n \sim$ few 10^3 cm^{-3}; T<20 K) bright CO lines in the absence of [CII] are expected and observed (e.g. Pineda, Langer & Goldsmith 2014), as only molecules with a low excitation energy, such as the low–J CO lines are excited.

First it is shown, that a cold cloud, with a temperature consistent with the low–J CO intensity ratio in the thermalised limit, which hypothetically has all its carbon in the form of C^+ by itself has a sufficiently low [CII] intensity consistent with the upper limits of the observations. By applying PDR-modelling, it is shown, that the predicted [CII] intensity stays below the upper limit for the observed intensity even if one includes a PDR-layer on such a dense and cold cloud fragment.

5.6.1 TEMPERATURE DEPENDENCY OF I([CII])

Observations by Liszt & Lucas (1998) and Pety, Lucas & Liszt (2008a) found an almost uniform CO(2–1)/CO(1–0) ratio of $\simeq$0.725 in the observed clouds. This would indicate a gas temperature of 14 K for a cloud in local thermal equilibrium (LTE). Pety, Lucas & Liszt (2008a) rejected such a LTE solution in favour of a non-LTE explanation with sub-thermally excited CO lines (Goldreich & Kwan 1974; Pety, Lucas & Liszt 2008a) with cloud-temperatures above 30 K, typically $T \approx 40$ to 80 K (Pety, Lucas & Liszt 2008a).

As it is shown in the previous section, the [CII] intensity expected from such a warm, low density cloud would be well above the observed upper limit. The following paragraphs show that for the observed column densities, a cold, dense cloud would have [CII] intensities well below the observed upper limit, even if the full column density has all carbon in the form of C^+.

By adapting formula A3 in Crawford et al. (1985) the [CII] emission for a low density cloud is given by

$$\begin{aligned} I([\mathrm{CII}]) &= 1.3 \times 10^{-3} e^{-91/T} X_{C^+}\, n(\mathrm{H})\, N(\mathrm{H})_{21} \Phi_\mathrm{b} \left[\frac{\mathrm{ergs}}{\mathrm{s\,cm^2\,sr}}\right] \\ &\approx 185\, e^{-91/T} X_{C^+}\, n(\mathrm{H})\, N(\mathrm{H})_{21} \Phi_\mathrm{b} \left[\mathrm{K}\,\frac{\mathrm{km}}{\mathrm{s}}\right], \end{aligned} \tag{5.7}$$

where $N(H)_{21}$ is the total hydrogen column density in units of 10^{21} cm^{-2} and $n(\mathrm{H})$ the volume hydrogen density in cm^{-3}. The following calculations use a C^+ abundance of X_{C^+}=1.4 $\times$ 10^{-4} (cf. Langer et al. 2014a). As the spatial extent of the clouds exceeds the beam of SOFIA and to take the clumpy structure of clouds into account a beam filling factor of Φ_b=0.5 is assumed, in order to have a conservative estimate.

Fig. 5.3 illustrates the expected I([CII]) for gas temperatures of T=14 K and 30 K and typical column and volume densities as found in the observed clouds. As an example, for a T=14 K and typical densities of $n(\mathrm{H})$=4500 cm^{-3} and $N(\mathrm{H})$=2 $\times 10^{21}$ cm^{-2} Equation (5.7) gives an $I([\mathrm{CII}])\approx$0.17 K km/s. That is well below the 3σ detection limit for the [CII] observations.

In the scenario of warm clouds with temperatures of $T \gtrsim$30 K this simple analysis confirms that the [CII] line should have been detectable for all velocity components, except for the lowest total hydrogen column densities. Even for a low beam filling factor of Φ_b=0.1, [CII] line detections would have been expected for both volume densities (cf. Fig. 5.3).

Low temperatures imply shielding of the clouds from the ambient radiation field. This can be realized by cloud cores embedded within large HI-clouds, which absorb the majority of the incoming radiation. The observed wide HI absorption lines embedding the narrow HCO^+ and CO velocity components (Section 5.3) can be interpreted this way. Effectively, such a shielding layer is a photon-dominated surface layer with carbon being atomic and ionized. I will now discuss if the observed intensities are consistent with such a PDR scenario.

5.6.2 PDR MODELING OF THE OBSERVATIONS

PDR-modeling can reproduce the observed CO intensities as well as the observed upper limits for [CII], as shown in the following paragraph.

The observations are modelled with the stationary KOSMA–τ PDR-model (Röllig et al. 2006; 2013; Röllig & Ossenkopf 2013; Andree-Labsch, Ossenkopf & Röllig 2014). The numerical KOSMA–τ code simultaneously solves the energy balance, chemical equilibrium and radiative transfer of spherical clumps. The chemical fraction of carbon in PDRs is handled as well (Röllig & Ossenkopf 2013). The clumps are characterized by their total hydrogen mass, the surface hydrogen volume density, the strengths of the incident FUV field and the metallicity. Only solar metallicities are considered. Pre-shielding of the penetrating FUV radiation by a HI envelope is not considered. The code is applicable for a single clump as well as for an ensemble of clumps. Both is tackled in the following. The radial volume density of the clump(s) is determined by a power law function of the clump radius and the individual surface hydrogen volume density (e.g. Stoerzer, Stutzki & Sternberg 1996; Cubick et al. 2008). Note that the KOSMA–τ code is a stationary PDR-model. The initial conditions of the cloud formation are not considered.

Single clumps and ensembles of clumps with total masses in the range of M=1-10 $M_\odot$ are modelled. They are embedded in the standard Draine field of χ=1. The calculations for the single clump refer to a beam filling factor of Φ_b=0.5.

Figure 5.5 shows that the upper intensity limits for [CII], the observed absolute CO intensities, as well as the observed CO(2–1)/CO(1–0) ratio of $\simeq$0.73$\pm$0.16 can be reproduced by PDR modelling. The model gives integrated line intensities in the order of I(CO(1–0)$\simeq$10 K km/s and I([CII])$\lesssim$0.3 K km/s for cloud volume hydrogen densities of $n(\mathrm{H})\approx10^{3.5}$ to 10^4 cm^{-3} for all the studied cases. Furthermore, the simulations give a ^{12}CO/^{13}CO ratio of $\sim$11 for a $n(\mathrm{H})\sim10^3$ cm^{-3} and $\sim$5 for a $n(\mathrm{H})\sim10^4$ cm^{-3}. The ratio is roughly in agreement with the observations. The ^{12}CO/^{13}CO ratio is affected by the density of the clumps. ^{12}CO is less self-absorbed in clumps with a lower density, so that the ^{12}CO/^{13}CO ratio is increased compared to denser clumps. A higher ^{12}CO/^{13}CO ratio can therefore be explained by a halo of smaller clouds around an ensemble of clumps with higher densities. Hence the clouds do not have to be diffuse to produce the observed ^{12}CO/^{13}CO ratio.

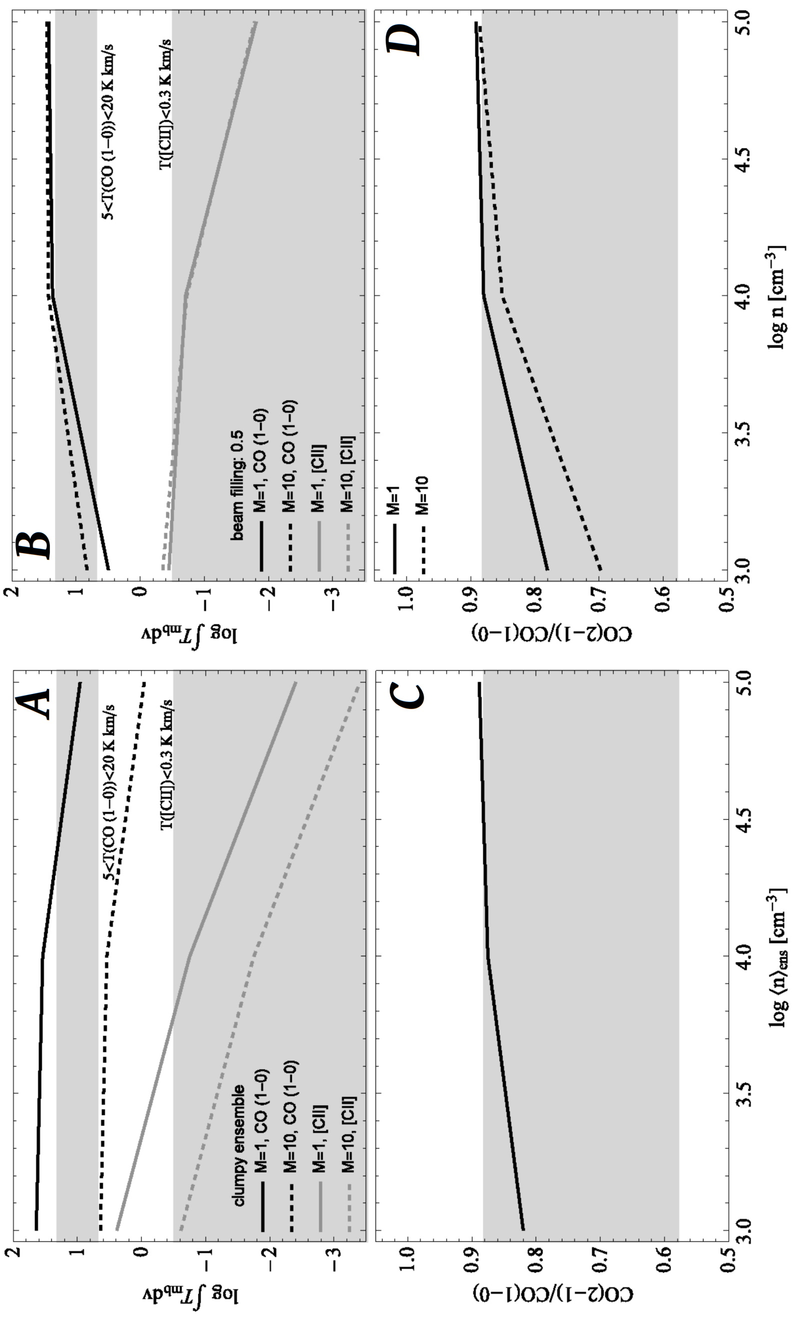

Figure 5.5: PDR-modeling (KOMSA–τ model; Röllig et al. 2006) of clumps with masses of M=1 and 10 $M_\odot$ for surface volume hydrogen densities of $n(\mathrm{H})=10^3$ to 10^5 cm^{-3}. The images on the left (A and C) illustrate the modelling for an ensemble of clumps. The images on the right (B and D) show the modelling for a single clump. For the single clump a beam filling factor of Φ_b=0.5 is anticipated.
The images at the top (A and B) show the modelled [CII] and ^{12}CO(1–0) integrated line intensities. The black and grey lines show the modelled integrated line intensities of CO(1–0) and [CII]. The style of the line marks the anticipated clump mass. The grey areas show the rough lower and/or upper limits of the here discussed CO(1–0) and [CII] observations.
The images at the bottom (C and D) illustrate the modelled CO(2–1)/CO(1–0) ratio for clumps with M=1 and 10 $M_\odot$. The range of the observed CO(2–1)/CO(1–0) ratio ($\simeq$0.73±0.16) is marked by the grey area.

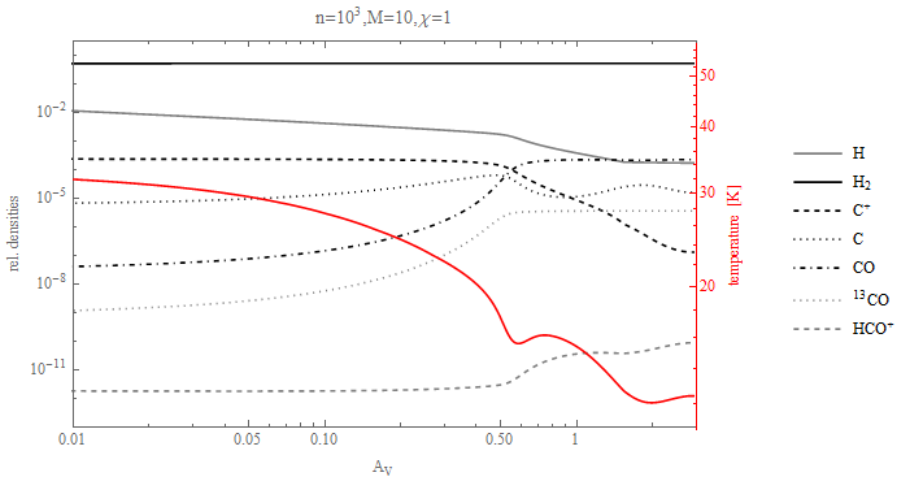

Figure 5.6: Chemical profile of a clump with a surface volume hydrogen densities of n(H)=10^3 cm^{-3} and a mass of 10 $M_\odot$ penetrated by a standard Drainefield of χ= 1. The relative densities of H^0, H_2, C^+, C^0, $^{12/13}$CO and HCO^+ as function of A_V are shown by the black/grey lines (left axis). The temperature profile within the clump is shown by the red line (right axis).

Note that the assumed cloud-masses in the PDR-model are consistent with the anticipated cloud diameters of the discussed clouds. A cloud mass of 10 $M_\odot$ and a density of n(H)=5000 cm^{-3} corresponds to a diameter of d_C≈0.4 pc; 1 $M_\odot$ is equal to d_C≈0.2 pc.

The modelled chemical profiles meet the expectations of a 'standard' PDR. The carbon towards the PDR-surface is dominated by C^+, while the inner region of the PDR is dominated by CO. The transition zone between C^+/C^0/CO is located at an A_V∼0.5 mag. C^+ is associated with kinetic gas temperatures of T∼30K to 20 K, while CO is associated with T∼15 K gas. The hydrogen is predominantly in molecular form throughout the simulated clumps. HCO^+ has a similar distribution as CO in all simulated cases. The fraction of HCO^+ increases beyond the C^+/C^0/CO transition zone. HCO^+ is formed at slightly higher A_V than CO (∼0.7 mag compared to ∼0.5 mag). The $^{12/13}$CO/HCO^+ ratio is thus maximal near the C^+/C^0/CO transition zone (^{12}CO/HCO^+≈1×10^7) and decreases towards the centre of the clumps (^{12}CO/HCO^+≈0.5×10^7). The simulations show no significant variations of the ratio in clumps with n(H)=10^3 cm^{-3} and n(H)=10^4 cm^{-3}. A detailed chemical profile and a temperature profile are shown in Figure 5.6.

However a ^{12}CO/^{13}CO ratio of higher than ∼5 requires clumps with masses significantly lower than 1 $M_\odot$, just because both CO lines tend to become optically thick, pushing the line ratio towards unity. Clumpy PDR ensembles do not suffer from this and are able to reproduce ratios ^{12}CO/^{13}CO>10 for higher masses as well.

Therefore, the observations can be explained as emission from PDRs. An ensemble of cold dense clumps with n(H)∼3000 to 10000 cm^{-3} penetrated by a Draine field of χ=1, reproduces the observed CO intensities, the upper limits for [CII], the ^{12}CO/^{13}CO line ratio and clump sizes. Note that the hydrogen volume densities are fully consistent with those calculated in Section 5.4.2 as well.

5.7 SUMMARY AND CONCLUSION

This chapter presents [CII] observations in two nearby molecular clouds near the lines of sight towards the quasars B0355+508 and B0212+735. Within the RMS of $\sim$ 0.1-0.3 K, in neither of the positions was a [CII]line detected.

The observed upper [CII] intensity limits of I([CII])$\lesssim$0.5 K km/s are in contradiction with the scenario proposed by Pety, Lucas & Liszt 2008a and Liszt & Pety 2012 of warm non-LTE diffuse clouds ($T \gtrsim$30 K) with sub-thermally excited CO bright lines. In diffuse clouds the photo-electric heating rate is at its maximum and the cooling is dominated by [CII]. The upper [CII] intensity limits in the observed clouds were estimated by balancing the heating with the cooling. If the observed clouds were indeed diffuse, the expected integrated [CII]intensities should be a factor $\sim$3 up to 15 above the 3σ detection limit for the cloud components identified in CO emissions.

The [CII] non detection implies that C^+ is less excited than expected for diffuse clouds. As lower densities are in conflict with the cloud sizes and column densities, the gas must therefore be colder. Cloud temperatures of $\sim$15 K are supported by the observed CO(2–1)/CO(1–0) ratios. In addition the total hydrogen column density in the clouds corresponds to an $A_\mathrm{v}$$\sim$1 to 4 mag and their volume density is typically n(H)$\sim$5000 cm^{-3}, which is hard to reconcile with clouds being diffuse. These densities classify the clouds as being in the translucent regime, or even as moderately dense molecular clouds.

The observed low–J CO absolute line intensities and their ratio, the non detection of [CII] 158μm within the observed upper limits and the observed ^{12}CO/^{13}CO ratio are consistent with a PDR–scenario (using the KOSMA–τ PDR model), in which PDR clump densities are in agreement with our derived column and volume densities. The observations, the derived column and volume densities and the size of the cloud are thus consistent with an ensemble of cold dense clumps.

In summary the observations, calculations and simulations indicate that the clouds along the line of sight towards B0355+508 and B0212+735 consist of an ensemble of cold dense clumps, with volume densities of n(H)$\sim$ $10^{3.5}$ cm^{-3} to 10^4 cm^{-3} and core temperatures of T $\sim$15 K. The observations are not compatible with the scenario of warm diffuse clouds.

The study is based on a small sample of positions and relatively short integration times. Further mapping would significantly increase the statistical representativeness of this study. It would be worth investigating if the emission from other clouds which have been identified as being diffuse are also consistent with a cold and dense clump scenario, once the [CII] intensity is observed and taken into account.

Chapter 6

Large scale distribution of [CI](1–0) and low–J CO transitions in the fourth quadrant of the Milky Way

The following chapter is dedicated to the study of the radial and latitudinal distribution of carbon monoxide and neutral atomic carbon in the fourth quadrant of the Milky Way. I will compare the distribution of [CI](1–0) relative to different low–J CO transitions and determine the radial distribution of gas perpendicular to the galactic disc. The width of the galactic disc (*'scale height'*) is discussed as well. The results will be compared with [CII] observations and simulated [CII]–maps as well as with the scale height of HI. This will shed light onto the composition of the ISM and will give an insight into the dominant processes which trigger the evolution of the ISM.

6.1 INTRODUCTION

Stars are born within dense regions of molecular clouds (cf. section 2.1). Different processes, such as supernovae, stellar winds, self-gravitational collapse of clouds or turbulences are proposed to trigger the agglomeration of (more or less) diffuse gas and to finally form dense clouds. It is currently a topic of research, which of these processes dominate. A number of theoretical studies proposed a phase where the molecular hydrogen is predominantly traced by C^+ and C^0, in the absence of CO (CO–dark H_2, Hollenbach, Takahashi & Tielens 1991, Wolfire et al. 2003 and Wolfire et al. 2010; cf. section 2.2). The fraction of CO–dark H_2 depends *inter alia* on the metallicity of the ambient medium (c.f section 2.2.4). The metallicity within the Milky Way decreases towards larger radial distances to the Galactic centre, R_{GC}, as well as towards larger vertical distance, z, from the Galactic plane (e.g. Koeppen & Cuisinier 1994; Molla et al. 1997; Schlesinger et al. 2014). Therefore a higher fraction of CO–dark H_2 towards larger R_{GC} and z is expected. Hence, the fraction of C^+ and C^0 compared to CO should increase towards higher galactic latitudes and R_{GC}.

This section will discuss these issues based on the vertical distribution of CO, C^0 and [CII] in the Milky Way. The distribution of gas perpendicular to the disc is affected by the hydrostatic pressure within the ISM, which reflects the mass distribution, the energy balance and its kinematics. The hydrostatic pressure of a cloud is given by the equilibrium of dispersing forces like the thermal pressure, the dynamical motion of the gas, the pressure by the radiation and the cohesive force of gravity (Langer, Pineda & Velusamy 2014a). It has a significant impact on the formation of GMCs and the formation of stars (Wong & Blitz 2002; Blitz & Rosolowsky 2004). The ambient hydrostatic pressure in the disc is directly and almost linearly connected to the star formation rate and the ratio of neutral and molecular gas (Blitz & Rosolowsky 2006). Thus, the hydrostatic pressure of the ISM is directly reflected in the width of the galactic disc, also denoted as the *'scale height', ($z_{1/2}$)*. It is of great interest to study the scale height of the ISM components in the galaxy. The precise relation between the hydrostatic pressure and the scale height is discussed in section 6.4.1.

A number of studies have focused on the latitudinal distribution of CO(1–0), based on spectrally resolved observations (e.g. Sanders, Solomon & Scoville 1984; Dame et al. 1987; Clemens et al. 1988; Malhotra 1994a;b; Jackson et al. 2006; Braiding et al. 2015). These studies found out that the predominant amount of molecular gas, traced by CO, is located in a thin layer of self-gravitating molecular clumps (Narayan & Jog 2002) centred around the galactic midplane at b=0°, and also high latitude clouds are observed (e.g. Knapp et al. 1985, Malhotra 1994a;b; Fukui et al. 2014). This layer has a typical half width of $z_{1/2}(R_0)$~70 pc for CO(1–0) at the location of the sun. The width of the layer (and thus those of H_2 traced by CO) increases towards higher distances from the Galactic Centre (Sanders, Solomon & Scoville 1984 ,Clemens et al. 1988; Malhotra 1994a;b) with $z_{1/2} \propto R_{\rm Gal}^{0.5}$ (e.g. Sanders, Solomon & Scoville 1984). A recent study investigated the scale height of [CII] in the Milky Way (Langer, Pineda & Velusamy 2014a). The result of this study was that the scale height of [CII] is higher than that of CO with a mean scale height of 86 pc for galactic distances between $R_{\rm GC}$~4 to 8 kpc. This [CII] scale height refers to the total [CII] emission perpendicular to the galactic disc, not only the [CII] emission which is associated with molecular gas. It was not possible to distinguish between the [CII] emission that is associated with molecular clouds and those from diffuse regions, due to the missing spectral information. Therefore, its radial distribution could be directly determined. It was therefore assumed that its radial distribution is similar to those of CO(1–0).

The scale height of other important carbon bearing transitions has not been studied so far, neither those of [CI](1–0), CO(2–1) nor CO(4-3). So it is of great interest to determine the radial distribution of their scale heights and compare it to CO(1–0) and [CII]. In this chapter I will first give an overview of the analysed data in section 6.2. Here, the emission of [CI](1–0) and CO will be compared as well. The radial distribution of the gas will be determined in section 6.3. The distribution of the observed transitions perpendicular to the galactic disc will be discussed in section 6.4.

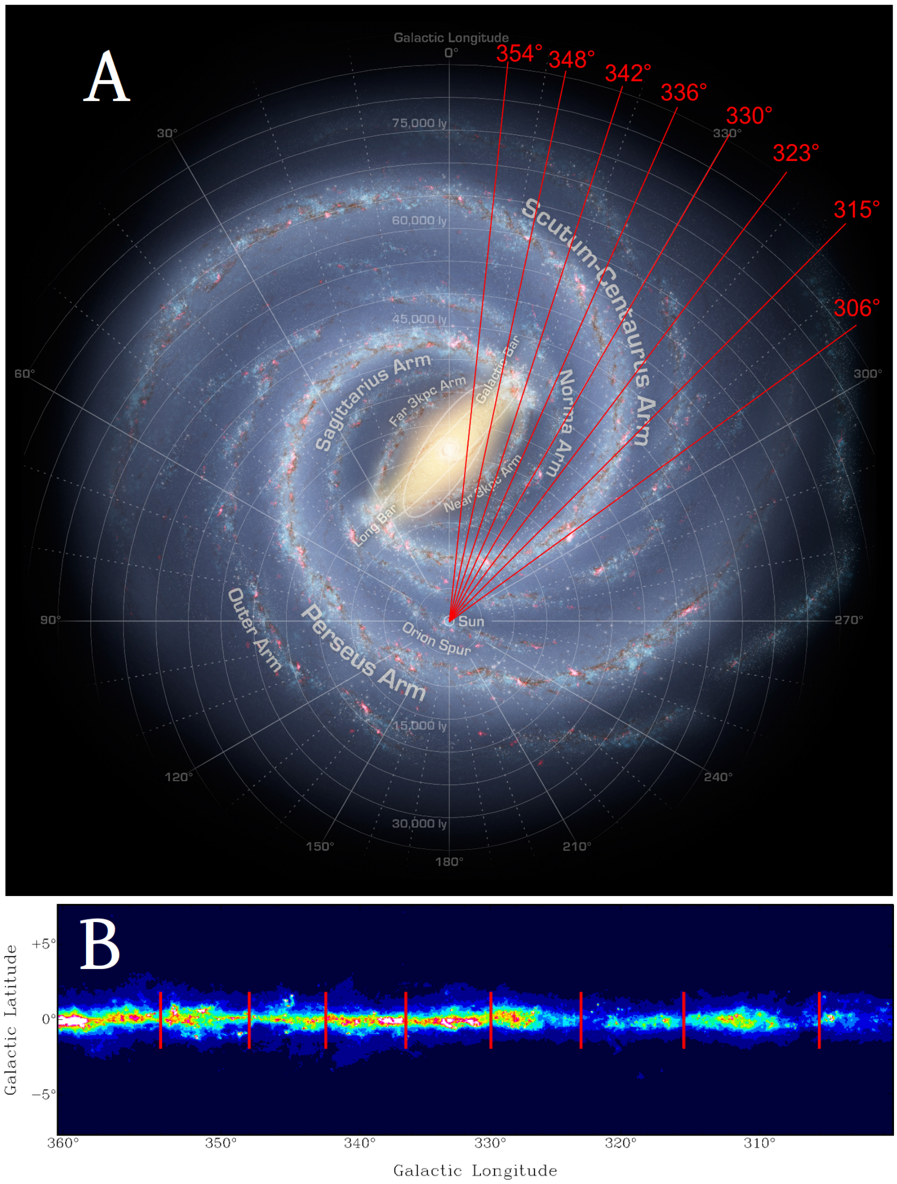

Figure 6.1: **Top**: Artist illustration of the Milky Way. The red stripes mark the line of sight of the b–stripes observed with AST/RO (image A).
Credit: R. Hurt, NASA/JPL-Caltech
Bottom: Image B shows the galactic plane at 857 GHz (Planck Collaboration et al. 2014a).The red stripes show the regions observed with AST/RO.

6.2 DATA PROCESSING AND OBSERVATIONAL RESULTS

This section provides an overview of the observational data used in the following analysis. The data processing is also described in the following.

6.2.1 DATA PROCESSING

The present analysis is based on observational data of the transitions ^{12}CO(4–3), ^{12}CO(2–1) and [CI](1–0) towards the galactic longitudes l = 306.0°, 315.6°, 323.1°, 300.0°, 336.4°, 342.5°, 348.0° and 354.0° between the galactic latitudes -2°<b<2°, in so called *'b–strips'* (cf. Figure 6.1). This data is provided by observations with the Antarctic Submillimeter Telescope and Remote Observatory, (*AST/RO*)[i] and is obtainable at the AST/RO homepage[ii]. The page provides likewise data of $l = 295°$, which are not considered in the following analysis, as the CO(4–3) and [CI](1–0) data have a relatively low quality compared to the other b–strips[iii].

The [CI](1–0) and CO(4–3) transitions were observed with the double sideband SIS waveguide receiver '*Wanda*', having a noise temperature of ∼172 K at 492 GHz (Walker et al. 1992; Honingh et al. 1997). The CO(2–1) data was observed with a SIS receiver with a double-sideband noise temperature of 80–170 K (Kooi et al. 1991). The spectrometer consisted of two higher resolution acousto-optical spectrometers (HRAOSs), each having 2048 channels and a bandwidth of 1.1 GHz (Schieder, Tolls & Winnewisser 1989), which corresponds to a resolution of 63 MHz (∼0.08 km/s for 230 GHz, ∼0.04 km/s for 492 GHz) per channel.

The data was observed in the on the flight mode. The data reduction was performed with the COMB data reduction package as described in (Stark et al. 2001). The spectra were converted to the main beam brightness scale with a main beam efficiency of 0.81 for CO(2–1) and 0.72 for CO(4–3). A first order baseline was removed from all the spectra (Stark priv. communication).

The data is provided in the form of 3 dimensional pv-diagrams, with the dimensions velocity, galactic latitude and main beam brightness temperature, T_{mb}. The data covers the velocity ranges from v=-150 km/s to +100 km/s, with a velocity resolution of Δv = 0.44 km/s, between the galactic latitudes b=±2°. The data is spatially oversampled, providing a latitudinal binning of 0.015°(≃54″). The CO(2–1) and [CI](1–0) datasets

i The Antarctic Submillimeter Telescope and Remote Observatory, AST/RO (Stark 1992; Stark et al. 2001), was an offset Gregorian submillimeter telescope located nearby the Amundsen–Scott South Pole Station at an altitude of 2847 m, operated between January 1995 and December 2005 (Stark 2013). The diameter of the primary mirror was 1.7m, corresponding to a beam size of ∼110″ at 492 GHz and ∼180″ for 230 GHz. The widths of the b–strips is equal to the beam-size. The telescope-optic was designed with an offset to its major axis to avoid undesired reflections and resonances. The primary mirror had an accuracy of ∼9 μm, allowing observation even in the Terahertz regime. AST/RO was the first ground based observatory which observed [NII] at 1.46 THz (Oberst et al. 2006; 2011). For further information to the AST/RO–design see Stark et al. (1997).

ii www.cfa.harvard.edu/∼aas/adair/www-docs/AST_RO.html

iii The data at $l = 295°$ has a large number of standing waves and artefacts, so that a reliable identification of sources is not possible

l	⟨RMS⟩ [K]				
	^{12}CO(1–0)	^{13}CO(1–0)	^{12}CO(2–1)	^{12}CO(4–3)	[CI](1–0)
306.00°	–	–	0.06	0.10	0.06
315.57°	0.11	0.06	0.04	0.08	0.05
323.13°	0.04	0.05	0.04	0.07	0.04
330.00°	0.02	0.04	0.06	0.04	0.04
336.42°	0.06	0.11	0.05	0.05	0.06
342.54°	0.04	0.05	0.05	0.06	0.05
348.00°	–	–	0.05	0.08	0.05
354.0°	–	–	0.05	0.08	0.05

Table 6.1: Mean RMS of the b–strips (-2°$\leq b \leq$2°) for a velocity resolution of 0.44 km/s.

have a mean RMS of ∼0.05 K referring to this resolution, while those of CO(4–3) are slightly higher with ∼0.08 K. The precise RMSs for the individual b–strips are listed in table 6.1.

Complementary data of ^{12}C^{16}O(1–0), ^{13}C^{16}O(1–0), ^{12}C^{18}O(1–0) and ^{12}C^{17}O(1–0) (denoted as ^{12}CO(1–0), ^{13}CO(1–0), C^{18}O(1–0) and C^{17}O(1–0) in the following) were observed with the 22-m diameter Mopra telescope[iv] at $l = 315.6°$, 323.1°, 300.0°, 336.4°, 342.5° and -2°$\leq b \leq$2° within the Mopra Southern Galactic Plane CO Survey (Burton et al. 2011) in April and May 2010. Each strip had a width of 6′ with an angular resolution of 35″ after the median filter convolution (Ladd et al. 2005; Burton et al. 2013a).

The Monolithic Microwave Integrated Circuit receiver (MMIC) of Mopra and the UNSW Mopra Spectrometer (MOPS) filter bank were used for the observations. MMIC covers the spectral range from 77 GHz to 117 GHz. The bandpass of MOPS has a width of 8 GHz. It was centred at 112.5 GHz to observe the four CO transitions simultaneously. The observations used the zoom mode of MOPS, with 4×137.5 MHz wide, dual–polarisation bands, each having 4096 channels (Burton et al. 2013a), resulting in a spectral resolution of ∼0.09 km/s. This observing strategy gave ^{12}CO(1–0) data in the velocity range between $v_{\rm LSR}$[v]=-204 km/s to +156 km/s, ^{13}CO(1–0) between $v_{\rm LSR}$=-114 km/s to +260 km/s, C^{17}O(1–0) between $v_{\rm LSR}$=-114 km/s to +260 km/s and finally C^{18}O(1–0) between $v_{\rm LSR}$=-131 km/s to +247 km/s.

The data was calibrated with LIVEDATA[vi]. The calibration process is described in detail in Burton et al. (2013a). The data was converted to the main beam brightness temperature using the main beam efficiency of $\eta_{\rm mb}$=0.42.

The position–velocity diagrams were created with the GRIDZILLA software package[vii]. To compare the Mopra data with the AST/RO–observation, I have regridded the data to the same spatial and spectral resolution, whereby a first order base line was subtracted from the spectra. The thus processed data have a RMS in the order of ∼ 0.05 K in the majority of

iv Mopra is a CSIRO telescope with a diameter of 22 m. It is located near Coonabarabran in NSW, Australia
v $v_{\rm LSR}$ is the velocity relative to the local standard of rest.
vi http://ww.atnf.csiro.au/computing/software/livedata
vii http://ww.atnf.csiro.au/computing/software/livedata

l	$\left\langle\frac{T_{\rm mb}(^{12}{\rm CO}(1-0)}{T_{\rm mb}([{\rm CI}](1-0)}\right\rangle$	$\left\langle\frac{T_{\rm mb}(^{13}{\rm CO}(1-0)}{T_{\rm mb}([{\rm CI}](1-0)}\right\rangle$	$\left\langle\frac{T_{\rm mb}({\rm CO}(2-1)}{T_{\rm mb}([{\rm CI}](1-0)}\right\rangle$	$\left\langle\frac{T_{\rm mb}({\rm CO}(4-3)}{T_{\rm mb}([{\rm CI}](1-0)}\right\rangle$
306.0°	–	–	3.9±2.4	1.7±0.9
315.6°	6.4±2.9	1.3±0.6	4.5±2.6	1.4±0.7
323.1°	5.3±3.8	1.3±0.8	4.3±3.4	1.4±0.8
330.0°	5.6±3.8	1.3±0.8	5.4±2.6	1.0±0.6
336.4°	5.6±3.5	1.6±0.9	4.8±2.6	1.3±1.2
342.5°	5.7±3.9	1.2±0.7	5.9±3.2	1.1±0.8
348.0°	–	–	6.0±3.6	1.8±0.8
354.0°	–	–	5.4±3.5	1.7±1.1
Mean	5.7±2.5	1.3±0.6	5.0±1.7	1.4±0.5

Table 6.2: Ratio of the brightness temperatures of [CI](1–0) to $^{12/13}$CO(1–0), CO(2–1) and CO(4–3). Only pixels are considered which show emission of both lines and have a S/N≥3. The weighted average ratios over all the galactic longitudes are listed in the bottom row.

the strips, referring to the same grid as the AST/RO data. The RMSs for the individual b–strips are listed in Table 6.1. I will use the ^{12}CO(1–0) and ^{13}CO(1–0) data in the following sections, as this study focuses on the emission of CO on large scales. The C^{18}O(1–0) and C^{17}O(1–0) transitions are commonly observed in the most dense regions of molecular clouds, and are therefore of minor interest for this study.

6.2.2 OBSERVATIONAL RESULTS

The AST/RO data is illustrated in the Figures 6.2 and 6.3.

All the different b–strips show several prominent spectral features with typical peak brightness temperatures of ∼2.5 to 4 K for [CI](1–0), ∼5 to 15 K for ^{12}CO(1–0), ∼1 to 3 K for ^{13}CO(1–0), ∼5 to 10 K for CO(2–1) and ∼2 to 18 K for CO(4–3). The major fraction of the line emission is observed at velocities between -100 km/s$\lesssim v_{\rm LSR}\lesssim$ 0 km/s. The data show strong correlation between [CI](1–0) and the CO line transitions. No significant [CI](1–0) emission could be detected outside the CO-emitting clouds. The [CI](1–0) emission is surrounded by pixels that show CO emission, both spatially and spectrally. Only 1 to 2 % of the pixels with a [CI](1–0) signal with $T_{\rm mb}\geq3\times$S/N do not exhibit a CO emission signal. A comparison of the pixels with $T_{\rm mb}\geq3\times$S/N shows that ∼1 to 2% of the pixels show [CI](1–0) emission in the absence of CO[viii]. This fraction is reduced to almost zero for pixels where the $T_{\rm mb}\geq5\times$S/N.

The ratio of the brightness temperatures of the ^{12}CO transitions relative to [CI](1–0) is on average ∼6 for ^{12}CO(1–0), ∼5 for ^{12}CO(1–0) and almost unity for ^{12}CO(4–3) (cf. Fig 6.10), similar as for ^{13}CO(1–0). Histograms of the ratios are illustrated in the Figures 6.6 to 6.9. The ratio is commonly maximal towards the edges of the regions with [CI](1–0) emission and minimal towards their centre as illustrated by the example of $T_{\rm mb}$(^{12}CO(2–1))/$T_{\rm mb}$([CI](1–0)) in the Figures 6.4 and 6.5. This can be explained by optical depth effects, which I will discuss in the following section.

The ^{12}CO(1–0) and ^{13}CO(1–0) data allow the estimation of the optical depths of ^{12}CO(1–0), τ_{12}, as elaborated in Section 4.3. The optical

viii The precise values for all the b–strips are listed in table 6.3. [CI](1–0) in the absence of CO(2–1) is shown by the white areas in the Figures 6.4 and 6.5 as well.

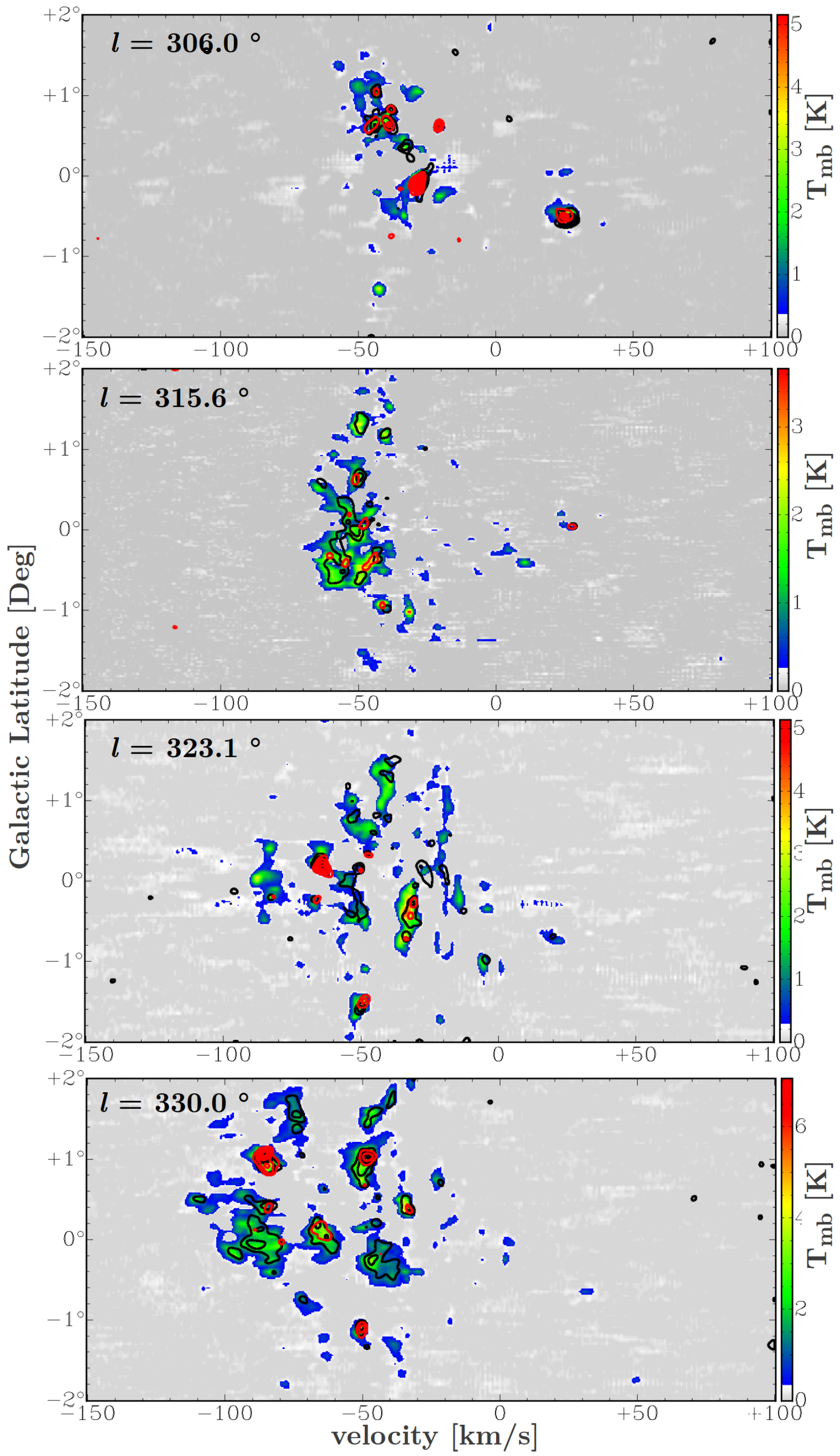

Figure 6.2: Illustration of the CO(2–1), CO(4–3) and [CI](1–0) emission within the *b*–strips at *l*=306.0°, 315.6°, 323.1 °and 330.0 °. CO(2–1) is shown by the colours. The emission of [CI](1–0) (black contours) and CO(4–3) (red contours) are superimposed. The contour lines of [CI](1–0) have steps of 0.25 K. The contour lines of CO(4–3) have steps of 0.5 K.

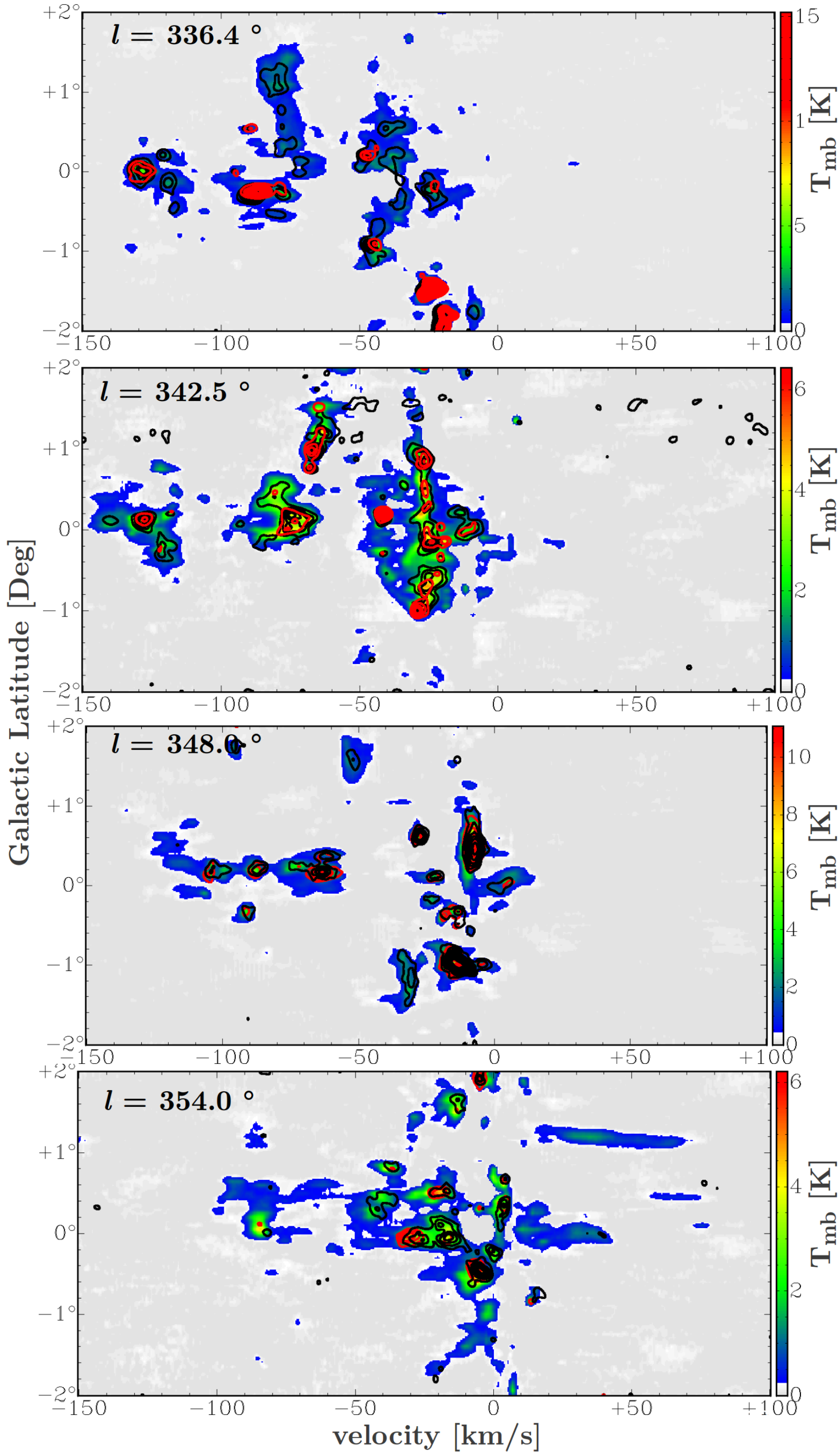

Figure 6.3: Illustration of the CO(2–1), CO(4–3) and [CI](1–0) emission within the b–strips at l=336.4°, 342.6°, 348.0 °and 354.0 °. CO(2–1) is shown by the colours. The emission of [CI](1–0) (black contours) and CO(4–3) (red contours) are superimposed. The contour lines of [CI](1–0) have steps of 0.25 K. The contour lines of CO(4–3) have steps of 0.5 K.

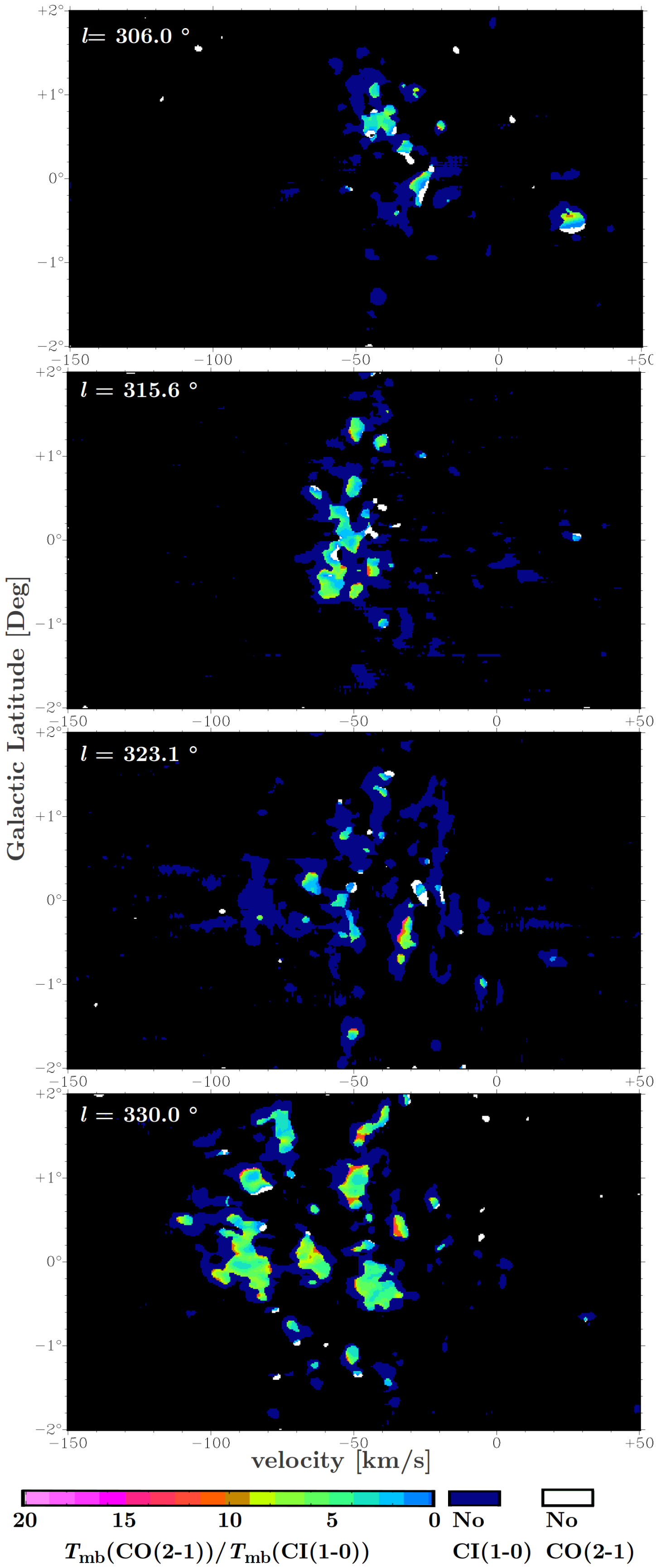

Figure 6.4: Ratios of T_{mb}(CO(2–1))/T_{mb}([CI](1–0)) in the b–strips towards l=306°, 315°, 323° and 330°. The ratio is illustrated by the colour coding. Positions with no [CI](1–0) but CO(2–1) are shown by the dark blue areas. Positions with [CI](1–0) in the absence of CO(2–1) are shown in white. Only pixels with a S/N>3×⟨RMS⟩ were considered.

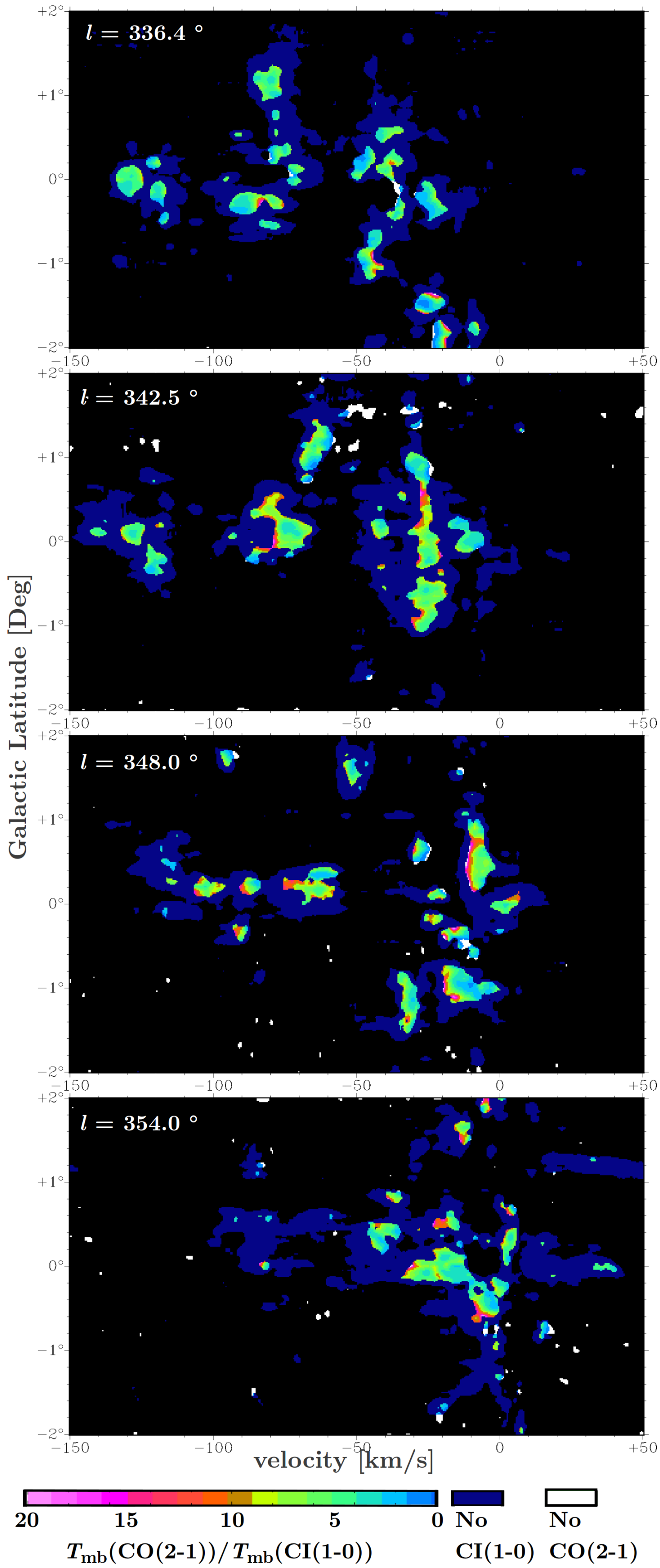

Figure 6.5: Ratios of $T_{\rm mb}$(CO(2–1))/$T_{\rm mb}$([CI](1–0)) in the b–strips towards l=336°, 342°, 348° and 354°. The ratio is illustrated by the colour coding as in Figure 6.4.

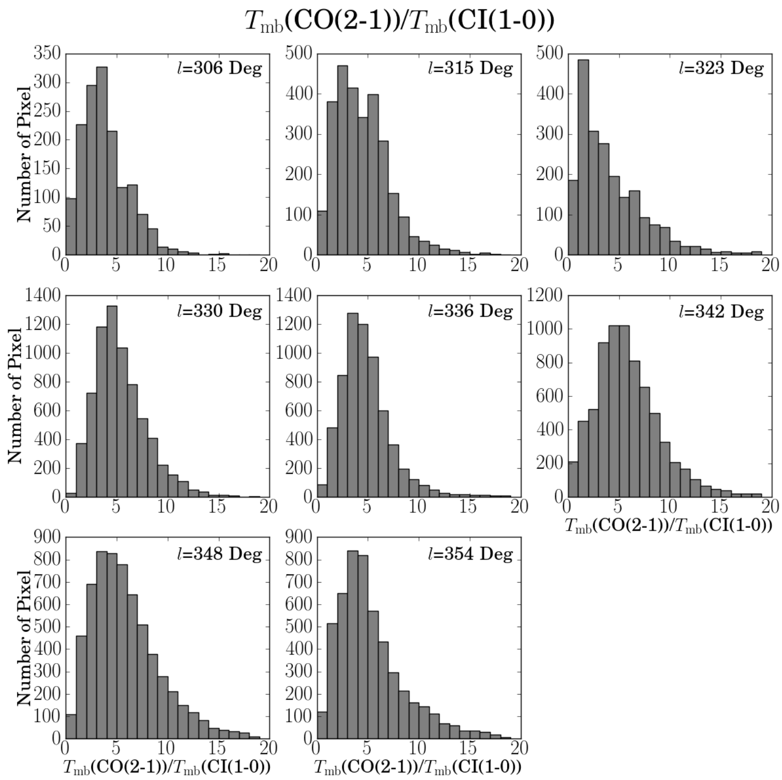

Figure 6.6: Histogram illustrating the amount of pixels at a certain ratio of $T_{\rm mb}$(CO(2–1))/$T_{\rm mb}$([CI](1–0)).

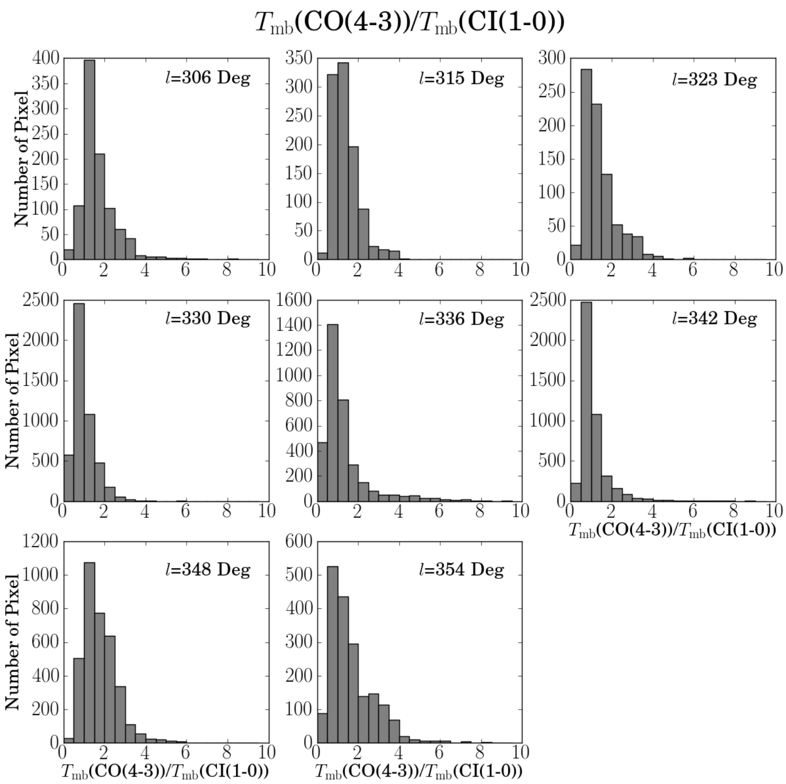

Figure 6.7: Histogram illustrating the amount of pixels at a certain ratio of $T_{\rm mb}$(CO(4–3))/$T_{\rm mb}$([CI](1–0)).

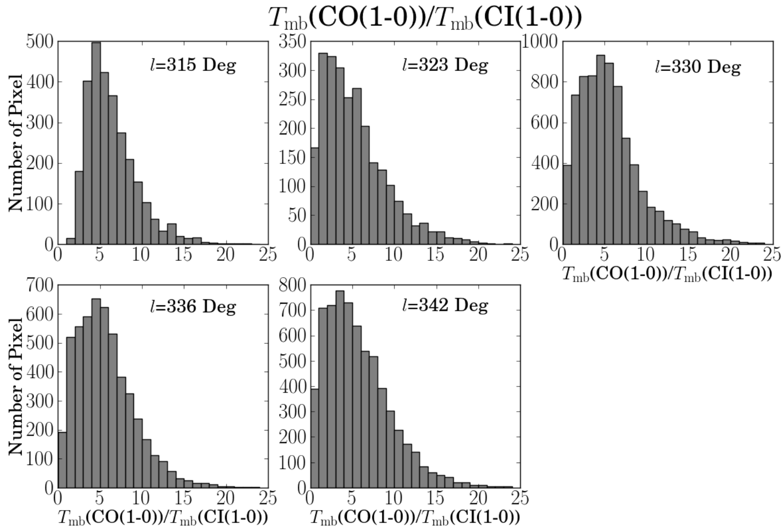

Figure 6.8: Histogram illustrating the amount of pixels at a certain ratio of $T_{\rm mb}(^{12}\rm CO(1\text{–}0))/T_{\rm mb}([\rm C\,I](1\text{–}0))$.

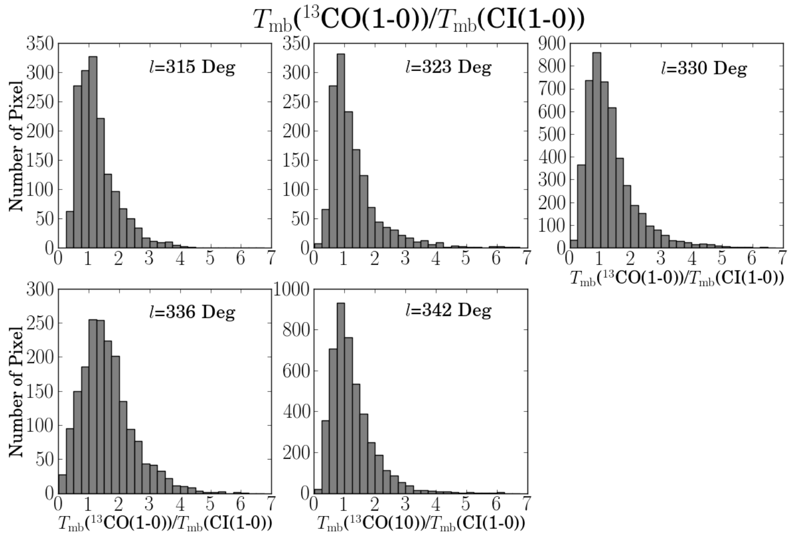

Figure 6.9: Histogram illustrating the amount of pixels at a certain ratio of $T_{\rm mb}(^{13}\rm CO(1\text{–}0))/T_{\rm mb}([\rm C\,I](1\text{–}0))$.

	^{13}**CO(1–0)**			^{12}**CO(1–0)**			^{12}**CO(2–1)**			^{12}**CO(4–3)**		
	✓	✓	×	✓	✓	×	✓	✓	×	✓	✓	×
	[CI](1–0)			**[CI](1–0)**			**[CI](1–0)**			**[CI](1–0)**		
	✓	×	✓	✓	×	✓	✓	×	✓	✓	×	✓
	[%]	[%]	[%]	[%]	[%]	[%]	[%]	[%]	[%]	[%]	[%]	[%]
306.0°	–	–	–	–	–	–	16	78	6	27	40	37
315.6°	23	48	29	25	71	3	19	79	2	15	39	46
323.1°	5	91	4	3	97	0	9	89	2	17	47	36
330.0°	11	81	8	8	91	1	29	70	0	34	46	21
336.4°	8	72	20	7	92	1	20	80	0	28	46	25
342.5°	14	76	9	9	89	2	22	78	0	32	43	26
348.0°	–	–	–	–	–	–	21	78	1	35	39	27
354.0°	–	–	–	–	–	–	14	84	2	21	32	47
Mean	12±7	74±14	14±9	10±8	88±9	1±1	20±7	80±5	2±2	26±7	42±5	33±9

Table 6.3: Fraction of pixels where [CI](1–0) was observed, respectively not observed, to pixels where CO was observed, respectively not observed. 100% correspond to the total number of pixels where either [CI](1–0) or/and the specific CO transitions was detected.

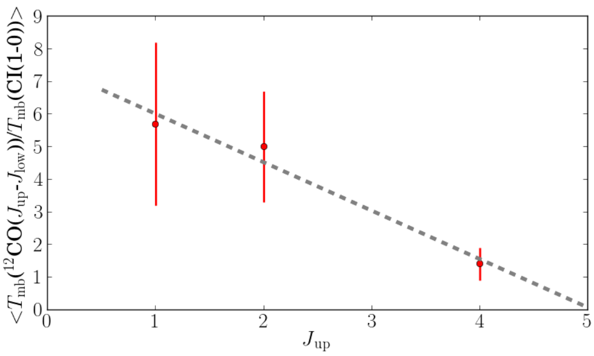

Figure 6.10: Mean ratio of the ^{12}CO brightness temperatures to those of [CI](1–0). The grey dotted line illustrates the linear fit to the ratios as function of J_{up}. The slope has a gradient of ~1.5 $1/J_{up}$.

depths are calculated by the numerical solution of equation (4.15)[ix] for each pixel. It was further assumed that the ^{12}CO/^{13}CO isotope ratio is equal to the value in solar neighbourhood, $x_{\frac{12}{13}}$=70. The radial gradient of $x_{\frac{12}{13}}$ in the Milky Way was neglected as the sources as observed in CO(1–0) lie within a distance of $\lesssim$4 kpc to the sun[x]. The calculation is further based on the assumption that ^{13}CO(1–0) is optically thin. If that is not the case τ_{12} would become larger. Note that τ_{12} can only be calculated for the positions where ^{13}CO(1–0) is detected as well. ^{12}CO(1–0) is optically thick in all positions where ^{13}CO(1–0) is observed. The optical depths vary between τ_{12}~10 and 15 for major parts of the molecular clouds and rise to τ_{12}~40–70 in their centres (cf. Fig 6.11). The calculated optical depths are illustrated in Figure 6.11. [CI](1–0) is presumably optically thin, while the optical depths of the ^{12}CO transitions is higher towards the centre of the molecular clouds. Hence the ratio of the ^{12}CO brightness temperatures to those of [CI](1–0) lowers towards the centre of the molecular clouds and increases towards the edges.

The present data suggests that the [CI](1–0) emission in the Milky Way arises primarily from the surface of molecular clouds where CO is photodissociated. Clouds that show [CI](1–0) emission in the absence of CO are not observed. Based on the present data the fraction of these clouds must be low compared to molecular clouds that show CO emission.

6.3 RADIAL DISTRIBUTION OF THE SOURCES

The galactic longitudes of the b–strips combined with the velocity information within the data, allow to determine the kinematic distances of the observed sources to the sun as well as to the Galactic Centre[xi]. With the distance of the source to the solar system, the angular latitudinal information can be transferred to a vertical distance in units of lengths. Then this is used to estimate the vertical distribution of the emission around the galactic midplane (scale height). With the distance of the source from the Galactic Centre it is possible to study the radial distribution of the

ix $\frac{T_{\rm mb}\left(^{12}{\rm CO}(J_{\rm u}-J_{\rm l})\right)}{T_{\rm mb}\left(^{13}{\rm CO}(J_{\rm u}-J_{\rm l})\right)} = \frac{1-e^{-x_{\frac{12}{13}}\times\tau_{13}}}{1-e^{-\tau_{13}}}$

x The radial distribution of the sources is discussed in section 6.3.

xi The method is described in van de Hulst, Muller & Oort (1954) and Kwee, Muller & Westerhout (1954) for the first time. These studies examined the distribution of HI in the Milky Way.

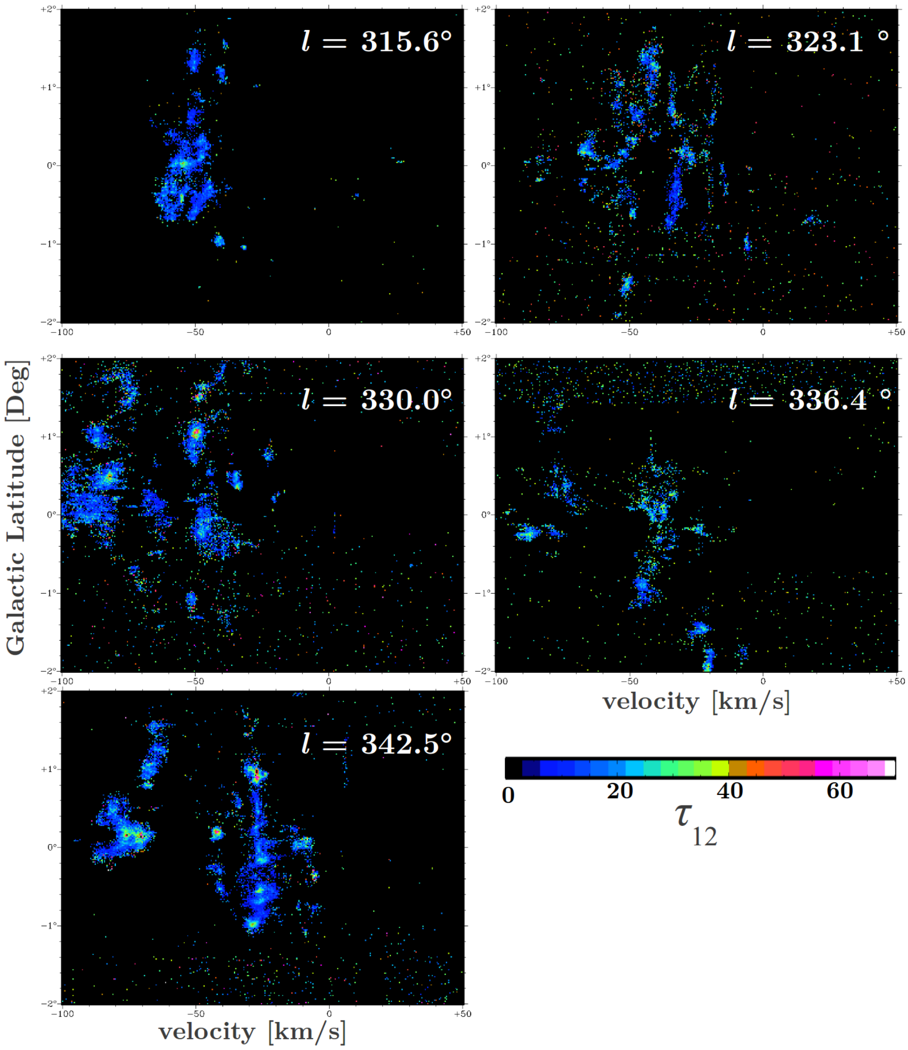

Figure 6.11: Optical depths of ^{12}CO(1–0), τ_{12} in the b–strips at l=315.6°, 323.1°, 330.0°, 336.4°and 342.5°. The optical depths are based on an assumed constant solar ^{12}CO/^{13}CO isotope ratio of $x_{\frac{12}{13}}$=70.

scale height as well (section 6.4), and to associate the observed sources with the spirals arms of the Milky Way (section 6.3.3).

6.3.1 GALACTIC ROTATION CURVE

This section discusses the relation between the observed v_{LSR} , the galactic longitudes and the distance of the sources to the Galactic centre and to the solar system. The following argumentation is mainly based on Burton et al. (2013a).

To determine the distance for a given galactic latitude and a v_{LSR} it is necessary to know the orbital motion of the gas around the Galactic Centre. This study uses the orbital speed given by the galactic rotation curve derived by McClure-Griffiths & Dickey (2007) for the inner galaxy,

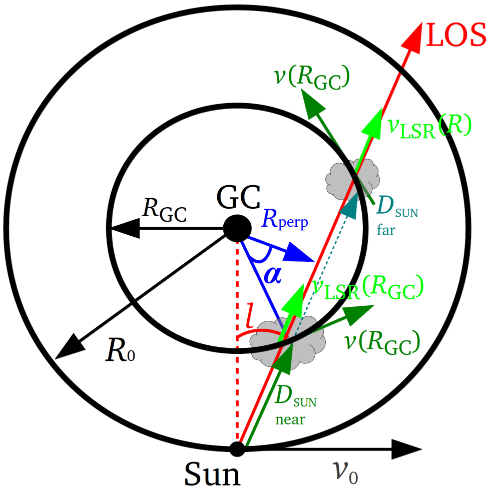

Figure 6.12: Illustration of the trigonometry used to calculate $D_\odot$ and $R_{\rm GC}$ from the $v_{\rm LSR}$ and the galactic latitude l.

$R_{\rm GC}\leq$8.5kpc[xii]. For the outer galaxy, <8.5kpc, the galactic rotation curve by Brand & Blitz (1993) was used.

$$v(R_{\rm GC}) = \begin{cases} v_0 \times \left(0.186\frac{R_{\rm GC}}{R_0} + 0.887\right) & \text{for } R_{\rm GC} \leq R_0 \\ v_0 \times \left(1.008\left(\frac{R_{\rm GC}}{R_0}\right)^{0.039} + 0.007\right) \times s_\kappa & \text{for } R_{\rm GC} > R_0 \end{cases} \tag{6.1}$$

To avoid a discontinuities at $R_{\rm GC} = R_0$ the galactic rotation curve by Brand & Blitz (1993) was scaled with the factor s_κ= 1.056. The IAU standard values of R_0=8.5 kpc and v_0= 220 km/s were further assumed as distance of the sun from the Galactic Centre and the orbital speed of the sun around the Galactic Centre (McClure-Griffiths & Dickey 2007). Note that this equations gives an orbital velocity of the sun around the Galactic Centre of $v(R_0)$= 236 km/s.

The projected velocity of a source relative to the local standard of rest is given by

$$v_{\rm LSR}(R_{\rm GC}) = v(R_{\rm GC})\cos(\alpha) - v_0\sin(l) \tag{6.2}$$

with α being the angle measured, as seen from the Galactic Centre, between the source and the tangential position along the line of sight for the galactic longitude (cf. Figure 6.12 and Burton et al. 2013a). The full trigonometry of these calculations is illustrated in Figure 6.12.

Both angles are related to each other by the distance from the Galactic Centre to the tangential position along the line of sight $R_{\rm perp}$ via $\cos(\alpha)$= $R_{\rm perp}/R_{\rm GC}$ and $\sin(l)$=$R_{\rm perp}/R_0$. Equation (6.2) can now be arranged to

$$v_{\rm LSR}(R_{\rm GC}) = \left(v(R_{\rm GC})\frac{R_0}{R_{\rm GC}} - v_0\right)\sin(l). \tag{6.3}$$

The distances of the source to the sun ($D_\odot$), the distance of the source to the Galactic Centre, and R_0 are related via

$$R_{\rm GC}{}^2 = R_0^2 + D_\odot{}^2 - R_0 D_\odot \cos(l). \tag{6.4}$$

xii The rotation curve by McClure-Griffiths & Dickey (2007) is based on fits to HI data from the Southern Galactic Plane Survey, (SGPS McClure-Griffiths et al. 2005), of the first and fourth quadrant of the Milky Way.

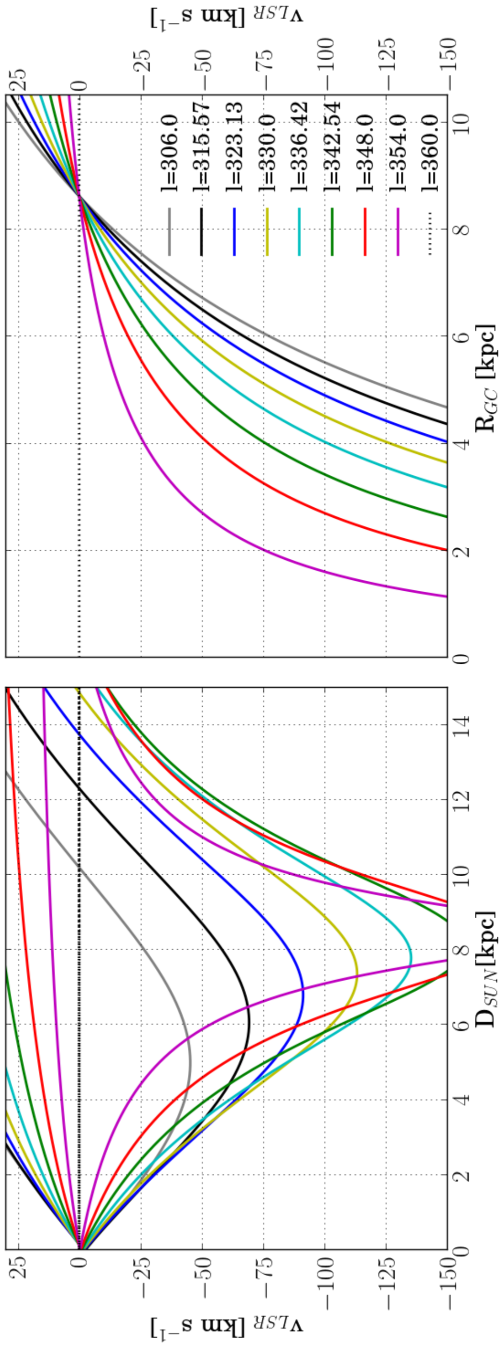

Figure 6.13: Kinematic distances from the sun, $D_{\odot}$, and from the galactic centre, R_{GC}, as function of the v_{LSR} for the galactic latitudes, discussed in this section.

Common Name of the spiral arms	a [kpc]	α	p
Sagittarius–Carina	0.246	0.242	13.6
Scutum–Crux(Centaurus)	0.608	0.279	15.6
Perseus	0.449	0.249	13.5
Norma–Cygnus	0.378	0.240	13.5

Table 6.4: Used parameters to describe the four spiral arms of the Milky Way. The values are taken from Steiman-Cameron, Wolfire & Hollenbach (2010).

The combination of the Equations (6.1), (6.3) and (6.4) allows to determine the distance of a source to the Sun as well as their distance to the Galactic Centre based on the observed source v_{LSR} at a the discussed galactic longitude.

These equations give two solutions for the source distances to the sun unless $l \neq n \times \pi/2$, $n \epsilon \mathbb{N}_0$, and no adequate solution for $l = n \times \pi$ as v_{LSR}=0 km/s for all distances in this case. The solution for the source distance to the Galactic Centre is unambiguous unless $l \neq n \times \pi$.

The distances to the sun and the distances to the Galactic Centre as function of the v_{LSR} at the galactic longitudes, discussed here, are shown in Figure 6.13.

Note that the calculated kinematic distances have high uncertainties. The motion of the gas within the molecular clouds and the motion of clouds within the spiral arm can result in uncertainties of up to 100% (Reid et al. 2009).

However, these calculations allow to determine the position of the observed sources within the Milky Way, as described in the following section. To compare the emissions with the spiral arms I first briefly discuss the spiral structure of the Milky Way.

6.3.2 SPIRAL STRUCTURE OF THE MILKY WAY

The spiral arms of the Milky Way can be described by logarithmic spirals (e.g. von der Pahlen 1911; Danver 1942; Roberts, Roberts & Shu 1975; Vallée 2008; Steiman-Cameron, Wolfire & Hollenbach 2010)[xiii]. A logarithmic spiral is given by

$$R_{\mathrm{GC}}(\phi) = a e^{\alpha\phi} \tag{6.5}$$

with a and α being constants. The orientation of the spiral is given be a, while α defines its pitch angle p. Hence, the shape function ϕ is described by

$$\phi(R_{\mathrm{GC}}) = \ln\left(\frac{R_{\mathrm{GC}}}{a}\frac{1}{\alpha}\right). \tag{6.6}$$

xiii von der Pahlen (1911) showed at the example of M33, M51 and M74 for the first time, that the spiral arms of galaxies can be described by logarithmic spirals. Danver (1942) concluded that the spiral of galaxies can be in general fitted by logarithmic spirals, based on a representative study of 98 galaxies. The theoretical work by Roberts, Roberts & Shu (1975) showed that density waves within an axisymmetric galaxy are described by logarithmic spirals as well. Vallée (2008) and Steiman-Cameron, Wolfire & Hollenbach (2010) provide current descriptions of the spiral arm structure. Both studies show no major differences.

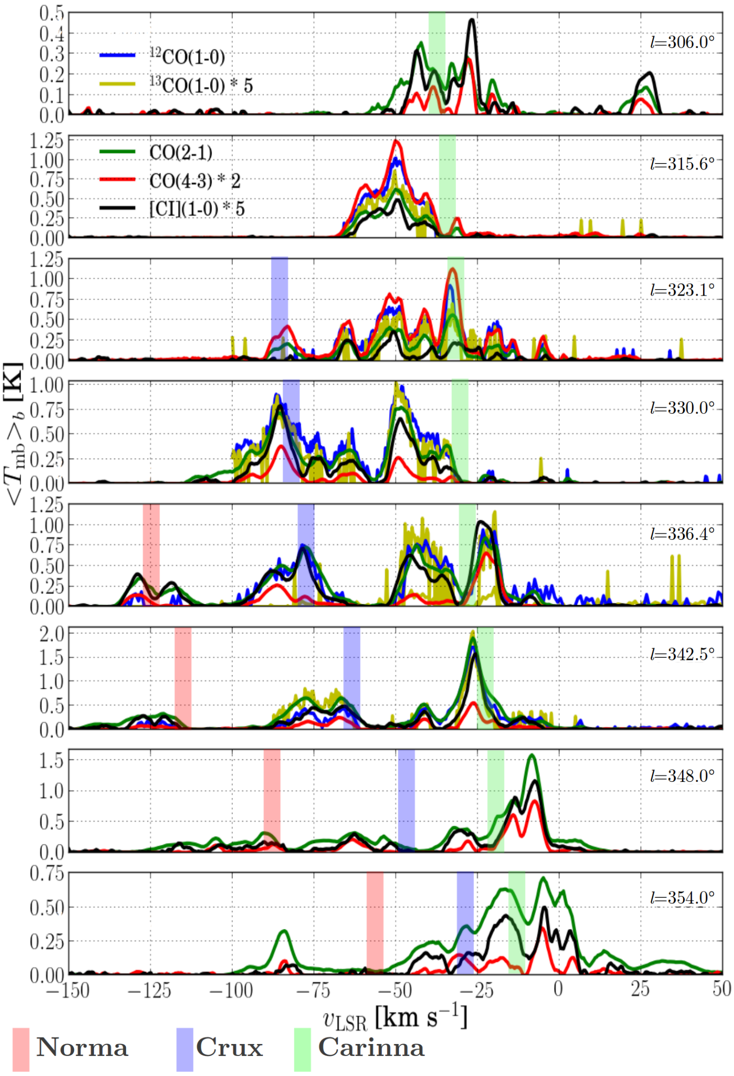

Figure 6.14: The mean main beam brightness temperature $\langle T_{\rm mb}\rangle$ of ^{12}CO(1–0) (blue), ^{13}CO(1–0) (yellow), ^{12}CO(2–1) (green), ^{12}CO(4–3) (red) and [CI](1–0) (black) as function of $v_{\rm LSR}$ for the b–strips discussed here. For the sake of a better comparison the $\langle T_{\rm mb}\rangle$ of ^{13}CO(1–0), CO(4–3) and [CI](1–0) were multiplied with factors shown in the legend. Position of spiral arms are marked by the coloured bars.

The pitch angle is given by

$$p = \arctan(\alpha). \tag{6.7}$$

The parameters a, α and p, for the different spirals arms are taken from Steiman-Cameron, Wolfire & Hollenbach (2010)[xiv], listed in Table 6.4. The thus estimated spiral arms are shown in Figure 6.15.

6.3.3 LOCATION OF THE OBSERVED EMISSION IN THE MILKY WAY

The emission within the b–strips is mainly associated with the spirals arms, as shown in the Figures 6.14 and 6.15. Almost all the features can

xiv Steiman-Cameron, Wolfire & Hollenbach (2010) derived the spiral arm parameters a, α and p from [CII] and [NII]205μm COBE/FIRAS and BICE maps of the Milky Way by fitting various spiral arm models to the longitudinal resolved data.

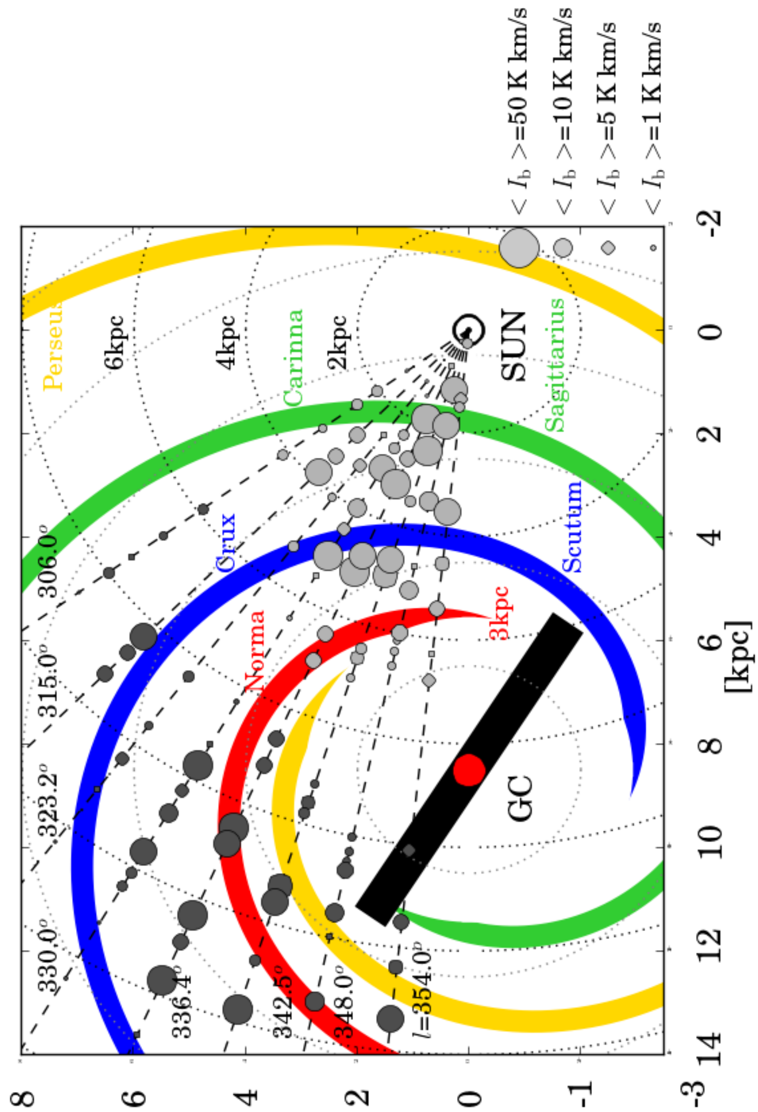

Figure 6.15: Spiral structure of the Milky Way, based on the model by Steiman-Cameron, Wolfire & Hollenbach (2010). The positions of the clouds are superimposed. The size of the circles correspond to the velocity integrated CO(2–1) intensity of the sources, average over the full range of the galactic latitudes (Δb=4 °). The average velocity integrated CO(2–1) intensity were calculated via a Gaussian decomposition of the average emission over the b–strips, shown in Figure 6.14. The ambiguity of the source distances is indicated by the colour coding: The near solution is shown by the light grey circle, while the far solution is shown in dark grey. For the sake of a better comparability the colour-code of the spirals is identical with those used in Vallée (2008). Their labels are shown in the same colour. Steiman-Cameron, Wolfire & Hollenbach (2010) gives no position angle for the galactic bar. The galactic bar is, therefore, shown for a position angle of 32°, as proposed by Vallée (2008). The position of the solar system is marked by the symbol '⊙', at a distance of 8.5 kpc from the Galactic Centre (red •). Isodistances, in steps of 2 kpc, around the Sun and the Galactic Centre are shown by the dotted circles.

be associated with the near side of the spiral arms. Dominant features arise from the Carina–Sagittarius arm at distances of $D_{\odot}$~1 to 3 kpc, the Crux–Scutum arm (alias Centaurus arm) at distances of $D_{\odot}$~4 to 5 kpc, as well as from the Norma and/or the 3 kpc arm at distances of $D_{\odot}$~6 to 7 kpc. The features of the Carina–Sagittarius arm are observed in all the b–strips. Those of the Crux arm are observed in all b–strips but at l=306.0° and 315°and those of the Norma arm in the b–strips at $l \geq 336.4°$.

The feature at v_{LSR}=+27 km/s, b=-0.5° at l=306.0° might have its origin in the outer Carina arm at a distance of $D_{\odot}$~13 kpc and z~110 pc above the galactic plane[xv].

6.4 VERTICAL AND RADIAL DISTRIBUTION OF THE EMISSION AROUND THE GALACTIC MIDPLANE

The following section is dedicated to determine the scale height, $z_{1/2}$, of [CI](1–0), CO(2–1) and CO(4–3). Their radial distribution is studied as well. These results are compared with the complementary Mopra CO(1–0) data and with the values of $z_{1/2}$(CO(1–0)) derived by Sanders, Solomon & Scoville (1984) and Clemens et al. (1988). Finally, the results are compared with the scale height of [CII] (Langer, Pineda & Velusamy 2014a) and HI (Dickey & Lockman 1990). First, I will give a brief introduction into the theoretical background of the scale height.

6.4.1 THEORETICAL BACKGROUND OF THE SCALE HEIGHT

As already mentioned the vertical distribution of the gas in a disc, estimated with the scale height, reflects the hydrostatic pressure within the disc. The scale height of a disc in hydrostatic equilibrium is determined by the equilibrium of the pressure in the ISM and the gravitational force of the mass in the disc. This includes the mass of the gas and the stars (Sanders et al. 1984) as well as the dark matter (Narayan & Jog 2002). In an isothermal disc the pressure depends on the velocity dispersion perpendicular to the disc of the considered medium $\langle v_{\mathrm{z}} \rangle$. The scale height is related to $\langle v_{\mathrm{z}} \rangle$ via (Talbot & Arnett 1975; Sanders, Solomon & Scoville 1984)

$$z_{1/2} = \frac{1}{2}\sqrt{\frac{\langle v_{\mathrm{z}}^2 \rangle}{2\pi G \rho(0)}} \tag{6.8}$$

where G is the gravitational constant and $\rho(z)$ the total density distribution of the considered medium along the z-axis. The vertical distribution of the density in a isothermal disc is described by a hyperbolic secant–function (accordingly also a cosine–function) via (Spitzer 1942; van der Kruit & Searle 1981a;b; Wegg et al. 2015)

$$\rho(z) = \frac{\rho(0)}{\cosh^2\left(\frac{z-z_{\mathrm{c}}}{z_{1/2}}\right)} = \rho(0)\,\mathrm{sech}^2\left(\frac{z-z_{\mathrm{c}}}{z_{1/2}}\right) \tag{6.9}$$

where z_{c} is the offset in vertical direction of the centre of the disc.

Gaussians are often used as an approximation of Equation (6.9) (e.g. Talbot & Arnett 1975; Sanders, Solomon & Scoville 1984; Langer, Pineda

xv The distance of a source from the galactic plane is calculated with Equation (6.12), cf. Section 6.4.

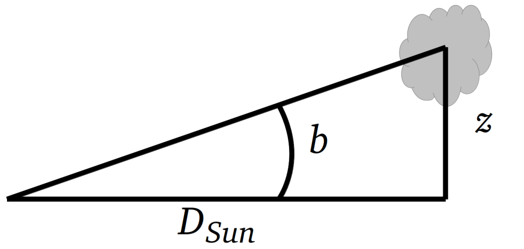

Figure 6.16: Schematic illustration of the trigonometrical relation between the distance from the sun $D_\odot$, the galactic latitude b and distance from the galactic plane z.

& Velusamy 2014a and Figure 6.20). Equation (6.9) can be than approximated by

$$f(z) = f(z_0)e^{-0.5\left(\frac{z-z_{\mathrm{c}}}{z_{1/2}}\right)^2} \tag{6.10}$$

The scale height $z_{1/2}$ is then related to the full width half maximum, FWHM, via

$$z_{1/2} = \frac{\mathrm{FWHM}}{2\sqrt{2\ln(2)}}. \tag{6.11}$$

In virial approximation the velocity dispersion of the gas is described by the Maxwell–Boltzmann distribution. In this case the square of the velocity dispersion $\langle v_z^2 \rangle$ is proportional to the temperature of the medium, $\langle v_{\mathrm{z}}{}^2 \rangle = \frac{3k_{\mathrm{B}}}{m} T$, with m being the mass of a gas particle. Colder gas phases therefore obtain a generally higher pressure and therefore lower scale heights compared to warmer gas phases (cf. Fig 6.20 and Langer, Pineda & Velusamy 2014a). This explains the different scale height of HI in the CNM and WIM where the gas temperature have values of $\sim 10^2$ K, and a few $\sim 10^3$ K. It also explains the different scale height of CO(1–0) and [CII]. As mentioned in Section 2.1 CO(1–0) is in general associated with lower gas temperatures (few $\sim 10^0$ to 10^1 K) than [CII] ($\sim 10^2$ to 10^4K), and thus, $z_{1/2}$(CO(1–0))<$z_{1/2}$([CII]).

If C^0 is associated with a gas phase in between CO and C$^+$ it would be expected that its gas temperatures are between those of CO and ionized carbon. In that case the observable scale height of the C^0 transitions should be higher than those of CO but lower than $z_{1/2}$([CII]).

6.4.2 OBSERVED DISTRIBUTION PERPENDICULAR TO THE DISC AND AN ALTERNATIVE DEFINITION OF THE SCALE HEIGHT

The distance of an emission from the galactic plane z can be calculated via the simple trigonometrical relation

$$z = \tan(b) \times D_\odot, \tag{6.12}$$

with $D_\odot$ being the (presumably) known distance of the source from the sun, and b being the the galactic latitude (cf. Figure 6.16).

The b–strips reflect the individual conditions at the specific longitudes. To minimize the impact of the local conditions and to gain a more general overview of the scale height at different galactic radii, it is necessary to integrate over a large sample of clouds within a certain range of R_{GC}. To determine their scale height they have to be within similar distances from the sun. To study the radial distribution of the scale height it is also necessary that the clouds have similar distances to the Galactic Centre.

Figure 6.17 illustrates R_{GC} and $D_{\odot}$ of the individual clouds for the different b–strips. More than 95% of the observed emission is associated with regions that have a width of $\Delta(D_{\odot})$=1 kpc and $\Delta(R_{\mathrm{GC}})\simeq$1 to 2 kpc. These regions are marked by the 'red boxes' in Figure 6.17. Its precise borders are listed in Table 6.6. Within these borders all the line emission at the same galactic latitude was integrated. The distance from the galactic plane was determined via Equation (6.12). It is assumed that the emission arises from the middle of the discussed $D_{\odot}$, with uncertainties of ±0.5 kpc. The thus derived latitudinal distributions of the line emission are shown in Figure 6.18. For the sake of a better comparability, the distributions are normalised to the specific maximal line emission within the chosen $D_{\odot}$ and R_{GC}.

Figure 6.18 shows the vertical profiles of [CI](1–0), ^{12}CO(1–0), CO(2–1) and CO(4–3) for distances up to $D_{\odot}$=7.5±0.5 kpc. The profile of the ^{13}CO(1–0) transitions are only shown for distances up to $D_{\odot}$=5.5±0.5 kpc, since no b–strips at l=306.0°, 348.0° and 354.0° are provided by the Mopra observations, and the v_{LSR} ranges to $v_{\mathrm{LSR}}\gtrsim$-110 km/s. The vertical distribution of the gas exceeds the observed latitudinal range of b=±2° for the inner $D_{\odot}\lesssim$3 to 4 kpc. Therefore the observations do not fully sample the vertical gas distribution for $D_{\odot}\lesssim$3 to 4 kpc.

All profiles have a non sech^2 profile and for this reason also a non Gaussian shape. The profiles are asymmetrical, have offsets from the galactic plane and show several individual features. They are therefore not fitable with a single Gaussian profile. Therefore, it is necessary to define the scale height and the vertical offset from the galactic plane by other criteria. I define the centroid offsets from b=0°, z_c, as the z–position of the mean emission

$$z_c = \frac{\int T_{\mathrm{mb}} z \, \mathrm{d}z}{\int T_{\mathrm{mb}} \mathrm{d}z}. \tag{6.13}$$

The scale height $z_{1/2}$ is defined as the square root of the variance of the z_c

$$z_{1/2} = \sqrt{\mathrm{Var(z_c)}} \tag{6.14}$$

$$= \sqrt{\frac{\int T_{\mathrm{mb}} (z_c - z)^2 \mathrm{d}z}{\int T_{\mathrm{mb}} \mathrm{d}z}}. \tag{6.15}$$

The uncertainties of the scale height were calculated via the statistical method *'bootstrap'*[xvi].

6.4.3 DISTRIBUTION OF [CI](1–0), CO(2–1) AND CO(4–3) IN THE FOURTH QUADRANT OF THE MILKY WAY

The perpendicular distribution of the normalised line emission for the different distances to the sun and the Galactic Centre are shown in Figure

xvi *Bootstrapping* is a statistical method which is based on the random sampling of the data points with replacement (Efron 1979; Efron & Tibshirani 1994). The uncertainty for a specific scale height, $z_{1/2}(R_{\mathrm{GC}})$, was determined via the square root of the variance of $2\times n\times\ln(n)^2$ randomly composed datasets. Each dataset consists out of the randomly composed n=267 data points of the specific latitudinal emission distribution.

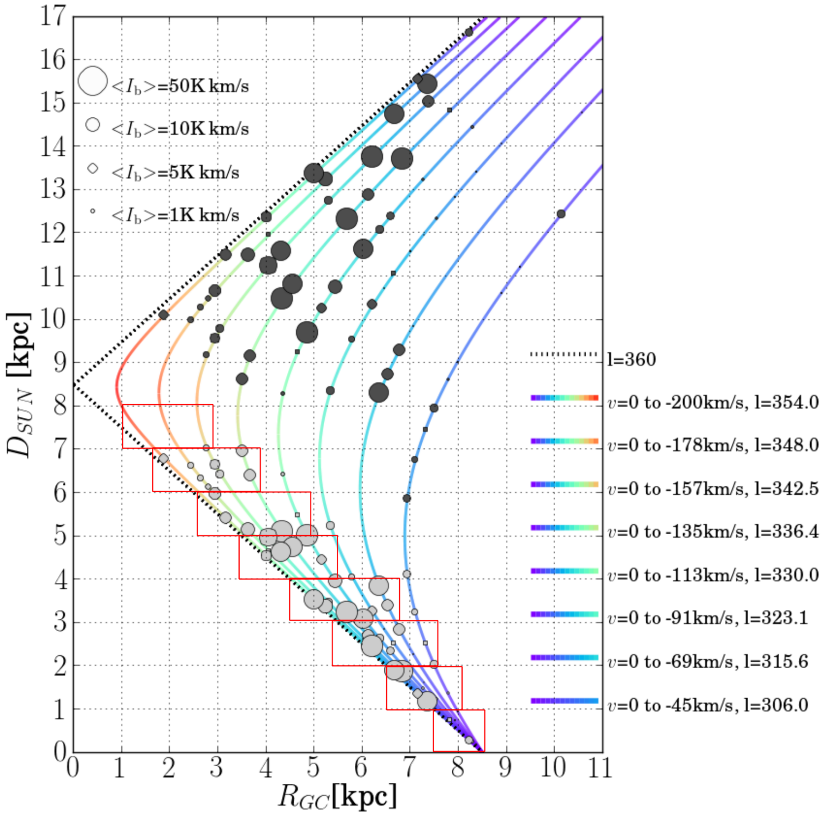

Figure 6.17: Illustration of $R_{\rm GC}$ and $D_\odot$ derived from the kinematic distances for all sources. The size of the circles correspond to the velocity integrated CO(2–1) intensity of the sources, averaged over the full range of the galactic latitudes discussed here (Δb=4°). The colour coding indicates the ambiguity of the source distances. The emission within the marked areas, shown by the 'red boxes', were integrated.

6.18. These profiles are complex and have an asymmetric shape. They show several individual features, with typical widths of $\sim$ 5 to 30 pc. The profiles are not single Gaussian. A Gaussian profile would require a large sample of positions (cf. e.g. Sanders, Solomon & Scoville 1984 or Langer, Pineda & Velusamy 2014a) The majority of the emission is located within the inner 100 pc around the centre of the disc. Nevertheless, several individual features can be observed at distances up to z~200 pc above the galactic disc. For $R_{\rm GC}$≥5.6±1.1 kpc the latitudinal distribution of the gas exceeds the shown range. This is caused by the observational limitation to the inner b=±2°.

The calculated z_c and $z_{1/2}$ for the different $R_{\rm GC}$ are summarized in table 6.6. The z_c and $z_{1/2}$ as function of $R_{\rm GC}$ are shown in Figure 6.19. The $z_{1/2}$ and z_c for $R_{\rm GC}$≥5.6±1.1 kpc have to be interpreted with caution because the data does not represent the complete latitudinal distribution of the gas.

All the lines, $^{12/13}$CO(1–0), ^{12}CO(2–1), ^{12}CO(4–3) and [CI](1–0), have nearly the same scale heights at the same $R_{\rm GC}$, within the uncertainties. The distribution of [CI](1–0) shows no significant differences to CO. The calculated scale heights vary between ~25 pc at $R_{\rm GC}$ =1.9±0.9 kpc to ~55 pc at $R_{\rm GC}$=4.7±1.1 kpc. The scale height increases towards the direction of the sun for the inner $R_{\rm GC}$(≤3.7±1.1 kpc). CO(4–3) has a

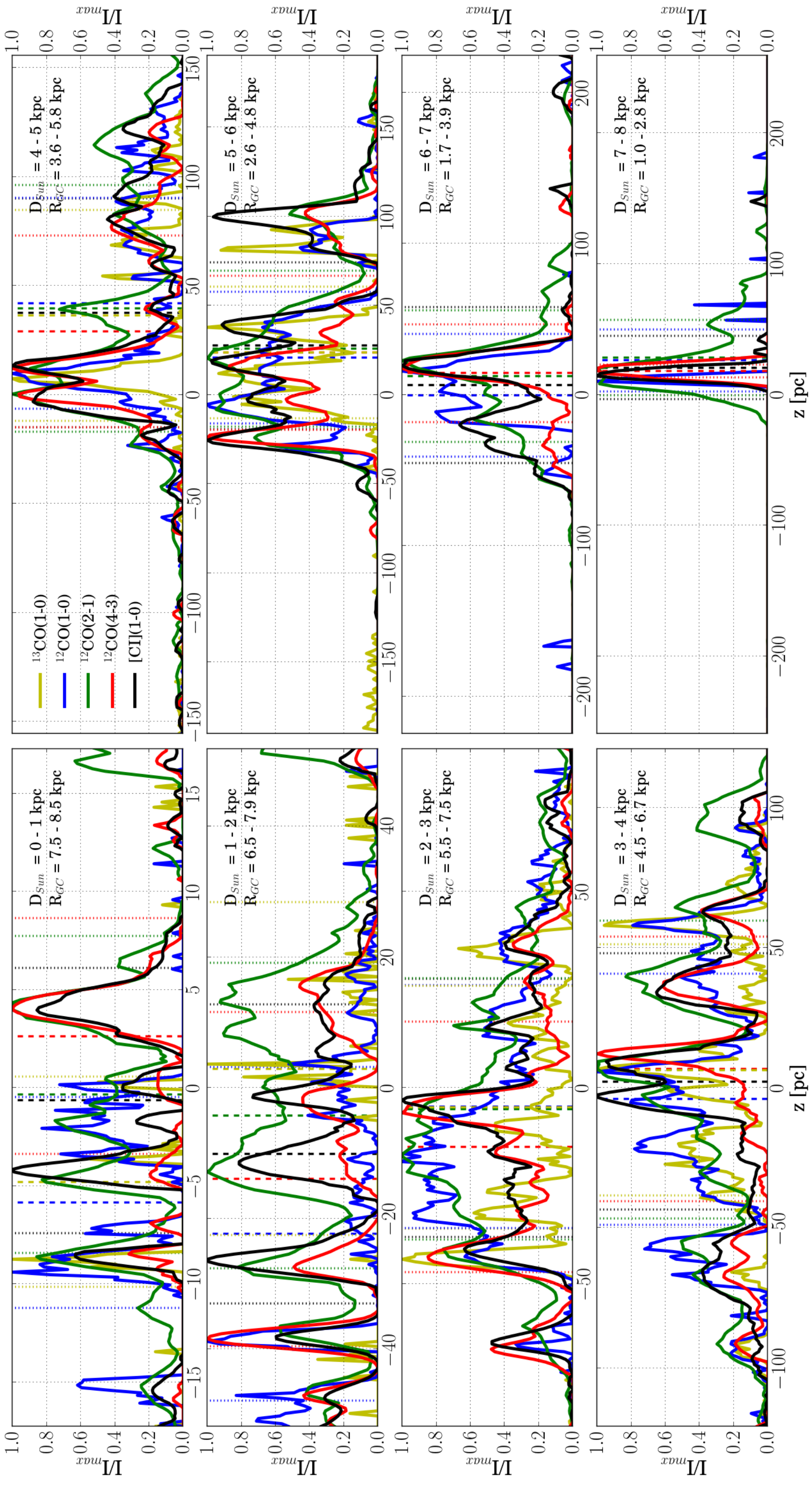

Figure 6.18: Derived vertical galactic distribution in parsec of the normalised ^{12}CO(1–0) (blue), ^{13}CO(1–0) (yellow), ^{12}CO(2–1) (green), ^{12}CO(4–3) (red) and [CI](1–0) (black) intensities for different distances to the sun, $D_{\odot}$, and to the Galactic Centre, R_{GC}. The used distances correspond to the distances marked by the red boxes in Figure 6.16. Only intensities which are 4 times above the respective noise were considered. The shown vertical distribution of gas is based on the middle values of the considered $D_{\odot}$ bins, i.e $D_{\odot}$=0.5, 1.5, 2.5 kpc... The dashed coloured lines mark the positions of the mean line emission. The dotted lines show the square root of the variance of the specific lines.

slightly lower scale height at low R_{GC}($\leq$3.7$\pm$1.1 kpc), compared to CO(2–1) and [CI](1–0). At higher R_{GC} all scale heights are similar. The scale height of [CI](1–0) and CO(2–1) are equal within the uncertainties as well. Note that the scale heights seem to decrease towards sources near the sun ($R_{GC}\gtrsim$5.6$\pm$1.1 kpc, $D_\odot\lesssim$3.5$\pm$0.5 kpc). This is presumably induced by the observational limitation to the inner b=$\pm$2°. The low scale height of CO(4–3) near the Galactic Centre has its origin presumably in the higher confusion limit, compared to CO(2–1) and [CI](1–0). Note again that almost all the profiles show a strong asymmetry in the emission and have no single Gaussian shape.

The $z_{1/2}$ of the inner R_{GC} can be fitted by a power law function

$$z_{1/2}(R_{GC}) = A \times {R_{GC}}^B \tag{6.16}$$

with power law exponents of B~0.5$\pm$0.2 for ^{12}CO(1–0), 0.5$\pm$0.4 for CO(2–1), 1$\pm$0.3 for CO(4–3) and 0.5$\pm$0.2 for [CI](1–0). Note that the probability of the fits is not high. The fit [CI](1–0) and CO(1–0) has a χ^2~8 and 9 respectively, CO(4–3) has a χ^2~14, while the χ^2 for CO(2–1) is ~2. The precise parameters are listed in table 6.5, and illustrated in Figure 6.18. The power law exponent of CO(4–3) might be caused by the relative high confusion limit of these observations. The fitted distributions are hence similar to the radial distribution for CO(1–0) $z_{1/2}(R_{GC}) = 26 \times {R_{GC}}^{0.47}$ found by Sanders, Solomon & Scoville (1984). The increase of the CO(1–0) scale height towards higher R_{GC} can be explained by the lower gravitational potential in the disc induced by the lower gas mass and density towards higher galactic distances (cf. Dame et al. 2001; Freeman & Bland-Hawthorn 2002).

The extrapolation of Equation (6.16) with the fitted parameters allows the estimation of the scale heights at the position of the sun, $z_{1/2}(R_0)$. The fit gives scale heights at the sun of $z_{1/2}(R_0)$=62$\pm$7 pc for [CI](1–0), 61$\pm$9 pc for ^{12}CO(1–0), 71$\pm$12 pc for CO(2–1) and 82$\pm$26 pc for CO(4–3) (cf. Table 6.5). These scale heights are consistent with the values found for ^{12}CO(1–0) by other studies, thus as $z_{1/2}(R_0)$=70$\pm$18 pc by Sanders, Solomon & Scoville (1984), 72$\pm$8 pc by Clemens et al. (1988) and 57 pc by Malhotra (1994a;b)[xvii].

The almost equal scale heights of CO and [CI](1–0) indicates that neutral carbon is associated with the CO–photodissociation layer in the Milky Way. An increase of the [CI](1–0) scale height relative to those of the CO transitions towards higher R_{GC} is not observed. An increase would have indicated a higher C^0 fraction compared to CO, and in the end a higher fraction of H_2 traced by C^0, compared to H_2 traced by CO, but that is not the case.

Now I will discuss the displacement of the line centroids from b=0°, z_c. In the following text positive z_c are associated with positive latitudes and vice versa for negative values. The data gives positive z_c~20 to 40 pc for the inner $R_{GC}\leq$4.3$\pm$0.7 kpc and negative offset of ~-10 to -20 pc for R_{GC}=6.5$\pm$1.0 and 7.2$\pm$0.7 kpc. The mean offset of all available lines at R_{GC}=8.0$\pm$0.5 kpc gives no significant displacement of the solar system

xvii These calculations are based on linear fits to CO(1–0) observations by Knapp et al. (1985). Malhotra (1994b) gives no error for $z_{1/2}(R_0)$

	$z_{1/2}(R_{GC})$=$A\times R_{GC}{}^{B}$			
	A	B	$z_{1/2}(R_0)$ [pc]	χ^2
^{12}CO(1–0)	19.2±2.6	0.54±0.22	61±9	8.7
CO(2–1)	23.7±4.0	0.51±0.06	71±12	2.1
CO(4–3)	9.4±2.9	1.01±0.32	82±26	14.2
[CI](1–0)	27.2±3.0	0.39±0.15	61±7	8.1

Table 6.5: Fit parameters of $z_{1/2}$ for ^{12}CO(1–0), CO(2–1), CO(4–3) and [CI](1–0) as a function of R_{GC} for the inner 6.1±0.6 kpc. The reliability of the specific fits are shown by the χ^2 values in the right column. The scale height of the line at the position of the sun, $z_{1/2}(R_0)$ is listed in column four.

from the galactic plane, z_c(8.0±0.5 kpc)=-1.5±8.5 pc. The offsets found here are consistent with the value found by Sanders, Solomon & Scoville (1984) of -5.4±10.0 pc based on CO(1–0) data.

The variation of the z_c along R_{GC} show the warping of the galactic plane. The data implies a warping with amplitudes of ∼60 pc and a wavelength of ∼3 to 4 kpc in direction towards the galactic centre, in accordance with the values found by Sanders, Solomon & Scoville (1984) and Clemens et al. (1988) for the first quadrant of the Milky Way.

6.4.4 COMPARISON OF THE PROFILES WITH [CII] AND HI OBSERVATIONS

The following section compares the vertical distribution of CO and [CI](1–0) with those of [CII] and HI, carried out from observational data.

[CII] emission arises from almost all phases of the ISM, such as molecular clouds, the CNM, the diffuse WNM and the HIM[xviii]. The vertical distribution of [CII] is a result of the emission from the different phases. In contrast, the vertical distribution of the CO and [CI](1–0) emission (as shown in this chapter) reflects exclusively the distribution of molecular gas. Therefore it is expected that the scale height of [CII] emission is higher than those of CO and [CI](1–0).

The scale height of [CII] in the Milky Way is discussed in Langer, Pineda & Velusamy (2014a). This study calculated the average [CII] scale height between $5^\circ<l<25^\circ$. The calculation is based on observations carried out with BICE[xix] and IRTS/FILM[xx]. The BICE and FILM observations have a low spectral resolution, $\Delta v \gtrsim 175$ km/s. Therefore, the radial distribution of the [CII] scale height could not be analysed. For the analysis all [CII] emissions between $5^\circ<l<25^\circ$was averaged to a single vertical profile. The profile is shown in 6.20. This profile almost have a Gaussian shape. The

xviii see section 2.1

xix The *Balloon-borne Infrared Carbon Explorer, BICE*, (Nakagawa et al. 1998) mapped the [CII] emission between b=±3° and 350° $<l<$25° with an angular resolution of 15 ′ and low velocity resolution of Δv=175 km/s

xx The *Far-Infrared Line Mapper (FILM)* onboard the *Infrared Telescope in Space (IRTS)* (Shibai et al. 1991; Makiuti et al. 2002) observed the [CII]emission in a circle, that crossed the galactic plane at l=50° and 230° with a velocity resolution of Δv=750 km/s

$D_\odot$	R_{GC}l – R_{GC}u	R_{GC}	^{13}CO(1–0)		^{12}CO(1–0)		CO(2–1)		CO(4–3)		[CI](1–0)	
			z_c	$z_{1/2}$	z_c	$z_{1/2}$	z_c	$z_{1/2}$	z_c	$z_{1/2}$	z_c	$z_{1/2}$
[kpc]	[kpc]	[kpc]	[pc]	[pc]	[pc]	[pc]	[pc]	[pc]	[pc]	[pc]	[pc]	[pc]
0 – 1	7.5 – 8.5	8.0±0.5	-4.8	6.6±6.6	-5.9	5.3±5.3	0.4	8.1±8.1	2.5	6.0±6.0	-0.7	6.7±6.7
1 – 2	6.5 – 7.9	7.2±0.7	2.5	23.2±8.5	-22.6	25.3±8.5	-4.5	23.3±7.8	-14.2	25.5±8.5	-10.4	22.8±7.7
2 – 3	5.5 – 7.5	6.5±1.0	-5.1	32.2±6.5	-5.0	30.9±6.3	-5.5	33.3±6.7	-15.3	31.8±6.5	-5.2	32.9±6.7
3 – 4	4.5 – 6.7	5.6±1.1	6.3	42.6±6.4	-4.1	44.7±6.6	6.5	53.1±7.8	6.6	47.0±7.2	2.2	45.7±6.9
4 – 5	3.6 – 5.8	4.7±1.1	36.2	45.4±5.9	41.7	48.1±5.6	39.4	56.5±6.6	28.9	43.8±5.4	37.3	52.4±6.2
5 – 6	2.6 – 4.8	3.7±1.1	23.6	36.9±5.1	20.6	36.8±3.7	25.6	43.6±4.0	23.4	43.0±4.1	27.3	46.6±4.3
6 – 7	1.7 – 3.9	2.8±1.1	–	–	-0.8	40.7±4.5	11.9	43.8±4.1	14.0	32.5±4.4	6.1	51.7±6.2
7 – 8	1.0 – 2.8	1.9±0.9	–	–	26.1	20.8±5.4	28.0	28.9±2.7	17.8	4.5±0.9	20.4	24.1±7.7

Table 6.6: $D_\odot$ and R_{GC} used to determine the vertical profiles as shown by the red boxes in Figure 6.17. Note that the uncertainties of z_c are equal to $z_{1/2}$.

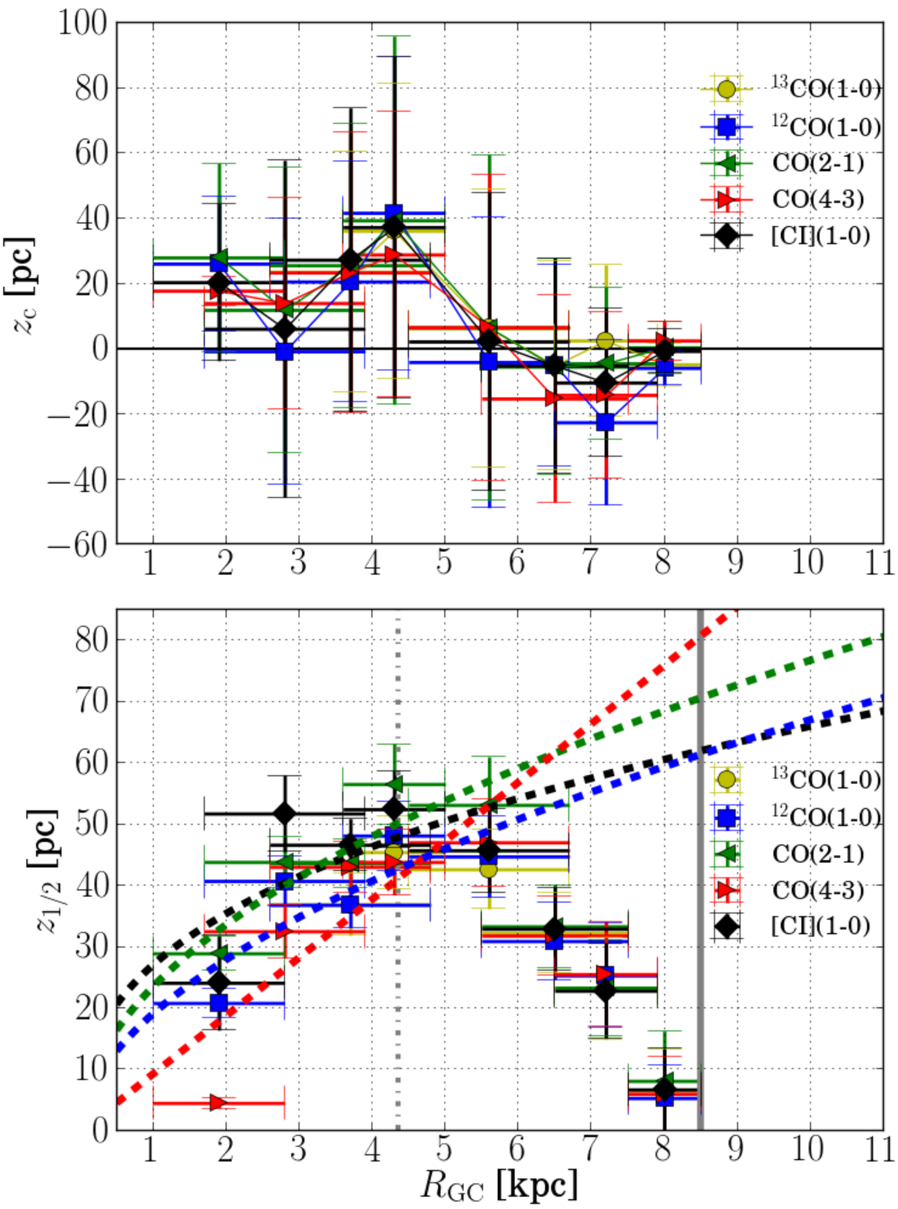

Figure 6.19: Radial distribution of z_c (upper image) and $z_{1/2}$ (lower image) as function of the distance to the Galactic Centre R_{GC} of ^{13}CO(1–0) (●), ^{12}CO(1–0) (■), CO(2–1) (◀), CO(4–3) (▶) and [CI](1–0) (◆). The scale heights for $R_{GC} <$ 4.3 kpc are fitted with the function $z_{1/2}(R_{GC})=A\times R_{GC}{}^{B}$, illustrated by the dashed lines. The fit parameters are listed in table 6.5. The position of the sun is marked by the solid grey line.

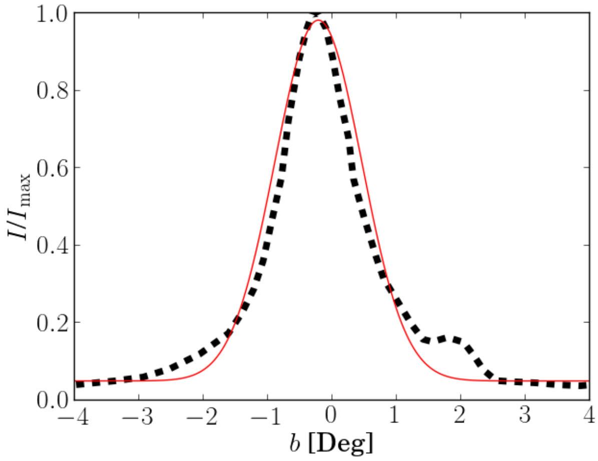

Figure 6.20: Latitudinal distribution of the normalised [CII] emission (dashed black line) average over $5° < l < 25°$ (Langer, Pineda & Velusamy 2014a). The plot is based on BICE and FILM data . A Gaussian fit to the distribution is shown by the red solid line.

shape results from the integral over the large number of clouds within these 20°. The BCIE+FILM data were combined to spectrally resolved [CII] data at b=0°[xxi], to estimate the distance of the mean emission from the sun. Langer, Pineda & Velusamy (2014a) calculated a [CII] scale height of $z_{1/2}$([CII])=73 pc as a mean value for $R_{\rm GC}$=3 to 7 kpc. Note that the [CII] scale height is effected by the warping of the galactic disc. Therefore it is an upper limit.

The fit of equation 6.16 give average scale heights of ∼50 pc for CO and [CI](1–0)[xxii] for the galactic distances of $R_{\rm GC}$=3 to 7 kpc. The average scale height of [CII], as estimated by Langer, Pineda & Velusamy (2014a), is higher than the average scale heights of CO and [CI](1–0) at the same galactic distances. The differences can be presumably (at least partially) explained by [CII] emission which arises from the WNM and HIM. This emission increases the scale height of [CII], compared to the $z_{1/2}$([CII]) that is based on [CII] emission from molecular clouds and the CNM. The scale height of the [CII] emission, that is associated with molecular clouds and the CNM could be similar to those of CO and [CI](1–0).

The scale height of HI and its radial distribution has been discussed for more than five decades (cf. Schmidt 1957; Woltjer 1962). Neutral atomic hydrogen is associated with the cold neutral medium as well as with the warm neutral medium[xxiii]. Therefore different HI scale heights for different phases are found. The scale height of HI in the CNM is $z_{1/2}$(HI)∼110 pc (Schmidt 1957; Baker & Burton 1979; Dickey & Lockman 1990), and ∼ 250 pc in the WNM (Lockman 1984; Dickey & Lockman 1990). This scale height of HI in the CNM shows no radial distribution within the inner 8.5 kpc (Schmidt 1957; Woltjer 1962; Boulares & Cox 1990; Dickey & Lockman 1990; Narayan & Jog 2002). It remains almost constant at $z_{1/2}$(HI)≈110pc. This coincidence is explained by the combined gravitational potential of the H^0, H_2 and of the stars (Narayan & Jog 2002). So the scale height of atomic hydrogen of the CNM exceeds those of CO and [CI](1–0) by a factor ∼5 at $R_{\rm GC}$∼2 kpc and ∼2 at the location of the sun.

xxi Spectrally resolved [CII] data at b=0° is provided by the Herschel/HIFI observations within the GOT C^+ project (Pineda et al. 2013)

xxii The fit gives scale heights of 48±5 pc for CO(1–0), 56±6 pc for CO(2–1) and 52±12 pc for [CI](1–0), as mean values for 3 kpc<$R_{\rm GC}$<7 kpc

xxiii For further details see Section 2.1.

6.4.5 COMPARISON WITH SIMULATED [CII] MAPS

The comparison of the shape of the profiles, as presented here, with numerical simulations can shed light onto the evolution of the gas and allow statements about the dominant dynamical processes within galactic discs. turbulences, shocks from supernovae and the local gravitational clumping of clouds dominates.

Recently, simulations of pieces of galactic discs were carried out within the SILCC project. (SILCC: Simulating the Life Cycle of molecular clouds, Walch et al. 2015; Girichidis et al. 2016; Franeck et al. 2016 submitted). Within this project the evolution of the ISM is simulated in boxes of $0.5{\times}0.5{\times}\pm5$ kpc, by using the mesh hydrodynamic code FLASH 4 (Fryxell et al. 2000). The simulations are based on physical conditions similar to those found in the solar neighbourhood. The simulations are based on self gravitating clumps with a gas surface density of 10 $M_{\odot}/\mathrm{pc}^2$. A simplified chemical network is provided, consisting of H_2, H^0, H^+, CO, C^+, O and e^-. The feedback of super novae is to the ISM is simulated. A constant supernova rate is assumed. The positions of the supernovae relative to the density of the gas vary for the different runs. Further an interstellar radiation field is assumed. The feedback by stellar-winds is not simulated.

In a post-processing step simulated [CII] emission maps were carried out based on these simulations, using the RADMC–3D code[xxiv] (Dullemond & Dominik 2004). Vertical profiles of the [CII] emission were calculated from these map (Franeck et al. submitted). The shape of the profiles is generally complex and cannot be described by a single Gaussian. Commonly they have an asymmetrical shape and show several local peaks with diameter of $\sim10^1$ pc around the galactic midplane. Faint emission is observed towards higher latitudes. An example of such a profile is shown in figure 6.21.

The shape of the profiles is influenced highly by the distribution of the supernovae. The emission around the galactic midplane arises form C^+ that is associated with molecular clouds and the CNM. The [CII] emission towards higher latitudes arising from the C^+ in the WNM and HIM. These simulation find [CII] scale heights of $\gtrsim$70 pc for the CNM. The simulations are in good agreement with the observations of CO and [CI](1–0) presented in this chapter. The concordance between the simulated [CII] emission in the CNM and the CO and [CI](1–0) observation might indicate that vertical distribution of the ISM in the Milky Way is influenced by supernovae which locally disrupt or compress the ISM.

For a further analysis, velocity resolved [CII] data would be required, complementary to the here presented observations[xxv].

6.5 DISCUSSION AND SUMMARY

This chapter analysed the distribution of [CI](1–0), $^{12/13}$CO(1–0), CO(2–1) and CO(4–3) perpendicular to the galactic disc (b=$\pm2°$) of eight galactic longitudes within the fourth quadrant of the Milky Way.

xxiv http://www.ita.uni-heidelberg.de/~dullemond/software/radmc-3d/

xxv Recently, SOFIA/UPGREAT observations are planned to provide complementary data for the b–strips, as analysed in this thesis.

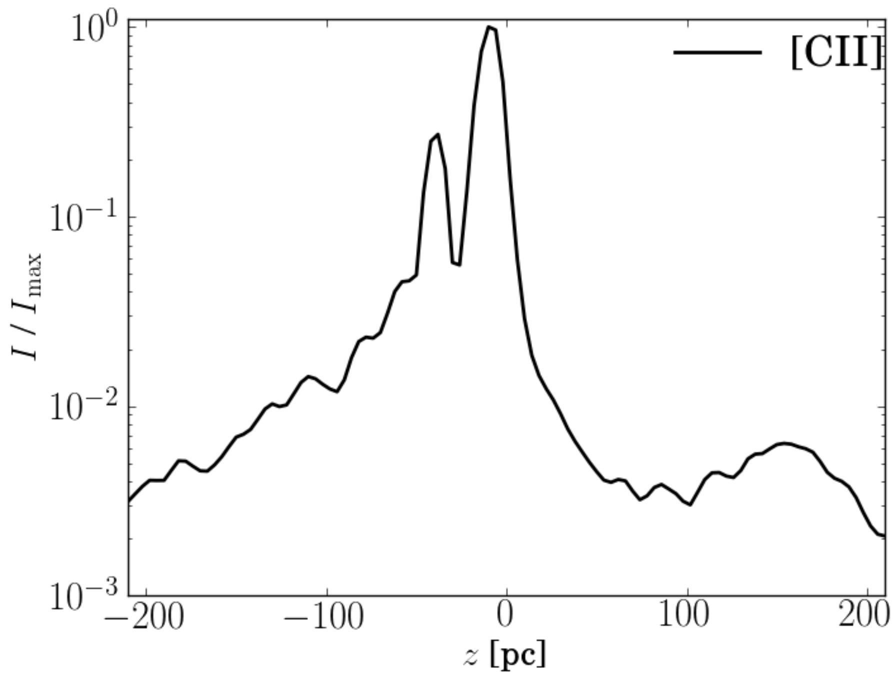

Figure 6.21: Profile of a synthetic [CII] emission map based on a simulation of a piece of a galactic disc, in a volume of 500 pc × 500 pc × ±0.5 kpc, carried out within the SILCC Project. Supernovae were implemented for these simulation. The supernovae are positioned randomly around the galactic plane, with a Gaussian probability for a certain position. This plot is based on a constant supernovae rate of 15 supernovae per Myr. The major fraction of the [CII] emission arises from molecular clouds around the galactic midplane. Faint [CII] emission is detected at larger distances to the midplane. Note that the shape of the profile is complex and has no Gaussian shape.

The observed emission arises preliminary from the galactic spiral arms. The observations show no significant differences between [CI](1–0), CO(1–0) and CO(2–1) at least in the inner galaxy (R_{GC}<8.5 kpc) neither radial from the Galactic Centre nor vertical from the galactic midplane. The [CI](1–0) emission shows a good match with ^{12}CO(2–1) and ^{12}CO(1–0). The observations show that on average only ∼1% to 2% of the detected [CI](1–0) is not associated with CO. That might indicate that most C^0 within the Milky Way arises from the surface of the CO photodissociation layer and that these lines arise from the same star forming matter. It indicates also that [CI](1–0) is no good tracer for CO dark H_2 in the Milky Way, at least for a large fraction of the positions in the Milky Way. This study is based on a relatively small sample of thin vertical strips. Therefore, it can not be excluded that there are other regions in the Milky Way, that show [CI](1–0) in the abscence CO[xxvi].

The observations show asymmetrical latitudinal profiles with local features, having diameters of 5 to 30 pc. They can not be described by a single Gaussian. The scale height of [CI](1–0), ^{12}CO(1–0) and CO(2–1) rises from $z_{1/2}$∼25-30 pc at R_{GC}≈2 kpc to $z_{1/2}$∼50 to 55 pc at R_{GC}≈4 kpc. The scale heights of the observed transitions can be fitted with power law functions. Within the uncertainties $z_{1/2} \propto {R_{GC}}^{0.5}$, which is consistent with the function found by Sanders, Solomon & Scoville (1984) and Clemens et al. (1988) for ^{12}CO(1–0). The extrapolation gives a $z_{1/2}(R_0)$=62±7 for [CI](1–0) and $z_{1/2}(R_0)$=71±12 for CO(2–1) at the location of the sun.

xxvi An example for detected C^0 that is not associated with CO is M17 SW (Pérez-Beaupuits et al. 2015).

Simulation within the SILCC-project give [CII] profiles that are similar to those of CO and [CI](1–0). Assuming that the [CII] has a similar distribution as CO and C^0, these simulations imply that major parts of the local structure of the Milky Way are triggered by supernova, which locally disrupt or compress the ISM.

Chapter 7

The distribution of carbon in M33

The following chapter investigates the distribution of carbon and hydrogen in the nearby galaxy M33. The investigations are focused on five representative major GMCs located on a ∼5 kpc long strip along the major axis of the galaxy, for which I present new [CI](1–0) observations. Combined with complementary $^{12/13}$CO(1–0), ^{12}CO(2–1) and [CII] data, from IRAM and Herschel, I am able to discuss the spectral and radial distribution of CO, C^0, and C^+ in M33. Additional complementary data, particular HI, [NII]122μm and FIR-emission, allows to estimate the fraction of molecular hydrogen in the discussed positions, particularly the fraction of CO dark H_2 traced by the neutral atomic and ionised carbon lines. The fraction of CO dark H_2, derived from the observations, is compared with those predicted by the PDR-model by Wolfire, Hollenbach & McKee (2010), for a half solar metallicity. The effect of different excitation temperatures within the different gas phases is also tested and discussed.

7.1 OBSERVATIONAL DATA OF M33

This Section describes the [CI](1–0) observations, which were performed with the CSO, APEX and Nanten2 telescopes. The data reduction process is also descibed. (Section 7.1.1). The complementary data used in the following analysis is described as well (Section 7.1.2).

7.1.1 [CI](1–0) OBSERVATIONS AND DATA PROCESSING

Between August 2012 and June 2015 we[i] observed the [CI](1–0) transition in the five prominent giant molecular clouds in M33, BCLMP691, GMC91, BCLMP302, GMC01 and GMCno06. The observations were performed with the Caltech Submillimeter Observatory, CSO (GMC01 and GMCno06), the Apex Pathfinder Experiment, APEX, (BCLMP691 and BCLMP302) and Nanten2 telescope (GMC91)[ii]. These five GMCs are located on a strip along the major axis of M33 at distances up to ∼ 3.3 kpc from the galactic centre (cf. Table 7.1 & Fig. 7.1). This observing strategy provides a sample from major structural elements of M33 along its major axis, as the galactic centre (GMC01), the main spiral arms (GMC91,

i These observations were carried out by Ed Chamber, Marc J. Royster and myself.
ii GMC01 and GMCno06 were observed in August 2012 with the CSO. BCLMP691 and BCLMP302 were observed in November 2013 and October 2014 with APEX. GMC91 was observed during several nights between July 2014 to June 2015 with the Nanten2 telescope.

(1) Position	(2) Alternative name	(3) Ra [J2000]	Dec [J2000]	(4) R_{M33} [kpc]	(5) Θ_{B} ["]
BCLMP691^{a}	GMCno01^{b}, #300^{c}	01:34:16.4	30:51:54.6	+3.29	13^{A}
GMC91^{b}	600N^{d}, #245^{c}	01:34:09.4	30:49:07.1	+2.52	37^{N}
BCLMP302^{a}	GMCno03^{b}, #256^{c}	01:34:06.6	30:47:26.0	+2.08	13^{A}
GMC01^{b} [CII] Peak	#108^{c}	01:33:52.2	30:39:15.8	-0.11	17^{C}
GMC01^{b} [CII] Flank	#108^{c}	01:33:52.9	30:39:25.1	-0.12	17^{C}
GMCno06^{b}	500S^{d}, #42^{c}	01:33:34.1	30:32:06.3	-2.03	17^{C}
Centre of M33		01:33:51.02	30:39:36.7	0.00	

Table 7.1: Coordinates and radial distances of the observed positions. The positions are shown in Figure 7.1 as well.
(1) Name of the GMC used in this paper.
(2) Alternative names of the GMC, $^{(a)}$ from Mookerjea et al. (2012), $^{(b)}$ from Rosolowsky et al. (2007); Buchbender et al. (2013), $^{(c)}$ CO(2–1) clump number from Gratier et al. (2012), $^{(d)}$ Nikola et al. in prep..
(3) Coordinates of the observed positions.
(4) lists the distance of the observing position centres to the galactic centre. The reference point for the centre of M33 is at Ra: 01:33:51.02, Dec: 30:39:36.7 (J2000). Positive values conform to distances north of the centre while negative values to distances south of the centre.
(5) Beam-size of the [CI](1–0) observations in arc-seconds. The super-scripted letters mark the telescope used for the observation; A=Apex, C=CSO and N= Nanten2.

BCLMP302, GMCno06) and a faint outer spiral arm (BCLMP691). A detailed description of the individual clouds is given in Section 7.1.3.

The observed positions were choosen, as a large amount of complementary data is available for these position, particular Herschel/Spire/PACS and HIFI data, and their bright [CII] emission and/or strong CO(2–1) emission (Kramer et al. 2010; Boquien et al. 2011; Gratier et al. 2010; Mookerjea et al. 2012; Xilouris et al. 2012; Braine et al. 2012a;b; Buchbender et al. 2013; Buchbender 2013; Druard et al. 2014; Mookerjea et al. 2016; Nikola et al. in prep.; Kramer et al. in prep).

Due to the faint [CI](1–0) emission (I([CI](1–0))$\lesssim 2\times10^{-7}$ erg cm^{-2}s^{-1}) only a single position was observed in all sources except GMC01, in which an additional position was observed. In the GMCs BCLMP691, BCLMP302 and GMC01 (alias GMC01 Peak) the [CI](1–0) observations were centred on the [CII] peak of the individual GMCs (cf. Fig. 7.22, 7.26 and 7.25). The second position in GMC01 (alias GMC01 Flank) was observed $\simeq 11''\approx$45pc to the northwest of the [CII]-peak of GMC01 . The [CII] peak of GMCno06 is within the beam of the [CI](1–0) observations. Nevertheless, the beam centre of the [CI](1–0) observations does not match the [CII] peak. It lies $\sim 7''$ to the north-east of the beam centre (Fig. 7.28). The GMC91 shows no distinct [CII] emission. Therefore, the observations were centred at the CO(2–1) peak (Fig. 7.23). Due to its missing [CII]-emission in GMC91, the [CI](1–0) observations were centred at the CO(2–1) peak (Fig. 7.23)..

The [CI](1–0) observations in the GMCs BCLMP691 and BCLMP302 were performed with the 12m Atacama Pathfinder Experiment (APEX, Güsten et al. 2006). The positions of GMC01 and GMCno06 were observed

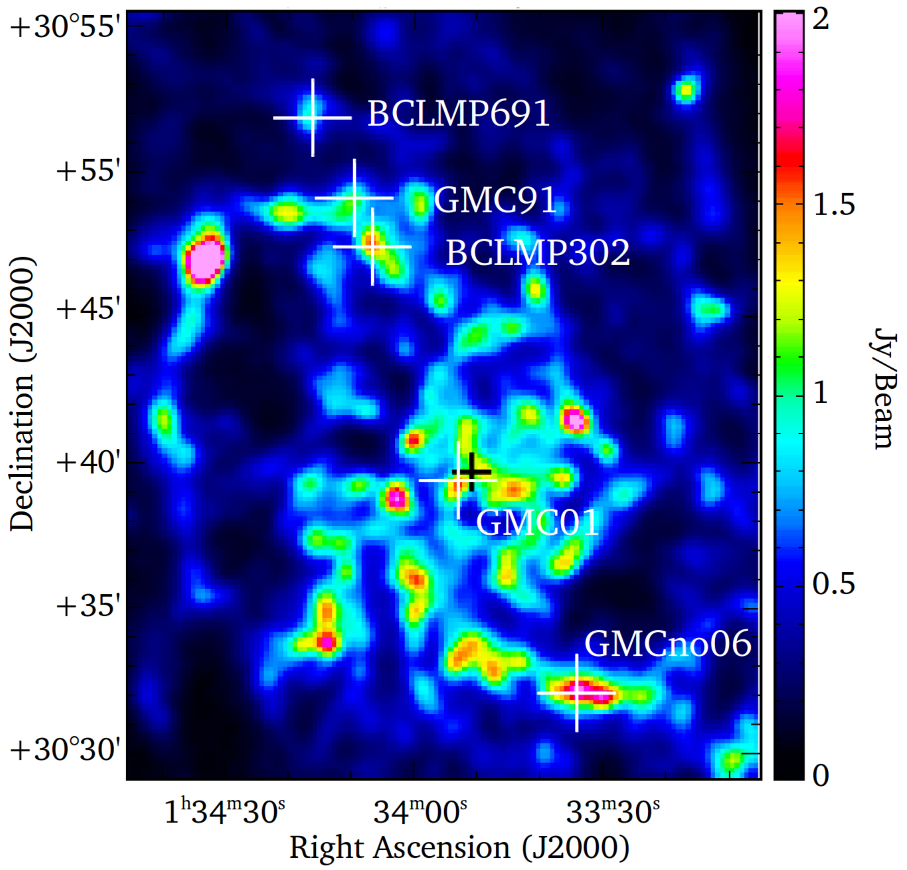

Figure 7.1: 350 μm Herschel-SPIRE map of M33 (Xilouris et al. 2012). This wavelengths shows the prominent northern and southern spiral arms of M33 as well as the GMCs discussed here. The white crosses mark the positions of the [CI](1–0) observations. The black cross displays the centre of M33 The angular distance between the two observed positions in GMC01 is 11″ (~45pc). For the sake of a better clarity GMC01 is therefore marked by a single cross. The coordinates of the positions are listed in Table 7.1.

with the 10.4m antenna of the Caltech Submillimeter Observatory (CSO, Phillips 1996). The observations of GMC91 were performed with the 4m antenna Nanten2 (Kawamura et al. 2005). The FWHM Θ_B of the [CI](1–0) observations are 12.7″ for APEX, 17″ for the CSO and 37″ for Nanten2.

The APEX observations were performed with the single pixel dual sideband SHIFI/APEX-3 receiver (Vassilev et al. 2008). The backend consists of two partially overlapping eXtended bandwidth Fast Fourier Transform Spectrometer (XFFTS), each with an individual bandwidth of 2.5 GHz and 32768 spectral channels, providing a total bandwidth of 4 GHz and a spectral resolution of 76 kHz (Klein et al. 2012).

The CSO observations were performed with the wide band 492 GHz low noise sis waveguide receiver using a FFTS with 8192 channels and a bandwidth of 4GHz as backend (Kooi et al. 1998; Kooi 2009; Kooi et al. 2010).

The Nanten2 observations were performed with the 460–490 GHz channel of the 2×8 pixel SMART receiver (Graf et al. 2002; 2008). The backends of SMART consist of sixteen eXtended bandwidth Fast Fourier Transfer Spectrometer (XFFTS; Klein et al. 2012) with a used bandwidth of 1 GHz and a spectral resolution of 76 kHz.

All [CI](1–0) observations were performed during very good weather conditions, pwv$\lesssim$0.5 mm. The system temperature ($T_{\rm sys}$) varies between

$T_{\rm sys}$~900-1200 K for the CSO, $T_{\rm sys}$~900-2100K for APEX and $T_{\rm sys}$~420-1100K for the Nanten2 observations. The observations of M33 from the APEX and Nanten2[iii] side, both located in the southern hemisphere, requireded excellent weather conditions (pwv$\lesssim$0.5mm) and relatively long integration time, as the source elevation is $\lesssim$36°. For example the summed on-source integration time on the position BCLMP302 was $\backsimeq$5 hours. The integration time for the positions observed with the CSO, located in the northern hemisphere on Mauna Kea[iv], were significantly shorter. For example the on-source integration time at the [CII] peak position of GMC01 was 16 minutes.

The data was reduced with the program *CLASS, version: jan14a*[v]. A fifth order baseline was fitted and subtracted from all data. Spectra that showed sinusoidal standing wave patterns, sinusoidal baselines with standing wave periods between 8 and 27 km/s were fitted to the spectra, similar as for the [CII] observations described in chapter 5. If the fit improved the RMS by more than 1/5 compared to a linear baseline fit, the fitted sinusoidal pattern was subtracted from the spectrum.

All data was converted to the main beam temperature scale via $T_{\rm mb}$= $T^*{}_{\rm A}/\eta_{\rm mb}$, using a main beam efficiency $\eta_{\rm mb}$= 0.60 for APEX, $\eta_{\rm mb}$ = 0.5 for the CSO and a $\eta_{\rm mb}$ = 0.5 for the Nanten2. Afterwards all the spectral data was regridded to have the same grid in velocity, and convolved to a velocity resolution of 2 km/s. The RMS of the APEX and CSO data varies between 0.009K (in GMC01 Flank) and 0.024K (in BCLMP691). The RMS of GMC91 is 0.061K. As uncertainties for the [CI](1–0) data I assume standard calibration uncertainties of 10%.

[CI](1–0) emission was detected in all positions, except in GMC91, with a signal to noise ratio better than or equal to S/N≥3.4.

7.1.2 COMPLEMENTARY DATA

Within the framework of the Herschel key program HERM33ES (Kramer et al. 2010) a large set of complementary data is provided, thus as [CII], [OI]63μm, [NII]122μm , $^{12/13}$CO(1–0), ^{12}CO(2–1) and HI. The combination of these data allows to study the distribution of the different carbon species and to determine the total amount of H_2 in the GMCs, discussed here. Furthermore, the data allows to determine the fraction of [CII] arising from the different gas phases. The fraction of CO dark H_2 can be determined as well.

High spectrally resolved CO(2–1) and HI maps are available for all positions. CO(1–0) spectra are provided for all positions but GMC01 Flank. The [CII], [NII]122μm and [OI]63μm was mapped in all positions with Herschel/PACS with a low spectral resolution Δv>100 km/s. Spectral resolved [CII] data is provided for all positions, but GMC91 and GMC01

iii APEX is located at the coordinates 22.97°S, 67.70°W. The location of Nanten 2 is roughly 10 km north of Apex (Coordinates: 23.01°S, 67.76°W).

iv Coordinates: 19.82°N, 155.48°W

v available at http://www.iram.fr/IRAMFR/GILDAS peak by Herschel/HIFI[vi] observations. The complementary data is discuss in detail in the following paragraph.

High spectrally resolved [CII] data (Θ_B=12″) was obtained from Herschel/HIFI observations (Mookerjea et al. 2012; Braine et al. 2012b; Mookerjea et al. 2016; Kramer et al. in prep.)[vii]. GMC91 and GMC01 Peak were not observed with Herschel/HIFI. Therefore no velocity resolved [CII] spectra are available for these positions[viii]. The centre position of the [CI](1–0) observations in BCLMP302 is located between the centre positions of three [CII] HIFI observations (cf. Fig 7.2). The [CII] spectra used for the analysis of this position was therefore composed by the average of the three spectra, weighted by the distances of their beam-centre to the centre of the [CI](1–0) observations.

The velocity integrated distribution of [CII], [OI]63μm and [NII]122μm emission was mapped with Herschel/PACS, in all positions. (Mookerjea et al. 2012; 2016; Nikola et al. in prep.). For the analysis I used the [NII]122μm data of the [CII] peak positions smoothed to a 12″ beam (Nikola et al. in prep.). In the position GMC01 Flank and GMCno06 the [NII]122μm data of the respective [CII] peak was used.

$^{12/13}$CO(1–0) data at a resolution of 21″ was observed with the EMIR-receiver at the IRAM 30m observatory (Rosolowsky et al. 2011; Buchbender et al. 2013).

^{12}CO(2–1) maps of M33 with Θ_B=10.7″ were obtained from IRAM 30m observations using the HERA receiver (Gratier et al. 2010; Druard et al. 2014).

Neutral hydrogen HI was mapped in the whole galaxy with the VLA at a resolution of Θ_B=12″ (Gratier et al. 2010).

Hα emission data ($\Theta_B \approx$0.3″) was obtained from observation with the 60cm Burrel-Schmidt telescope of the Kitt Peak National Observatory by Hoopes & Walterbos (2000).

Continuum maps at 24μm, 70μm (Spitzer, Tabatabaei et al. 2007) and 100μm to 500μm (Herschel/PACS and Spire Boquien et al. 2011; Xilouris et al. 2012) are provided as well.

The complementary HI and CO(2–1) data was convolved to the respective beamsize of [CI](1–0), to compare the data. The Herschel/HIFI [CII] spectra have not been convolved as only single positions with $\Theta_B \approx$12″ were observed. In BCLMP302 and BCLMP691 the beam sizes of [CI](1-0) and [CII] are almost equal, Θ_B=12″. In GMC01 and GMCno06 the beam of [CI](1–0) (Θ_B=17″) exceeds those of [CII] (Θ_B=17″ and Θ_B=12″). PACS maps show distinctive [CII] peaks in these position (Fig. 7.28. 7.26). As a consequence the integrated [CII] intensities and peak temperatures are

vi The PACS receiver was a Bolometer while HIFI was a Heterodyne instrument. Bolometer are used for sensitive continuum observations. They do not provide spectral information. Heterodyne receivers are used to for observations with a high spectral resolution. See appendix A for further details.

vii Mookerjea et al. (2012) and Mookerjea et al. (2016) discusses the distribution of [CII] in BCLMP302 and around the centre of M33 (GMC01). [CII] in BCLMP691 is discussed in Braine et al. (2012b). Kramer et al. in prep. will discuss the [CII] distribution of the southern main spiral arm, including the position GMCno06.

viii Future observations with SOFIA/upGREAT can provide [CII]–spectra of GMC01 Peak.

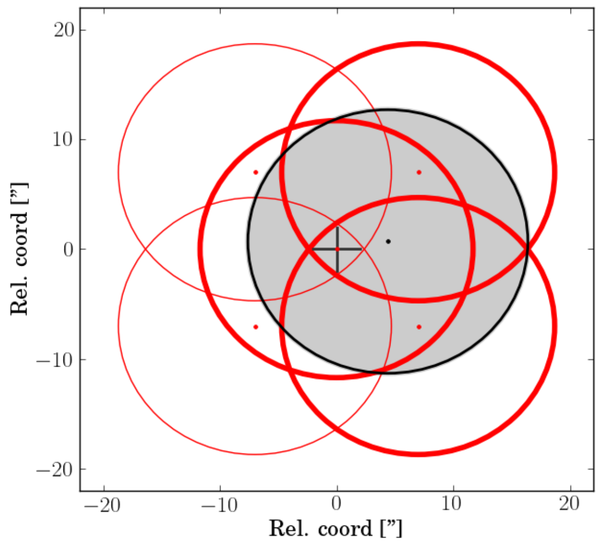

Figure 7.2: Illustration of the [CII] (red circles) and [CI](1–0) (black circle) beams around the [CII] peak of BCLMP302. The diameter of the circles correspond to the respective beam size. The [CII] spectra used to compound the spectra for the analysis are shown by the thick red circles. The black cross marks the position of the [CII] peak at Ra:1:34:06.3 Dec:30:47:25.3 (J2000).

presumably higher and the line widths are presumably narrower compared to a [CII] beam that would be equal to the [CI](1–0) observations.

7.1.3 OVERVIEW OF THE OBSERVED CLOUDS

The following paragraph gives a brief overview of the observed GMC. Their precise physical properties are described in Section 7.6.

7.1.3.1 BCLMP691

*BCLMP*691 (alias GMCno01 in Rosolowsky et al. 2007, #300 in Gratier et al. 2012) is an Hα region (Hoopes & Walterbos 2000) located in the northern region of M33 in a distance of 3.3 kpc from the nucleus. This GMC is the major star forming region on a faint spiral arm or spur with a moderate SF-rate of 12.2 ± 1.7 $M_\odot$ Gyr^{-1} pc^{-2} (Buchbender et al. 2013). This arm or spur is primarily visible at 350 & 500 μm. BCLMP691 is associated with a O–B star accumulation (#38 in Humphreys & Sandage (1980)), in the optical. For a detailed further description I recommend Braine et al. (2012a) and Braine et al. (2012b).

7.1.3.2 GMC91

*GMC*91 (Rosolowsky et al. 2007, alias #245 in Gratier et al. 2012) is located at the northern main spiral arm. At the position of GMC91 the arm changes its orientation from north-west to west (cf. Figure 7.1). The northern arm also hosts the prominent GMC NGC604, the second brightest Hα region in the local group which is also located at a prominent knee point of this spiral arm. GMC91 lies in a distance of ≈2.5kpc to the galactic centre.

GMC91 shows the most intense low J–CO emission in the sample of positions discussed in the present paper, and is one of the brightest CO emitters in the whole galaxy M33. [CII] PACS-map show only diffuse emission, that cannot be associated with the CO-emission.

IR continuum dust emission maps from 24 μm to 500μm show no distinguishable emission, which is associated with the CO peak (cf. Boquien et al. 2011; Xilouris et al. 2012; Buchbender et al. 2013; Boquien et al. 2014). The emission indicates a low star formation rate of $\sim 4\ M_\odot\ \mathrm{Gyr}^{-1}\ \mathrm{pc}^{-2}$ (Buchbender et al. 2013).

7.1.4 BCLMP302

*BCLMP*302 (alias GMCno03 in Rosolowsky et al. 2007 and #256 in Gratier et al. 2012) is the seconds largest and brightest GMC in the northern arm of M33 in a distance of ≈2.1 kpc to the galactic centre. It is located at the southern end of the same knee point of the northern spiral arm in which also GMC91 is located. The distance between these two GMCs is ≈450 pc.

The morphology of BCLMP302 is complex. The majority of CO and dust emission is observed in an elongated bow–like structure with a total length of ∼250 pc (cf. Fig. 7.25). This structure can be roughly divided into an elongated northern complex and compact southern complex. The majority of the CO emission arises from the northern complex. The dust emission (Spitzer 8 μm, 24 μm & 100 μm) arises from both complexes with a focus at the southern CO-structure. The 8 μm & 24 μm dust emission might indicate embedded star formation in this complex (Buchbender 2013). A bright young optical star cluster, with O and B–type stars, is observed between these two complexes [ix]. Its age is set to ∼ 3-10 Myr (Murphy et al. 2011). For a detailed description of the main molecular zone I recommend Buchbender (2013).

Herschel/PACS maps (Mookerjea et al. 2012) show that the [CII] emission arises ∼40pc east of the main molecular zone. Furthermore, these maps show that the spatial morphology of [OI]63μm is very similar to the [CII] morphology (Mookerjea et al. 2012).

7.1.5 GMC01

*GMC*01 (alias #108 in Gratier et al. 2012, ID#106 in Gordon et al. 1999a) is a bright Hα region (Gordon et al. 1999b) with a distance of $\sim 27'' \simeq 110$ pc to the centre of M33. The high Hα, FUV (G_0=50 Habing units) and NIR emission indicate the highest star formation rate (65 $M_\odot$ GYr^{-1} pc^{-2}) of the sources, discussed here (Gordon et al. 1999a; Calzetti et al. 2007; Buchbender 2013). The FUV and [CII] emission reach their highest value within the discussed GMCs as well.

7.1.6 GMCNO06

*GMCno*06 (alias #42 in Rosolowsky et al. 2007) is a the major star forming region and most massive GMC on the prominent inner southern arm, in a radial distance of 2.0 kpc from the centre of M33. GMCno06 has the second highest star formation rate (SFR≈36 $M_\odot$ GYr^{-1} pc^{-2}, Buchbender 2013) and hydrogen column density of the positions discussed here. It is also associated with a bright O–B star accumulation (#13 in Humphreys & Sandage 1980). The cloud complex hosts the most luminous X-ray binary

ix The star cluster is denoted as #71 in Humphreys & Sandage (1980). It was observed in detail with the HST by Bedin et al. (2005)

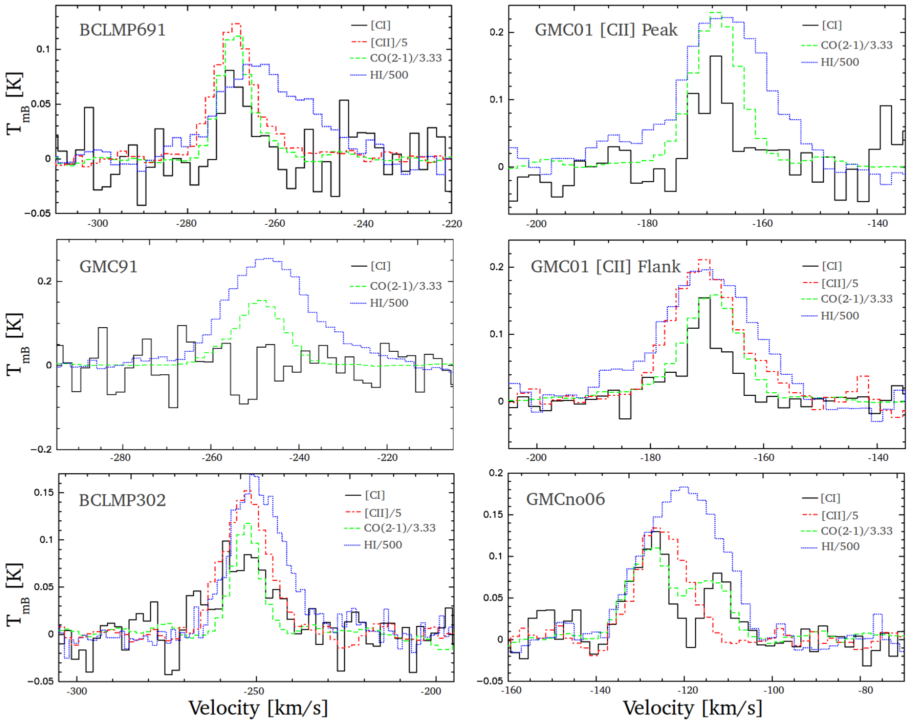

Figure 7.3: $^3P_1 \rightarrow {}^3P_0$[CI] spectra for the individual GMCs are shown by the black solid line. The beam of the [CI](1–0) data is 12.7″ for BCLMP691 and BCLMP302, 17″ for GMC01 and GMCno06 and 37″ for GMC91. The spectra of HI (blue dotted) and ^{12}CO(2–1) (green dashed) are superimposed. They are scaled to the respective beam-size of [CI](1–0). All [CII] spectra refer to data with a beam size of 12″ (red, dotted-dashed). For a better understanding the HI, CO(2–1) and [CII] spectra were multiplied with a scale factor. The scale-factors are shown in the individual plots.

M33 X-7 (Ra: 1:33:34.12, Dec: 30:32:11.6 (J2000)) known so far (Valsecchi et al. 2010) with an average luminosity of 5×10^{37} erg s^{-1} (Pietsch et al. 2004).

7.1.7 OVERVIEW OF THE OBSERVATIONAL RESULTS

The [CI](1–0) spectra are shown in Figure 7.3. The complementary HI, ^{12}CO(2–1) and [CII] spectra are superimposed.

All regions, but GMC91, show HI, [CII], [CI](1–0), $^{12/13}$CO(1–0) and ^{12}CO(1–0) emission. No [CI](1–0) and [CII] emission has been detected in GMC91.

To determine the precise line parameters, Gaussian were fitted to these lines. All the line–parameters (line widths Δv, central velocities $v_{\rm LSR}$, and the velocity integrated line intensities I, in K km s^{-1}) are listed in Table 7.2. The integrated intensity of [CII] in the position GMC01 Peak as well as the integrated intensities of [NII]122μm were determined from the fluxes of the Herschel/PACS data. The fluxes of [NII]122μm, [CII] as well as for [CI](1–0), CO(2–1) and HI are listed in Table 7.3.

The observed fluxes emphasize the importance of [CII] as a cooling line for the ISM, and particular for the molecular gas phase (cf. Table 7.3). [NII]122μm emission is exclusively associated with the ionised phase. As shown in the following (Section 7.2.4) $\gtrsim$25% of the [CII] emission arises from the molecular phase. In this phase the majority of the energy is

Position	Line	$v_{\rm LSR}$ [km/s]	Δv [km/s]	$\int T_{\rm mb}\,{\rm d}v$ [K km/s]
BCLMP691	[CI](1–0)	-269.4±1.9	6.3±0.8	0.54±0.14
	^{12}CO (1–0)*	-267.3±0.1	8.7±0.3	5.65±0.60
	^{13}CO (1–0)*	-266.4±0.4	7.8±1.1	0.54±0.11
	^{12}CO (2–1)	-269.3±0.2	7.4±0.2	3.2±0.4
	[CII]	-269.4±0.3	10.7±0.3	9.9±1.0
	HI	-263.2±0.7	23.7±0.7	1085±112
	[NII]122μm			0.49±0.09
GMC91	[CI](1–0)	– –	– –	<0.2
	^{12}CO (1–0)*	-248.1±0.1	10.2±0.1	17.2±1.78
	^{13}CO (1–0)*	-248.2±0.3	9.2±0.9	2.17 ±0.27
	^{12}CO (2–1)	-248.2±0.1	12.0±0.1	19.01±1.91
	[CII]^a	– –	– –	<0.72
	HI	-246.8±0.2	23.0±0.5	1548±157
	[NII]122μm			0.22±0.05
BCLMP302	[CI](1–0)	-253.7±1.3	15.1±2.7	1.06±0.21
	^{12}CO (1–0)*	-256.8±0.1	8.1±0.2	7.69±0.78
	^{13}CO (1–0)*	-257.5±0.3	7.7±0.6	0.80±0.09
	^{12}CO (2–1)	-252.8±0.2	8.4±0.4	3.66±0.54
	[CII]	-252.8±0.4	14.6±0.5	11.3±1.4
	HI	-250.3±0.2	17.8±0.4	1524±156
	[NII]122μm			0.23±0.09
GMC01 [CII] Peak	[CI](1–0)	-169.0±0.5	6.6±1.2	0.98±0.19
	^{12}CO (1–0)*	-268.5±0.1	8.3±0.2	8.47±0.90
	^{13}CO (1–0)*	-268.6±0.4	9.1±1.2	0.79±0.09
	^{12}CO (2–1)	-168.3±0.1	9.5±0.2	8.05±0.81
	[CII]^a	– –	– –	23.31±2.40
	HI	-166.7±0.3	17.0±0.7	917±97
	[NII]122μm			0.51±0.05
GMC01 [CII] Flank	[CI](1–0)	-170.5±0.4	8.4±1.3	1.13±0.12
	^{12}CO (1–0)*	-269.3±0.1	–	–
	^{13}CO (1–0)*	-269.3±0.1	–	–
	^{12}CO (2–1)	-169.1±0.1	10.8±0.3	6.02±0.61
	[CII]	-170.6±0.2	14.0±0.5	14.97±1.6
	HI	-169.9±0.3	18.3±0.7	798±84
GMCno06 A	[CI](1–0)	-127.9±0.6	9.5±1.2	1.32±0.16
	^{12}CO (1–0)*	-269.3±0.1	10.2±0.1	8.72±0.9
	^{13}CO (1–0)*	-227.9±0.6	10.8±0.9	0.57±0.10
	^{12}CO (2–1)	-127.9±0.2	10.0±0.9	4.34±0.4
	[CII]	-124.7±0.4	17.3±0.4	14.20±1.64
	HI**	-119.8±0.1	21.0±0.2	1854±187
	[NII]122μm			0.51±0.05
GMCno06 B	[CI](1–0)	112.3±0.86	5.5±1.4	0.58±0.14
	^{12}CO (1–0)*	114±1.5	7.3±2.8	1.45±0.27
	^{13}CO (1–0)*	-111-5±1.0	4.2±2.9	0.19±0.06
	^{12}CO (2–1)	-113.9±0.3	9.1± 1.0	2.53±0.30
	[CII]	–	–	–
	HI**	-119.8±0.1	21.0±0.2	1854±187

Table 7.2: Parameters of single Gaussian fits to the [CII], [CI](1–0), CO(2–1) and HI spectra. The integrated line intensities of [NII]122μm intensities as well as of [CII] intensities in the position GMC01 Peak were calculated from their fluxes (cf. Table 7.3, Nikola et al. in prep.) via Equation (4.16).
* The CO(1–0) data refer to a beam of 21″.
** The HI spectra shows no double peak in GMCno06. The HI values in GMCno06 A and GMCno06 B refer to a fit with a single Gaussian. They are identical for both clouds.

radiated by [CII]. It radites ~50 to 100 times the energy that is radiated by [CI](1–0) and CO(2–1). Furthermore, these fluxes reveal that the [CI](1–0) transitions radiates more energy than CO(2–1) in the majority of the positions (up to ~ 5 times more).

In general [CII] is the broadest carbon line, with an average line width of ~10-20 km/s. The line widths of CO(2–1) are relative constant in all positions, with a typically Δv(CO(2–1))~7 to 12 km/. The line width of CO(2–1) exceeds rhe one of of [CI](1–0) or is of similar width within the uncertanties, Δv([CI])~5-10, in all positions but BCLMP302. [CII] and [CI](1–0) have similar line width (~15 K km/s) in BCLMP302, while CO(2–1) has the narrowest line.

The central velocities of the individual lines match within the uncertainties, in almost all the positions. An exception is the GMCno06, in which two CO(2–1) and [CI](1–0) velocity components were observed (component *A* and *B*; cf. Fig. 7.3, and Table 7.2) while the [CII] emission is only associated with the component *A*. These two CO and [CI](1–0) velocity components are associated with two nearby GMCs, cloud A and B. These clouds overlap partially spatially within the beam (cf. Fig 7.28). Therefore the spectra arises from tow different clouds, not from a CO and [CI](1–0) selfabsorption.

The observations indicate that [CII] , [CI](1–0) and CO emissions arise from different regions within the GMCs. The different transitions trace different phases of the gas, otherwise the lines would have the same widths and central velocity. In general, the observations are consistent with a C^+/C^0/CO layer structure, as described in Section 2.2.1 and proposed by Tielens & Hollenbach (1985a). All the molecular clouds (expect GMC91) have the characteristic of a PDR. CO and C^0 are associated exclusively with molecular gas. In this cases [CI](1–0) arises from the photodissociation layer of CO. The widths of the [CII]–lines can be explained by C^+ that is associated with the ionised, neutral and molecular phase. Hence its line width is broader compared to CO and [CI](1–0). The GMC BCLMP302 is an exception, as [CI](1–0) and [CII] have similar line widths. This indicates a phase where [CII] and C^0 trace the same H_2, while CO is absent. This meets the expectations of the model proposed by Hollenbach, Takahashi & Tielens (1991), Wolfire et al. (2003) and Wolfire, Hollenbach & McKee (2010).

The following sections will determine the column densities of C^+, C^0 and CO in the molecular phase. The calculations are based on an assumed C^+/C^0/CO layer structure of the PDRs. Based on these column densities I will determine the fraction of H_2 traced by the different carbon species. As C^+ is associated with the ionised, neutral and molecular phase it is necessary to determine the fraction of [CII] that arises from the different phases.

Position	$\mathcal{I}$([CII]) [erg cm^{-2} s^{-1}] 10^{-5}	$\mathcal{I}$([CI](1–0)) [erg cm^{-2} s^{-1}] 10^{-8}	$\mathcal{I}$(CO(2–1)) [erg cm^{-2} s^{-1}] 10^{-8}	$\mathcal{I}$([NII]122μm) [erg cm^{-2} s^{-1}] 10^{-6}	$\mathcal{I}$(HI) 10^{-30}
BCLMP691	6.97±0.14	6.60±1.59	12.02±0.10	7.6±1.4	3.2±0.3
GMC91	<0.51	<2.2	23.88±0.15	3.4±0.7	4.5±0.5
BCLMP302	5.18±0.13	19.06±2.44	4.59±0.21	3.6±1.4	4.5±0.5
GMC01 Peak	9.34±0.21	11.97±1.95	10.10±0.15	7.8±0.8	2.7±0.3
GMC01 Flank	8.29±0.34	13.81±1.47	7.56±0.18	7.8±0.8	2.3±0.2
GMCno06 (cloud A)	8.72±0.19	16.10±1.95	5.49±0.24	3.2±0.9	5.4±0.6
GMCno06 (cloud B)	–	7.09±1.59	3.36±0.21	–	–

Table 7.3: Fluxes of [CII], [CI](1–0), ^{12}CO(2–1) and [NII]122μm The fluxes of [NII]122μm as well as the [CII] flux in the position GMC01 Peak are obtained from Nikola et al. in prep.. Almost all other fluxes were derived via Equation (4.16). The used integrated velocity integrated line intensities are listed in Table 7.2.

7.2 CARBON AND HYDROGEN COLUMN DENSITIES IN M33

The following section is dedicated to the column densities of hydrogen CO, C^0 and C^+. These column densities will be calculated via the observed $^{12/13}$CO(1–0), CO(2–1), [CI](1–0), [CII] and HI line intensities. The column densities of H^0, CO, C^0 and C^+allow the calculation of the molecular hydrogen column densities and the total hydrogen column densities (Section 7.2.6 and 7.2.7). Based on these column densities I will derive the relative fraction of CO dark H_2 relative to the total contribution of H_2 (Section 7.2.8).

First I will discuss the column densities of HI, CO, C^0 and C^+.

7.2.1 NEUTRAL ATOMIC HYDROGEN COLUMN DENSITIES

The H^0 column densities are calculated via Equation (A.11) [x], for an assumed optically thin case. The $N(H^0)$ derived by this means varies vary between $\sim$1.5 to 3$\times$ 10^{21} cm^{-2}. The HI emission exceeds the beam of [CI](1–0) observations. Therefore the calculations of $N(H^0)$ are based on an assumed beam filling factor of Φ_B= 1. The derived $N(H^0)$ for the individual positions are summarised Table 7.13.

7.2.2 CO COLUMN DENSITIES IN LTE

The following section describes the calculation of the total CO column densities, N(CO) for clouds in an assumed local thermal equilibrium[xi]. All available CO transitions (^{13}CO(1–0), ^{12}CO(1–0) and ^{12}CO(2–1)) in the observed positions were used for these calculations. I will investigate two different approaches.

I: The first approach uses the ^{13}CO(1–0), ^{12}CO(1–0) and ^{12}CO(2–1) data to derive the optical depth, excitation temperature as well as of the beam filling factor needed for the CO column density calculations.

II: The first approach gives to CO excitation temperatures below the ambient dust temperature of ($\sim$6 K versus $\sim$20 K)[xii]. This discrepancy might have its origin in different regions in which the dust emission and the low–J CO transitions arises. Low–J CO transitions arise from the cold central regions of molecular clouds. This gas is almost completely shielded against the penetrating radiation field, which has not to be the case for dust. Dust can be observed also in region in which the radiation field is higher, and also the temperature. The second approach calculates the CO column densities in the case that the CO excitation temperatures are equal to the dust temperatures.

At first I will discuss approach I. The three CO transitions ($^{12/13}$CO(1–0) and ^{12}CO(2–1)) allows the determination of all parameters needed for

x $N(H^0) = 1.823 \times 10^{18} \int T_{mb}(HI) dv$

xi This method is described in detail in Section 4.2.

xii Approach I gives T_{ex}(CO(2–1))$\sim$6 K. Buchbender (2013) calculated dust temperatures of T(Dust)$\sim$20 K. Note that the excitation temperatures of CO(2–1), T_{ex}(CO(2–1))$\sim$6 K, are consistent with the T_{ex} derived for other sources (e.g. Liszt & Lucas 1998) the CO column density calculations: the optical depth τ, excitation temperature T_{ex} as well as of the beam filling factor in the observed clouds Φ_{B}. The optical depth of ^{13}CO(1–0), τ_{13}, is numerically calculated via relation 4.15[xiii]. A ^{12}C/^{13}C ratio of $x_{\frac{12}{13}}$=56 is assumed. This ratio was found as the mean ratio of the integrated line intensities of [^{12}CII] and [^{13}CII] in BCLMP691 (Braine et al. 2012b)[xiv]. This approach assumes that both lines are optically thin. If the lines are optically thin the isotope ratio of ^{12}C and ^{13}C is equal to those of the integrated intensities. In the case of optically thick ^{12}[CII] , the used ^{12}[CII]/^{13}[CII] ratio would underestimate the real ^{12}C/^{13}C ratio by a factor τ_{12}/(1-exp(-τ_{12})). It was further assumed that the isotope ratio is constant for all discussed positions. That does not necessarily has to be the case. The ^{12}C/^{13}C isotope ratio has a radial gradient within the Milky Way, from $\sim$30 at the galactic centre to $\sim$90 at the sun (Clayton 2003). Note that the $x_{\frac{12}{13}}$=56 is similar to the value used in Buchbender (2013) of $x_{\frac{12}{13}}$=60.

The value found for τ_{13} varies between 0.1 to 0.3, which corresponds to an optical depths of $\tau_{12}\sim$6 to 17 for ^{12}CO(1–0). These values indicate that the low–J ^{12}CO transitions are optically thick in all positions, discussed here.

The excitation temperatures for the different transitions were calculated with Equation (4.6)[xv]. The beam filling factor Φ_{B} was preliminary kept as an open variable at this stage, and was determined at the end of these calculations. The column density of ^{13}CO, N_{tot}(^{13}CO) are calculated with Equation (4.14)[xvi]. The total column density of ^{12}CO, N_{tot}(^{12}CO) is calculated by the multiplication of N_{tot}(^{13}CO) with the isotope ratio $x_{\frac{12}{13}}$. Note that Φ_{B} is still undetermined. These calculations are based on an assumed local thermal equilibrium, that means that the excitation temperatures are equal for all the transitions discussed here. Hence, the CO column densities can be calculated from the CO(2–1) observations, as described in the following section. The following calculations are based on the assumption that ^{12}CO(2–1) and ^{12}CO(1–0) have identical excitation temperature, T_{ex}, and beam filling factors, Φ_{B}). The CO(2–1) data was in addition convolved to the same spatial resolution as the CO(1–0) data (Θ_{B}(CO(1–0))=21.4″), for the sake of consistency. In the position GMC01 Flank no complementary CO(1–0) data is available. Therefore it was assumed that the optical depths, excitation temperature and beam filling factor in this position are equal to the values in GMC01 Peak. The total CO column densities N_{tot}(^{12}CO) should be equal, regardless of the CO

---

xiii $\frac{T_{\mathrm{mb}}(^{12}\mathrm{CO(1\text{–}0)})}{T_{\mathrm{mb}}(^{13}\mathrm{CO(1\text{–}0)})} = \frac{1-e^{-x_{\frac{12}{13}}\times\tau_{13}}}{1-e^{-\tau_{13}}}$

xiv Braine et al. (2012b) search for [^{13}CII] emission on the 'blue'shoulder of five [^{12}CII] spectra near/at the centre of BCLMP691. [^{13}CII] has a frequency equivalent offset of +11 km/s relative to the centre of the [^{12}CII] transition. They fit the [^{12}CII] spectra with a Gaussian. The fit gives an excess of [CII]–emission on the blue side of the spectra. This excess is explained by the additional emission of [^{13}CII], resulting in a ratio of I([^{12}CII])/I([^{13}CII])≈56±41.

xv $T_{\mathrm{ex}} = \frac{h\nu}{k_{\mathrm{B}}} \times \left[\ln\left((1-e^{-\tau})\Phi_{\mathrm{B}}\frac{h\nu}{k_{\mathrm{B}}}\frac{1}{T_{\mathrm{mb}}+\mathcal{J}(T_{\mathrm{CMB}})}+1\right)\right]^{-1}$

xvi $N = \frac{\tau}{1-e^{-\tau}} \times \frac{8\pi\nu^3}{c^3}\frac{Q}{g_u}\frac{1}{A_{ul}}\frac{e^{\frac{h\nu}{k_{\mathrm{B}}T}}}{\left(1-e^{-\frac{h\nu}{k_{\mathrm{B}}T_{\mathrm{mb}}}}\right)}\frac{1}{\mathcal{J}_\nu(T_{\mathrm{ex}})-\mathcal{J}_\nu(T_{\mathrm{BG}})\Phi_{\mathrm{B}}}\int T_{\mathrm{mb}}\mathrm{d}v$

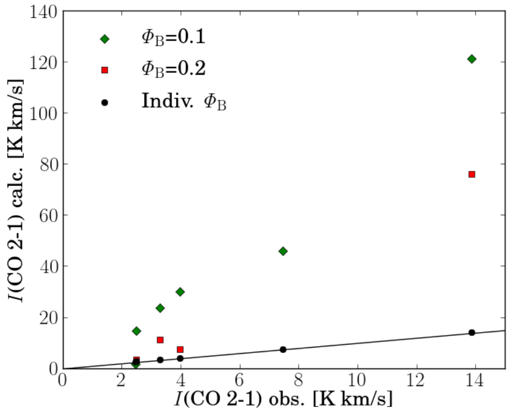

Figure 7.4: Observed integrated CO(2–1) v.s. calculated integrated CO(2–1) line intensities for different beam filling factors, based on the optical depth calculated from the $T_B(^{12}CO)/T_B(^{13}CO)$ ratio. The black solid line represents the ratio of 1 between both I(CO(2–1)). The black • represent the best fit of the calculated I(CO(2–1)) with individual Φ_B as listed in Table 7.5. The best fit give Φ_B between 0.1 to 0.7 with a mean value of 0.3±0.2. .

transition used. The beam filling factor and thus the excitation temperature can be now numerically calculated by equating the total CO column densities based on the observed $I(^{12}CO(1\text{–}0))$ and $I(^{12}CO(1\text{–}0))$.

This method gives optical depth of τ_{12}∼6 to 17 and beam filling factors between Φ_B∼0.1 (GMCno06 B) to 0.7 (GMC91). The beam filling factor average over all positions is $\langle\Phi_B\rangle$ 0.3±0.2. The excitation temperatures have typical values between $T_{ex}\sim 5$ to 8 K with a mean of $\langle T_{ex}\rangle = 6\pm1$ K. The GMCs have CO column densities between N(CO)∼5 to 33 × 10^{17} cm^{-2} with a mean of $\langle N(CO)\rangle$=13±6 × 10^{17} cm^{-2}. Note that these column densities are average over the beam. The total column densities in the clouds is given by dividing the beam average column densities with the bean filling factors. The T_{ex}, Φ_B and N(CO) for the individual positions are summarised in Table 7.5.

Now I will will discuss the approach II.

The excitation temperatures of ∼6 K, derived in the previous paragraph, are in the order of the ground level energy of the CO(1–0) transition ($E(CO(1-0))/k_B \approx$ 5.5K. cf. Section 4.1). These temperatures are expected in the cold cores of molecular clouds, in which the CO(1–0) transition dominates (e.g. Parikka et al. 2015), but not as mean temperatures of the molecular gas in a GMC. Higher excitation temperatures are excepted and derived for higher J CO transitions. For example Okada et al. (2015) estimated T_{ex}∼20 to 150 K for N159 based on CO(3–2) data. Buchbender (2013) derived cold dust[xvii] temperatures of ∼20 K for the positions, discussed here (cf. Table 7.5). If the gas is thermalised[xviii] the dust temperature can be equal to the gas temperatures (e.g. Goldsmith 2001). CO(1–0) has a critical density of ∼3000 cm^{-3} for collisions with H_2 in the optically thin limit. The critical density is reduced in the optically thick regime, as $n_{crit}\propto\tau^{-1}$[xix] This, the critical densities is reduce to ∼600 cm^{-3} for a τ=5 and to ∼300 cm^{-3} for a τ=10.

The following calculations assume that the CO excitation temperatures are equal to the cold dust temperatures. This approach gives optical depths of τ_{12}∼5 to 30, beam filling factors of 1 to 6% and beam average

xvii Cold dust is typically associated with CO gas (Braine et al. 2010; Xilouris et al. 2012; Buchbender 2013). Warm dust has higher temperatures of T ∼50-60 K and is typically associated with [CII] emission.

xviii $n > n_{crit}$, cf. Section 4.2.

xix For details see Section 4.2. Note that the term $\frac{1-e^{-\tau}}{\tau}$ in Equation (4.2) can be approximated by $\left(1-e^{-\tau}\right)\times\tau^{-1} \xrightarrow{\tau\to\infty} \tau^{-1}$ in the optical thick case.

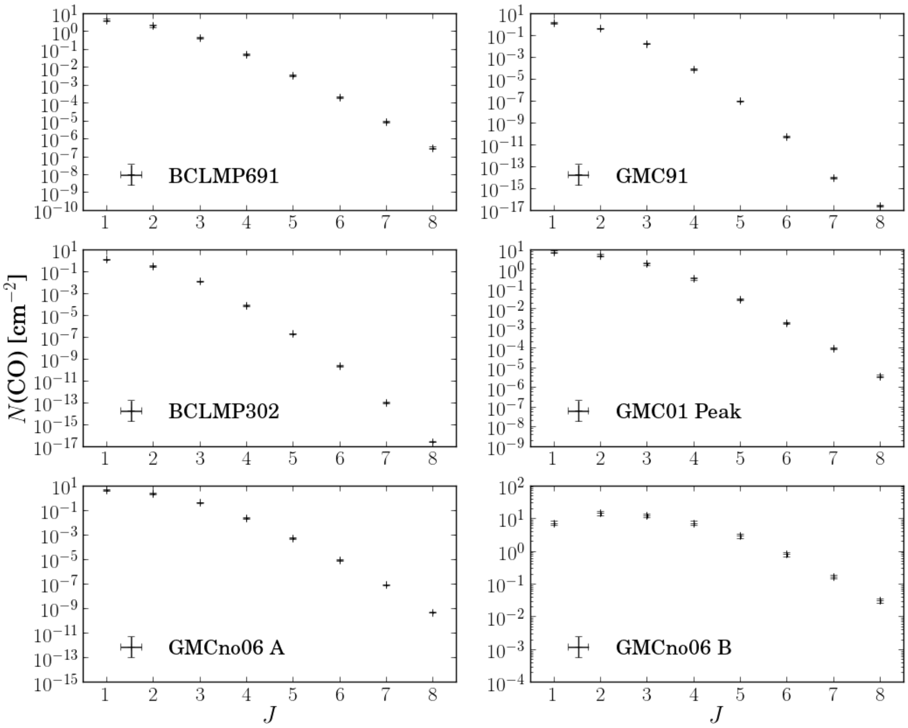

Figure 7.5: CO column densities for the different transitions modelled with RADEX.

CO column densities of $\sim$2 (GMCno06 B) to 34 (GMC91) $\times$ 10^{17} cm^{-2} with a mean of $\langle N(CO)\rangle$=12 $\pm$ 10 $\times$ 10^{17} cm^{-2}. The beam average CO column densities are thus of similar order for both approaches.

The following paragraph discusses the different beam filling factors of both approaches.

Approach I gives Φ_{B}=0.4 for BCLMP302. This beam filling factor is consistent with high angular resolved ^{12}CO(1–0) maps of BCLMP302[xx], $\Theta_{\mathrm{B}}\approx 4'' \hat{\approx}$15pc, as shown in Fig. 11.3 in Buchbender (2013). The beam filling factors of Approach II are also consistent with beam filling factors found in other nearby extragalactic sources as for example the LMC (e.g. Okada et al. 2015), in which $\Phi_{\mathrm{B}}\approx$0.3 to 0.4 were derived.

The beam filling factors of approach II are roughly one order below those of approach I ($\Phi_{\mathrm{B}}\sim$0.03 v.s. $\Phi_{\mathrm{B}}\sim$0.3). The beam filling factors of approach II are hard to reconcile with the size of the clouds. If the depths of the GMCs is equal to its diameter ($d_{\mathrm{C}}\sim$50 pc), the surfaces of the individual clumps within the beam should superimpose and roughly fill the surface the beam.

On the other hand, an ensemble of CO clumps could explain the low beam filling factor. A beam filling of 3% would imply small bright dense CO–clumps that emit all the observed CO emission. Such a beam filling factor is hard to reconcile with dense gas tracers as HCO^+ and HCN, which were observed by Buchbender (2013) in all positions, discussed here. These tracers require a shielding from the penetrating FUV field. Small clump sizes can hardly provide this shielding.

xx This map was observed with the Plateau de Bure interferometer (PdB)

	T_{ex}(CO(1–0))	τ_{12}
BCLMP691	7.5	7.3
GMC91	4.4	10.0
BCLMP302	4.2	4.6
GMC01 Peak	13.7	1.3
GMCno06 A	7.6	4.3
GMCno06 B	100.	0.07

Table 7.4: Optical depth and excitation temperatures of ^{12}CO(1–0) from RADEX-simulations

The ratio of the observed CO(1–0) and CO(2–1) line intensities were modelled with the statistical equilibrium radiative transfer code RADEX[xxi] (van der Tak et al. 2007) (cf. Fig. 7.5. The simulations give similar T_{ex}, τ_{12} and N(CO) as derived for Approach I, in the majority of the positions 7.2.2. The simulations give CO(1–0) excitation temperatures between T_{ex}= 4.2 to 13.6 K and optical depths of ^{12}CO(1–0) τ_{12}=1.3 to 10.4. One exception is the cloud GMCno06 B in which the observations imply an CO(2–1) excitation temperatures of ∼100 K and an optical depths τ_{12}=10^{-1}.

In summary it can be concluded that the approach I (T_{ex}∼6 K, Φ_{B}∼0.3) presumably reflects the real conditions within the clouds, also approach I and II give similar N(CO) in the end. Nevertheless, I will consider the column densities of approach I and II in the following discussions. It allows to compare the impact of the different approaches to the total carbon column densities and in the end to the amount and distribution of H_2.

7.2.3 COLUMN DENSITIES OF NEUTRAL ATOMIC CARBON

The following paragraphs are dedicated to the calculation of the neutral atomic carbon column density $N(\text{C}^0)$ The calculations are based on an assumed thermal equilibrium in the observed clouds.

The calculations are based exclusively on the [CI](1–0) observations, due to the lack of [CI](2–1) data. This lack of [CI](2–1) data prevents the direct calculation of its excitation temperature (cf. e.g. Stutzki et al. 1998; Schneider et al. 2003; Glover et al. 2015). If both transitions were available, the T_{ex} could be calculated directly from the ratio of their integrated line intensities[xxii].

Lo et al. (2014) proposed that the lower limit of the [CI](1–0) excitation temperature is given by the CO excitation temperatures. This approach gives an absolute lower limit, but higher T_{ex} are likely as discussed below. Excitation temperatures of ∼6 K, as derived for CO (see previous section), are uncommon for C^0 in PDRs. The ground level energy of the [CI](1–0) transition is E/k_{B}=23.6 K. For a significant excitation of C^0

xxi http://var.sron.nl/radex/radex.php
The model

xxii C^0 has only two transitions (cf. Section 4.1). The excitation temperature of neutral atomic carbon is directly given by the relative population of the different energy levels, and hence by the ratio of their integrated line intensities:
$T_{\text{ex}}= 38.8 \times \left[\ln\left(2.11\frac{I([\text{CI}](1-0))}{I([\text{CI}](2-1))}\right)\right]^{-1}$ [K] (e.g. Schneider et al. 2003).

(1)	(2) τ_{12}	(3) Φ_B	(4) T_{ex} [K]	(5) $N(^{12}CO)$ $10^{16}cm^{-2}$
Approach I: T_{ex} derived from $^{13/12}CO(1–0)$ and $^{12}CO(2–1)$ data				
BCLMP691	6.9	0.2	5.1±0.1	11.6±1.2
GMC91	6.2	0.7	6.1±0.8	14.4±1.5
BCLMP302	9.1	0.4	5.6±0.3	4.9±0.5
GMC01 Peak	8.4	0.2	8.1±0.6	15.0±1.5
GMC01 Flank[a]	8.4	0.2	8.1±0.6	9.2±0.9
GMCno06 A	7.8	0.2	5.2±0.1	20.5±2.1
GMCno06 B	16.9	0.1	6.6±0.1	5.2±0.5
Mean	9.2±3.6	0.3±0.2	6.2±1.0	13.1±5.7
Approach II: T_{ex} equal to T_{Dust}				
BCLMP691	13.6	0.02	23±1	5.9±1.1
GMC91	19.2	0.06	20±1	24.4±3.9
BCLMP302	28.1	0.03	20±1	5.7±1.1
GMC01 Peak	11.3	0.04	25±1	14.5±2.5
GMC01 Flank[a]	11.3	0.04	25±1	11.5±1.9
GMCno06 A	6.8	0.02	23±1	4.8±0.4
GMCno06 B	4.7	0.01	23±1	2.0±0.3
Mean	14.0±7.9	0.03±0.01	22±2	12.1±9.6

Table 7.5: Derived beam average CO column densities for different excitation temperatures.
(2), (3) & (4) Derived optical depth τ, beam filling factors Φ_B and excitation temperatures. The dust temperatures are obtained from Buchbender (2013)
(5)Beam average CO column densities estimated from the CO(2–1).
[a] For GMC01 Flank it was assumed that τ, T_{ex} and Φ_B are equal to the corresponding values in GMC01 Peak.

the excitation temperatures must be at least in the order of this ground level energy. Schneider et al. (2003) derived, for example, T_{ex} of $\gtrsim$60 K in S106 IR based on [CI](2–1) and [CI](1–0) observations. Okada et al. (2015) derived median excitation temperatures of T_{ex}70-80 K in N159 in the LMC and Pérez-Beaupuits et al. (2015) found T_{ex}~40 to 100 K in M17. Furthermore, equal [CI](1–0) and CO excitation temperatures (and equal beam filling factors) gives negative values within the logarithm of Equation (4.7)[xxiii] in three clouds, and consequently to an infinite optical depth, which is non-physical (cf. Table 7.6) Therefore, the excitation temperatures of [CI](1–0) must be higher, to be consistent with the observations.

Neural atomic carbon column densities for different T_{ex} are listed in Table 7.6. At lower temperature I assume a T_{ex}~10 K. This temperature is close to the calculated CO excitation temperatures and gives $\tau<\infty$ for all positions. The C^0 column densities were calculated for temperatures tahht are equal to the dust temperatures (T_{ex}=25 K), for T_{ex}=50 K and for T_{ex}=75 K. It was further assumed that the beam filling factors of [CI](1–0) are equal to those of CO (Φ_B= 0.1 to 0.4).

xxiii $\tau = -\ln\left(1 - \frac{k_B}{\Phi_B h\nu}\left(T_{mb} + \mathcal{J}(T_{CMB})\right) e^{\frac{h\nu}{k_B T_{ex}} - 1}\right)$

(1)	(2) $\tau_{[CI](1-0)}$	(3) Φ_B	(4) T_{ex} [K]	(5) $N(C^0)$ $10^{16}cm^{-2}$
T_{ex} derived from $^{13/12}CO(1–0)$ and $^{12}CO(2–1)$ data				
BCLMP691	–	0.2	5.1±0.1	–
GMC91	<0.1	0.7	6.1±0.8	<0.1
BCLMP302	0.63	0.4	5.6±0.3	0.9±0.1
GMC01 Peak	0.72	0.2	8.1±0.6	1.0±0.2
GMC01 Flank	0.63	0.2	8.1±0.6	1.1±0.2
GMCno06 A	–	0.2	5.2±0.1	–
GMCno06 B	–	0.1	6.6±0.1	–
Mean		0.3±0.2	3.0±1.7	1.0±0.2
T_{ex}=10 K				
BCLMP691	0.18	0.2	10	0.5±0.11
GMC91	<0.1	0.7	10	<0.2
BCLMP302	0.07	0.4	10	0.9±0.2
GMC01 Peak	0.33	0.2	10	0.9±0.2
GMC01 Flank	0.30	0.2	10	1.0±0.2
GMCno06 A	0.31	0.2	10	1.2±0.2
GMCno06 B	0.52	0.1	10	0.6±0.1
Mean		0.3±0.2	10	0.8±0.3
T_{ex}=25 K				
BCLMP691	0.03	0.2	25	0.8±0.2
GMC91	<0.1	0.7	25	<0.3
BCLMP302	0.011	0.4	25	1.6±0.3
GMC01 Peak	0.05	0.2	25	1.5±0.3
GMC01 Flank	0.04	0.2	25	1.7±0.3
GMCno06 A	0.04	0.2	25	2.0±0.3
GMCno06 B	0.07	0.1	25	0.9±0.2
Mean		0.3±0.2	25	1.2±0.7
T_{ex}=50 K				
BCLMP691	0.01	0.2	50	1.2±0.3
GMC91	<0.1	0.7	50	<0.4
BCLMP302	0.004	0.4	50	2.3±0.45
GMC01 Peak	0.02	0.2	50	2.1±0.4
GMC01 Flank	0.02	0.2	50	2.5±0.4
GMCno06 A	0.02	0.2	50	2.9±0.5
GMCno06 B	0.03	0.1	50	1.3±0.3
Mean		0.3±0.2	50	2.0±0.7
T_{ex}=75 K				
BCLMP691	0.006	0.2	75	1.4±0.4
GMC91	<0.1	0.7	75	<0.5
BCLMP302	0.003	0.4	75	2.6±0.5
GMC01 Peak	0.011	0.2	75	2.5±0.5
GMC01 Flank	0.010	0.2	75	2.8±0.4
GMCno06 A	0.010	0.2	75	3.3±0.5
GMCno06 B	0.016	0.1	75	1.5±0.4
Mean		0.3±0.2	75	2.3±0.8

Table 7.6: Derived beam average C^0 column densities for different excitation temperatures.
(2), (3) & (4) Derived optical depth τ, beam filling factors Φ_B and excitation temperatures. The dust temperatures are obtained from Buchbender (2013)
(5)Beam average C^0 column densities. The mean values are based on the positions where a clear $N(C^0)$ was calculated (GM91 is excluded in all cases).

The optical depth of [CI](1–0), $\tau_{[\mathrm{CI}](1-0)}$, are calculated for all positions with Equation (4.7)[xxiv]. For all excitation temperatures in all positions the optical depths below 1 were derived. The highest optical depths are found for a T_{ex}~10 K where $\tau_{[\mathrm{CI}](1-0)}$~0.1 to 0.5. Therefore, [CI](1–0) is optically thin in all the positions. These optical depths are consistent with the results of other studies, for example Okada et al. (2015), Lo et al. (2014) and Pérez-Beaupuits et al. (2015).

The total C^0 column densities were derived with Equation (A.4)[xxv]. For GMC91 an upper limit $N(C^0)$ is listed, as no [CI](1–0) emission has been detected. The lowest beam average $N(C^0)$ are derived for $T_{\mathrm{ex}}\sim$ 10 K, where $N(C^0)\sim0.5$ to 1.2×10^{16} cm^{-2}. The $N(C^0)$ almost doubles to $N(C^0)\sim0.8$ to 2×10^{16} cm^{-2} for T_{ex}=25K . Excitation temperatures of T_{ex}=50 K and 75 K give almost similar C^0 column densities of $N(C^0)\sim1$ to 3×10^{16} cm^{-2}.

The derived C^0 column densities are thus lower than the CO column densities for T_{ex}~6 K in all cases. The $N(C^0)/N(\mathrm{CO})$ ratio does never exceed 3/4 (GMCno06 B for T_{ex}=75 K).

7.2.4 COLUMN DENSITIES OF IONISED CARBON

This Section aims to calculate and discuss the column densities of ionised carbon.

The emission of singly ionised carbon can arise from the ionised, neutral and molecular gas phase. In contrast, CO and C^0 are associated exclusively with molecular gas[xxvi]. The observed total integrated [CII] line intensity, $I([\mathrm{CII}])_{\mathrm{tot}}$, is a composition of the [CII] emission that is associated with the ionised, neutral atomic and molecular hydrogen gas;

$$I([\mathrm{CII}])_{\mathrm{tot}} = I([\mathrm{CII}])_{\mathrm{H}^+} + I([\mathrm{CII}])_{\mathrm{H}^0} + I([\mathrm{CII}])_{\mathrm{H}_2} \tag{7.1}$$

All these gas phases have different physical properties, in particular different temperatures and densities (cf. Section 2.1). These different properties have to be considered when the total column density of ionised carbon, $N(C^+)_{\mathrm{tot}}$, is calculated. The total column density of C^+ is given by the sum of the column densities of the individual gas phases;

$$N(C^+)_{\mathrm{tot}} = N(C^+)_{\mathrm{H}^+} + N(C^+)_{\mathrm{H}^0} + N(C^+)_{\mathrm{H}_2} \tag{7.2}$$

with $N(C^+)_{\mathrm{H}^+}$ being the C^+ column density in the ionised phase. $N(C^+)_{\mathrm{H}^0}$ is the column density in the neutral phase and $N(C^+)_{\mathrm{H}_2}$ is those in molecular gas. The C^+ column densities within a phase can be in general calculated from the integrated [CII] intensities via equation (A.7)[xxvii].

To determine the total C^+ column density, it is necessary to calculate the $N(C^+)$ and $I([\mathrm{CII}])$ within the different gas phases. In the following paragraphs there will be discussed a method to determine $N(C^+)$ and $I([\mathrm{CII}])$ within the different gas phases. The argumentation is inspired

xxiv see previous footnote

xxv $N(C^0) = 5.94\times10^{15}\times\frac{Q\tau([\mathrm{CI}](1-0))}{1-e^{-\tau([\mathrm{CI}](1-0))}\Phi_{\mathrm{B}}}\int T_{\mathrm{mb}}([\mathrm{CI}](1-0))\mathrm{d}v$; cf. Section A

xxvi See Section 2.2.1 for further details.

xxvii $N(C^+) = 2.9\times10^{15}\left(1+0.5e^{\frac{\Delta E}{k_{\mathrm{B}}T_{\mathrm{ex}}}}\left(1+\frac{n_{\mathrm{crit}}}{n(\mathrm{H_x})}\right)\right)\frac{\tau}{1-e^{-\tau}}I([\mathrm{CII}])$
See Section 4.2 and Apendix A in particular for further details.

by Langer et al. (2014b). They investigated the [CII] emission and C^+ column densities in the neutral atomic and in the molecular phase. The fraction of [CII] emission that arises from the ionised hydrogen gas was not considered. The approach by Langer et al. (2014b) is elaborated in the following by including the [CII] emission from HII gas.

7.2.4.1 C^+ in ionised hydrogen

The fraction of the total [CII]emission that arises from the ionised gas can be estimated via the transitions of single ionised nitrogen at [NII]122μm and [NII]205μm. Both transitions arise almost exclusively from HII regions (Malhotra et al. 2001; Abel 2006). The emissions of [CII] and [NII]205μm show a power law in HII regions Abel (2006):

$$\log\left(\mathcal{I}([\mathrm{CII}])_{\mathrm{HII}}\left[\frac{\mathrm{erg}}{\mathrm{cm}^2\ \mathrm{s}}\right]\right) = 0.937 \times \log\left(\mathcal{I}([\mathrm{NII}]_{205\mu\mathrm{m}})\left[\frac{\mathrm{erg}}{\mathrm{cm}^2\mathrm{s}}\right]\right) + 0.689 \tag{7.3}$$

This correlation allows in general the estimation of $I([\mathrm{CII}])_{\mathrm{H}^+}$. Equation (7.3) has to be adopted for [NII]122μm as only [NII]122μm but no [NII]205μm data is available for the observed positions.

In HII regions it can be assumed that the proton density is equal to the electron density, n_{Hii}=n_{e} (e.g. Lang 2013), as all hydrogen is ionised. A study of 25 HII regions in M33 found an almost constant electron density of n_{e}=100 cm^3 in all these regions (Rubin et al. 2008). Therefore the following calculation assume that this density represents the n_{e} in the positions discussed here as well. The integrated intensities of $[\mathrm{NII}]_{122\mu\mathrm{m}}$ and $[\mathrm{NII}]_{205\mu\mathrm{m}}$ show an almost constant ratio $I([\mathrm{NII}]_{122\mu\mathrm{m}})/I([\mathrm{NII}]_{205\mu\mathrm{m}}=$ 3, for an electron density of $n_{\mathrm{e}}\simeq$100 cm^{-2} (Rubin 1985; Malhotra et al. 2001).

The ratio of $I([\mathrm{NII}]_{122\mu\mathrm{m}})/\ I([\mathrm{NII}]_{205\mu\mathrm{m}} = 3$ combined with Equation (7.3), allows the calculation of the [CII] emission that arises from the ionised gas, $I([\mathrm{CII}])_{\mathrm{HII}}$:

$$\begin{aligned} \mathcal{I}([\mathrm{CII}])_{\mathrm{HII}}\left[\frac{\mathrm{erg}}{\mathrm{cm}^2\ \mathrm{s}}\right] &= 1.75 \times \left(\mathcal{I}([\mathrm{NII}]_{122\mu\mathrm{m}})\left[\frac{\mathrm{erg}}{\mathrm{cm}^2\ \mathrm{s}}\right]\right)^{0.937} \\ \Leftrightarrow I([\mathrm{CII}])_{\mathrm{HII}}\left[\frac{\mathrm{K}}{\mathrm{km\ s}}\right] &= 2.48 \times 10^5 \left(\mathcal{I}([\mathrm{NII}]_{122\mu\mathrm{m}}\left[\frac{\mathrm{erg}}{\mathrm{cm}^2\ \mathrm{s}}\right]\right)^{0.937} \end{aligned} \tag{7.4}$$

The [NII]122μm fluxes combined with Equation (7.4) gives $I([\mathrm{CII}])_{\mathrm{H}^+}\sim 2$ to 4 K km/s for the positions discussed here. This corresponds to $\sim$ 10 to 40 % of the total [CII] emission. The $I([\mathrm{CII}])_{\mathrm{H}^+}$ for the different positions are listed in Table 7.8.

This approach assumes that the $C^+$and N^+ gas in the ionised phase are mixed in the discussed positions. In that case the line width and central velocity of [CII] and [NII]122μm should be similar. Based on the available data it is not possible to justify this assumption, as the spectral resolution of the [NII]122μm PACS data is not sufficient enough [xxviii]. In the positions GMC01 Flank and GMCno06 [NII]122 μm data from the specific [CII] peak is used. PACS maps of GMC01 (Nikola et al. in prep.) show a similar spatial distribution of [NII]122μm and [CII]. Therefore, the amount of [CII] from the ionised gas is presumably overestimated in the

xxviii PACS has a spectral resolution of $\sim$290 km/s for [NII]122μm (*PACS Observer's Manual* (http://herschel.esac.esa.int/Docs/PACS/html/pacs_om.html), Poglitsch et al. 2010.

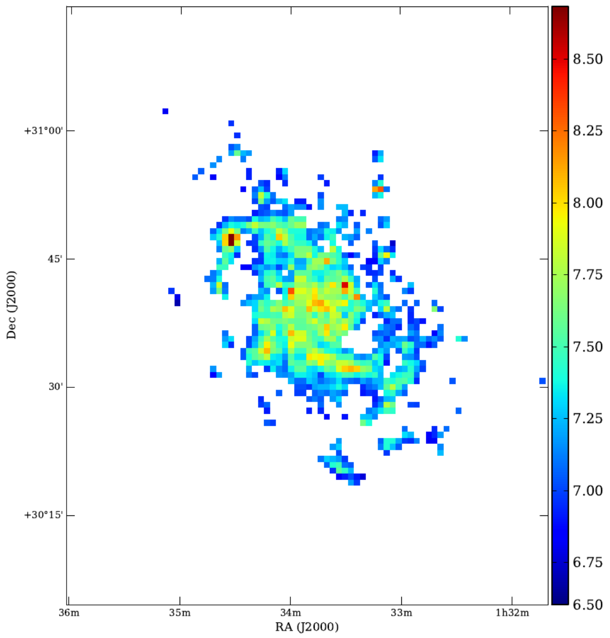

Figure 7.6: TIR emission map of M33 from Boquien et al. (2011). The colours show the solar luminosities per kpc^2 on a decimal log scale.

position GMC01 Flank and in consequence also $N([\mathrm{C\,II}])_{\mathrm{HII}}$. The calculated $I([\mathrm{C\,II}])_{\mathrm{HII}}$ represent the lower limits, as the ratio of $I([\mathrm{C\,II}])_{\mathrm{HII}}$ to the total [C II] emission increases in a low metallicity environment (cf. Section 2.2.3).

The following paragraph is dedicated to the calculation of the C^+ column densities in the ionised phase.

Rubin et al. (2008) derived electron excitation temperatures of $T_{\mathrm{ex}}(e^-)\approx$ 8000 to 10000 K for the 25 H II regions in M33. The following calculations are based on an assumed medium excitation temperature of T_{ex}=9000 K. Furthermore, it is assumed that the gas is optically thin. This results in critical densities of n_{crit}=48 cm^{-3} for collisions of C^+ with electrons[xxix]. Variations of the used excitation temperatures of $\sim$10% lead to minor changes of the critical density. A variation of $\pm$1000 K changes the critical density by $\simeq\pm$2 cm^{-3}. A critical density of 48 cm^{-3} and an excitation temperature of T_{ex}=9000 K results in C^+ column densities of $N(C^+)_{H^+}\sim$1 to 2 $\times 10^{16}$ cm^{-2} in the ionised phase. All column densities are listed in Table 7.9. Variations of $T_{\mathrm{ex}}\pm$1000 K change the calculated C^+ column densities in the ionised phase by less than $\lesssim$1%. These values are based on a beam filing factor of 1, Φ_{B}=1, as H II gas commonly fills a large volume[xxx].

The following section deals with the C^+ column densities in the neutral phase.

n(HI) via thermal pressure for for T=100 K						
(1)	(2)	(3)	(4)	(5)		
	$L_{\rm TIR}$ $[10^6 L_{\rm sun}]$	G_0 [Habing]	$P_{\rm min}/k_{\rm B}$ $[10^4 {\rm cm}^{-3}{\rm K}]$	$n_{\rm min}(T)$ $[10^2\ {\rm cm}^{-3}]$		
				T = 75 K	T = 100 K	T = 200 K
BCLMP691	1.7	14	1.0±0.1	1.2±0.4	0.9±0.3	0.5±0.2
BCLMP302	2.0	17	1.1±0.2	1.3±0.5	1.0±0.4	0.5±0.2
GMC01	5.9	51	2.4±0.3	2.9±1.0	2.2±0.8	1.1±0.4
GMCno06	3.1	27	1.5±0.2	1.8±0.7	1.4±0.5	0.7±0.2

Table 7.7: Hydrogen volume densities derived from the ambient FUV field.
(1)Source. (2) far-infrared surface brightness $L_{\rm TIR}$. (3) FUV field in Habing units calculated from the ambient TIR field with G_0=$2\pi L_{\rm TIR}/1.6 \times 10^{-3}$ (Mookerjea et al. 2012; Braine et al. 2012b). The used L$_{TIR}$ of the observed regions were obtained from Boquien et al. (2011). (4) Thermal pressure derived from Equation (4.19) (5) Via Equation (4.21) calculated lower limits of the hydrogen column density for gas surface temperatures of 75,100 and 200 K.

7.2.4.2 [CII] from the neutral phase

The C^+ column density and the [CII] emission from the neutral atomic gas phase can be estimated from the column density of neutral atomic carbon. In H^0 regions it can be assumed that the entire carbon is present in ionised form[xxxi]. In principle, the C^+ column density can be, therefore, estimated via the carbon-hydrogen abundance X_C. It needs to be considered, however, that not all carbon is gaseous in the neutral and molecular phase. A fraction of the carbon is depleted by dust grains[xxxii]. This depletion has to be considered when $N(C^+)_{H^0}$ is calculated. From Figure 3 in Garnett et al. (1999) I have calculated a hydrogen-carbon abundance of X_C=8.5 $\times$ 10^{-5} for a half solar metallicity of Z=0.5 $Z_\odot$. This value is ~60% of the abundance found in the Milky Way of $X_{C\,MW}$= 1.4 $\times$ 10^{-4} (Sofia et al. 1997). Approximately ~40% (Cardelli et al. 1996) to ~60% (Sofia et al. 1994; Snow & Witt 1996) of the total amount of carbon is present in this gas phase. Mookerjea et al. (2016) assumes a medium fraction of 50%. Along the same line of reasoning, the following calculations assume that 50% of the carbon is depleted on dust grains, which results in an adopted carbon-hydrogen abundance of X_C^*=$X_C/2$ = 4.25$\times$ 10^{-5}. Hence, the C^+ column density in the neutral phase is given by

$$N(\mathrm{C}^+)_{\mathrm{H}^0} = X_\mathrm{C}^* \times N\mathrm{H}^0 \tag{7.5}$$

The $N(H^0)$ used for the calculations are listed in Table 7.13[xxxiii]. Equation (7.5) gives C^+ column densities in the neutral phase of $N(C^+)_{HI}$~0.6 to 1.2 10^{-17} cm^{-2}. All these column densities are listed in Table 7.9.

The integrated [CII] emission in the neutral phase can be calculated by solving Equation (A.7)[xxxiv] for $I([CII])_{H^0}$,

$$I([\mathrm{CII}])_{\mathrm{H}^0} = \frac{N(\mathrm{C}^+])_{\mathrm{H}^0}\,(1-e^{\tau})}{2.9\times 10^{15}\left(1+0.5e^{\frac{\Delta E}{k_\mathrm{B}T_\mathrm{ex}}}\left(1+\frac{A_{ul}[\mathrm{CII}]}{C_{ul}(\mathrm{H}^0)n(\mathrm{HI})}\right)\right)\tau} \tag{7.6}$$

The optical depth of [CII] is unknown in the observed positions. Studies of [^{13}CII] and [^{12}CII] observations have found optical depths of $\tau \gtrsim 1$ for [^{12}CII] in various GMCs (Stacey et al. 1991; Graf et al. 2012; Ossenkopf et al. 2013). Hence, a possible contribution of the optical depth is to consider, when $I([CII])_{H^0}$ is calculated. Therefore, the C^+ column densities are calculated for an assumed optical depth of τ=1 and, in addition, for the optically thin limit. A lower limit for hydrogen volume density in the neutral phase $n(H^0)$ can be estimated by the hydrogen volume density at a PDR–surface for a given FUV-field G_0 and an assumed PDR surface gas temperatures via the thermal pressure (cf. Section 4.6, Equation

xxix Equation (4.2) is used to calculate the critical densities, $n_{\mathrm{crit}} = (1-e^{-\tau})/\tau \times A_{\mathrm{ul}}/C_{\mathrm{ul}}$. The de–excitation collision rate coefficient is calculated with Equation (A.10).

xxx Compact HII regions are observed as well. For examples see the catalogue by (Wood & Churchwell 1989) and Garay & Lizano (1999) for a discussion of the physical properties in compact HII regions.

xxxi see Section 2.2.1 and (Langer et al. 2014b).

xxxii I.a. a fraction of the dust particles consists

xxxiii $N(H^0)$ is calculated in Section 7.2.1.

xxxiv $N(\mathrm{C}^+) = 2.9\times 10^{15}\left(1+0.5e^{\frac{\Delta E}{k_\mathrm{B}T_\mathrm{ex}}}\left(1+\frac{n_\mathrm{crit}}{n(\mathrm{H_x})}\right)\right)\frac{\tau}{1-e^{-\tau}}I([\mathrm{CII}])$

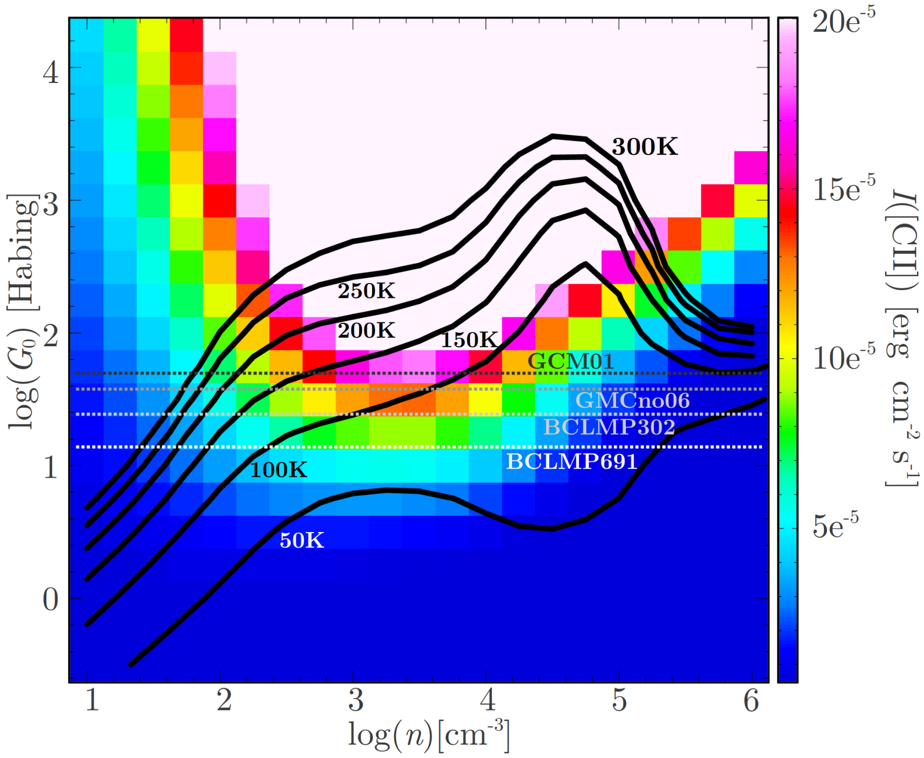

Figure 7.7: Simulations of the plane parallel homogeneous PDR-model by Kaufman, Wolfire & Hollenbach (2006).
The colours show the [CII]emission at the PDR surface as function of the FUV field and the hydrogen volume density. The black isolines show the corresponding PDR surface gas temperature between 50 to 300 K. The dashed gray lines mark the derived FUV field strengths in the discussed positions.

(4.21)[xxxv], Wolfire et al. 2003). The strength of the ambient FUV field can be calculated from the far-infrared surface brightness L_{TIR} via Equation (4.17)[xxxvi] (e.g. Mookerjea et al. 2012; Buchbender 2013). The L_{TIR} in the individual positions were obtained from the dust continuum data observed by Spitzer and Herschel between 3.6μm to 500μm. The data was fitted by Boquien et al. (2011) by use of of the the Silicate-Graphite-PAH model from Draine & Li (2007) and as well as by Buchbender (2013) (cf. Figure 7.6). The derived G_0 values are in the order 15-50 Habing units. The L_{TIR} as well as the precise G_0 values for the individual positions are listed in Table 7.7. The gas temperatures and the [CII] excitation temperature in the neutral phase can not be directly calculated from the observations Mookerjea et al. (2016) has assumed an excitation temperatures of 100 K for BCLMP302 and GMC01. The same temperature was assumed by Langer et al. (2014b) as mean gas temperature for the neutral phase in the Milky Way. Braine et al. (2012b) estimated [CII] excitation temperatures between ~90 K based on 24 μm and 70μm SPIRE data and ~200 K based on the plane parallel PDR-model by Kaufman et al. (1999) in BCLMP691. In order to consider the uncertain [CII] excitation tem-

xxxv $n(H^0) \simeq \dfrac{8500\, G_0' \frac{Z_d'}{Z_g'}}{\left(1+3.1\left(G_0' \frac{Z_g'}{\zeta_t'}\right)^{0.365}\right) \times 1.1\, T} \quad \left[\mathrm{cm}^{-3}\right]$

xxxvi $G_0 = 4\pi 0.5 L_{\mathrm{TIR}}$

peratures, the [CII] emission and C^+ column densities will be calculated for T_{ex}([CII]) = 200 K, 100 K and 75 K. Furthermore, it is assumed that the dust/PAH and gas metal abundances are equal, Z'_d=Z'_g. The fraction of dust compared the gas is lower in a low metallicity environment, and therefore the shielding of the radiation within the GMCs is less effective. Thus the gas ionisation rate, ζ_t, in a low metallicity environment is higher compared to the Milky Way. Dalgarno (2006) discusses different models and observations of the gas ionisation rate. He concludes that the ζ_t range from 10^{-16} s^{-1} to 10^{-15} s^{-1} between the dense cores in molecular clouds to the inter-cloud medium (Dalgarno 2006). A gas ionisation rate of ζ_t=3 $\times$ 10^{-16} s^{-1} is assumed in the following section (Geballe et al. 1999; 2007; Indriolo et al. 2007). Lower gas ionisation rates would result in lower n(H). Equation (4.21) gives $n(H^0)$ between $n(H^0)$~50 to 100 cm^{-3} for 200 K, $n(H^0)$~90 to 200 cm^{-3} for a gas temperature of 100 K and $n(H^0)$~120 to 300cm^{-3} for 75 K. All volume densities for the individual positions and temperatures are listed in Table 7.7. The assumed gas temperatures are upper limits and the volume densities are lower limits as they represent the values on the surface of a PDR. Note that the derived lower limits for the H^0 volume densities are below the critical densities for collisions of C^+ with H^0, $n(H^0) \ll n_{crit}(H^0)$. This might indicate that C^+ gas is not thermalised. Thus, the assumption that the gas surface temperature is equal to the excitation temperature is not stringent.

Simulations with the plane parallel homogeneous PDR-model by Kaufman, Wolfire & Hollenbach (2006) of the PDR surface support the derived H^0 volume densities of a few 10^2 cm^{-3} and gas temperatures between around 100 to 200 K for the calculated G_0 and the remaining [CII] emission (cf. Fig. 7.7).

Equation (7.6) gives for τ=1 $I([CII])_{HI}$ of ~ 4 to 12 K km/s for T_{ex}=75 K, $I([CII])_{HI}$~2.5 to 8 K km/s for 100 K and $I([CII])_{HI}$ of ~ 1 to 3 K km/s for 200 K. The integrated [CII] intensities at =75 K correspond to ~40 to 85% of the total [CII] emission, while the [CII] at 200 K correspond to 10 to 20% of the total [CII] emission. In the optically thin limit, the contribution of the [CII] emission is roughly higher by a factor of 1.5. The differences between $I([CII])_{H^0}$ at different T_{ex} have their origin in the high uncertainties of the temperature and the volume density. This has a significant impact on the [CII] emission from the molecular phase as elaborated in the following section.

7.2.4.3 [CII] from the molecular phase

The [CII] emission from the molecular phase can be calculated via

$$I([\mathrm{CII}])_{H_2} = I([CII])_{\mathrm{tot}} - I([CII])_{H^+} - I([CII])_{H^0}. \qquad (7.7)$$

This term gives the [CII] emission that arises from the regions in which the molecular hydrogen is predominant. The derived $I([CII])_{H_2}$ are listed in Table 7.8. $I([CII])_{H_2}$ is a function of the assumed excitation temperature in the neutral phase as $I([CII])_{H^0}$ depends on this temperature. The majority of the [CII] emission arises from the neutral phase at low temperatures while the $I([CII])_{H_2}$ is minimal. In the opposite case, the $I([CII])_{H^0}$ are minimal and the $I([CII])_{H_2}$ are maximal. Equation (7.7) gives a mean [CII] emission from the molecular phase of ~7 for a excitation temperature of 75 K and an assumed τ=1. On average, this is ~40% of the total [CII] emission. For a $T_{\rm ex}$=200 K, on average ∼70% of the [CII] emission arises from the molecular phase with a mean [CII] emission of $I([\rm CII])_{\rm H_2}$ of ∼ 10 K km/s. In the optical thin case, these $I([\rm CII])_{\rm H_2}$ are roughly lower by a factor of 2 for $T_{\rm ex}$=75 K and remain almost constant for $T_{\rm ex}$=200K compared to a τ=1.

I will now discuss the C^+ column densities in the molecular gas phase. The main obstruction for its determination is the unknown excitation temperature in the atomic and molecular phases. It can be assumed, that the temperatures of the molecular gas phase are lower than those of the neutral phase[xxxvii]. The upper limit of the gas temperature in the molecular phase is thus given by the temperature of the neutral phase. Its lower limit is given by the gas temperature of the H_2 traced by C^0. In the following, it is assumed that the gas temperature for H_2 traced by C^+ is equal to the medium temperature between these upper and lower limits. As gas temperature for the H_2 traced by C^0, I assume 75 K. Furthermore, it is assumed that the derived gas temperature is equal to the excitation temperature. The $T_{\rm ex}([\rm CII])_{\rm H_2}$ is thus given by $T_{\rm ex}([\rm CII])_{\rm H_2}$=($T_{\rm ex}([\rm CII])_{\rm HI}$+75K)/2 ($T_{\rm ex}([\rm CII])_{\rm H_2}$= 75 K, 88 K and 138 K).

The density within the molecular phase is higher than in the neutral phase. Therefore, it is assumed that the optical depth is τ=1 and that $n(\rm H_2)=n_{\rm crit}(\rm H_2)$.

The critical densities for C^+ in the molecular phase $n_{\rm crit}(\rm H_2)$ are of the order of 2 to 3 $\times 10^3$ cm^{-3} for the discussed temperatures [xxxviii]. They were calculated by use of the deexcitation rates for collisions of C^+ with H_2 (Equation (A.9)[xxxix]).

The column density of C^+ in the molecular phase is calculated with Equation (A.7). All derived $N(\rm C^+)H_2$ are listed in Table 7.9. The $N(\rm C^+)H_2$ have values between ∼7 cm^{-2} for $\tau\to0$ and $T_{\rm ex}([\rm CII])_{\rm H_2}$=75 K to ∼25 cm^{-2} for τ=1 and $T_{\rm ex}([\rm CII])_{\rm H_2}$=138 K, which is between ∼20% and ∼35% of the total calculated C^+ column density. The fraction of C^+ ions in the molecular phase increases for high excitation temperatures. This can be explained by the method, chosen to calculate $N(\rm C^+)_{\rm HI}$ (cf. Section 7.2.4.2). $N(\rm C^+)_{\rm HI}$ is constant for all temperatures- therefore, $I([\rm CII])_{\rm HI}$ lowers towards higher temperatures in the neutral phase. The remaining [CII] emission arises from the molecular phase. Its intensity increases with the an increasing temperature. Therefore, $N(\rm C^+)_{\rm H_2}$ and $N(\rm C^+)_{\rm tot}$ are increased towards higher temperatures.

The $N(\rm C^+)_{\rm H^0}$ and $N(\rm C^+)_{\rm H_2}$ in the position GMCno06 A needs to be taken with caution. The peak of the HI spectra in GMCno06 (Fig 7.3) is located almost in the middle between the CO and [CI] peaks of the clouds GMCno06 A and B, while [CII] is only associated with GMCno06 A. Therefore, the calculated C^+ column densities are, at least partially, based on the HI emission that is not associated with the [CII] emission

xxxvii see Section 2.2.1

xxxviii The critical densities are $n_{\rm crit}(\rm H_2)\sim2.2\times10^3$ cm^{-3} for $T([\rm CII])_{\rm H_2}$ = 75 K, ∼2.5 $\times10^3$ cm^{-3} for $T([\rm CII])_{\rm H_2}$ = 88 K and ∼3.0 $\times10^3$ cm^{-3} for $T([\rm CII])_{\rm H_2}$ = 138 K

xxxix $C_{ul}(\rm H_2) = \left(4.55 + 1.6\times e^{100K/T}\right)\times10^{-10}\rm cm^3 s^{-1}$

	H^+ phase		H^0 phase		H_2 phase	
	$I([\mathrm{CII}])_{H^+}$		$I([\mathrm{CII}])_{H^0}$		$I([\mathrm{CII}])_{H_2}$	
	[K km/s]	%	[K km/s]	%	[K km/s]	%
$\tau \to 0$	$T_{\mathrm{ex\,HI}}$=75 K, $T_{\mathrm{ex\,H_2}}$=75 K					
BCLMP691	3.9±0.5	39	4.2±0.4	42	1.8 ±0.5	18
BCLMP302	1.9±0.3	17	7.8±0.8	69	1.6±0.4	14
GMC01 Peak	4.0±0.4	17	6.9±0.7	30	12.4±1.3	53
GMC01 Flank	4.0±0.4	27	6.0±0.7	40	5.0±0.7	33
GMCno06 A	1.7±0.2	12	12.0±1.2	85	0.5±1.0	3
Mean	3.1±1.1	23±10	7.4±2.6	53±21	4.2±4.4	24±17
τ=1						
BCLMP691	3.9±0.5	39	2.6±0.3	27	3.4±0.6	34
BCLMP302	1.9±0.3	17	4.9±0.5	44	4.4±0.6	39
GMC01 Peak	4.0±0.4	17	4.4±0.5	19	14.9±1.5	64
GMC01 Flank	4.0±0.4	27	3.8±0.4	25	7.2±0.9	48
GMCno06 A	1.7±0.2	12	7.6±0.8	54	4.9±1.0	34
Mean	3.1±1.1	23±10	4.7±1.7	34±13	7.0±4.2	43±11
$\tau \to 0$	$T_{\mathrm{ex\,HI}}$=100 K, $T_{\mathrm{ex\,H_2}}$=88 K					
BCLMP691	3.9±0.5	39	2.5±0.3	25	3.5±0.6	35
BCLMP302	1.9±0.3	17	4.8±0.5	42	4.6±0.5	40
GMC01 Peak	4.0±0.4	17	4.5±0.5	19	14.9±1.5	64
GMC01 Flank	4.0±0.4	27	3.9±0.4	26	7.1±0.9	47
GMCno06 A	1.7±0.2	12	7.6±0.8	54	4.9±1.0	34
Mean	3.1±1.1	23±10	4.6±1.7	33±13	7.0±4.1	44±11
τ=1						
BCLMP691	3.9±0.5	39	1.6±0.2	16	4.4±0.7	45
BCLMP302	1.9±0.3	17	3.0±0.3	27	6.3±0.7	56
GMC01 Peak	4.0±0.4	17	2.8±0.4	12	16.5±1.7	71
GMC01 Flank	4.0±0.4	27	2.4±0.3	16	8.5±1.0	57
GMCno06 A	1.7±0.2	12	4.8±0.5	34	7.7±1.2	54
Mean	3.1±1.1	23±10	2.9±1.1	30±17	8.7±4.2	57±8
$\tau \to 0$	$T_{\mathrm{ex\,HI}}$=200 K, $T_{\mathrm{ex\,H_2}}$=138 K					
BCLMP691	3.9±0.5	39	0.9±0.1	9	5.1±0.7	52
BCLMP302	1.9±0.3	17	1.7±0.1	15	7.6±0.9	67
GMC01 Peak	4.0±0.4	17	1.7±0.1	7	17.6±1.8	76
GMC01 Flank	4.0±0.4	27	1.5±0.1	10	9.5±0.5	63
GMCno06 A	1.7±0.2	12	2.8±0.1	20	9.6±1.3	68
Mean	3.1±1.1	23±10	1.7±0.7	12±5	9.9±4.2	65±8
τ=1						
BCLMP691	3.9±0.5	39	0.6±0.1	6	5.5±0.8	55
BCLMP302	1.9±0.3	17	1.1±0.1	10	8.2±1.0	73
GMC01 Peak	4.0±0.4	17	1.1±0.1	5	18.2±1.8	78
GMC01 Flank	4.0±0.4	27	0.9±0.1	6	10.0±1.1	67
GMCno06 A	1.7±0.2	12	1.8±0.2	13	10.1±1.34	75
Mean	3.1±1.1	23±10	1.1±0.4	8±3	10.4±4.2	70±8

Table 7.8: [CII] emission in the three gas phases for different temperatures in the neutral phase and molecular phase for optically thin case and an optical depth of τ=1.

in GMCno06 A. The calculated $N(\mathrm{C}^+)^0_H$ in GMCno06 A are thus upper limits and the $N(\mathrm{C}^+)_{\mathrm{H}_2}$ are lower limits.

7.2.4.4 Conclusion to C^+ in the different gas phases

The previous sections have dealt with the C^+ distribution in the ionised, neutral and molecular phase for different excitation temperatures and optical depths. The derived [CII] intensities for the different gas phases are listed in Table 7.8. The C^+ column densities are listed in Table 7.9.

The sum of the C^+ column densities over all the phases gives the total C^+ column density, $N(\mathrm{C}^+)_{\mathrm{tot}}$, (cf. Equation (7.2)[xl]). The beam averaged total mean C^+ column density varies between $\sim 2\times 10^{17}$ cm^{-2} for gas temperature of 75 K in the optically thin limit and $\sim 3.5\times 10^{17}$ cm^{-2} for high temperatures and τ=1. Within the individual GMCs, the total column density varies around a factor ~2 to 3, in which GMC01 has in general the highest $N(\mathrm{C}^+)$tot and BCLMP691 has the lowest the lowest $N(\mathrm{C}^+)$tot.

Roughly 1/4 of the [CII] emission arises from the ionised phase, regardless of the ambient gas temperature in the neutral and the molecular phase. The fraction of I([CII]) from the neutral and molecular phase depends on the assumed gas temperatures and the optical depth. The [CII] emission from the molecular phase is higher for higher gas temperatures, while the contribution from the neutral phase is lower. In general, the contribution of [CII] emission from the molecular phase is higher compared to the emission from the neutral and ionised phase. The derived fractions of the [CII] emission are similar to the fractions found in other studies. Pérez-Beaupuits et al. (2015) derived relative fractions of the [CII] emission of ~39%, 18% and 46% for the ionised, neutral and molecular phase in M17. Pineda et al. (2013) found out that the majority of the [CII] emission arises from the molecular phase (~ 50%) followed by the ionised and neutral phase where ~30% and 20% of the [CII] emission arises.

The main obstruction for a precise determination of the $N(\mathrm{C}^+)$ is an unknown excitation temperature in the different gas phases. Tracer for these temperatures are required. A possible tracer is the linear molecule CH^+. This molecule can be used to estimate the excitation temperature of [CII] in the neutral atomic phase[xli] (Gnacinski, Krogulec & Krelowski 2007; Menten et al. 2011). Unfortunately a bright atmospheric ozone line harms the observation of $^{12}\mathrm{CH}^+$ from the ground[xlii]. Therefore this line can be only observed from space. $^{13}\mathrm{CH}^+$ can be in general observed from the ground based observatories[xliii], but this line is relatively faint (Menten et al. 2011).

xl $N(\mathrm{C}^+)_{\mathrm{tot}} = N(\mathrm{C}^+)_{\mathrm{H}^+} + N(\mathrm{C}^+)_{\mathrm{H}^0} + N(\mathrm{C}^+)_{\mathrm{H}_2}$

xli CH^+ is commonly associated with the reaction $\mathrm{C}^+ + \mathrm{H}_2 \rightarrow \mathrm{CH}^+ + \mathrm{H}^0$. Therefore it is expected to arise in the neutral atomic phase.

xlii $^{12}\mathrm{CH}^+$ has rotational transitions at ν=835.1 (J=1–0), 1669.3 GHz (J=2–1), 2501.4 GHz (J=(3–2))...

xliii $^{13}\mathrm{CH}^+$ is observed with the APEX telescope (Menten et al. 2011)

	$N([\text{C}\,\text{II}])_{\text{HII}}$ [10^{16} cm^{-2}]	%	$N([\text{C}\,\text{II}])_{\text{HI}}$ [10^{16} cm^{-2}]	%	$N([\text{C}\,\text{II}])_{\text{H}_2}$ [10^{16} cm^{-2}]	%	$N([\text{C}\,\text{II}])_{\text{tot}}$ [10^{16} cm^{-2}]
$\tau\to0$	$T_{\text{ex}}([\text{C}\,\text{II}])^0_H$=75 K, $T_{\text{ex}}([\text{C}\,\text{II}])_{\text{H}_2}$=75 K						
BCLMP691	1.9±0.2	15	8.4±0.8	63	3.0±0.6	22	13.3±1.4
BCLMP302	1.0±0.1	6	11.8±1.2	77	2.6±0.5	17	15.4±1.5
GMC01 Peak	2.0±0.2	7	7.1±0.7	24	20.2±2.0	69	30.6±3.1
GMC01 Flank	2.0±0.2	12	6.2±0.7	38	8.1±1.0	50	16.3±1.7
GMCno06 A	0.9±0.1	5	14.3±1.4	90	0.7±1.1	5	15.9±1.6
Mean	1.5±0.5	9±4	9.6±3.0	58±24	6.9±7.1	33±23	18.3±7.7
τ=1							
BCLMP691	1.9±0.2	10	8.4±0.8	44	8.7±1.0	46	19.0±1.9
BCLMP302	1.0±0.1	4	11.8±1.2	49	11.4±1.2	47	24.2±2.5
GMC01 Peak	2.0±0.2	4	7.1±0.7	15	38.6±3.9	81	49.0±4.9
GMC01 Flank	2.0±0.2	8	6.2±0.7	23	18.5±1.9	69	26.7±2.7
GMCno06 A	0.9±0.1	3	14.3±1.4	52	12.6±1.6	45	27.8±2.9
Mean	1.5±0.5	6±3	9.6±3.0	37±15	14.1±6.0	58±15	29.4±6.7
$\tau\to0$	$T_{\text{ex}}([\text{C}\,\text{II}])^0_H$=100 K, $T_{\text{ex}}([\text{C}\,\text{II}])_{\text{H}_2}$=88 K						
BCLMP691	1.9±0.2	12	8.4±0.8	53	5.4±0.7	34	15.7±1.7
BCLMP302	1.0±0.1	5	11.8±1.2	59	7.1±0.8	36	19.9±2.0
GMC01 Peak	2.0±0.2	6	7.1±0.7	22	23.0±2.3	72	33.4±3.4
GMC01 Flank	2.0±0.2	10	6.2±0.7	32	11.0±1.2	57	19.2±2.0
GMCno06 A	0.9±0.1	4	14.3±1.4	63	7.5±1.1	33	22.7±2.3
Mean	1.5±0.5	7±3	9.6±3.0	46±16	18.0±12.5	46±16	22.2±12.9
τ=1							
BCLMP691	1.9±0.2	9	8.4±0.8	40	10.8±0.5	51	21.1±2.2
BCLMP302	1.0±0.1	3	11.8±1.2	42	15.5±0.3	55	28.3±2.9
GMC01 Peak	2.0±0.2	4	7.1±0.7	14	40.4±0.3	82	50.8±5.1
GMC01 Flank	2.0±0.2	7	6.2±0.7	21	20.8±0.5	72	29.0±3.1
GMCno06 A	0.9±0.1	3	14.3±1.4	42	18.8±0.8	55	34.0±3.5
Mean	1.5±0.5	5±3	9.6±3.0	32±12	21.2±10.2	63±12	32.6±10.6
$\tau\to0$	$T_{\text{ex}}([\text{C}\,\text{II}])^0_H$=200 K, $T_{\text{ex}}([\text{C}\,\text{II}])_{\text{H}_2}$=138 K						
BCLMP691	1.9±0.2	11	8.4±0.8	48	7.3±0.8	41	17.6±1.8
BCLMP302	1.0±0.1	4	11.8±1.2	50	10.8±0.3	46	23.6±2.4
GMC01 Peak	2.0±0.2	6	7.1±0.7	21	25.1±0.2	73	35.5±3.6
GMC01 Flank	2.0±0.2	9	6.2±0.7	28	13.5±0.4	62	21.7±2.2
GMCno06 A	0.9±0.1	3	14.3±1.4	50	13.7±0.8	47	28.9±3.0
Mean	1.5±0.5	7±3	9.6±3.0	39±12	14.1±6.0	54±12	25.5±6.7
τ=1							
BCLMP691	1.9±0.2	9	8.4±0.8	37	12.3±0.4	54	22.6±2.3
BCLMP302	1.0±0.1	3	11.8±1.2	38	18.6±1.9	59	31.4±3.2
GMC01 Peak	2.0±0.2	4	7.1±0.7	14	41.1±4.1	82	51.5±5.3
GMC01 Flank	2.0±0.2	7	6.2±0.7	20	22.6±2.3	73	30.8±3.2
GMCno06 A	0.9±0.1	2	14.3±1.4	37	24.1±2.5	61	39.3±4.0
Mean	1.5±0.5	5±3	9.6±3.0	29±10	23.7±9.6	66±10	35.1±10.1

Table 7.9: C^+ column densities in the three gas phases and their relative fraction for excitation different temperatures in the optically thin case ($\tau\to0$) as well as for a optical depth τ=1 in the neutral and molecular phase.
The column densities in the positions GMCno06 A are based on the $[\text{C}\,\text{II}]_{\text{H}_2}$ emission calculated from the total H I emission in GMCno06.

	Compositions of the $N(\mathbf{C})_{H_2}$					
	$N(\mathbf{C}^+)_{H_2}$		$N(\mathbf{C}^0)$		$N(\mathbf{CO})$	
	$T_{ex}(C^+)_{H^0}$ =200 K $T_{ex}(C^+)_{H_2}$ =138 K	$T_{ex}(C^+)_{H^0}$ =75 K $T_{ex}(C^+)_{H^0}$ =75 K	$T_{ex}(C^0)$ K =75 K	$T_{ex}(C^0)$ = 10 K	$T_{ex}(CO)$ $\approx$6 K*	$T_{ex}(CO)$ = T_{dust}
Case I	✓		✓			✓
Case II		✓		✓		✓
Case III	✓		✓		✓	
Case IV		✓		✓	✓	

Table 7.10: Used C^+ , C^0 and CO column densities for ($N(C)_{H_2}$ in the Cases I, II , III and IV. The specific column densities are defined by their excitation temperature. The used column densities are listed in the upper and lower columns of the tables 7.9($N(C^+)$), Table 7.6 ($N(C^+)$) and Table 7.5 (N(CO)).
* The $T_{ex}\approx$6 K* represent the mean excitation temperatures of the CO column densities in the upper half of Table 7.5.

7.2.5 TOTAL CARBON COLUMN DENSITIES IN THE MOLECULAR PHASE

The following section aims to determine the total contribution of carbon in the molecular phase. The total hydrogen column densities are calculated and discussed in the following section.

The total carbon column density in the molecular phase is given by the sum of the column densities of CO, C^0 and C^+ in the H_2 phase in the observed positions

$$N(C)_{H_2} = N(C^+)_{H_2} + N(C^0) + N(CO) \tag{7.8}$$

It was assumed that all CO and C^0 are located in the molecular phase.

The CO, C^0 and C^+ column densities are dependent on the assumptions made for the calculations. It is hard to get a precise estimate of the parameters needed to calculate the different carbon column densities as shown in the previous sections. Different total carbon column densities can be calculated for the different assumptions.

Different possible total carbon column densities will be discussed in the following. This is necessary to reflect and study the different possible carbon compositions. The four cases are chosen to study the maximal and minimal $N(C)_{H_2}$ as well as to study the upper and lower limits the CO dark H_2 fraction.

CASE I: In this case,the total carbon column density is composed of the C^+ and C^0 column densities which show the highest values in Table 7.9 and 7.6. These are the C^+ column densities $N(C^+)_{H_2}$ calculated for $T_{ex}([CII])_{H^0}$= 200K and $T_{ex}([CII])_{H_2}$=138 K for an optical depth τ=1 (Table 7.9) and the $N(C^0)$ calculated for a T_{ex}=75 K. I choose the CO column densities that were calculated for $T_{ex}\sim$6 K (Approach I Table 7.5).

CASE II: In this case, the $N(C)_{H_2}$ is composed of the lower C^+ and C^0 column densities. The CO column densities are calculated for

Total carbon column densities in the molecular phase				
	Case I	Case II	Case III	Case IV
	$N(\mathrm{C})_{\mathrm{H_2\ I}}$	$N(\mathrm{C})_{\mathrm{H_2\ II}}$	$N(\mathrm{C})_{\mathrm{H_2\ III}}$	$N(\mathrm{C})_{\mathrm{H_2\ IV}}$
	10^{16}	10^{16}	10^{16}	10^{16}
	cm^{-2}	cm^{-2}	cm^{-2}	cm^{-2}
BCLMP691	19.4±4.5	15.1±2.0	25.1±4.4	9.4±2.0
GMC91	24.4±5.8	14.4±2.7	14.4±2.7	24.4±5.8
BCLMP302	26.6±6.2	8.4±1.4	25.8±6.0	9.2±2.0
GMC01 Peak	57.6±13.1	45.1±9.4	58.2±12.8	44.5±9.8
GMC01 Flank	36.6±7.8	18.3±3.3	34.3±7.4	20.6±4.0
GMCno06 A	31.8±8.1	24.2±2.8	49.3±8.4	6.7±2.6
GMCno06 B	3.3±2.0	5.9±2.0	6.6±2.0	2.6±2.0
Mean	26±17	19±12	31±17	17±13
Mean*	26±18	20±13	33±17	16±14
Mean**	29±17	22±13	39±13	18±14

Table 7.11: The total carbon column densities in the different discussed cases.
Mean: Average over all positions
Mean*: Average over positions in which [CI](1–0) was detected (all positions but GMC91)
Mean**: Average over positions in which [CI](1–0) and [CII] were detected (all positions but GMC91 and GMCno06 B)

excitation temperatures that are equal to the dust temperatures (approach II). The C^+ column densities in this case are those calculated for $T_{\mathrm{ex}}([\mathrm{CII}])_{\mathrm{H^0}}=T_{\mathrm{ex}}([\mathrm{CII}])_{\mathrm{H_2}}=75$ K in the optically thin limit. For C^0I choose the column densities calculated for a $T_{\mathrm{ex}}=10$ K. Furthermore, I choose the $N(\mathrm{CO})$ calculated for $T_{\mathrm{ex}}=T\mathrm{dust}\approx20$K.

CASE III: In this this case $N(\mathrm{C})_{\mathrm{H_2}}$ is composed of the upper column densities of $N(C^+)$ and $N(C^0)$ and of the $N(\mathrm{CO})$ of approach II.

CASE IV: This $N(\mathrm{C})_{\mathrm{H_2}}$ is composed of the lower column densities of $N(C^+)$ and $N(C^0)$ and the $N(\mathrm{CO})$ calculated for $T_{\mathrm{ex}}\sim6$ K.

The different column densities used for the different cases are illustrated in Table 7.10. The total carbon column densities calculated for the different cases are summarised in Table 7.11. The total $N(\mathrm{C})_{\mathrm{H_2}}$ have mean values between $\sim18\times10^{16}\mathrm{cm}^{-2}$ (Case II and IV) and $\sim30\times10^{16}\mathrm{cm}^{-2}$ (Case I and III).

The fraction of the column densities of the different carbon species relative to the total $N(\mathrm{C})_{\mathrm{H_2}}$ are summarised in Table 7.12.

The mean fraction of $N(C^+\ )$ to the $N(\mathrm{C})_{\mathrm{H_2}}$ varies between $\sim$69% (CASE I). These values refer to the positions in which C^+ was detected, the GMC91 and BCLMP691 B are excluded. The fraction of the mean C^0 fraction varies between $\sim$8% (Case IV) and $\sim$5% (Case II). The mean fraction of $N(\mathrm{CO})$ to the total $N(\mathrm{C})_{\mathrm{H_2}}$ varies between $\sim$24% (Case I) and $\sim$62% (Case II).

The relative fraction of C^+ and CO to the total carbon column densities in the cases I and III are similar to the ones found in other studies.

For example, the study of Okada et al. (2015) found out that $\sim$20% to 25% of the carbon is CO and $\sim$60% to 70% of the carbon is C^+in the

LMC. The fraction of C^0 varies between ∼10 and 20%. Note that this study does not consider any [CII] emission from the neutral and ionised phase.

These $N(\mathrm{C})_{\mathrm{H_2}}$ allow the calculation of the column densities of H_2 and, thus, of the total hydrogen column density as described in the following section.

7.2.6 MOLECULAR HYDROGEN COLUMN DENSITIES

The column density of molecular hydrogen can be estimated from the amount of carbon in the molecular phase. Each carbon species traces a particular fraction of the molecular gas. Molecular hydrogen consists of two protons. Therefore, total molecular hydrogen column densities can be calculated via

$$N(\mathrm{H_2})_{\mathrm{tot}} = N(\mathrm{H_2})_{\mathrm{C^+}} + N(\mathrm{H_2})_{\mathrm{C^0}} + N(\mathrm{H_2})_{\mathrm{CO}} \tag{7.9}$$

$$= \frac{1}{2}\frac{N(\mathrm{C^+})_{\mathrm{H_2}} + N(\mathrm{C^0}) + N(\mathrm{CO})}{X^*_{\mathrm{C}}} \tag{7.10}$$

These calculations assume that half of the carbon in the molecular zones is depleted on dust grains, X^*_{C}=$X_{\mathrm{C}}/2 = 4.25 \times 10^{-5}$ (cf. Section 7.2.4.4).

The derived beam average H_2 column densities have mean values of ∼4 $\times 10^{21}$ cm^{-2} (Case II and IV) to ∼7 $\times 10^{21}$ cm^{-2} (Case I and III). The $N(\mathrm{H_2})$ of the different cases are summarised in Table 7.13. These molecular hydrogen column densities were calculated from the beam average carbon column densities and were not divided by the uncertain beam filling factors. Hence, these column densities are in fact lower limits.

The fraction of H_2 traced by CO, C^0 and C^+ is equal to the relative distribution of the carbon species to the total amount of carbon (Table 7.12). C^+ traces ∼1/3 (cases II and IV) to 2/3 (cases I and II) of all molecular hydrogen. Roughly ∼1/4–1/3 (case II and IV) to 3/5 (case I and III) of the H_2 is traced by CO. On average, C^0 traces less than 1/10 of the H_2.

Now, it is possible to calculate the total hydrogen column density (Section 7.2.7), the fraction of CO dark H_2 (Section 7.2.8) and the that one molecular hydrogen to the total amount of hydrogen (Section 7.2.9).

7.2.7 TOTAL HYDROGEN COLUMN DENSITIES

The total hydrogen column density is given by the sum of the hydrogen column densities of the ionised, neutral and molecular phase.

$$N(\mathrm{H})_{\mathrm{tot}} = N(\mathrm{H^+}) + N(\mathrm{H^0}) + 2 \times N(\mathrm{H_2})_{\mathrm{tot}}{}^{\mathrm{xliv}}. \tag{7.11}$$

The ionised phase contains no dust grains in a first approximation (e.g. Mookerjea et al. 2016). Therefore, it can be assumed that all the carbon is gaseous in this phase . Hence, the hydrogen column density in the ionised phase can be estimated via $N(\mathrm{H^+})$=$N(\mathrm{C^+})_{\mathrm{H^+}}/X_{\mathrm{C}}$. When $N(\mathrm{H})_{\mathrm{tot}}$ is

xliv Molecular hydrogen consists of 2 protons. Therefore, the molecular hydrogen column density is muliplied by a factor two

	Case I			Case II			Case III			Case IV		
	$\frac{N(C^+)_{H_2}}{N(C)_{H_2}}$	$\frac{N(C^0)_{H_2}}{N(C)_{H_2}}$	$\frac{N(CO)_{H_2}}{N(C)_{H_2}}$	$\frac{N(C^+)_{H_2}}{N(C)_{H_2}}$	$\frac{N(C^0)_{H_2}}{N(C)_{H_2}}$	$\frac{N(CO)_{H_2}}{N(C)_{H_2}}$	$\frac{N(C^+)_{H_2}}{N(C)_{H_2}}$	$\frac{N(C^0)_{H_2}}{N(C)_{H_2}}$	$\frac{N(CO)_{H_2}}{N(C)_{H_2}}$	$\frac{N(C^+)_{H_2}}{N(C)_{H_2}}$	$\frac{N(C^0)_{H_2}}{N(C)_{H_2}}$	$\frac{N(CO)_{H_2}}{N(C)_{H_2}}$
BCLMP691	64±17	6±2	30±9	20±8	3±1	77±10	49±12	5±2	46±9	32±12	5±2	63±14
GMC91	<8	<2	100±24	<13	<1	100±28	<13	<4	100±19	<8	<1	100±25
BCLMP302	70±18	9±1	21±7	31±12	10±3	59±12	72±18	9±3	19±5	28±8	9±3	62±15
GMC01 Peak	71±17	4±1	25±7	65±15	2±1	33±9	71±17	4±1	26±6	66±12	2±1	31±9
GMC01 Flank	62±15	7±2	31±8	44±12	6±1	50±12	66±16	7±2	27±7	39±16	5±1	56±13
GMCno06 A	76±20	9±3	15±5	3±4	7±1	92±10	49±12	6±1	45±8	10±11	18±5	72±17
GMCno06 B	<57	38±24	62±37	<32	10±4	90±31	<7	19±7	81±25	<73	22±6	78±58
Mean	49±31	10±12	41±28	23±23	5±4	72±23	44±29	7±5	49±28	25±22	9±8	66±19
Mean*	57±26	12±12	31±15	27±23	6±3	67±21	51±25	8±5	41±21	29±21	10±7	61±15
Mean**	69±5	7±2	24±6	33±21	5±3	62±21	61±10	6±2	33±11	35±18	8±6	57±14

Table 7.12: The total carbon column densities in the different cases discussed here. Mean: Average over all positions
Mean*: Average over positions in which [CI](1–0) was detected (all positions but GMC91)
Mean**: Average over positions in which [CI](1–0) and [CII] were detected (all positions but GMC91 and GMCno06 B)

calculated, $N(\mathrm{H}^+)$ is commonly neglected (e.g Langer et al. 2014b) as it participates $\lesssim$5% to the $N(\mathrm{H})_{\mathrm{tot}}$ (cf. Table 7.13).

The hydrogen column densities for the ionised, neutral and molecular phase as well as the total hydrogen column density $N(\mathrm{H})$ in the different cases are listed in Table 7.13. The total hydrogen column densities have mean values of $\sim 15 \times 10^{21}$ cm^{-2} in the cases I and III. The mean values of the cases II and IV are roughly 1/3 lower compared to the cases I and II with mean values of $\sim 10 \times 10^{21}$ cm^{-2}. GMC01 has the highest hydrogen column density of all discussed clouds, GMCno06 B has the lowest $N(\mathrm{H})_{\mathrm{tot}}$.

7.2.8 CO DARK H_2 IN M33

The previous calculations allow the estimation of the CO-dark H_2 gas fraction, $\mathfrak{f}(\mathrm{DG})$, in M33. The derived $\mathfrak{f}(\mathrm{DG})$ will be compared to the results from the Milky Way and to theoretical predictions by Wolfire, Hollenbach & McKee (2010).

CO dark H_2 gas means all gas that is not directly associated with CO emission, according to the definition of Leroy et al. (2011). The column density of CO dark H_2 can be calculated from $N(\mathrm{H}_2)$ that is calculated from C^0 and C^+ column densities.

$$N\,(\mathrm{DG}) = N(\mathrm{H}_2)_{\mathrm{C}^+} + N(\mathrm{H}_2)_{\mathrm{C}^0} \tag{7.12}$$

The fraction of CO dark H_2 gas, $\mathfrak{f}(\mathrm{DG})$, is given by the ratio of $N\,(\mathrm{DG})$ to the total hydrogen column density[xlv],

$$\mathfrak{f}(\mathrm{DG}) = \frac{N\,(\mathrm{DG})}{N\,(\mathrm{H}_2)_{\mathrm{tot}}} \tag{7.13}$$

As the hydrogen column densities are directly calculated from the specific carbon column densities Equation (7.13) can be expressed by

$$\mathfrak{f}(\mathrm{DG}) = \frac{N\,(\mathrm{C}^+)_{\mathrm{H}_2} + N\,(\mathrm{C}^0)}{N\,(\mathrm{C}^+)_{\mathrm{H}_2} + N\,(\mathrm{C}^0) + N\,(\mathrm{CO})} \tag{7.14}$$

The fractions of CO dark H_2 for the different cases are summarised in Table 7.14. The calculated mean fraction varies between ∼40% (case IV) and ∼80% (case I). The largest share of the CO dark H_2 fraction is traced by [CII] emission (∼80 to 90 %), while only a minor fraction is traced by [CI](1–0) (∼ 10 to 20%). The position GMCno06 B is an exception as all CO dark H_2 gas is traced by the [CI](1–0) in this position.

The fraction of CO dark H_2 in the Milky Way is derived by Langer et al. (2014b) based [CII] observations carried out with Herschel/HIFI. The C^0 transitions are not considered in this study. They derived a mean

xlv I use the same definition for $\mathfrak{f}(\mathrm{DG})$ as given by equation (1) in Wolfire, Hollenbach & McKee (2010). This definition defines the relative fraction of CO dark H_2 to the total amount of molecular hydrogen. It does not give the fraction of CO dark H_2 to the total amount of hydrogen, which includes the contribution of H^0 as well (cf. Section 7.2.9).

	N(HII))	$N(H^0)$	$N(H_2)$				N(H)			
			Case I	Case II	Case III	Case IV	Case I	Case II	Case III	Case IV
	10^{21} cm^{-2}	10^{21} cm^{-2}	10^{21} cm^{-2}	10^{21} cm^{-2}	10^{21} cm^{-2}	10^{21} cm^{-2}	10^{21} cm^{-2}	10^{21} cm^{-2}	10^{21} cm^{-2}	10^{21} cm^{-2}
BCLMP691	0.24±0.01	1.97±0.05	4.5±1.0	3.5±0.5	5.9±1.0	2.2±0.5	11.1±2.1	9.1±1.0	13.8±2.1	6.4±1.0
GMC91	–	2.83±0.05	5.7±01.4	3.4±0.6	3.4±1.4	5.7±1.4	14.3±2.8	9.6±1.3	9.6±1.3	14.3±2.8
BCLMP302	0.18±0.01	2.77±0.05	6.3±1.5	2.0±0.3	6.1±1.5	2.2±0.5	15.3±2.9	6.7±0.8	14.9±2.9	7.1±1.0
GMC01 Peak	0.24±0.01	1.67±0.06	13.6±3.1	10.6±2.2	13.7±3.1	10.5±2.3	28.8±6.2	22.9±4.4	29.1±6.0	22.6±4.6
GMC01 Flank	0.24±0.01	1.45±0.05	8.6±1.8	4.3±0.8	8.1±1.8	4.9±0.9	18.7±3.7	10.1±1.6	17.6±3.5	11.2±1.9
GMCno06 A	0.11±0.01	1.69±0.15	7.5±1.9	5.7±0.7	11.6±1.9	1.6±0.4	16.7±3.8	13.1±1.3	24.9±4.0	4.8±0.8
GMCno06 B	0.11±0.01	1.69±0.15	0.8±0.5	2.4±0.5	1.5±0.5	0.6±0.5	3.3±1.0	4.5±1.0	4.8±1.0	2.9±1.0
Mean	0.16±0.08	2.0±0.5	7.2±4.0	4.4±2.9	7.2±4.0	3.9±3.2	15.4±7.2	10.8±5.5	16.4±7.8	9.9±6.3
Mean*	0.19±0.06	1.9±0.4	7.8±4.0	4.6±3.1	7.8±4.0	3.7±3.3	15.6±7.7	11.0±5.9	17.5±7.9	9.2±6.5
Mean**	0.20±0.05	1.9±0.5	9.1±3.1	5.2±3.0	9.2±3.1	4.3±3.3	18.1±5.9	12.4±5.7	20.0±6.0	10.4±6.5

Table 7.13: Ionised, neutral, molecular and total hydrogen column densities in the different cases.
The mean values show the average over all positions.
Mean* is the average over all positions in which [CI](1–0) was observed (all positions but GMC91)
Mean** is the mean value over all positions in which [CII] was detected (all positions but GMC91 and GMCno06 B)

	Relative fraction of CO dark H_2, $\mathfrak{f}$(DG)			
	Case I	Case II	Case III	Case IV
BCLMP691	0.70±0.10	0.23±0.09	0.54±0.08	0.37±0.11
GMC91	<0.08	0.013	<0.14	< 0.08
BCLMP302	0.79±0.11	0.41±0.12	0.81±0.12	0.38±0.11
GMC01 Peak	0.75±0.10	0.67±0.10	0.74±0.10	0.68±0.10
GMC01 Flank	0.69±0.10	0.50±0.10	0.73±0.10	0.44±0.09
GMCno06 A	0.85±0.11	0.08±0.07	0.55±0.08	0.28±0.16
GMCno06 B	0.38±0.59	0.10±0.36	0.19±0.30	0.22±0.75
Mean*	0.69±0.16	0.43±0.25	0.59±0.21	0.36±0.12
Mean**	0.77±0.06	0.51±0.21	0.67±0.12	0.40±0.10

Table 7.14: Fraction of CO dark H_2relative to the total H_2 column densities. For GMC01 I applied the mean value of both positions.
Mean* represents the mean value of all positions in which [CI](1–0) was detected, i.a all positions but GMC91.
Mean** represents the mean value of the positions in which [CII] emission was observed. GMC91 and GMCno06 B are not considered in this case.

$\mathfrak{f}$(DG)=∼20% for dense molecular clouds[xlvi] in the Milky Way. Averaged over all sources with [CII] emission (sources with CO and no CO) the $\mathfrak{f}$(DG) is 44%±28% in the Milky Way (Langer et al. 2014b). The $\mathfrak{f}$(DG) in M33 are calculated for clouds that show an emission of ^{13}CO(1–0) and ^{12}CO(1–0) as well. The derived $\mathfrak{f}$(DG) in M33 are ∼2 to 4 times higher compared to the mean value values in dense molecular clouds in Milky Way. They are even one to two times higher compared to the mean $\mathfrak{f}$(DG) in the Milky Way. The observations are consistent with the expectations. Due to metallicity effects (as for example an increased photodissociation rate of CO at low Z), it is expected that the $\mathfrak{f}$(DG) is higher in M33 compared to the Milky Way. [xlvii].

In the following, I will compare the derived $\mathfrak{f}$(DG) with the predictions of the PDR model of Wolfire, Hollenbach & McKee (2010). This model estimated the fraction of CO dark H_2 as a function of the metallicity and the total hydrogen column density via Equation (2.1)[xlviii].

Figure 7.8 shows the $\mathfrak{f}$(DG) discussed here as a function of the specific total hydrogen column density. The predictions by the Wolfire, Hollenbach & McKee (2010)–model are superimposed. The $\mathfrak{f}(\mathrm{DG})_{\mathrm{W10}}$ are plotted for the same parameters as used in Langer et al. (2014b) for the sake of a better comparability. These parameters are: $k_{æ}$=2.0 and $\Delta A_{\mathrm{V,DG}}$=2.0 for Z=0.5$Z_{\odot}$, and $k_{æ}$=0.8, $\Delta A_{\mathrm{V,DG}}$=0.8 for Z=$Z_{\odot}$. They give a $\mathfrak{f}(\mathrm{DG})_{\mathrm{W10}}$ of ∼0.95 to 0.5 for a hydrogen column density between $N(\mathrm{H})_{\mathrm{tot}}$=0.1 and 3×10^{22} cm^{-2} in the case of Z=0.5$Z_{\odot}$ and $\mathfrak{f}(\mathrm{DG})_{\mathrm{W10}}$ of ∼0.9 to 0.15 for Z=$Z_{\odot}$.

The CO dark H_2 fraction in M33 meets the expectations of the model by Wolfire, Hollenbach & McKee (2010) for Z=0.5$Z_{\odot}$ in the cases I and III. A slope of $\mathfrak{f}(\mathrm{DG})(N(\mathrm{H})_{\mathrm{tot}})$ towards higher N(H)tot could not be observed but can also not be excluded within the uncertainties. The mean fractions

xlvi Dense molecular clouds were defined as clouds that show ^{13}CO(1–0) and ^{12}CO(1–0) emission (Langer et al. 2014b)
xlvii See Section 2.2.3
xlviii $\mathfrak{f}(\mathrm{DG})_{\mathrm{W10}} = 1 - \left[1 + \left(\frac{k_{æ}-1}{3-k_{æ}}\right) \frac{0.76\,\Delta A_{\mathrm{V,DG}}}{Z' N_{22}(\mathrm{H})}\right]^{-\frac{3-k_{æ}}{k_{æ}-1}}$

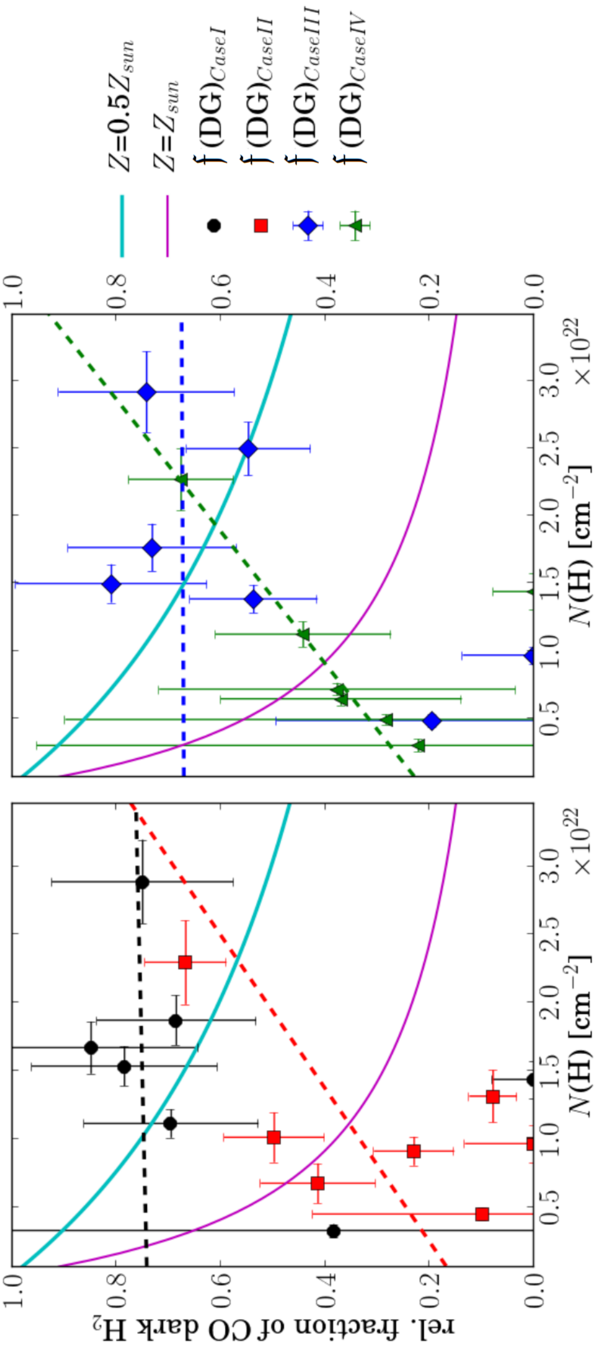

Figure 7.8: Relative fraction of CO dark H_2 ($\mathfrak{f}$(DG)) as function of N(H)tot in the studied Case I (black ●), Case II (■) Case III (blue ◆) and Case IV (▲). The lines show the CO dark H_2 fractions calculated with Equation (2.1) for a $k_æ$=2.5 and $\Delta A_{\rm V,DG}$=2.5 for a metallicity of Z=0.5$Z_\odot$ (**cyan**—) and Z=$Z_\odot$ (**violet**—).

remains almost constant at $\mathfrak{f}$(DG)∼80% and 70% along $N(\mathrm{H})_{\mathrm{tot}}$ in these two cases.

The calculated CO dark H_2 fractions are below the expectation for Z=0.5$Z_\odot$ in the cases II and IV. They are roughly in the order of the expectations for Z=$Z_\odot$ The slope of $\mathfrak{f}(\mathrm{DG})(N(\mathrm{H})_{\mathrm{tot}})$ increases towards higher hydrogen column densities which is counter-intuitive. Lower $\mathfrak{f}$(DG) are expected towards higher $N(\mathrm{H})_{\mathrm{tot}}$as the size of the CO zone shrinks towards lower clump sizes, while the widths of the C^+ and C^0 stay almost constant[xlix].

The comparison indicates that a [CII] excitation temperatures of 75 K (Cases II and IV) does not represent the real conditions in the positions discussed here. [CII] excitation temperatures of 200 K (Cases I and III) give similar $\mathfrak{f}$(DG) as expected by Wolfire, Hollenbach & McKee (2010). Therefore these T_{ex}([CII]) might be a better estimation for the clouds in M33. In this case, the fraction of CO dark H_2 increases towards lower metallicities. Furthermore, the study indicates that the major fraction of CO dark H_2 in M33, ∼90 %, is traced by C^+, while C^0 traces only a minor fraction. These values relate to the total emission. The spectral distribution of CO dark H_2 will be discussed in Section 7.5.2.

7.2.9 FRACTION OF MOLECULAR GAS IN M33

The fraction of the molecular hydrogen is defined via

$$f(\mathrm{H_2}) = \frac{2\times N(\mathrm{H_2})}{2\times N(\mathrm{H_2})_{\mathrm{tot}} + N(\mathrm{H^0})} \tag{7.15}$$

$$= 1 - \frac{N(H^0)}{N(\mathrm{H})_{\mathrm{tot}}} \tag{7.16}$$

The H_2 fractions are listed in table 7.15. The calculations show that the major fraction of the hydrogen in the positions discussed here is molecular.. The H_2 fraction is on average $\gtrsim$70 % in all cases with the lowest $f(\mathrm{H_2})$ (case IV, $f(\mathrm{H_2})$∼0.7). The highest $f(\mathrm{H_2})$ are derived for the cases I and III with an average $f(\mathrm{H_2})$∼0.90 over the positions in which [CII] was detected. The $N(\mathrm{H^0})$ are roughly constant for the all clouds[l]. Therefore, the total hydrogen column densities and, hence, the fraction of H_2 are directly correlated to the total molecular hydrogen column densities (c.f Equation (7.16)). Hence, the position GMC01 peak has the highest $f(\mathrm{H_2})$ in all cases ($f(\mathrm{H_2})$∼0.95), while the position GMCno06 B has the lowest $f(\mathrm{H_2})$ of ∼0.5 to 0.65.

xlix For further details see Section 2.2.3.
l see Section 7.2.1

	Fraction of H_2, $f(H_2)$			
	Case I	Case II	Case III	Case IV
BCLMP691	0.82±0.22	0.78±0.11	0.86±0.18	0.69±0.17
GMC91	0.80±0.25	0.70±0.15	0.70±0.16	0.80±0.25
BCLMP302	0.82±0.22	0.59±0.10	0.81±0.22	0.61±0.14
GMC01 Peak	0.94±0.26	0.93±0.23	0.94±0.26	0.93±0.25
GMC01 Flank	0.92±0.23	0.86±0.17	0.92±0.24	0.87±0.20
GMCno06 A	0.90±0.28	0.87±0.12	0.93±0.19	0.65±0.17
GMCno06 B	0.48±0.31	0.62±0.26	0.65±0.23	0.42±0.34
mean	0.81±0.15	0.76±0.12	0.83±0.11	0.71±0.16
mean*	0.81±0.16	0.77±0.13	0.85±0.10	0.70±0.17
mean**	0.88±0.05	0.80±0.12	0.89±0.05	0.75±0.13

Table 7.15: Molecular hydrogen fractions given by the different carbon species. The average values over all positions are listed in the row marked by *mean*.
The row *mean** lists the average H_2 fractions over the clouds in which C^0 was detected (all positions excluding GMC91)
mean** shows the average H_2 fractions over the clouds in which [CII] was detected (excluding GMC91 and GMCno06 B)

7.3 H2 CONVERSION FACTORS

H_2–CO conversion factors are a common tool to estimate the H_2 column density from the observed integrated ^{12}CO line intensities . H_2–[CI](1–0) conversion factor are proposed as an alternative for the H_2–CO conversion factors (Offner et al. 2014; Lo et al. 2014; Glover et al. 2015; Glover & Clark 2015). This section aims to calculate H_2 –CO(2–1) and H_2 –[CI](1–0) conversion factors ($X_{CO(2-1)}$and X_{CI}) based on the derived total molecular hydrogen column densities and the observed integrated line intensities. H_2–[CII] conversion factors based on the total integrated [CII] emission and the $I([\mathrm{CII}])_{H_2}$ from the molecular phase will be also be calculated (Section 7.3.1). These conversion factors will be compared to established conversion factors as well as to theoretical predictions (Section 7.3.2). I would like to refer to Section 4.8 for the the explanation of the theoretical background of the H_2 conversion factors.

7.3.1 H2 CONVERSION FACTORS OF THE OBSERVED INTEGRATED LINE INTENSITIES OF CO(2–1), [CI](1–0) AND [CII]

The H_2–line conversion factor can be calculated from the derived total molecular hydrogen column density and the integrated line intensity via [li]

$$X_{\mathrm{line}} = \frac{N(\mathrm{H_2})_{\mathrm{tot}}}{I(\mathrm{line})} \tag{7.17}$$

I also consider the upper and lower H_2 column densities of the discussed cases in the observed clouds, to determine the upper and lower limits of the conversion factors.

li Derived from Equation (4.24); $N(\mathrm{H_2}) := X_{\mathrm{CO}} \times I(\mathrm{CO}(1-0))$

The H_2–CO(2–1) conversion factors vary between $X_{\mathrm{CO(2-1)}}$=1 and 20 $\times$ 10^{20} s cm^{-2} K^{-1} km^{-1} with a mean value of $\langle X_{\mathrm{CO(2-1)}} \rangle$~3 as lower limit and ~15 s cm^{-2} K^{-1} km^{-1} as an upper limit.

The H_2–[CI](1–0) conversion factor vary between X_{CI}=0.5 to 14 $\times$ 10^{21} s cm^{-2} K^{-1} km^{-1} with a mean between $\langle X_{\mathrm{CI}} \rangle$~2 to 9 $\times$ 10^{21} s cm^{-2} K^{-1} km^{-1}

The [CII] emission arises from different gas phases, not only from molecular gas. Therefore, two H_2–[CII] conversion factors are calculated. One conversion factor is based on the total observed integrated [CII] intensity, $X_{\mathrm{CII_{tot}}}$. The other one is based on the [CII] emission that arises from the molecular phase $X_{\mathrm{CII_{H_2}}}$. The H_2–[CII]$_{tot}$ conversion factors based on the total integrated [CII] intensity varies between $X_{\mathrm{CII_{tot}}}$=0.6 and 6 $\times$ 10^{20} s cm^{-2} K^{-1} km^{-1} with a mean between $\langle X_{\mathrm{CII_{tot}}} \rangle$~1.3 and 5.5 $\times$ 10^{20} s cm^{-2} K^{-1} km^{-1}. The [CII] emission that arises from the molecular phase gives $X_{\mathrm{CII_{H_2}}}$ between 5 and 15 $\times$ 10^{21} s cm^{-2} K^{-1} km^{-1} with a mean of ~7 to 8 $\times$ 10^{21} s cm^{-2} K^{-1} km^{-1}.

The upper and lower limits of the conversion factors for the individual positions as well as the average over all positions are listed in Table 7.16. An illustration of the different H_2 conversion factors is shown in Figure 7.9.

The derived conversion factors will be compared with established and proposed conversion factors in the following section.

7.3.2 ESTABLISHED H_2 CONVERSION FACTORS

The following paragraphs discuss established H_2 conversion factors. I will give a summary of the H_2 conversion factors for CO discussed by Wilson (1995), Bolatto et al. (2013) and Israel (1997) as well as H_2–[CI] (1–0) conversion factors proposed by Offner et al. (2014) and Glover & Clark (2015) for a half solar metallicity, Z=0.5$Z_{\odot}$. Afterwards, I will determine these conversion factors for the positions discussed here. For further details on these conversion factors, please refer to Section 4.8.

7.3.2.1 H_2–CO conversion factors

Within uncertainties of ~30%, a $X_{\mathrm{CO(1-0)}}$=2$\times$$10^{20}$ cm^{-2} K km s^{-1} is established for the ^{12}CO(1–0) line in the Milky Way (Bolatto, Wolfire & Leroy 2013; cf. Section 4.8). In a low metallicity environment such as M33, the H_2–CO conversion factor is, in general, higher compared to the value found in the Milky Way. In the first place, the H_2–CO conversion at different metallicities can be approximated via equation (4.25)[lii]. In the case of M33, this equation gives a conversion factor of X_{CO}= 4 $\times$ 10^{20} cm^{-2}, a factor two times higher compared to the value in the Milky Way. Equation 4.25 gives, thus, a constant $X_{\mathrm{CO(1-0)}}$ of 4 $\times$ 10^{20} cm^{-2} for ^{12}CO(1–0) in a half solar metallicity environment.

It is adequate to adopt a H_2–CO(1–0) conversion factor for the ^{12}CO(2–1) transition. CO(2–1) observations are available for all positions discussed here. In addition its beam size matches roughly those of the [CI](1–0) and [CII] observations. The H_2–CO(1–0) conversion factor can be transformed

lii $X_{\mathrm{CO}\,Z} = \frac{X_{\mathrm{CO}\odot}}{Z}$

(1)	(2)		(3)		(4)		(5)	
	$X_{\mathrm{CII_{tot}}\,x_C}$		$X_{\mathrm{CII_{H2}}\,x_C}$		$X_{\mathrm{CI}\,x_C}$		$X_{\mathrm{CO}\,x_C}$	
	upper limit 10^{20} $\frac{s}{\mathrm{Kkmcm^2}}$	lower limit 10^{20} $\frac{s}{\mathrm{Kkmcm^2}}$	upper limit 10^{20} $\frac{s}{\mathrm{Kkmcm^2}}$	lower limit 10^{20} $\frac{s}{\mathrm{Kkmcm^2}}$	upper limit 10^{21} $\frac{s}{\mathrm{Kkmcm^2}}$	lower limit 10^{21} $\frac{s}{\mathrm{Kkmcm^2}}$	upper limit 10^{20} $\frac{s}{\mathrm{Kkmcm^2}}$	lower limit 10^{20} $\frac{s}{\mathrm{Kkmcm^2}}$
BCLMP691	4.6±1.1	1.1±0.3	8.3±1.9	6.1±1.3	8.4±1.9	2.0±0.41	14.2±3.3	3.4±0.7
GMC91	–	–	–	–	–	–	3.2±0.7	1.5±0.3
BCLMP302	5.6±1.3	1.0±0.2	7.6±1.8	6.8±1.4	5.9±1.4	1.0±	11.2±2.6	1.9±0.4
GMC01 Peak	5.8±1.3	2.3±0.5	7.5±1.7	4.2±0.9	13.8±3.1	5.3±2.38	17.6±4.0	6.8±1.5
GMC01 Flank	5.8±1.2	1.6±0.3	8.6±1.8	4.9±0.9	7.6±1.6	2.2±1.61	14.3±3.0	4.0±0.8
GMCno06 A	5.3±1.4	0.6±1	7.4±1.9	15.7±3.7	5.7±1.5	0.6±0.2	17.2±4.4	1.8±0.4
GMCno06 B	–	–	–	–	1.3±0.8	0.5±0.4	3.1±1.8	1.2±0.9
mean	–	–	–	–	–	–	11.5±5.7	2.9±1.8
mean*	–	–	–	–	8.3±2.9	1.9±1.7	12.9±4.9	3.2±1.9
mean**	5.4±0.5	1.3±0.6	7.9±0.5	7.2±4.5	8.9±3.0	2.2±1.7	14.9±2.3	3.6±1.8

Table 7.16: H_2 conversion factors for the integrated line intensities of CO(2–1), [CI](1–0) and [CII]. The values are based on the molecular hydrogen column densities that are listed in Table 7.13. The mean values of the conversion factors at the end of the list refer to all positions in which the specific line was detected. The mean* considers all positions in which [CII] was detected, the position GMC91 and GMCno06 B are excluded.

$X_{\mathrm{CII_{tot}\,x_C}}$ 10^{20} $\frac{\mathrm{s}}{\mathrm{Kkmcm^2}}$	$X_{\mathrm{CII_{H2}\,x_C}}$ 10^{20} $\frac{\mathrm{s}}{\mathrm{Kkmcm^2}}$	$X_{\mathrm{CI_{x_C}}}$ 10^{21} $\frac{\mathrm{s}}{\mathrm{Kkmcm^2}}$	$X_{\mathrm{CO_{x_C}}}$ 10^{20} $\frac{\mathrm{s}}{\mathrm{Kkmcm^2}}$
$3.3\pm^{2.5}_{2.6}$	$7.7\pm^{0.7}_{4.4}$	$4.5\pm^{6.3}_{4.2}$	$7.2\pm^{10.0}_{6.1}$

Table 7.17: Mean $I(\mathrm{CO}(2\text{–}1))$, $I([\mathrm{CI}](1\text{–}0))$, $I([\mathrm{CII}])$ and $I([\mathrm{CII}])_{\mathrm{H_2}}$ conversion factors

(1)		(2)
		$X_{\mathrm{CO}\,L_{\mathrm{TIR}}}$
	L_{TIR}	$X_{\mathrm{CO(2-1)}}$
	10^6	10^{20}
	$L_\odot$	$\frac{\mathrm{s}}{\mathrm{cm^2\ K\ km}}$
BCLMP691	1.7	2.5
GMC91	1.3	1.9
BCLMP302	2.0	2.9
GMC01 Peak	5.9	8.6
GMC01 Flank	5.9	8.6
GMCno06 A	3.1	4.5
GMCno06 B	3.1	4.5
Mean⋆		4.1±2.4

Table 7.18: L_{TIR}, $X_{\mathrm{CO(2-1)}}$ and H_2 column densities derived from CO(2–1). The Mean⋆ represents the mean value of the conversion factor as function of L_{TIR} whereby the conversion factors of the positions GMC01 Flank and GMCno06 B have not been considered. The conversion factor at these positions are based on the same L_{TIR} as used in GMC01 Peak and GMCno06 A therefore are no independent variables.

to a H_2–CO(2–1) via the ratio of the integrated CO(2–1) and ^{12}CO(1–0) line intensities, $I(\mathrm{CO}(2\text{–}1))/I(\mathrm{CO}(1\text{–}0))$. Druard et al. (2014) observed an almost constant CO(2–1)/CO(1–0) integrated line intensity ratio of 0.80 in M33[liii] This $I(\mathrm{CO}(2\text{–}1))/I(\mathrm{CO}(1\text{–}0))$ ratio gives a $X_{\mathrm{CO(2-1)}}= 5.0 \times 10^{20}\ \mathrm{cm^{-2}}$ for M33.

7.3.2.2 H_2–CO conversion factor as a function of L_{TIR}

Israel (1997) proposed to use a CO-H_2 conversion factor that correlates with the far-infrared surface brightness in a low metallicity environment (cf. Section 4.8).

According to Israel (1997), the H_2-^{12}CO(1–0) conversion factor in a half solar metallicity environment is given by[liv]

$$X_{\mathrm{CO}} = 1.17 \times 10^{20} \frac{L_{\mathrm{TIR}}}{10^6 \times L_\odot} \left[\mathrm{cm^{-2}K^{-1}km^{-1}}\right] \tag{7.18}$$

liii The mean CO(2–1) v.s CO(1–0) integrated line intensity ratio is 0.85±0.38, in the positions.

liv See Section 4.7 as well.

Equation (7.18) can be adopted to a H_2–CO(2–1) conversion factor by the use of an assumed constant I(CO(2–1))/I(CO(1–0))=0.8 (Druard et al. 2014) (cf. Section 7.3.2.1)

$$X_{\mathrm{CO(2-1)}} = 1.46 \times 10^{20} \frac{L_{\mathrm{TIR}}}{10^6 \times L_\odot} \tag{7.19}$$

The used far–infrared surface brightness L_{TIR} for the individual positions regions were obtained from Boquien et al. (2011). The used L_{TIR} and the derived $X_{\mathrm{CO(2-1)}}$ are listed in Table 7.18. The derived conversion factors vary between $X_{\mathrm{CO(2-1)}}$~2 and 9 × 10^{20} s cm^{-2} K^{-2} km^{-1} with a mean value of $\langle X_{\mathrm{CO(2-1)}}\rangle$=4.2±2.4. Within the uncertainties, the derived $\langle X_{\mathrm{CO\ TIR}}\rangle$ is identical to the 'constant' conversion factor derived in Section 7.3.2.1.

7.3.2.3 H_2–[CI](1–0) conversion from simulations

H_2-[CI](1–0) conversion factors for M33 are already discussed in Section 4.8.

Glover & Clark (2015) calculated H_2-[CI](1–0) conversion factor of $X_{\mathrm{CI}\ 0.5Z}$ ~0.3 ×10^{22} s cm^{-2} K^{-1} km^{-1} for G_0=10 and a $X_{\mathrm{CI}\ 0.5Z}$ ~0.5 ×10^{22} s cm^{-2} K^{-1} km^{-1} for G_0=100. Note that the sources in M33 are penetrated by radiation fields of G_0~15 to 50. (cf. Table 7.7).

7.3.3 COMPARISON OF THE H_2 CONVERSION FACTORS AND SUMMARY

This section compares the different H_2 conversion factors that were calculated in the previous sections. The H_2 conversion factors and their mean values for the individual positions are illustrated in Figure 7.9.

As demonstrated in Figure 7.9, the derived $X_{\mathrm{CO(2-1)}}$ and X_{CI} match the 'established' conversion factors within the uncertainties.

The H_2–CO(2–1) conversion factors ($X_{\mathrm{CO(2-1)}}$~4×10^{20} K^{-1} km^{-1} cm^{-2}) are at the lower edge of the CO(2–1) conversion factors derived from the line observations presented here. This corresponds to the conversion factors derived from the cases II and IV ($X_{\mathrm{CO(2-1)}}$~3×10^{20} K^{-1} km^{-1} cm^{-2}). In these cases, the carbon in the molecular phase is dominated by CO in the majority of the positions (cf. Table 7.12). The conversion factors derived for the upper column densities ($X_{\mathrm{CO(2-1)}}$~15×10^{20} K^{-1} km^{-1} cm^{-2}) are almost 2 to 4 times higher than the mean values from literature. In these cases, the carbon in the molecular phase is dominated by C^+(Table 7.12). This could indicate that the $N(H_2)$ are overestimated in the cases I and III, or vice versa that the established H_2 conversion factors tend to underestimate the H_2 column densities at low metallicities.

The averaged CO(2–1)-H_2 conversion factors by Israel (1997) are equal to the conversion factor derived in Section 7.3.2.1. Both H_2-CO(2–1) conversion factors have mean values of ~4×10^{20} s K^{-1} km^{-1} cm^{-2} in M33. The individual CO(2–1) conversion factors based on Israel (1997) have a higher correlation with the $X_{\mathrm{CO(2-1)}}$ derived from the observations, compared to the constant conversion factors. In the positions GMC91 and GMC01 Peak, the conversion factor based on Israel (1997) lies within the

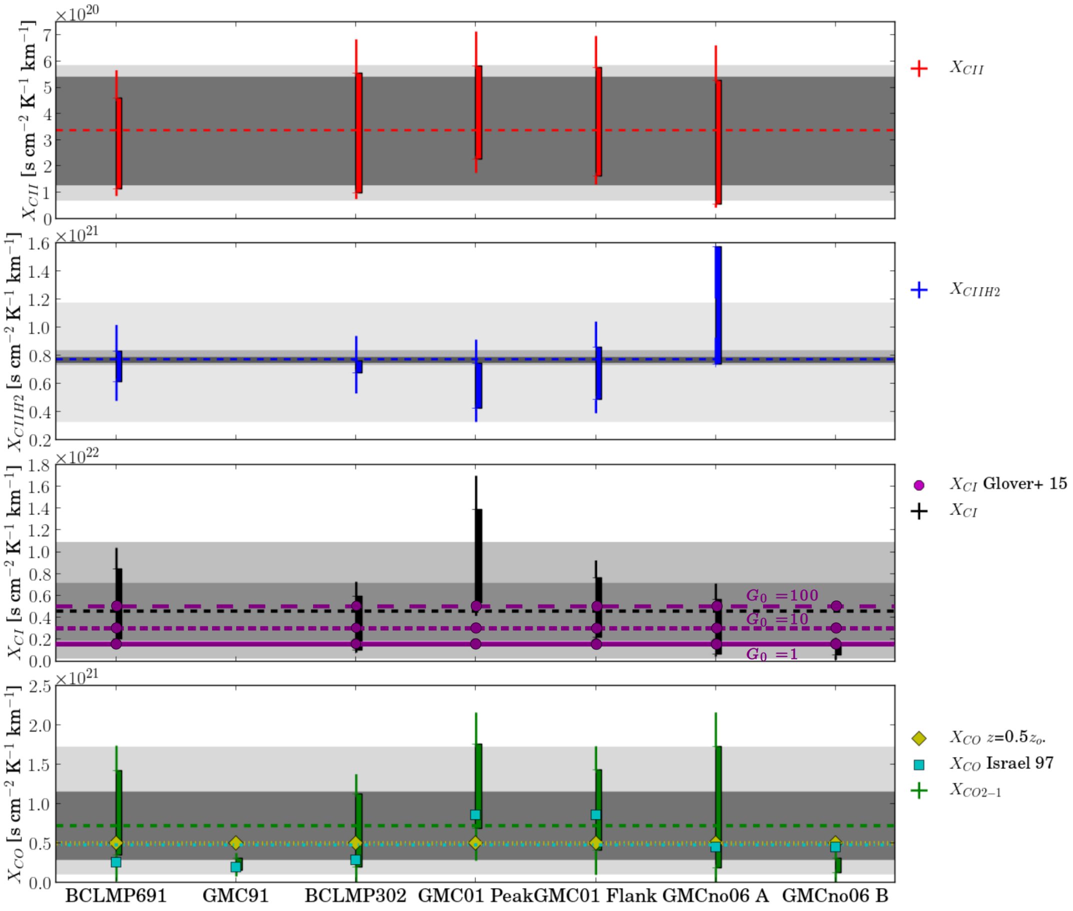

Figure 7.9: Comparison of different H_2 conversion factors for the integrated CO(2–1), [CI](1–0) emission as well as the total [CII] emission and the [CII] emission arising from the molecular phase in the individual positions.
Top: H_2-[CII] conversion factors: The red bars show the range between the upper and lower limits of the conversion factors. The uncertainties are shown by the thin errorbars. The dark gray area shows the range of the possible mean values for the conversion factors. The light grey area at the top and button shows the maximal range of the standard deviation around the mean values.
Upper Middle: H_2-[CI](1–0) conversion factors from the [CII] emission in the molecular phase.
Lower Middle: The black bars mark the $X_{[\mathrm{CI}](1-0)-\mathrm{H}_2}$ derived in Section 7.3.1 Its mean value is shown by the black dashed- line (– –). The magenta • and the magenta lines show the [CI](1–0)-H_2 conversion factor derived by Glover & Clark (2015) for different strengths of the radiation field, (— for G_0=1, ··· for G_0=10 and - - - for G_0=100).
Bottom: CO(2–1)-H_2 conversion factors derived from the total CO(2–1) emission (green bars). The mean value is shown by the green dashed line (– – –). Cyan ■ marks the conversion factors derived with Eq. (7.19) as function of the L_{TIR}. The mean value over all positions is shown by the dashed cyan line (– –). The yellow ♦ and the solid line (—) show the expected 'constant' $X_{\mathrm{CO}(2-1)-\mathrm{H}_2}$ for a z=0.5$z_\odot$ derived with Eq. (4.25).

limits of the conversion factors derived from the observations which does not apply for the constant conversion factor from Section 7.3.2.1.

The H_2–[CI](1–0) conversion factors by Glover & Clark (2015) for G_0=10 to G_0=100 are consistent with the conversion factors derived from the observed integrated [CI](1–0) line intensities of $X_{\mathrm{CI}}\sim 2$ to 9×10^{21} s K^{-1} km^{-1} cm^{-2}. This indicates that a H_2–[CI](1–0) conversion factor could be a reliable tool to calculate the amount of H_2 at Z=0.5$Z_\odot$.

The H_2–[CII] conversion factors are relatively constant in all positions. I derived a $X_{\mathrm{CII_{tot}}}\sim 5.5 \times 10^{20}$ s K^{-1} km^{-1} cm^{-2} based on the total integrated [CII] emission and a $X_{\mathrm{CII_{H_2}}}\sim 1.3 \times 10^{20}$ s K^{-1} km^{-1} cm^{-2}. It would be worth to investigate if similar [CII] conversion factors can be found in other sources as well. If this is the case, a $[\mathrm{CII}]_{tot}$-H_2 conversion factor, or at least a $[\mathrm{CII}]_{\mathrm{H_2}}$-$H_2$[lv] could be an additional, reliable tool to estimate the amount of H_2 in galaxies. This idea is similar as those of Madden et al. (e.g. 2011) who proposed a H_2 to (CO+[CII]) conversion factor for low metallicity galaxies.

7.4 RADIAL DISTRIBUTION OF THE HYDROGEN AND CARBON COLUMN DENSITIES AND OF THE RADIATION FIELD

This section investigates the radial distribution of carbon and hydrogen as function of the distance to the galactic centre of M33, R_{M33}. The radial distribution of CO dark H_2 is studied as well. The distances of the sources vary between R_{M33}~0.1 kpc (GMC01) an ~3.5 kpc (BLMCP691). All the distances are listed in Table 7.1. The observed radial distributions will be compared with results from Druard et al. (2014) and Tosaki et al. (2011) [lvi].

7.4.1 RADIAL DISTRIBUTION OF HYDROGEN COLUMN DENSITIES

Figure 7.10 illustrates the $N(\mathrm{H})$, $N(\mathrm{H}^0)$ and $N(\mathrm{H}_2)$ as function of R_{M33} for the different cases. The neutral hydrogen column densities remain almost constant over R_{M33}. The fit of $N(\mathrm{H}^0)$ with an exponential decay function[lvii] as function of R_{M33} implies a slight increase towards higher R_{M33} (cf. Table 7.19 and Figure 7.10). The fit gives a negative scale length of $l_e\approx$-5.8±4.7 kpc. These observations can be explained by an almost constant amount of H^0 in the neutral phase between the ionised and molecular phase. The result is consistent with previous studies by Druard et al. (2014) and Tosaki et al. (2011). They haven't found any significant radial distribution for HI.

The molecular hydrogen column densities become lower along R_{M33} in all the cases and, therefore, the total hydrogen column densities $N(\mathrm{H})$ lowers as well. The fit to $N(\mathrm{H}_2)$ with an exponential decay function gives an exponential scale lengths of $l_e\approx$ 2.4±1.5 kpc in case III to 1.4±0.7 kpc in case IV. The fit to $N(\mathrm{H})$ gives exponential scale length between $l_e\approx$ 2.9±1.9 kpc (case III) and 1.9±1.0 (case IV). The precise fit results are summarised in Table 7.19. The scale length of the total hydrogen column densities are of the order of the scale length found by Druard et al. (2014). They found a scale lengths of $\langle l_e(N(\mathrm{H}))\rangle$=2.2 kpc for the inner 3.5 kpc of M33. The calculations imply that the overall mass of the GMCs decreases towards larger distances to the galactic centre of M33, in particular the mass and the size of the inner regions of the GMCs, in which the hydrogen is molecular.

---

lv Additional NII205μm or NII122μm or at least HII and HI data would be required to calculate $X_{\mathrm{CII_{H_2}}}$ conversion factor.

lvi Druard et al. (2014) and Tosaki et al. (2011) investigated the radial distribution of H^0 and H_2 based on HI , CO maps (J=1–0 and 2–1 respectively).

lvii $N(\mathrm{H}^0)=a\times e^{-\varrho_{\mathrm{d}} R_{\mathrm{M33}}}$

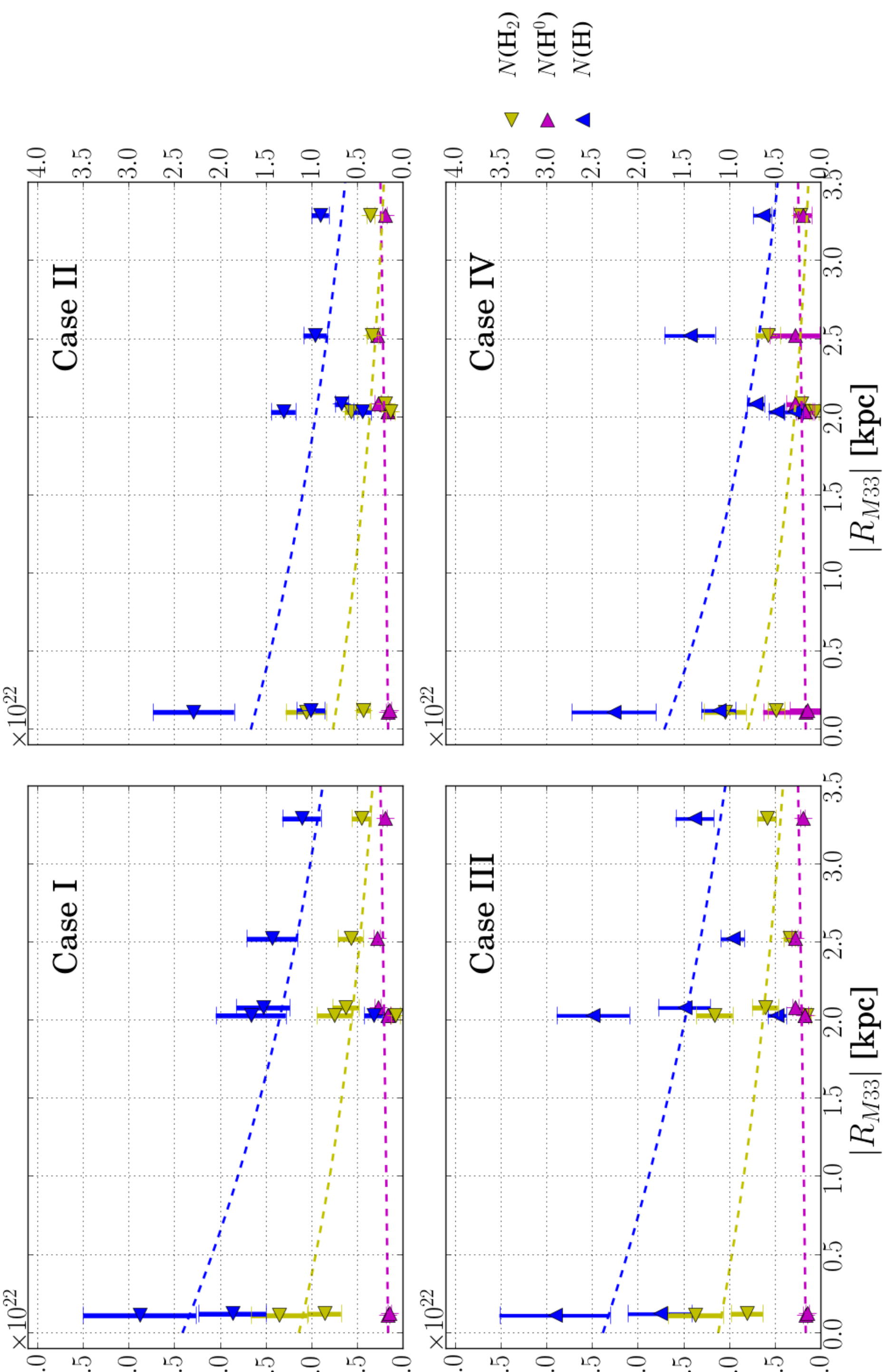

Figure 7.10: Derived fraction of molecular hydrogen as function of the radial distance to the centre of M33, R_{M33} in the Cases I, II, III and IV. Southern positions (negative distances in Table 7.1) are plotted at positive distances as well. The magenta dashed lines (– – –) illustrate the radial distribution of $N(\mathrm{H}^0)$. The yellow – – – show the $N(\mathrm{H}_2)$ and the blue – – – show the radial distribution of the total hydrogen column densities $N(\mathrm{H})= N(\mathrm{H}^0)+2\times N(\mathrm{H}_2)$.

	a 10^{21} [cm^{-2}]	$\varrho_{\rm d}$ [kpc^{-1}]	$l_{\rm e}$ [kpc]	a 10^{21} [cm^{-2}]	$\varrho_{\rm d}$ [kpc^{-1}]	$l_{\rm e}$ [kpc]
		Case I			Case II	
$N(\mathrm{H}^0)$	1.6±0.2	-0.12±0.10	-5.8±4.7	1.6±0.2	-0.12±0.10	-5.8±4.7
$N(\mathrm{H}_2)$	11.4±1.8	0.35±0.13	2.0±0.8	7.7±2.0	0.37±0.14	1.9±0.7
$N(\mathrm{H})$	24.1±3.6	0.29±0.17	2.4±1.4	16.6±4.1	0.28±0.18	2.5±1.6
		Case III			Case IV	
$N(\mathrm{H}^0)$	1.6±0.2	-0.12±0.10	-5.8±4.7	1.6±0.2	-0.12±0.10	-5.8±4.7
$N(\mathrm{H}_2)$	11.2±2.9	0.19±0.17	2.5±1.5	8.0±2.1	0.51±0.25	1.4±0.7
$N(\mathrm{H})$	23.8±5.7	0.24±0.15	2.9±1.9	17.1±4.4	0.37±0.20	1.9±1.0

Table 7.19: Fit parameters of for the radial distribution of $N(\mathrm{H}^0)$, $N(\mathrm{H}_2)$ and $N(\mathrm{H})$. These column densities were fitted with an exponential decay function, $N(\mathrm{H}) = a \times e^{-\varrho_{\rm d} R_{\rm M33}}$. The specific scale lengths $l_{\rm e}$ is calculated from the exponential decay constant $\varrho_{\rm d}$ via $l_{\rm e}$= ln(0.5)/(-$\varrho_{\rm d}$).

	a	m [kpc^{-1}]	a	m [kpc^{-1}]
	Case I		Case II	
$N(\mathrm{C}^+)/N(\mathrm{C})$tot	0.70±0.06	0.00±0.03	0.48±0.04	0.08±0.02
$N(\mathrm{C}^0)/N(\mathrm{C})$tot	0.07±0.07	0.00±0.01	0.06±0.01	-0.0±0.02
$N(\mathrm{CO})/N(\mathrm{C})$tot	0.24±0.08	0.00±0.04	0.45±0.19	0.12±0.08
	Case III		Case IV	
$N(\mathrm{C}^+)/N(\mathrm{C})$tot	0.70±0.11	-0.06±0.05	0.07±0.09	0.01±0.03
$N(\mathrm{C}^0)/N(\mathrm{C})$tot	0.06±0.02	0.01±0.06	0.07±0.01	0.01±0.04
$N(\mathrm{CO})/N(\mathrm{C})$tot	0.23±0.14	0.06±0.05	0.48±0.90	0.07±0.03

Table 7.20: Parameters from fitting the relative fractions of the C^+,C^0 and CO column densities to the total carbon column density as function of $R_{\rm M33}$ in the Cases I, II, III and IV. The fractions in which fitted with a linear function $N(\mathrm{X})/N(\mathrm{C})$tot=$a$+$m\times$ $R_{\rm M33}$. Positions which show no [CII] emission were not considered in the fit (positions GMC91 and GMCno06 B)

7.4.2 RADIAL DISTRIBUTION OF RELATIVE CARBON FRACTIONS

Figure 7.11 shows the radial distribution of the fraction of the specific carbon column densities in the molecular phase to the total carbon column densities in the molecular phase, $N(\mathrm{CO}/\mathrm{C}^0/\mathrm{C}^+)_{\mathrm{H}_2}/N(\mathrm{C})_{\mathrm{H}_2}$.

The fractions of all lines do not show any favourite gradient along $R_{\rm M33}$ in case I. The fraction of all species stays almost constant. In all other cases, the fraction of CO shows a trend to higher relative fraction towards higher $R_{\rm M33}$, while the fraction of C^+ decreases. In case II, a constant distribution of C^+ is possible within the uncertainties. The fraction of C^0 doesn't show any significant gradient along $R_{\rm M33}$ in all the cases. Linear fits to the relative carbon fractions are listed in table 7.20.

The results will be discussed in detail at the end of this section. At first, I will discuss the radial distribution of CO dark H_2.

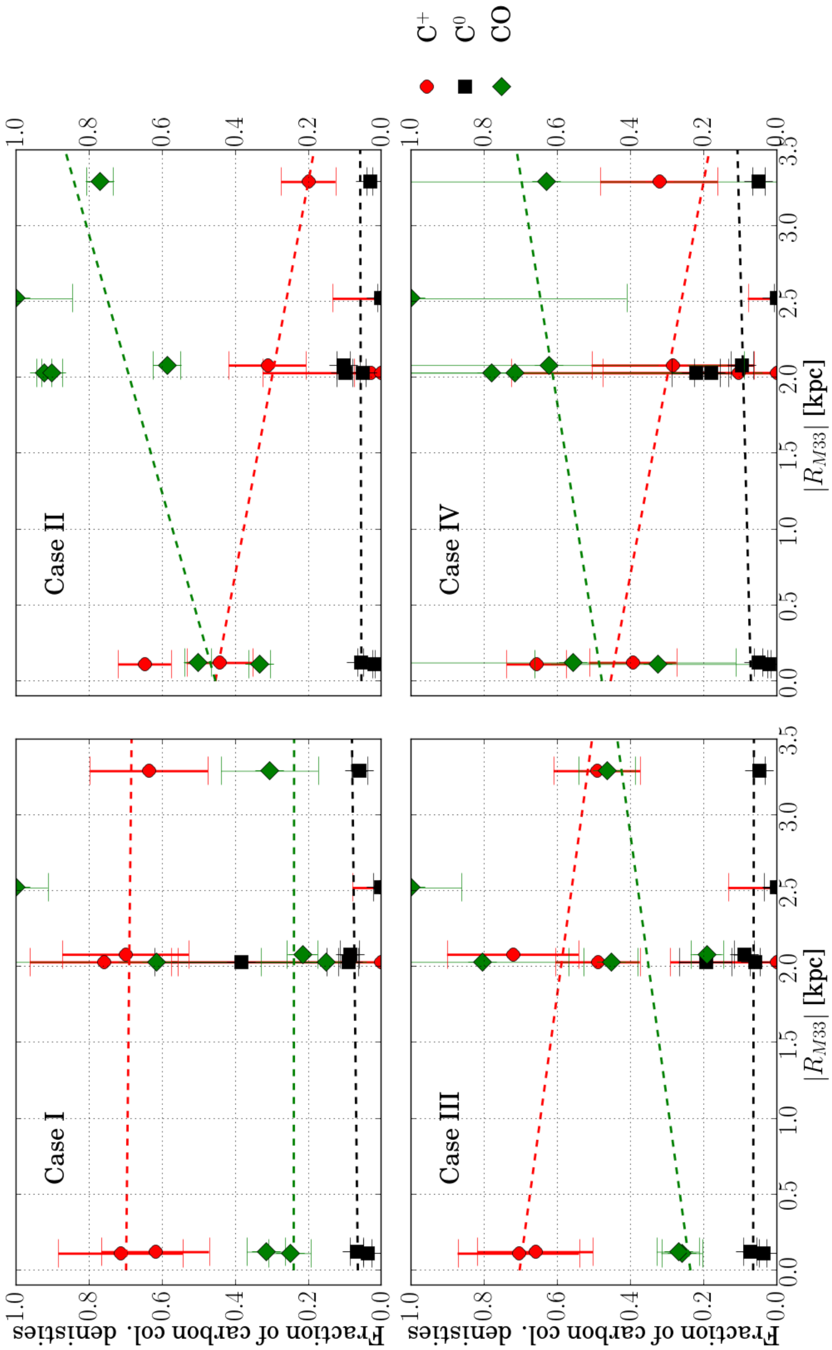

Figure 7.11: Derived relative fractions of the C^+, C^0 and CO column densities to the total $N(C)$ in all discussed cases plotted as function the radial distance to the centre of M33, R_{M33}. Southern positions (negative distances in Table 7.1) are plotted at positive distances as well. The solid line shows the linear fit though the positions in which [CII], [CI](1–0) and CO(2–1) were detected.

7.4.3 RADIAL DISTRIBUTION OF THE CO DARK H_2

In general, the radial distribution of $\mathfrak{f}$(DG) is similar to distribution of C^+. C^+ traces most of it. The radial distributions of CO dark H_2 fractions relative to the total amount of H_2 are shown in Figure 7.12. The $\mathfrak{f}$(DG) shows no distinctive radial gradient in case I, within the uncertainties. In all other cases, the $\mathfrak{f}$(DG) decreases towards larger R_{M33}. A positive gradient can not be excluded for the case III within the uncertainties. The $\mathfrak{f}$(DG) has a scale lengths of $l_{\mathrm{e}}{\approx}21$ in case I. The scale lengths is $\sim$1.5 in the cases II and IV, and $\sim$7 in the case III.

7.4.4 DISCUSSION OF THE RADIAL DISTRIBUTIONS

The decrease of $N(\mathrm{H_2})$ and $N(\mathrm{H})_{\mathrm{tot}}$ as well as the relative constancy of $N(\mathrm{H}^0)$ found along the galactic radius of M33 is expected. In a galactic disc, the average mass surface density decreases towards higher galactic distances (e.g. Schmidt 1985). On the other hand, the radial distribution of the carbon species is surprising. The C^+ fraction shows a decrease towards larger R_{M33} while the fraction of CO increases (cases II, III and IV) (or both fractions stay constant, case I). The radial distributions in the cases II, III and IV are hard to reconcile with the standard picture of PDRs and the mass distribution of molecular gas in galaxies. The size of the CO core should lower towards a lower clump mass surface densities, while the size of the C^+ layers in the molecular phase should almost stay constant[lviii]. Therefore, an increase of the C^+ and CO dark H_2 fraction as well as a decrease of the CO fraction would have been expected. Such a distribution was found in the Milk Way by the GOT C^+ project Langer et al. (2014b). They found an increase of the CO dark H_2 fraction towards larger distances to the galactic centre. The increase can be described by a linear fit with a slope of $\sim$0.03 $\mathfrak{f}$(DG)/kpc.

The observed radial distribution of the carbon species allow two different explanations.

A possible explanation is, that the case I (and maybe case III) provides a reliable description of the physical conditions in the positions, discussed here. The amount of C^+ is underestimated in the cases II and IV. This explanation is consistent with the conclusion drawn in Section 7.2.8[lix].

On the other hand, the observations could be explained by a gradient of the ambient radiation field along R_{M33}. The penetration depth of the FUV radiation into a clump is lower at a fainter UV radiation. This gives a a narrower C^+ layer in the molecular phase. Finally this leads to a higher fraction of CO towards larger distances to the centre of M33. Observations show a decrease of the L_{TIR} towards higher R_{M33} (cf. Figure 7.6; Boquien et al. 2011). L_{TIR} is proportional to the ambient FUV field, in a first approximation[lx]. Therefore, the ambient radiation field lowers towards larger R_{M33} as well. The radial distribution of G_0 is illustrated in Figure 7.13. The radial distribution of G_0 has a scale lengths of $l_{\mathrm{e}}(G_0){\approx}1.7$ kpc. This scale lengths are lower than the scale lengths of

lviii The effect of different clump sizes and mass surface densities is described in Section 2.2.3 and is illustrated in Figure 2.7.

lix I compared the CO dark H_2 fraction with the predictions of the PDR-model by Wolfire, Hollenbach & McKee (2010)

lx cf. Section 4.5; $G_0 = 4\pi 0.5 L_{\mathrm{TIR}}$

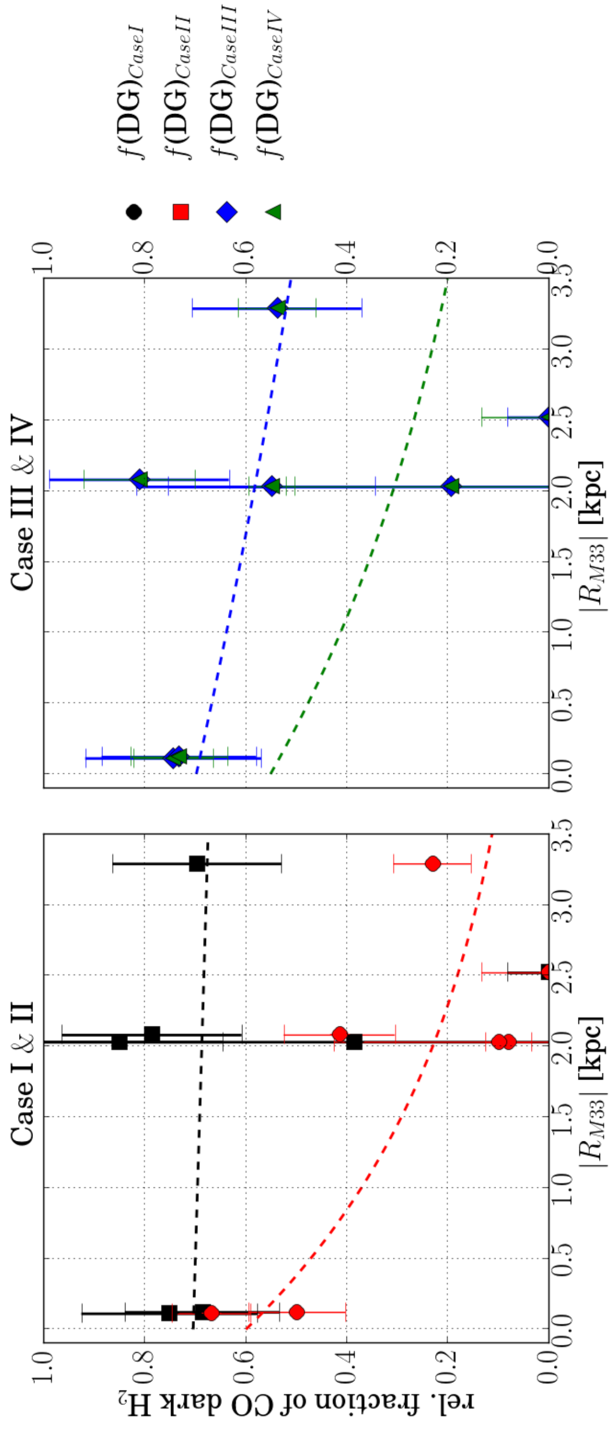

Figure 7.12: Derived CO dark H_2 fraction as function of the radial distance to the centre of M33, R_{M33}. Southern positions (negative distances in Table 7.1) are plotted at positive distances as well. The solid line shows the linear fit to the f(CO dark H_2).

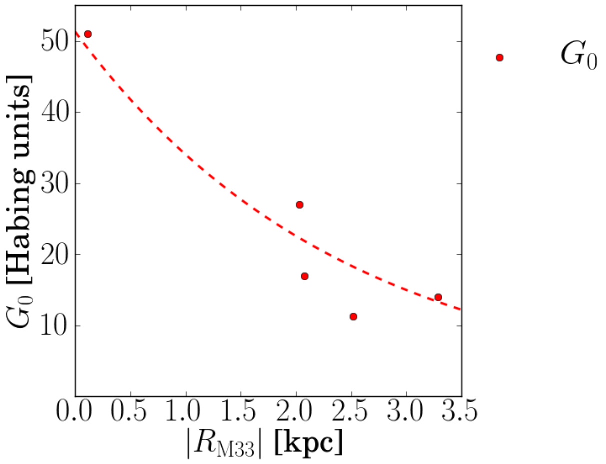

Figure 7.13: Radial distribution of G_0 in the observed positions as function of $R_{\rm M33}$. The G_0 were calculated from the $L_{\rm TIR}$ (Boquien et al. 2011) via the relation G_0=4 π 0.5 $L_{\rm TIR}$. The red dotted line shows the exponential fit to the G_0.

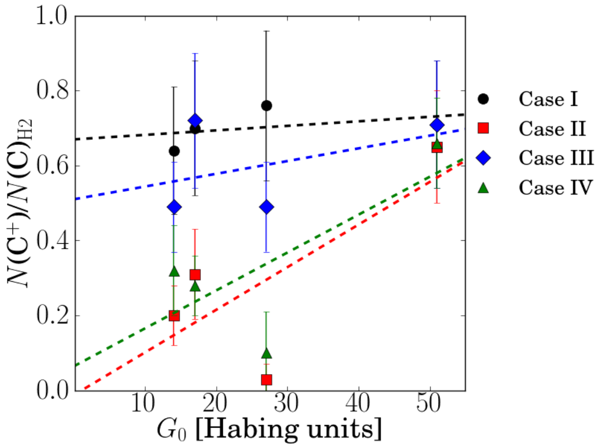

Figure 7.14: $N(\mathrm{C}^+)$ as function of G_0 in the Cases I (●), II (■), III (blue ♦) and IV (▲). The dashed lines show the linear fits to $N(\mathrm{C}^+)$.

N(H) (Table 7.19). This means that the strength of the ambient UV–field decreases more along $R_{\rm M33}$ compared to the total hydrogen column densities. Therefore, the FUV radiation has a lower penetration depths at higher $R_{\rm M33}$. The width of the C^+ layer in the molecular phase lowers faster than the size of the CO core towards higher $R_{\rm M33}$ and, thus, the fraction of C^+ relative to those of CO as well. This might be another explanation for the observed radial distributions of the carbon species. The fraction of C^+ as function of G_0 is illustrated in Figure 7.14.

In summary, the molecular hydrogen densities decrease towards larger distances to the galactic centre. The fraction of C^0 shows no radial distribution in M33. The radial distributions of C^+ (in the molecular phase) and CO and $\mathfrak{f}$(DG) in case I, are roughly consistent with the expectations for GMCs with a decreasing column density towards larger $R_{\rm M33}$. The fraction of C^+ and CO remains constant along $R_{\rm M33}$ in this case. This distribution is consistent with observations in the Milky Way by Langer et al. (2014b) as well. The fraction of C^+ decreases while the fraction of CO increases towards larger distances to the galactic centre. In general, this can be explained by the decrease of the ambient radiation field towards larger $R_{\rm M33}$.

7.5 SPECTRAL DISTRIBUTION CARBON AND HYDROGEN

The calculations in the previous sections were based on line intensities that were integrated over the full velocity range of the lines. These intensities allowed to determine the total column densities of C^+, C^0, CO, $H^0$and H_2 , the total fraction of CO dark H_2 in the clouds. They also allowed to calculate H_2 conversion factors and to study the radial distribution of the gas. Spectral informations were not directly needed for these calculation.

The following section deals with the spectral distribution of C^+, C^0, CO in the molecular phase, as well as of the CO dark H_2. Spectral informations allow to study the kinematics within the clouds. They allow to investigate gas that arises from different regions within the clouds. Spectral informations allow to distinguish between different sources along the line of sight, which was for example the case in GMCno06. The spectral information allowed to distinguish between GMCno06 A and GMCno06 B. Spectral data allow to study the distribution of the different carbon species, and to allocate the position of CO dark H_2 in the clouds.

The following section discusses the velocity resolved distribution of the C^+, C^0 and CO column densities in the molecular phase of the Cases I , II, III and IV. The velocity resolved distribution of the CO dark H_2 gas, its relative fraction to the total H_2column densities and the fraction of molecular hydrogen in the observed positions is discussed as well. The discussion is restricted to the positions BCLMP691, BCLMP302, GMC01 Flank and GMCno06. For these positions, spectral resolved data for all carbon species is available.

The following analysis is based on spectra that are smoothed to velocity bins of dv=2 km/s width. This width provides an adequate signal to noise ratio and allows to study the spectral distribution of the different lines. The column densities of C^+, C^0, CO and H^0 are calculated with the same initial parameters (gas temperature, excitation temperature, critical densities etc.) as used for the Cases I, II, II, and IV (cf. Section 7.2). The specific lines trace from different regions in the clouds. I assume that the physical conditions within these regions are roughly constant, as otherwise different line transitions would be observed. In the following analysis, only velocity bins with a S/N≥1 were considered. A problem of this method is the quality of the individual line spectra. The [CI](1–0) spectra have a higher RMS compared to the [CII] and CO observations. Therefore, the spectral distribution of C^0 is concentrated on the bins around the specific line peak of the [CI](1–0) observations.

At first I will discuss the spectral distribution of the C^+, $C^0$and CO column densities (Section 7.5.1). The velocity resolved distribution of CO dark H_2 is described in Section 7.5.2. The distribution of the H_2 gas fraction relative to the total amount of hydrogen is discussed in Section 7.5.3.

7.5.1 SPECTRAL DISTRIBUTION OF CARBON

The spectral distribution of the C^+ (red), C^0 (black), and CO (green) column densities are illustrated in Figure 7.15 (Cases I and II) and 7.16 (Cases III and IV).

The spectral distribution of $N(\mathrm{CO})$ and $N(\mathrm{C}^0)$ have a similar shape as the spectra of ^{12}CO(2–1) and [CI](1–0) as these column densities are directly proportional to the observed main beam brightness temperatures[lxi]. The spectral distribution of CO(2–1) is broader compared to [CI](1–0) in the majority of the positions (BCLMP691, GMC01 and GMCno06 A&B), and therefore also the column densities of CO to C^0. BCLMP302 is an exception. In this position, the [CI](1–0) line is broader than CO(2–1) and [CII]. The same applies for the C^0 column density.

The velocity resolved distribution of the [CII] emission in the molecular phase and, thus, of the C^+ column densities arise from the specific velocity bins in which $T_{\mathrm{mb}}([\mathrm{CII}])_{\mathrm{H_2}} = T_{\mathrm{mb}}([\mathrm{CII}])_{\mathrm{tot}} - T_{\mathrm{mb}}([\mathrm{CII}])_{\mathrm{H^+}} - T_{\mathrm{mb}}([\mathrm{CII}])_{\mathrm{H^0}}$ >0. It is assumed that the velocity distribution of the HII emission is equal to the one of HI. In the Cases I and III $T_{\mathrm{mb}}([\mathrm{CII}])_{\mathrm{H_2}}>0$ in almost all velocity bins. In these two cases, the spectral distribution of $N(\mathrm{C}^+)_{\mathrm{H_2}}$ is roughly similar to the observed [CII] spectra. In the Cases II and IV, the [CII] emission in the molecular phase is narrower than those of [CI] and CO. In these cases, the [CII] emission from the molecular phase is concentrated on the velocity bins around the [CII]peak (BCLMP691, GMC01 and GMCno06 A) or to the red side of the spectra (BCLMP302).

Differences between the column densities are highlighted by the spectral distribution of the relative carbon fractions. The spectral distribution of the relative carbon fractions in the molecular phase is illustrated in Figure 7.17 (Cases I and II) and 7.18 (Cases III and IV). The relative fraction of the carbon species in the velocity bins around the line centres are roughly equal to the relative carbon fractions averaged over the full spectrum as listed in Table 7.12. The carbon at the sides of the spectra is dominated by C^+ in the majority of the positions in the Cases I and III. Expectations are the red wing of BCLMP302 and GMCno06 A as well as both wings of GMCno06 B. A significant faction of carbon is C^0 at these positions.

The carbon at the spectral edges is dominated by CO in the Cases II and IV. An exception is BCLMP302, once more where, in which C^0 and C^+ dominates, and the red wing of BCLMP691 where roughly 1/4 to 1/2 of the carbon is C^+.

7.5.2 SPECTRAL DISTRIBUTION OF CO DARK $\mathrm{H_2}$ GAS

Now, I will discuss the spectral distribution of the CO dark $\mathrm{H_2}$ fraction, $\mathfrak{f}$(DG). The spectral distribution of the CO dark $\mathrm{H_2}$ fraction (Section 7.2.8) is shown in the Figures 7.17 (Cases I and II) and 7.18 (Cases III and IV).

The fraction of CO dark $\mathrm{H_2}$ shows a characteristical shape in the majority of the positions in the cases I and III. Around the centre of the spectra the $\mathfrak{f}$(DG) is minimal with a typical $\mathfrak{f}$(DG) of $\sim$60% to 80%. Almost all $\mathrm{H_2}$ is CO dark ($\mathfrak{f}$(DG)$\simeq$1) towards the wings of the spectra. In BCLMP691, GMC01 and GMCno06 A the CO dark gas is commonly associated with C^+. C^0 traces a significant fraction of the CO dark $\mathrm{H_2}$ at the edges in BCLMP302 as well ($\sim$30% up to 100%). The GMCno06 A and B are an

lxi cf. Equation (4.14);

$$N = \frac{\tau}{1-e^{-\tau}} \times \frac{8\pi\nu^3}{c^3}\frac{Q}{g_u}\frac{1}{A_{ul}}\frac{e^{\frac{h\nu}{k_{\mathrm{B}}T}}}{\left(1-e^{-\frac{h\nu}{k_{\mathrm{B}}T_{\mathrm{mb}}}}\right)}\frac{1}{\mathcal{J}_\nu(T_{\mathrm{ex}})-\mathcal{J}_\nu(T_{\mathrm{BG}})\Phi_{\mathrm{B}}}\int T_{\mathrm{mb}}\mathrm{d}v$$

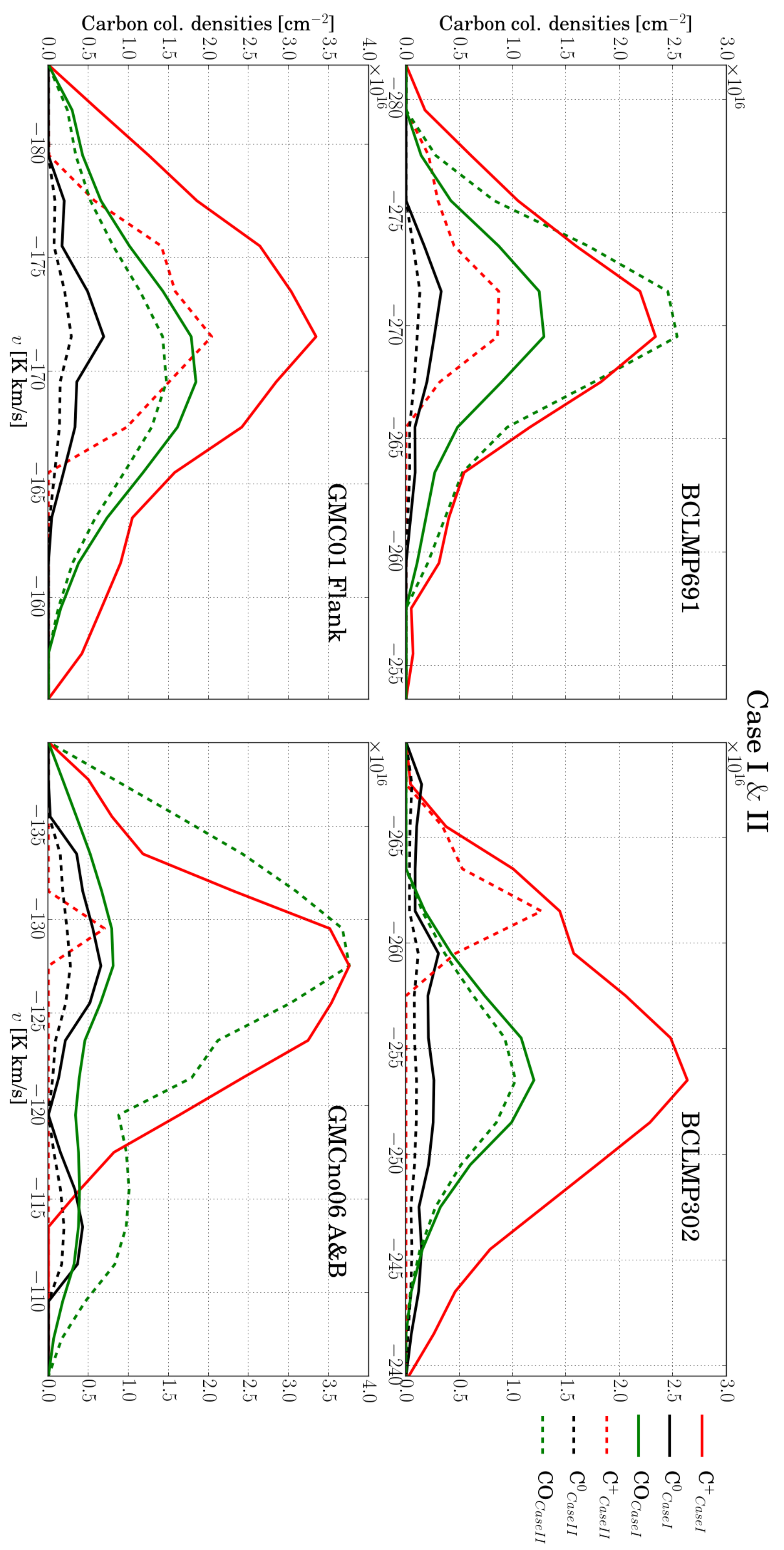

Figure 7.15: Distribution of the C^+, $C^0$and CO column densities for the carbon column density compositions 'case I and II' in the clouds at the positions BCLMP691, BCLMP302, GMC01 Flank and GMCno06 along the velocity axis in velocity bins with a width of 2 km s^{-1}.

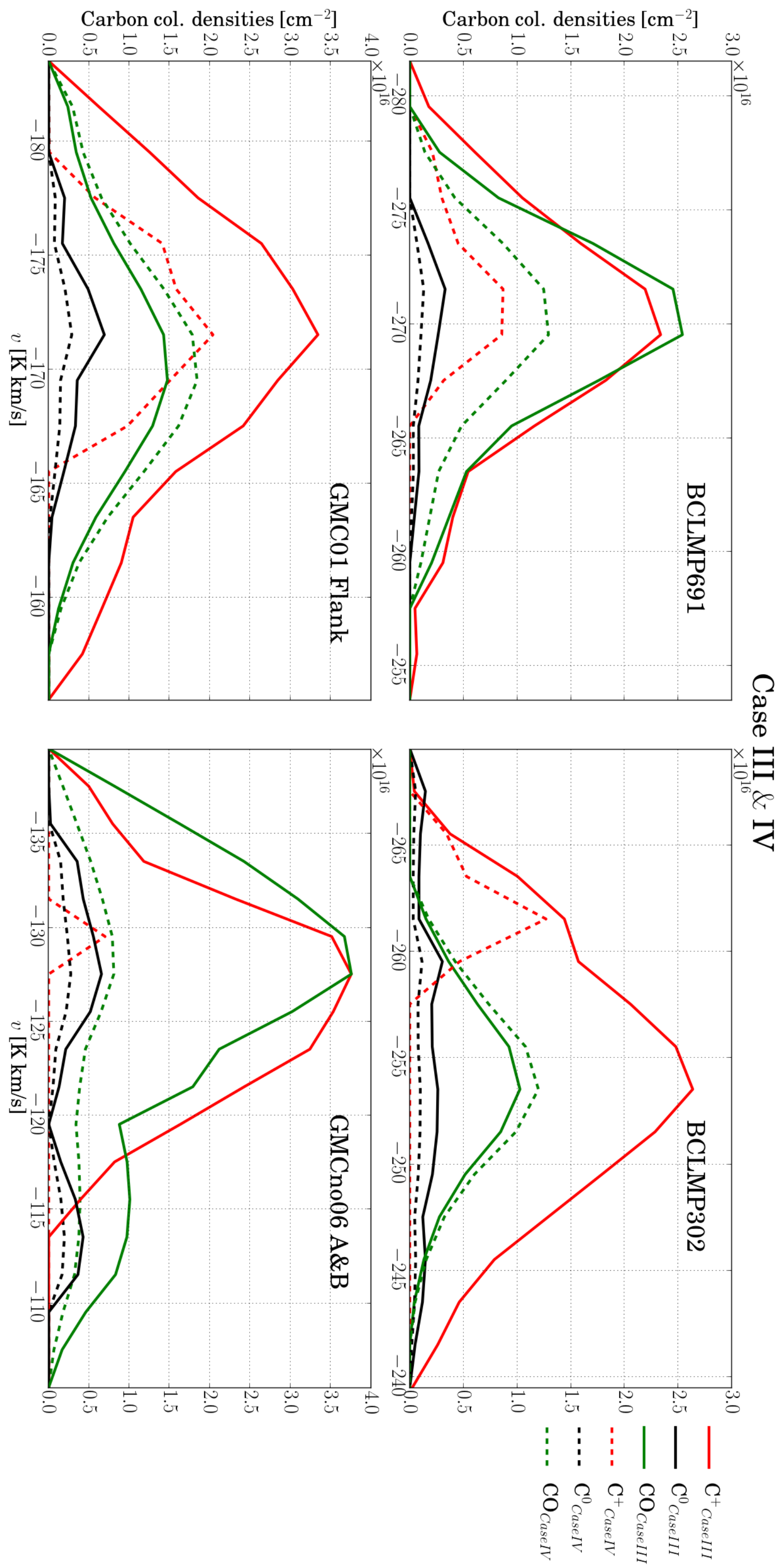

Figure 7.16: Distribution of the C^+, $C^0$and CO column densities for the carbon column density compositions 'case III and IV' in the clouds at the positions BCLMP691, BCLMP302, GMC01 Flank and GMCno06 along the velocity axis in velocity bins with a width of 2 km s^{-1}.

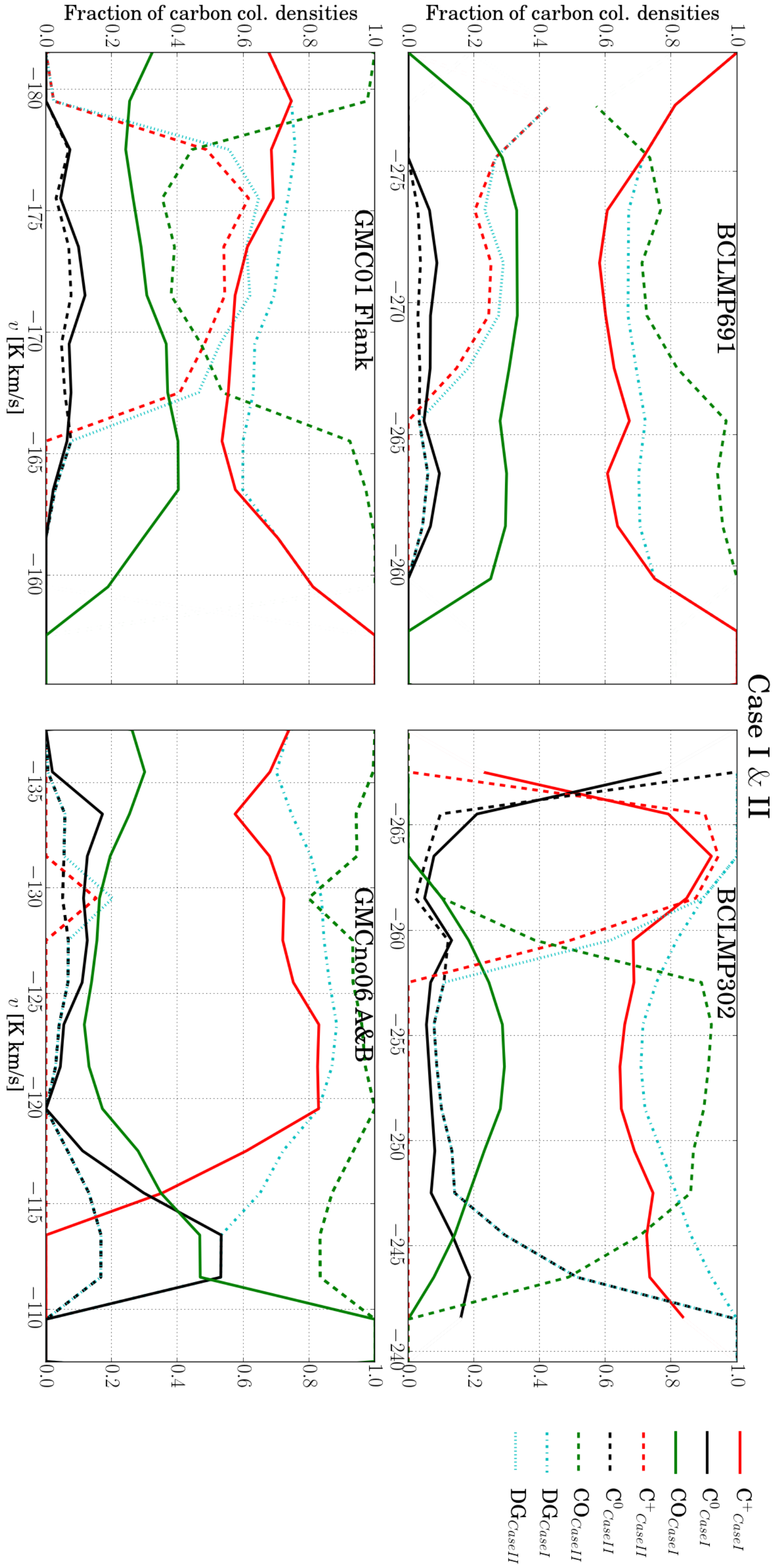

Figure 7.17: Relative fraction of the C^+, C^0 and CO column densities relative to the total carbon column densities for the carbon column density compositions Case I and II.

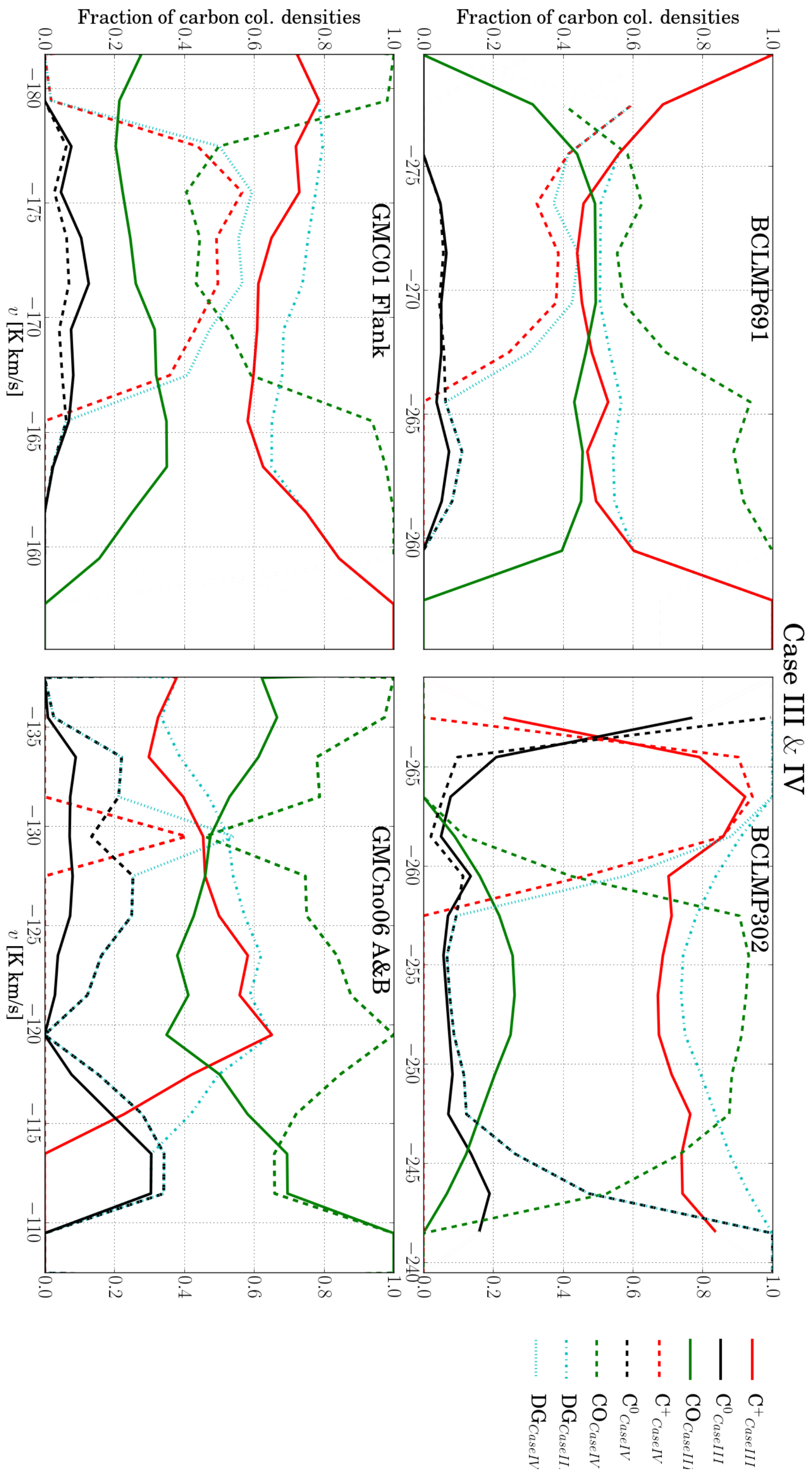

Figure 7.18: Relative fraction of the C^+, C^0 and CO column densities relative to the total carbon column densities for the carbon column density compositions Case III and IV.

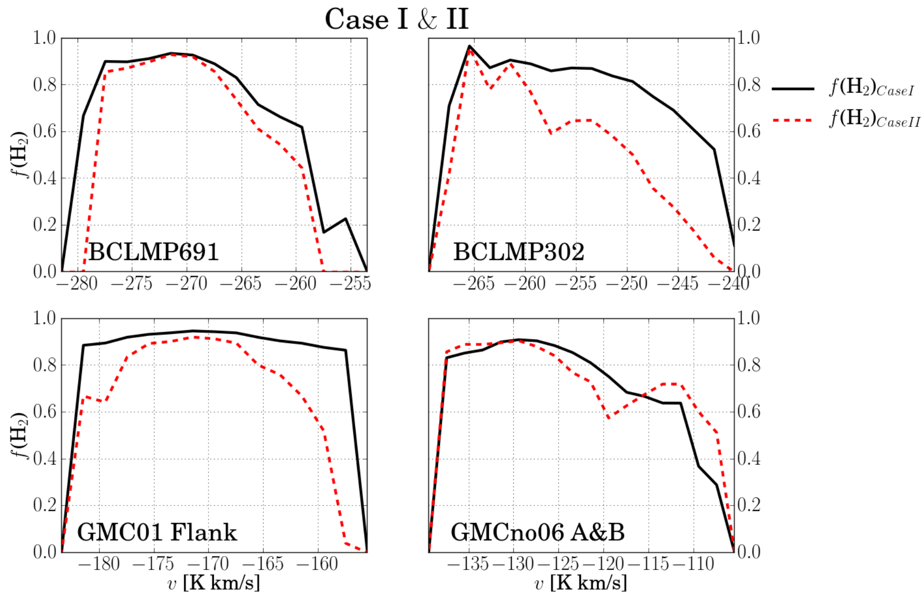

Figure 7.19: Distribution of the H_2 fraction in the clouds at the positions BCLMP691, BCLMP302, GMC01 Flank and GMCno06 along the velocity axis in velocity bins with a width of 2 km s^{-1} for the N(C) compositions case I and II.

exception. The $\mathfrak{f}$(DG) remains almost constant over their entire width at $\mathfrak{f}$(DG)≈0.5 to 0.75 (cloud A) and $\mathfrak{f}$(DG)≈ 0.6 (cloud B)and decreases to 0 at the blue wing.

In the cases II and IV the $\mathfrak{f}$(DG) are generally lower compared to the case III and IV, with a $\mathfrak{f}$(DG)∼0.1 to 0.5. In these cases the CO dark H_2 fractions decrease towards the edges, except for BCLMP302, in which $\mathfrak{f}$(DG)=1. The decrease of the $\mathfrak{f}$(DG) is induced by narrow spectral distribution of ${C^+}_{H_2}$ and C^0 compared to CO.

7.5.3 SPECTRAL DISTRIBUTION OF THE MOLECULAR GAS FRACTION

The spectral distribution of molecular hydrogen to the total amount of hydrogen are illustrated in the figures 7.19 and 7.20. H_2 is expected to be located towards the centre of clouds, surrounded by a layer of atomic neutral (and ionised) hydrogen.

The H_2 fraction reaches its maximum roughly around the centre of the spectra and decreases towards the edges. This spectral distribution is pronounced in the cases II and IV as well as in clouds with a low total total hydrogen column density (GMCno06 B). The H_2 fraction is ∼70% to 90% at the line centres and decreases to ∼20 to 40% towards the edges.

In general the fraction of molecular hydrogen is higher in the cases I and III compared to the cases II and IV. In the cases I and III the differences of $f(H_2)$ between the centre and the edges of the spectra are less pronounced. H_2 has a peak fraction of ∼95% in all positions in these two cases. Towards the flanks the fraction decreases to ∼ 50 to 60%.

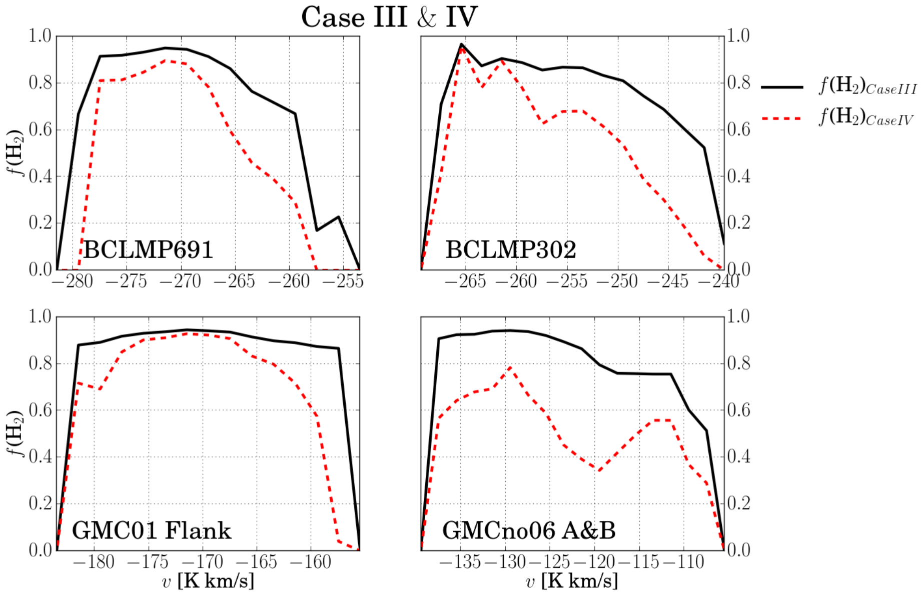

Figure 7.20: Distribution of the H_2 fraction in the clouds at the positions BCLMP691, BCLMP302, GMC01 Flank and GMCno06 along the velocity axis in velocity bins with a width of 2 km s^{-1} for the N(C) compositions case III and IV.

7.5.4 DISCUSSION OF THE SPECTRAL DISTRIBUTION

The observations show that carbon in the molecular phase has no uniform distribution in the positions discussed here. C^+, C^0 and CO are present at different velocities and thus in different regions of the GMCs.

The spectral distribution of the cases I and III can be explained by a C^+/C^0/CO layer structure. C^+ traces the H_2 of the outer layer of the molecular hydrogen and CO the H_2 in the centre of the cloud. The molecular hydrogen is surrounded by a layer of neutral hydrogen. H_2 is almost exclusively associated with C^+ towards the wings of the spectra. BCLMP302 is an exception. A significant fraction of the H_2 is associated with C^0 at the red edge of BCLMP302 as well. These observations indicate a gas phase in which the H_2 is associated C^+ and C^0 in the absence CO, as it was proposed by Hollenbach, Takahashi & Tielens (1991), Wolfire, McKee, Hollenbach & Tielens (2003) and Wolfire, Hollenbach & McKee (2010)[lxii]. The distribution of C^0 is relatively narrow, compared to CO and C^+, in all other clouds. This indicates that C^0 is located at the surface of the CO photodissociation layer in these clouds, and that CO and C^0 are associated with the same star forming matter in most of the positions.

The spectral distribution of the C^+ column densities and the $\mathfrak{f}$(DG) in the cases II and IV, are hard to reconcile with a C^+/C^0/CO layer structure. The observations might indicate narrow C^+ and C^0 layers in the molecular phase, or even H_2 that is associated with C^+ in the inner regions of the molecular phase while CO is associated with the outer regions. This might indicate that the $N(C^+)_{H_2}$ are underestimated in the the cases II and IV. Vice versa the assumptions in the cases I and III lead to spectral distributions which are in agreement with the assumptions for a molecular

lxii See also Section 2.2.1. Possible causes for the spectral distribution of C^+, C^0 and CO in BCLMP302 will be discussed in Section 7.6.3.

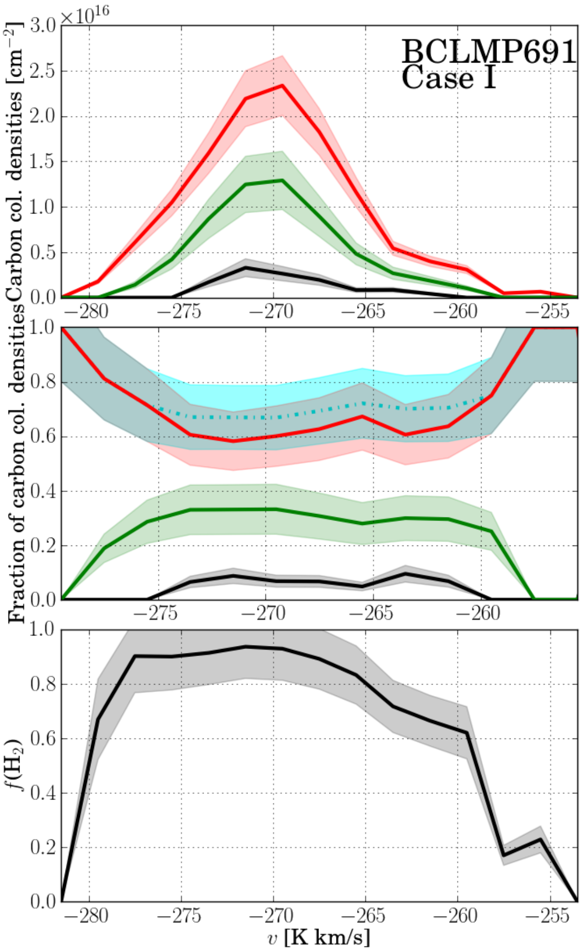

Figure 7.21: Uncertainties of the carbon column densities, the fraction of the carbon column densities, the fraction of CO dark H_2 and the fraction of molecular hydrogen at the example of BCLMP691 for the Case I. The lines and the corresponding coloured areas, in the upper two images, show the distribution of the different carbon species (red C^+, black C^0, grenn CO). The cyan area shows the fraction of CO dark H_2. The image at the button shows the spectral distribution of $f(H_2)$.

clouds.

The discussions in the previous sections indicate, that the cases I and III represent the real composition of the gas in the molecular clouds, discussed here. The fraction of CO dark H_2, the radial distribution and the spectral distribution of the different gas species in the cases II and IV are hard to reconcile the standard picture of molecular clouds. That is not the case for the cases I and III.

The individual positions will be discussed in detail, in the following section. I will use the column densities that were calculated for the cases I and III in the following discussion.

7.6 THE OBSERVED REGION IN DETAIL

The previous discussion was focused on the general distribution of carbon and hydrogen in M33. The observations in the individual clouds are worth to be discussed, as they allows to study the local conditions in a broader context and to gain an impression of the variety of the different GMCs and their environment.

7.6.1 BCLMP691

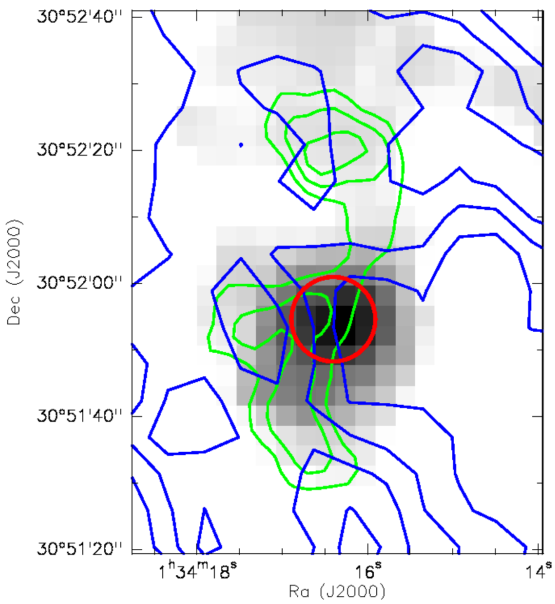

Figure 7.22: Grey image [CII] image of BCLMP691 (Nikola et al. in prep.). Green contours show the CO(2–1) emission, blue contours show HI. The red circle marks the intrinsic Beam size of the APEX [CI](1–0) observations

The BCLMP691 can be described as the most 'standard'–like GMCs in the sample of discussed positions. The distribution of carbon is consistent with a $C^+/C^0/CO$ layer structure. Within the uncertainties all discussed carbon lines peak at the same velocity. The broadest line is [CII]while [CI](1–0) is the most narrow line. Roughly 80% of the hydrogen is molecular form. Almost 2/3 of the H_2 is traced by C^+ while ∼1/3 by CO. The fraction of H_2 traced by C^0 of 6% is the lowest value of the discussed clouds. Roughly ∼70% of the H_2 is not associated with CO and is thus CO dark H_2.

7.6.2 GMC91

In GMC91 is characterised by a strong and broad CO emission, while no [CI](1–0) and [CII] is observed. The observed CO(2–1) line has a widths of Δv∼12 km/s. This is the broadest CO(2–1) line in the current sample of sources discussed here. The integrated [CII] line intensity has a upper

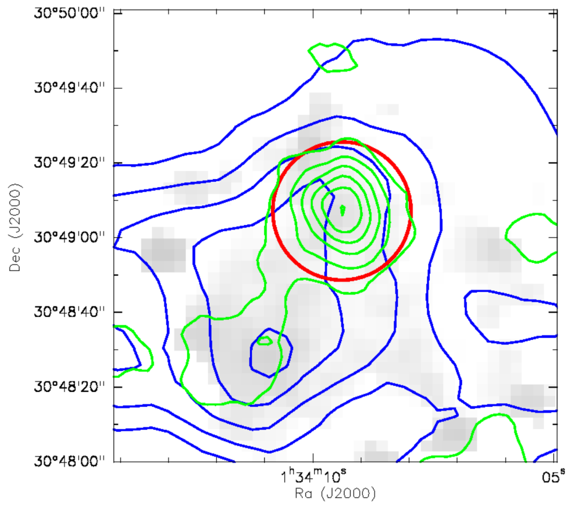

Figure 7.23: Grey image [CII] image of GMC91 (Nikola et al. in prep.). Green contours show the CO(2–1) emission, blue contours show HI. The red circle marks the intrinsic Beam size of the Nanten2 [CI](1–0) observations

limit of $\lesssim$0.72 K km/s (Nikola et al. in prep.). I([CI](1–0)) has an upper limit of $\sim$0.2 K km/s . The HI emission is widely spread around the point like CO peak.

The GMC91 has a total hydrogen column density of $N(\mathrm{H})_{\mathrm{tot}}\sim 14 \times 10^{21}$ cm^{-2}, with $\sim$80% of the hydrogen being H_2. All molecular hydrogen is traced by CO.

The following paragraph gives a possible explanation for the observed bright and broad CO lines, as well as the absence of [CII] and [CI](1–0) In general the observations can be explained by the kinematic within the northern spiral arm of M33, as shown in the following.

Observation in M51 found clouds with bright and broad low J-CO lines but no or faint [CII] and Hα emission (Schinnerer et al. 2013; Pety et al. 2013). Meidt et al. (2013) explained these observations by the dynamical environment of the GMCs. Strong streaming motions can stabilise GMCs by their high dynamical pressure and prevent a collapse of these clouds. Strong streaming motions can be found at the edges of spiral arms (Meidt et al. 2013). Therefore, those GMCs have only faint or even no star formation. Due to the low number of stars within these GMCs, the ambient radiation field is faint. As a consequence, CO is not photodissociated and carbon can hardly be ionised. Therefore almost all carbon is CO, in these clouds.

The shape of the northern spiral arm indicates strong streaming motions in this GMC. The northern spiral arm of M33 has a kneed structure as well. This structure is illustrated and emphasised in Figure 7.24. A kneed spiral structure indicates spirals shock waves in the spiral arms (Chernin 1999; Efremov 2010). The dynamical pressure is at its highest level in the kneeing points.

GMC91 is situated directly at a kneeing point of the northern spiral arm[lxiii]. Furthermore, the optical depth of the ^{12}CO(1–0) line of τ_{12}=6 is

lxiii NGC604 is also situated at a kneeing of the northern spiral arm. NGC604 is the second most massive GMC in the local group.

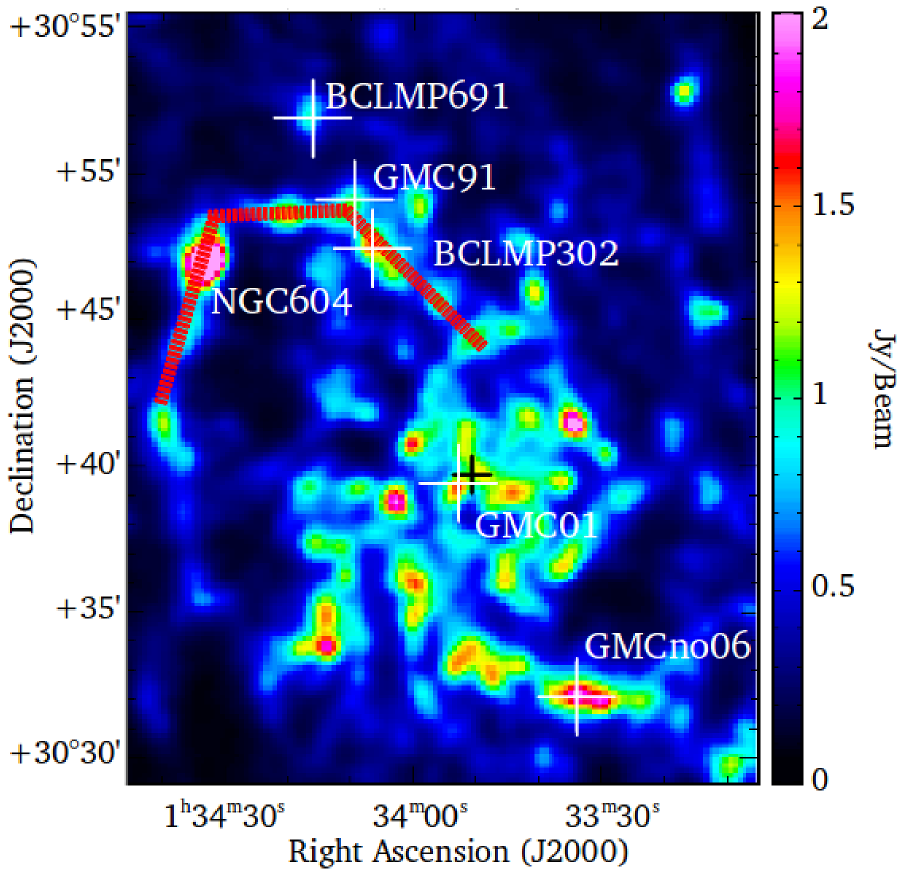

Figure 7.24: 350 μm Herschel-SPIRE map of M33 (Xilouris et al. 2012). The red dotted lines emphasise the kneed structure of the northern spiral arm of M33. The position of GMC91 at one knee is marked by the white crosses. The giant molecular cloud NGC504 at an other knee point is marked as well.

the lowest in this sample of clouds, while the $N(H_2)$ is of similar order as found in the other clouds. This indicates a low volume density in GMC91, which can be explained by a high dynamical pressure.

The model by Meidt et al. (2013) gives thus a possible explanation for the observed bright CO lines and missing ionised and neutral carbon lines in GMC91.

7.6.3 BCLMP302

[CI](1–0) was observed at the [CII] peak of BCLMCP302. The [CII] peak is located ~40 pc to the east of the CO emission regions (cf. Figure 7.25)

A distinctive characteristic at the observed position is the line-width of [CI](1–0). $\Delta v_{[CI]}$. The line-width of $\Delta v_{[CI]}$=15.1± km/s is the broadest [CI](1–0) line within the sample of here presented observations. The width clearly exceeds the line width of the CO line of Δv_{CO}=8.4±0.4 km/s. Within the uncertainties $\Delta v_{[CI]}$ could have a similar line-width as [CII] ($\Delta v_{[CII]}$=14.6±0.5km/s) and HI (Δv_{HI}=17.8±0.4km/s)(cf. Table 7.2).

Within the observed beam I derived a $N(H)_{tot}$~13 cm^{-2} , in which ~80±22% is molecular gas. CO traces ~20% of the H_2, while C^0 ~10% and C^+ ~70%. Roughly 80% of the H_2 is CO dark.

As consequence of the broad [CII] and [CI](1–0) lines all H_2 at the left spectral wing of BCLMP302 is CO dark (cf. Figure 7.17). The excess of

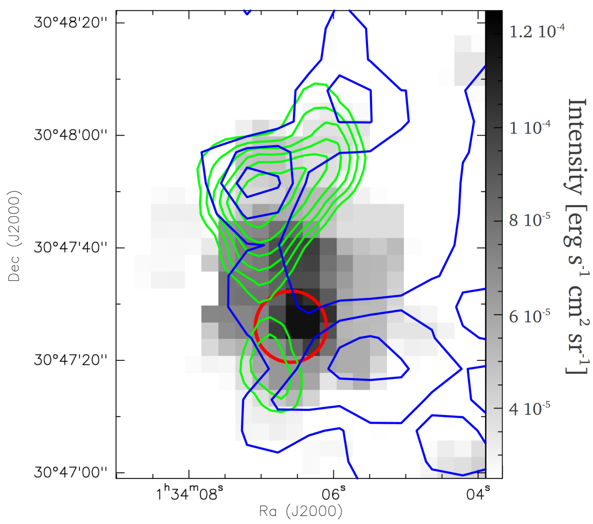

Figure 7.25: [CII] PACS image of BCLMP302 (Mookerjea et al. 2012). Green contours CO(2–1), blue contours HI. The red circle marks the intrinsic Beam size of the APEX [CI](1–0) observations

[CII] emission in the molecular phase, and thus of CO dark H_2, at this position is consistent with the study by Mookerjea et al. (2016). At the left wing of BCLMP302 the $N(C^0)/N(C)_{tot}$ rises to ∼80%.

The line-width and the central velocity of the CO(2–1) line at the observed position and at the peak of the southern CO complex are almost identical (Δv = 8.7±0.3, v_{LSR}=252.8±0.2 compared to Δv = 8.4±0.4, v_{LSR}=252.8±0.2). This might be that the observed CO(2–1) emission arises from the flank of the southern CO complex which lies within the beam. In that case the observed CO(2–1) emission has an other spatial origin as the [CII] emission (cf. Fig. 7.25).

The almost identical widths of the [CI](1–0) and [CII] lines and their similar spectral shape indicates that the [CI](1–0) arises from the same region as [CII], in a distance of ∼40 pc from the central molecular zone.

7.6.3.1 Possible origin of the broad [CI](1–0) line in BCLMP302

I will now discuss possible origins of the broad [CI](1–0) line in BCLMP302 and the excess of C^0 and C^+ at the left spectral.

The observations might indicate a diffuse cloud in the stage in which the diffuse ionised gas recombines to neutral gas (cf. e.g. Beuther et al. (2014)) while only few carbon monoxide has jet been formed. Oxygen might have not yet bounded to carbon, which causes the bright [OI]63μm line and the faint CO(2–1) emission at the left wing. The clouds density has to become denser to recombine ionised carbon to neutral atomic carbon and finally to form CO . HI and [CII] peak emission shows a slight shift of ∼3km/s and ∼1km/s relative to [CI](1–0). This velocity shift could be accompanied by a density gradient between the more diffuse C^+ and H^0 and the more dense C^0 and CO. A possible origin for the velocity (and density) might be a slow collision of diffuse clouds. No double peak structure or an asymmetrical line structure can be observed in HI and [CII]. That might indicate that the velocity of the collision would be relatively slow $\lesssim$3km/s. In that case the spatial distribution of [CI](1–0) and [CII]

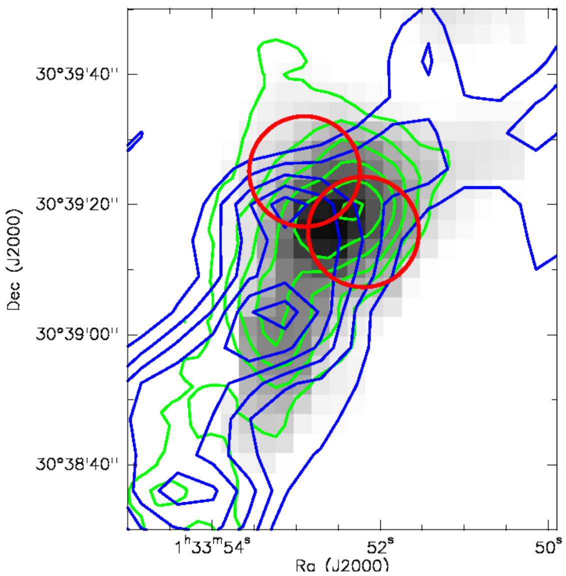

Figure 7.26: The grey image shows the [CII] distribution in GMC01 (Nikola et al. in prep.). Green contours show the CO(2–1) emission, blue contours show HI. The two red circles mark the positions of the [CI](1–0) observations. The diameter corresponds to the intrinsic Beam size of the CSO [CI](1–0) observations (∼27”).

might be different. For a further analysis a [CI](1–0) map is needed.

Also a temporary UV shadowing of the cloud could cause the broad [CI](1–0) line. The formation of C^0 is more efficient in clouds that are cooled down compared to clouds which are in thermal equilibrium (Stoerzer, Stutzki & Sternberg 1997). Ionised carbon recombines to C^0 rapidly in the absence of UV radiation (within few 10^4 years, Stutzki et al. 1997). The timescale to from CO from C^0 is higher; a few 10^{5-6} years (Stoerzer, Stutzki & Sternberg 1997; Stutzki et al. 1997). This mechanism in non-equilibrium regions leads to an enhanced [CI] abundance in a PDR for $\sim 10^{5-6}$ years. As [CI] had just formed from [CII], both lines should have similar spectra and a similar spatial distribution. This scenario would require a UV-shadowing of a cloud with a diameter of few 10 pc for $\sim$ few $10^4 - 5$ years.

Another scenario is the dissolution of the cloud by the nearby bright star cluster. The UV radiation arising from the star cluster could have photodissociated almost all the CO in the observed position. The remnants of the photodissociation, oxygen and neutral carbon, are further penetrated by UV. C^0 ionises and forms C^+. Hence, the line widths of [CII] and [CI](1–0) would have their origin in the formation of C^+ out of C^0. The fraction of [CII] compared to [CI](1–0) could shows an gradient in direction to the star cluster in that case. The carbon nearby the star cluster would ionise first. The velocity shift between [CII] and [CI](1–0) could be interpreted this way.

Maps of neutral carbon transitions would be required to test these scenarios.

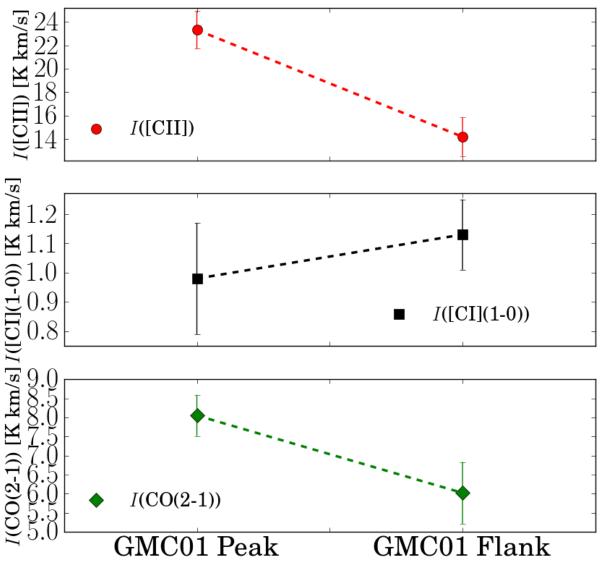

Figure 7.27: Integrated CO(2–1), [CI](1–0) and [CII] intensities in the positions GMC01 Peak and GMC01 Flank.

7.6.4 GMC01

GMC01 has hydrogen column density of $\sim 30\times10^{21}$ cm^{-2} at the [CII] Peak and $\sim 20\times10^{21}$ at the position GMC Flank. In both positions, the fraction of molecular hydrogen fraction is almost equal with $f(H_2)\sim 0.99$ to 0.95

Almost 75% of the H_2 is CO dark in the [CII]-peak position and $\sim$70% in GMC01 Flank. In both positions, the majority of the H_2 is traced by C^+($\sim$70% and 60%). Only $\sim$5% of the H_2 is associated with C^0. CO traces $\sim$25% to $\sim$30% of the H_2. In a simple spherical cloud with a C^+/C^0/CO layer structure (e.g. Sternberg & Dalgarno 1995) the opposite $\mathfrak{f}$(DG) distribution would be expected. The $\mathfrak{f}$(DG) should be higher at the flanks of a GMC and lower in their centre. The difference can be explained by the (spatial) distribution of the gas species. CO(2–1) peaks $\approx 7''\simeq$30pc north-east of the [CII] peak. Noticeable is distribution of the integrated [CI](1–0) line intensities. The I([CI](1–0)), and thus the calculated $N(C^0)$, is higher in GMC01 Flank than in the [CII]peak position. [CII] and CO(2–1) have their highest emission in GMC01 peak (cf. Figure 7.27). This indicates, that the structure of the carbon is complex in GMC01. The distribution of [CI](1–0) is unlike the distribution CO(2–1) and [CII]. For a further investigation, maps of the C^0 transition are needed.

7.6.5 GMCNO06

The CO and [CI](1–0) spectra in GMCno06 show two velocity components at a $v_{\rm LSR}\approx$-128 and -113 km/s These two velocity components are associated with two nearby GMCs, cloud A and B. These clouds overlap partially spatially in the beam (cf. Fig 7.28). This creates the double peak in the spectra spectra. Hence, the observed 'dip' is no selfabsorption. The CO peaks of cloud A and B have a projected spatially distance of $\sim$85 pc. [CII] peaks $\sim$10pc south of the CO peak of could A. The [CI](1–0) observations were performed roughly in the middle between the CO peaks of these GMCs. The beam of the [CI](1–0) includes the CO peak of cloud A as well as the [CII] peak. [CII] is spectrally associated with cloud A ($v_{LSR}\approx$-125 km/s). CO(2–1) and [CI](1–0) have a

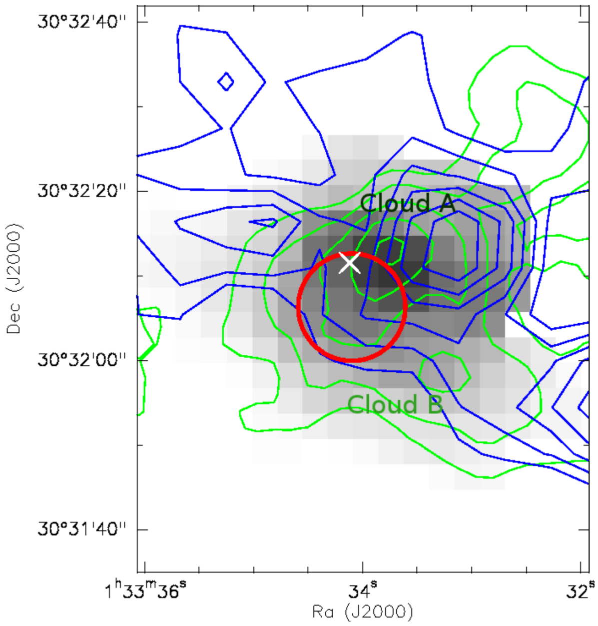

Figure 7.28: The grey image shows the [CII] distribution in GMCno06 (Nikola et al. in prep.). Green contours show the CO(2–1) emission, blue contours show HI. The two red circles mark the positions of the [CI](1–0) observations. The diameter corresponds to the intrinsic Beam size of the CSO [CI](1–0) observations. The white cross marks the position of the X-ray binary M33-X7. The cloud GMCno06 A is associated with the northern CO(2–1) peak close to M33-X7. GMCno06 B is associated with the fainter CO peak south-south-east of the CO(2–1) peak of GMCno06 A. The diameter corresponds to the intrinsic Beam size of the CSO [CI](1–0) observations (~27").

similar line-width within the uncertainties, in cloud A (Δv([CI])=9.5±1.2 to Δv(CO)=10.0±0.9). In cloud B [CI](1-0) is significantly more narrow (Δv([CI])=5.5±1.4 to Δv(CO)=9.1±1.0). The HI spectra is not directly associated with one of the clouds. The HI spectra superimposes the spectra of CO, [CI](1–0) and [CII]. The central peak velocity of HI ($v_{\rm LSR}$(HI)≈-120 km/s) lies roughly in the middle of the central the velocities found for CO and [CI](1–0).

Cloud A has a $N(\rm H)_{tot}\approx 25\times10^{21}$ cm^{-2}. Cloud B has the lowest hydrogen column density in this sample of clouds with an $N(\rm H)_{tot}\approx 25\times10^{21}$ cm^{-2}. The fraction of H_2 in GMCno06 A is ~90% and ~50% in cloud B. About ~75% of the carbon in cloud A is C^+ , ~10% is C^0 , and 15% is CO. This is the highest relative fraction of C^+ and C^0 and the lowest fraction of CO in this sample of discussed clouds, leading to a $\mathfrak{f}$(DG) of ~85%. This fraction stays almost constant over the whole spectrum.

With cloud B no [CII] emission is associated. Thus all the carbon is in C^0 and CO. Averaged of the whole spectra of cloud B roughly 40% of the carbon(and thus of the CO dark gas) in cloud B is neutral carbon. At the [CI](1–0) this fraction rises to ~55%. At least of the right spectral flank of cloud B all the carbon is associated with CO.

7.7 SUMMARY AND CONCLUSION

I presented [CI](1–0) observations of five prominent GMCs (BCLMP691, GMC91, BCLMP302, GMC01 and GMCno06) along the galactic radius of M33. The observations were set directly at, or close to, the [CII] peak of these GMCs. Based on complementary [CII], [NII]122μm , $^{12/13}$CO(1–0), ^{12}CO(2–1) and HI data I was able to derived the beam average column densities of CO, C^0, C^+ and H^0. Combined with HI and [NII]122μm data I have determined the C^+ column density and the [CII] emission from the molecular, neutral atomic and the ionised phase. The molecular hydrogen column densities were determined from the carbon column densities in the molecular phase. I also derived the fraction of CO dark H_2. The radial and spectral distribution of the different gas species was discussed. The H_2 column densities and the observed integrated intensities allowed to determine H_2 conversion factors for the integrated intensities of CO(2–1), [CI](1–0), [CII] as well as the [CII] emission from the molecular phase. The individual position were discussed in detail as well.

The C^0 and C^+ column densities were calculated for different excitation temperatures. I have calculated $N(C^+)$ for assumed [CII] excitation temperatures between 75 K to 200 K in the atomic phase and 75 K to 138 K in the molecular phase in the optically thin limit and for a τ=1. I can conclude, that the uncertainties of the [CII] excitation temperatures are the main obstacle to calculate the C^+ column densities. The total column densities are on average $N(\mathrm{CO})\sim12\times10^{16}\mathrm{cm}^{-2}$, $N(\mathrm{C}^0)\sim12\times10^{16}\mathrm{cm}^{-2}$and $N(\mathrm{C}^+)\sim20\times10^{16}\mathrm{cm}^{-2}$($T_{\mathrm{ex}}$=$T_{\mathrm{ex}}$([CII])$_{\mathrm{H}^0}$=75K, $\tau\rightarrow0$) to $\sim35\times10^{16}\mathrm{cm}^{-2}$ (T_{ex}=200K, τ=1). Roughly $\sim$2/3 of the C^+ column density and 25% (T_{ex}=75K, $\tau\rightarrow0$) to 70% (T_{ex}=200K, τ=1) of the [CII] emission is associated with H_2.

I have studied four different carbon compositions. These compositions allowed to study the maximal and minimal amount of H_2 in the different positions. The cases I and III were based on an [CII] excitation temperature of 200 K in the the atomic phase and a τ=1 in the molecular phase. The cases II and IV were based on an assumed optically thin limit and [CII] excitation temperature of 75 K in the the atomic phase. C^+ is associated with $\sim$25% (cases II and IV) to $\sim$70% (cases I and III) of the molecular hydrogen, CO traces in average between $\sim$70% and 25% of the H_2. C^0 is associated with $\sim$5 to 10 % of the H_2. The average fraction of CO dark H_2 is $\sim$40% (cases II and IV) to 80% (cases I and III) in M33. The first fraction is roughly equal to the $\mathfrak{f}$(DG) found in the Milky Way. The second is roughly twice this value. These fraction of CO dark H_2 was compared with the prediction of the PDR model of Wolfire, Hollenbach & McKee (2010) for a Z=0.5$Z_\odot$. The cases I and III are in good agreement with the theoretical predictions.

I have calculated maximal and minimal H_2 conversion factors The derived H_2 conversion factors have lower and upper limits of $X_{\mathrm{CO(2-1)}}\sim3.5$ to 15 $\times10^{20}$ s $\mathrm{K}^{-1}\mathrm{km}^{-1}\mathrm{cm}^{-2}$, $X_{\mathrm{CI}}\sim2$ to 9 $\times10^{21}$ s $\mathrm{K}^{-1}\mathrm{km}^{-1}\mathrm{cm}^{-2}$, $X_{\mathrm{CII}}\sim1$ to 8 $\times10^{20}$ s $\mathrm{K}^{-1}\mathrm{km}^{-1}\mathrm{cm}^{-2}$ and $X_{\mathrm{CII}_{\mathrm{H}_2}}\sim7$ to 8 $\times10^{20}$ s $\mathrm{K}^{-1}\mathrm{km}^{-1}\mathrm{cm}^{-2}$ These conversion factors are roughly consistent with the H_2–CO conversion factors by Bolatto, Wolfire & Leroy (2013) (adapted for Z=0.5$Z_\odot$) and Israel (1997) as well as H_2–[CI](1–0) conversion factors based on numerical simulations for a half solar metallicity.

Towards larger distances to the galactic centre of M33 the total and molecular hydrogen column densities decrease. They have a scale lengths of $\sim$2 to 3 kpc. The radial distribution of the carbon species either showed no gradient (case I) or the amount of C^+ decreases towards larger R_{M33}, while the amount of CO increases (cases II, III and IV). A significant radial gradient was not observed for C^0 in all the cases. These radial distribution can be in general explained by the radial gradient of the ambient radiation field. The scale lengths of the ambient radiation field are less than the scale lengths of $N(\mathrm{H})$ and $N(\mathrm{H_2})$, thus that the size of the C^+ layer shrinks faster compared to the size of the CO core.

C^+ , C^0, CO and the fraction of CO dark H_2 have different spectral distributions in the molecular phase (C^+ from the neutral atomic and the ionised phased are excluded in the comparison). In the cases I and II the majority of the carbon at the edges of the spectra is C^+. CO and C^0 are located preliminary the centre of the spectra, which is consistent with a C^+/C^0/CO layer structure. In the cases II and IV the carbon at edges of the spectra is dominated by CO. In these cases C^0 and C^+ are allocated towards the centre of the spectra. CO dark H_2 has almost a similar distribution as C^+ in most of the cases and the positions. Exceptions are the GMC91, BCLMP302 and GMCno06. GMC91 shows no [CII] and CO emission, such that no CO dark H_2 was detected. A significant fraction of the H_2 at the red wing of BCLMP302 is associated with C^0, while CO is absent. These observations presumably indicate a gas phase in which the H_2 is associated C^+ and C^0 in the absence CO, as it was proposed by Hollenbach, Takahashi & Tielens (1991), Wolfire, McKee, Hollenbach & Tielens (2003) and Wolfire, Hollenbach & McKee (2010). The cloud GMCno06 B shows no [CII] emission. Therefore all the CO dark H_2 is associated with C^0.

In summary it can be concluded that the C^+ column densities are deeply affected by the assumed excitation temperatures within the different gas phases. This uncertainty affects all the calculation that are based on these values, such as the amount of H_2, the fraction of CO dark H_2 as well as their radial and spectral distribution. Furthermore the study shows that most of the CO dark H_2 is traced by [CII]. [CI](1–0) traces only a minor fraction of this gas, in most of the positions.

Part IV

CONCLUSION AND OUTLOOK

Chapter 8

Summery, Conclusion and Outlook

This thesis serves *a study of distribution of carbon in the nearby universe*. It was motivated by the overall question "What is distribution of carbon in the ISM and what conclusions can be drawn for the ISM in general?" In order to shed light on this question, I have investigated the distribution and the composition of C^+, C^0 and CO based on representative samples of sources in the Milky Way and M33. Three major samples were analysed, each providing an insight into different aspects of the ISM.

At first, I have investigated the nature and composition of clouds along the line of sight towards the quasars B0355+508 and B0212+735 (chapter 5). These clouds were originally observed by the absorption of mm-waves towards these quasars. CO(1–0) and CO(2–1) emission was observed around the line of sight towards the quasars and identified to be associated with these clouds because of their matching velocity characteristics with the mm-wave absorption spectra (Liszt & Lucas 1998; Liszt & Pety 2012). These clouds were identified as warm non-LTE diffuse clouds with a temperature of $T \gtrsim 30$ K and subthermal excited CO lines. In diffuse clouds, the photo-electric heating efficiency is maximal and the cooling is dominated by [CII]. If the clouds were indeed diffuse, [CII] emission lines with an integrated line intensity of a few $\sim 10^0$ K km/s were expected. Observations, carried out with SOFIA/GREAT, did not found such [CII] emission. [CI](1–0) observations (carried out with Nanten2/SMART) of an other similar cloud also show no detection. Due to the lack of alternative cooling mechanisms of diffuse clouds, it is concluded that the clouds towards the line–of–sight of B0355+508 and B0212+735 are not diffuse clouds. Furthermore, this thesis also provided an alternative explanation. The observed CO line intensities, the ratio of CO(2–1) to CO(1–0) and of ^{13}CO to ^{12}CO, the calculated molecular hydrogen column densities, the size of the clouds and the upper limits for [CII] are fully consistent with an ensemble of cold dense clumps with temperatures of $\sim$15 K and volume densities of $n(\mathrm{H}) \sim 10^{3.5}\mathrm{cm}^{-3}$ to $10^4\mathrm{cm}^{-3}$. This explanation was developed by analytical calculations of the expected [CII] line intensities for a kinetic gas temperature of 15 K (this temperature is implied by the CO(2–1) to CO(1–0) ratio) and by simulations of clumps with the KOSMA–τ PDR model.

The large scale latitudinal and radial distribution of carbon in the fourth quadrant of the Milky Way was tackled in chapter 6. The study was based on the analysis of spectrally resolved latitudinal observations of

$^{12/13}$CO(1–0), CO(2–1), CO(4–3) and [CI](1–0), at eight galactic longitudes between l=306° and 354°and b=±2°. Kinematic distances from the sun and from the Galactic Centre were determined by the velocity and longitudinal information within the datasets. The vertical distribution of the lines was determined based on the distances. The observations were set in relation to the spiral arms as well. The observations do not show any significant differences between [CI](1–0), CO(1–0) and CO(2–1) within in the inner galaxy (R_{GC}<8.5 kpc) neither radial from the Galactic Centre nor vertical from the galactic midplane. This might indicate that most of the [CI](1–0) emission within the Milky Way arises from the surface of the CO photodissociation layer and that these lines arise from the same star forming matter.

The observed latitudinal profiles have an asymmetrical shape with local features with diameters of 5 to 30 pc. The profile can not be described by a single Gaussian. The scale height of [CI](1–0), ^{12}CO(1–0) and CO(2–1) rises from $z_{1/2}\sim$25-30 pc at $R_{\mathrm{GC}}\approx$2 kpc to $z_{1/2}\sim$50 to 55 pc at $R_{\mathrm{GC}}\approx$4 kpc. The scale heights of the observed transitions can be fitted with power law functions, $z_{1/2}\propto {R_{\mathrm{GC}}}^{0.5}$. The calculations give $z_{1/2}(R_0)$=62±7 pc for [CI](1–0) and $z_{1/2}(R_0)$=71±12 pc for CO(2–1) at the location of the sun.

The observed profiles were compared with simulated [CII] profiles carried out within the SILCC-project. The observed CO and [CI](1–0) profiles show strong similarities to the simulations. In conclusion, this might indicate that major parts of the local structure of the Milky Way are triggered by supernovae, which locally disrupts or compresses the ISM.

The distribution of carbon and hydrogen in the nearby galaxy M33 was investigated in the case study of five GMCs situated on the major axis of this galaxy. M33 has a half solar metallicity, Z=0.5$Z_{\odot}$. I have presented [CI](1–0) observations of these GMCs. The observations were set directly at, or close to, the [CII] peak of these GMCs. With the use of complementary [CII], $^{12/13}$CO(1–0), ^{12}CO(2–1), HI and [NII]122μm data, I was able to determine the column densities of all major carbon species, CO, C^{0}and C$^+$as well as the column densities of neutral atomic hydrogen. The amount of molecular hydrogen could be directly determined from the carbon column densities. In addition, the data allowed to derive the fraction of CO dark H_2. Furthermore, I have discussed the radial and spectral distribution of the different gas species. H_2 conversion factors for the observed line transitions were also calculated. Finally, the individual position were discussed in detail.

CO and C^0 are associated exclusively with H_2. C$^+$ is situated in all gas phases. I have determined the column densities of the C$^+$ in the different gas phases as well as the fraction of the [CII] emission that arises from the different phases, for assumed [CII] exception temperature between 75 K and 200 K in the optically thin limit and for an assumed τ=1. The uncertainty of the [CII] excitation temperature is the main obstacle for the calculation of the C$^+$ column densities. The total column densities of the different carbon species, found in the GMCs are on average N(CO)∼12×10^{16}cm^{-2}, N(C^0)∼12×10^{16}cm^{-2}and N(C$^+$)∼20 ×10^{16}cm^{-2}(T_{ex}=75 K, $\tau\to$0) to ∼ 35× 10^{16}cm^{-2}(T_{ex}= 200 K, τ= 1). Roughly ∼2/3 of the C$^+$ column density and 25% (T_{ex}=75 K, $\tau\to$0) to 70% (T_{ex}= 200 K, τ=1) of the [CII] emission is associated with H_2. The column densities of molecular hydrogen, $N(H_2)$, and the fractions of CO dark H_2, $\mathfrak{f}(DG)$, were calculated from the carbon column densities. Different possible total carbon column densities were discussed. This approach allowed to investigate the maximal and minimal $N(H_2)$ and $\mathfrak{f}(DG)$ of the individual positions.

C^+ can be associated with ~25% (T_{ex}=75 K, $\tau \to 0$) to ~70% (T_{ex}=200 K, τ=1) of the molecular hydrogen, CO can be associated in average with ~70% to 25% of the H_2. C^0 is associated with ~5 to 10 % of the H_2. The average fraction of CO dark H_2 is ~40% to 80% in M33. These $\mathfrak{f}(DG)$ fractions for the cases with an T_{ex}=200 K and $\tau \to 1$ are in good agreement with the theoretical predictions by the PDR model of Wolfire, Hollenbach & McKee (2010) for a $Z=0.5Z_{\odot}$. This fraction roughly twice the $\mathfrak{f}(DG)$ in the Milky Way.

H_2 conversion factors were derived from calculated $N(H_2)$ and the observed integrated line intensities of CO(2–1), [CI](1–0) and [CII]. A H_2 conversion factor based on the [CII] emission that arise from the molecular phase was calculated as well. The derived H_2 conversion factors have lower and upper limits of $X_{CO(2-1)}$~3.5 to 15 $\times 10^{20}$ s $K^{-1}km^{-1}cm^{-2}$, X_{CI}~2 to 9 $\times 10^{21}$ s $K^{-1}km^{-1}cm^{-2}$, X_{CII}~1 to 8 $\times 10^{20}$ s $K^{-1}km^{-1}cm^{-2}$ and $X_{CII_{H_2}}$~7 to 8 $\times 10^{20}$ s $K^{-1}km^{-1}cm^{-2}$ These conversion factors are roughly consistent with established H_2–CO conversion factors and H_2–[CI](1–0) conversion factors based on numerical simulations.

The total and molecular hydrogen column densities decrease towards larger distances to the galactic centre of M33, with a scale lengths of ~2 to 3 kpc. The radial distribution of the carbon species in the different cases was surprising. Either they do not show any gradient or the amount of C^+ decreases towards larger distances to the centre of M33, while the amount of CO increases. The amount of C^0 is almost constant in all cases. In general, this radial distribution could be explained by the radial gradient of the ambient radiation field. The scale lengths of the ambient radiation field are less than the scale lengths of $N(H)$ and $N(H_2)$.

C^+, C^0 and CO are present at different velocities within the clouds. The spectral distributions of C^+ (in the molecular phase), C^0, CO and the fraction of CO dark H_2 shows major differences in the different cases. In the cases of an assumed [CII] excitation temperature of 200 K and τ=1, the majority of the carbon at the edges of the spectra is C^+. CO and C^0 are located in preliminary the centre of the spectra. This distribution is consistent with the existence of a C^+/C^0/CO layer structure. In the cases with a [CII] excitation temperature of 75 K and τ=0 the carbon at the edges is dominated by CO. C^+ is only at the centre in these cases. The fraction of CO dark H_2 has an almost similar distribution as C^+. An exception is the C^0 distribution the GMC BCLMP302. In this position, a significant fraction of H_2 at the red edge is associated with C^0 while CO is absent.

The study shows that the calculated C^+ column densities are deeply affected by the assumed (as unknown) excitation temperatures within the different gas phases. This uncertainty affects the amount of H_2, the fraction of CO dark H_2 and their radial and spectral distribution.

In general it can be concluded that the cases with an assumed [CII] excitation temperature of 200 K and τ=1 are probably a better estimate for the conditions within the clouds. The majority of the CO dark H_2 is associated with C^+. C^0 has a lower spectral distribution than CO. That indicates that C^0 is associated with the CO photodissociation layer in M33, similar as in the Milky Way. [CI](1–0) in the absence of CO is only been observed in a single position.

This thesis studied various aspects of the ISM in the Milky Way and M33. Many conclusions were drawn, that were already mentioned above. Nevertheless I would like to point out the following conclusions as the essence of this thesis:

- The gas towards the line of sight to B0355+508 and B0212+735 is seen as warm diffuse gas with subthermal excited CO lines with temperatures of $T \gtrsim 30$ K, for roughly two decades. This study has shown that this can not be case. This study indicates that the clouds along the line of sight consist of an ensemble of cold dense clumps with $T \sim 15$ K and $n \sim 10^{3.5}$ cm^{-3} to 10^4 cm^{-3}.
- [CI](1–0) has not been observed in the absence of CO(1–0) and CO(2–1) in most of the positions analysed in this thesis. This is the case for the Milky Way and for M33. This indicates that most of the C^0 arises from the surface of the CO photodissociation layer in the Milky Way and in M33. Nevertheless, there are a few positions that show [CI](1–0) in the absence of CO. This study found a single position (BCLMP302 in M33) in which C^0 and C^+ are present while CO is not.
- This study indicates, that the majority of H_2 can be traced by low–J CO transitions and [CII]. [CI](1–0) was not observed in the absence of CO transitions or [CII].
- The observed vertical profiles of CO and [CI](1–0) have an asymmetrical shape and can not be described by a single Gaussian. The profiles have a similar shape, such as the [CII] profiles carried out within the SILCC–project. This might indicate that the local structure of the Milky Way is triggered by supernovae to a large degree.
- The CO dark H_2 fraction is presumably higher towards a lower metallicity. Probably up to $\sim 2/3$ of the H_2 is CO dark in M33. The majority of this gas is traced by [CII], not by [CI](1–0).
- I would also like to point out that the calculations of the C^+ column density and the [CII] intensities are dominated by the assumed [CII] excitation temperatures in the different gas phases. The assumption deeply affect the estimated total amount of carbon and hydrogen in the positions of interest.
- Furthermore, this thesis highlights the importance of spectral resolved line observations in order to study the ISM. A large fraction of the study would have been impossible without the spectral information.

This thesis is based on relatively small samples of positions. The significance of all the different aspects discussed here could be highly improved, if the number of studied positions were increased.

The study of the clouds towards the line of sight to the B0355+508 and B0212+738 was based in total on four positions with a relatively short integration time. A [CII] mapping of these sources would significantly increase the statistical representativeness of the study. Furthermore, it would be worth to investigate if the emission from other clouds which have been identified as diffuse are also consistent with a cold and dense clump scenario, once the [CII] intensity is observed and taken into account.

[CII] observations of the *b*–strips, complementary to [CI](1–0) and the CO transitions, would allow to determine the radial and vertical distribution of C^+ in the fourth quadrant in the Milky Way and to provide a overall picture of carbon in the fourth quadrant of the Milky Way. Its vertical could be compared with the results, presented here. The vertical distribution of CO dark H_2 could be determined. The compassion of [CII] observations with the SILCC simulations would allow further statements about the main mechanisms that trigger the local distribution of matter in the ISM. These observations are already planed to be performed with SOFIA/upGREAT. It would be worth to determine the column densities of CO, C^0 and C^+ in the *b*–strips. This would allow to determine the amount of molecular hydrogen within these strips, and to study its vertical and radial distribution.

Nevertheless, it is interesting to study distribution of CO, C^0 and C^+ based on additional positions. The distribution of [CI](1–0) (and partially [CI](2–1)) was recently mapped at b=0° between the galactic longitudes l=323.6° to 341.4° with Nanten2/SMART. These observations were carried out within the framework of this thesis. Complementary [CII] and CO observations are provided by Herschel/HIFI observations of GOT C^+ project and the Mopra Southern Galactic Plane CO Survey.

It would be also worth to study the [CI](2–1) transition at 809.3 GHz in the Milky Way and in M33. This transition might have an other distribution compared to [CI](1–0) and, therefore. might trace other regions of the ISM. Complementary [CI](2–1) would allow to determine precise excitation temperatures for the C^0 transitions as well. A map of the [CI](1–0) and [CI](2–1) emission of the GMC BCLMP302 would allow to investigate the origin of C^0 in the absence of CO. I would also like to mention that the present allocation of telescopes harms the observations of the frequencies above $\nu \gtrsim 350$ GHz in the northern hemisphere from ground based observatories.

Calculations of the C^+ column densities require a reliable estimate of the [CII] excitation temperatures in the different gas phases. In future it could be useful to observe tracers for these temperatures. For example CH^+ could be a tracer for the temperatures within the neutral atomic phase.

In summery this thesis had shed light on many aspects of the distribution of carbon in the nearby universe and had suggested many possible explanations for various questions. Nevertheless many aspects remain open and require a further investigations. I dare to say that the combination large scale spectral resolved CO, [CII], [CI](1–0) and [CI](2–1) maps, combined with tracers for the gas temperatures of C^+ , provide a reliable tool to study major aspects of the ISM as, for example, the distribution of molecular hydrogen.

Part V

APPENDIX

Appendix A

Column densities of CO, C^0, C^+ and H^0

The following chapter contains a brief discussion concrete Einstein A_{ul} coefficients and partition functions Q of carbon monoxide, neutral atomic carbon and atomic ionised carbon. Equations used to derive the column densities of these carbon species and of neutral atomic hydrogen are also discussed.

A.1 COLUMN DENSITIES OF CO

Carbon monoxide is a dipolar linear molecule. The rate coefficient for the spontaneous emission A_{ul} of a dipole molecule as CO for a specific J is given by

$$A_{ul} = \frac{64\pi^4\nu^3}{3hc^3}|\mu^2|\frac{J}{J+1} \tag{A.1}$$

with $|\mu^2|$ being the matrix element of permanent electronic dipole moment. ^{12}CO and ^{13}CO have a permanent magnetic dipole moment of $|\mu|\approx 0.11$ Debye[i].

For rotational transitions, the statistical weights are equal to the degeneracy, $g_J = 2\ J + 1$. The rotational partition function of a linear molecule with a dipole is, in consequence given by

$$Q = \sum_{J=0}^{\infty}(2J+1)e^{\frac{hB_0 J(J+1)}{k_\mathrm{B}T_\mathrm{ex}}} \tag{A.2}$$

$$\approx \frac{k_\mathrm{B}T_\mathrm{ex}}{hB_0} + \frac{1}{3} \tag{A.3}$$

B is the rotational constant with $B = \nu/(2\ J_u)$. Column densities as function of the excitation temperature at the example of ^{13}CO are shown in Figure A.1.

A.2 COLUMN DENSITIES OF C^0

The column density of neutral atomic carbon $N(\mathrm{C}^0)$ can be calculated from the observed [CI](1–0) line intensity via (c.f. Schneider et al. (2003))

$$N(C^0) = 5.94 \times 10^{15} \times \frac{Q\,\tau([\mathrm{CI}](1-0))}{1 - e^{-\tau([\mathrm{CI}](1-0))}\,\Phi_\mathrm{B}} \int T_\mathrm{mb}([\mathrm{CI}](1-0))\,\mathrm{d}v \tag{A.4}$$

i 1 Debey=10^{-18} erg$^{1/2}$ cm$^{3/2}$

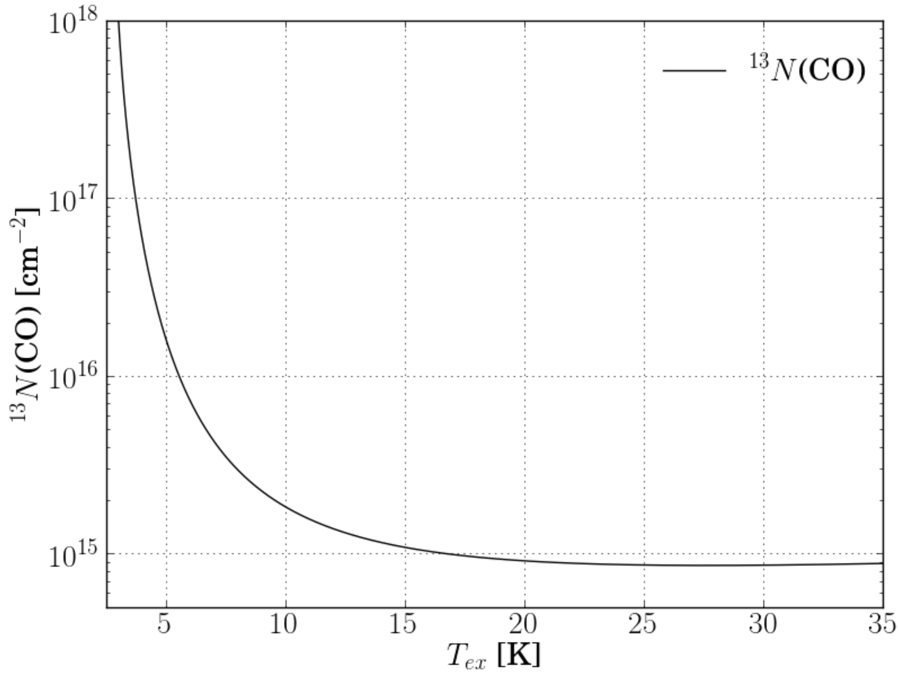

Figure A.1: Column densities of ^{13}CO in cm^{-2} as function of T_{ex} for an integrated ^{13}CO(2–1) line intensity of $\int T_{\mathrm{mb}}([\mathrm{C\,II}])\mathrm{d}v = 1$ K km/s in the optically thin limit.

with E_1/k_{B}=23.62 K and E_2/k_{B}=62.4 K. The partition function is given by

$$Q = \frac{1 + 3e^{-E_1/k_{\mathrm{B}}T_{\mathrm{ex}}} + 5e^{-E_2/T_{\mathrm{ex}}}}{3e^{-E_1/k_{\mathrm{B}}T_{\mathrm{ex}}}} \tag{A.5}$$

The optical depth of [CI](1–0) is given by

$$\tau([\mathrm{C\,I}](1-0)) = -\ln\left(1 - T_{\mathrm{mb}}\frac{e^{E_1/k_{\mathrm{B}}T_{\mathrm{ex}}}}{E_1}\right) \tag{A.6}$$

Figure A.2 shows the calculated $N(\mathrm{C}^0)$ as function of the excitation temperature for a $\int T_{\mathrm{mb}}([\mathrm{C\,I}](1\text{–}0))\mathrm{d}v$= 1 K km/s

A.3 COLUMN DENSITIES OF C^+

The C^+ column density can be approximated via (Goldsmith et al. 2012)

$$N(\mathrm{C}^+) = 2.9\times10^{15}\left(1 + 0.5e^{\frac{E}{k_{\mathrm{B}}T_{\mathrm{ex}}}}\left(1 + \frac{n_{\mathrm{crit}}}{n(\mathrm{H_x})}\right)\right) \frac{\tau}{1-e^{-\tau}}\frac{1}{\Phi_{\mathrm{B}}}\int T_{\mathrm{mb}}([\mathrm{C\,II}])\,\mathrm{d}v \tag{A.7}$$

with E/k_{B}=91.2 K.

The specific critical density can be calculated with Equation 4.2, $n_{\mathrm{crit}} = (1-e^{-\tau})/\tau \times A_{\mathrm{ul}}/C_{\mathrm{ul}}$. C^+ is present in almost all gas phases of the ISM (c.f. Section 2.1). Neutral atomic carbon in the main collision partner of C^+ in the WNM and CNM. In the molecular gas phase collisions with H_2 dominate.

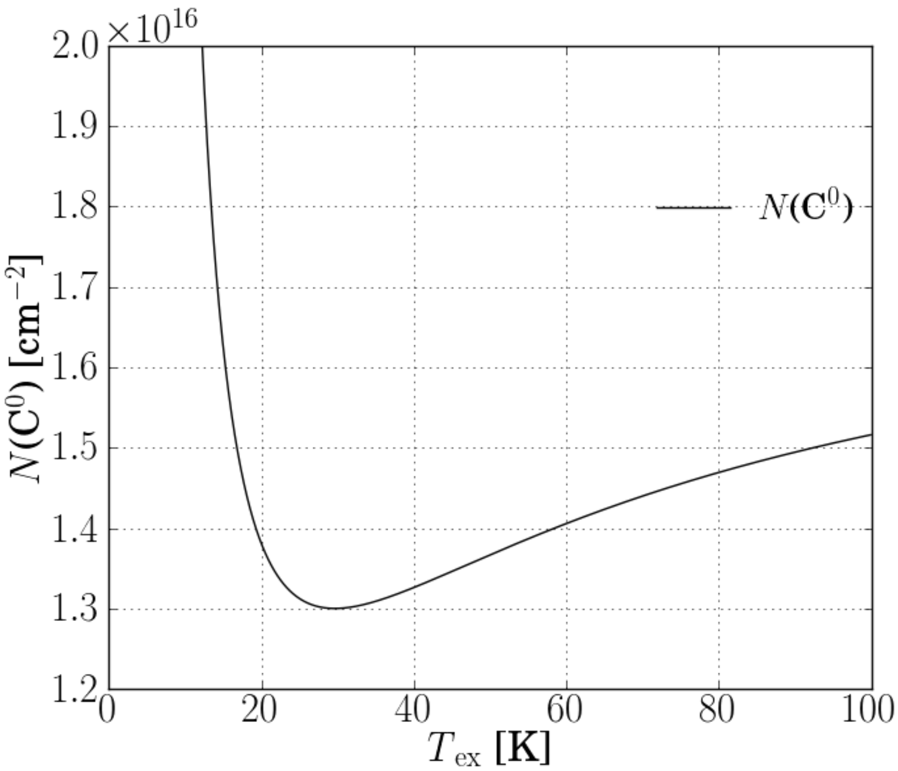

Figure A.2: Column densities of neutral atomic carbon in cm^{-2} as function of T_{ex} for an integrated [CI](1–0) line intensity of $\int T_{\mathrm{mb}}\,\mathrm{d}v = 1$ K km/s in the optically thin limit.

The collisional rate coefficient of C$^+$ for collisions with H^0 , $C_{\mathrm{ul}}(\mathrm{H}^0)$, can be fitted by (Goldsmith et al. 2012)

$$C_{\mathrm{ul}}(\mathrm{H}^0) = 7.6 \times 10^{-10}(T/100)^{0.14}\mathrm{cm}^3\mathrm{s}^{-1} \tag{A.8}$$

This fit is valid for temperatures between 20 K $\leq T \leq$ 2000 K. Equation (A.8) gives, for example, $n_{\mathrm{crit}}(\mathrm{H}^0)$= 3.1 $\times$ 10^3 cm^3 for T=100 and $n_{\mathrm{crit}}(\mathrm{H}^0)\simeq$ 2.8 $\times$ 10^3 cm^3 for T=200 K in the optically thin limit.

The collisional rate coefficient for collisions of C$^+$ with H$_2$ (Wiesenfeld & Goldsmith 2014) can be fitted by

$$C_{ul}(\mathrm{H}_2) = \left(4.55 + 1.6 \times e^{100K/T}\right) \times 10^{-10}\mathrm{cm}^3\mathrm{s}^{-1} \tag{A.9}$$

This expression is valid for clouds in LTE and temperature between $\sim$20 K to $\sim$400 K. This equation gives, for example, $n_{\mathrm{crit}}(\mathrm{H}_2)$=4.41 $\times 10^3$ cm^{-3} for T_{ex}=100 K, and 4.15 $\times$103 cm^{-3} for T_{ex}=200 K in the optically thin limit.

The collisional rate coefficient of C$^+$ for collisions with electrons can be estimated via (Goldsmith et al. 2012)

$$C_{ul}(e^-) = 8.7 \times 10^{-8}(T/2000)^{-0.37}\mathrm{cm}^3\mathrm{s}^{-1} \tag{A.10}$$

Figure A.3 shows the C$^+$ column densities for different excitation temperatures and hydrogen volume densities at the example of lines with an integrated intensity of $\int T_{\mathrm{mb}}$([CII])= 1 K km/s. The plot shows the solution for collisions with H^0 and H$_2$.

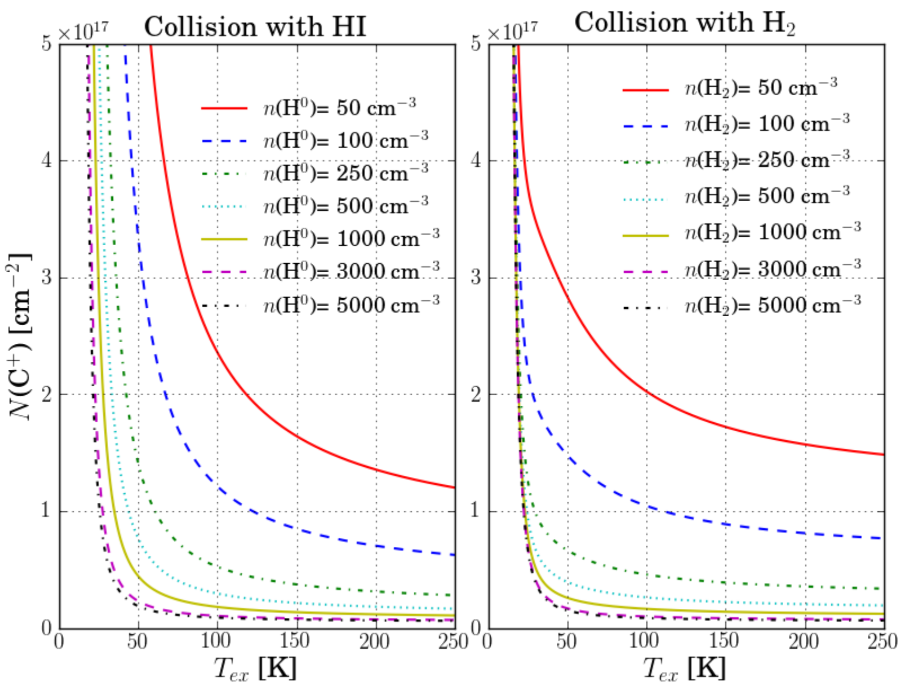

Figure A.3: Column densities of $[^{12}\mathrm{C}\,\textsc{ii}]$ in cm^{-2} for different neutral (left) and molecular (right) hydrogen volume densities as function of T_{ex} for an integrated [CII] line intensity of $\int T_{\mathrm{mb}}\, \mathrm{d}v = 1$ K km/s in the optically thin limit. The main collision partners are H^0 (left) and H_2(right), respectively.

A.4 COLUMN DENSITY OF NEUTRAL ATOMIC HYDROGEN

The column density of optically thin neutral atomic hydrogen in a local thermal equilibrium can be approximated via (e.g. Rohlfs & Wilson 2000)

$$N(\mathrm{H}^0) = 1.823 \times 10^{18} \int T_{\mathrm{mb}}(\mathrm{H\,\textsc{i}})\mathrm{d}v \tag{A.11}$$

This approximation is valid for brightness temperatures that are lower than the kinetic temperature.

It has to be considered that H^0 is the most abundant species in the ISM. Hence the HI transition may become optically thick. This can be accompanied by *HI-self absorption* (*HISA*; e.g. Burton, Liszt & Baker 1978). The strength of HISA can be used to calculate N(HI) as well. For further details, I recommend Dickey (2002).

Appendix B

Observation techniques in Radio Astronomy

The following section will give a brief overview of the technical background of radio telescopes and radio observations. The following section is based on the description in Wilson, Rohlfs & Hüttemeister (2009), Carlhoff (2013) and Guan (2013). For details of a theoretical background of telescopes and observing techniques I recommend Wilson, Rohlfs & Hüttemeister (2009). The influence of the atmosphere to the observations are elaborated in Guan (2013).

B.1 OBSERVATIONS WITH SINGLE DISH TELESCOPES

This thesis is based on data from single dish telescopes. These telescopes are the most common type in the millimetre and sub–millimetre astronomy. They consist of a system of mirrors, commonly a circular parabolic primary mirror and a secondary mirror (sometimes more mirrors are needed) that directs and focuses the incoming radiation into the optics of the receivers. This telescope designs aims to reach a high directivity. The angular extent of the received radiation is called beam pattern. The beam pattern is the Fourier transform of the aperture. It depends on the precise geometry and the observed frequency. The beam pattern of a parabolic single dish telescope is approximately described by a sinc function, with a maxima at its centre. As the function is cut-off at the edges it shows additional smaller maxima beside the beam centre, the so called side lobes. Further deviations are caused by the precise telescope geometry, as for example the position of the secondary mirror. Nevertheless the main beam almost have a Gaussian shape. Its full widths half maximum defines the resolution of the telescope. It can be approximated by

$$\Theta_{\mathrm{FWHM}} \approx 1.22 \times \frac{c}{\nu D} \tag{B.1}$$

with c being the speed of light, D the diameter of the primary mirror and ν the frequency of the observed line.

The incoming radio signal is converted to an electrical signal by receivers. Different receivers are in use, depending on requirements. I will describe Bolometers and Heterodyne receivers in the following, as these are of relevance for this thesis.

Bolometers are widely used for broad band and sensitive continuum observations. The incoming photons heats an absorber. This heating is measured and can be used to calculate the amount of the incoming energy.

This technique is highly sensitive to incoming the energy, but is does not provide any spectral informations. Velocity informations can be provided by the use of filters. PACS and SPIRE[i] are prominent receiver, that used the bolometer technique.

Spectra with a high spectral resolution are often observed with Heterodyne receivers in radio astronomy. The receiver mixes the incoming radiation with a sinus wave of a local oscillator (LO) and converts the signal to a lower frequency. The mixed signal contains still the spectral information of the incoming radiation. For example HIFI, GREAT and SMART use the Heterodyne technique.

The spectral information is observed via spectrometers, the so called back ends of the receiver. There are different types of spectrometers. The data used in this thesis was observed with accusto-optical spectrometers (AOSs) and Fast Fourier–transform spectrometers (FFTSs)[ii]. AOSs convert the signal into an acoustical signal which creates sound waves in a so called Bragg-cell[iii]. The sound waves change the refraction of the cell, which changes the deflation of laser beam, that shines to the cell. Finally the position change of the laser beam is detected by a CCD. AOSs are more and more replaced by FFTSs in the modern time, as they have less stringent temperature requirements and have higher resolutions. The time dependent signal is directly digitised by the FFTSs and transformed into a spectrum.

The observed intensity I_ν is commonly expressed by the brightness temperature T_B in radio astronomy, as mentioned in section 4.2. The brightness temperature is the black body equivalent temperature of the source with a temperature T. In the Rayleigh-Jeans approximation T_B is proportional to I_ν

$$T_\mathrm{B} = \frac{c^2}{2k_\mathrm{B}\nu^2} I_\nu \tag{B.2}$$

The receiver does not measure the brightness temperature. It detects the antenna temperature, T_A instead. The antenna temperature reflects external influences to the source signals as the attenuation by the atmosphere or a possible shielding of the antenna by a membrane[iv]. The detected emission that arises exclusively from the sky can be calculated by the division of T_A with the forward efficiency, η_{fw}

$$T_\mathrm{A}^* = \frac{T_\mathrm{A}}{\eta_\mathrm{fw}} \tag{B.3}$$

T_A^* contains all the emission observed that is detected from the sky. Commonly astronomers are interested in the temperature that is detected within the main-beam, the so called main-beam brightness temperature T_mb. The fraction of emission that arises from the main-beam is given by

i Both receiver were allocated at the Herschel space observatory

ii The AST/RO data was observed with used AOSs. The other observations analysed in this thesis are based on FFTs.

iii The Bragg-cell consist of a special crystal, such as tellurium dioxide (TeO_2), led molybdate ($PbMoO_4$) or crystalline quartz.

iv The Nanten2 telescope, , for example, is protected by a membrane against the environmental conditions.

so called the main-beam efficiency η_{mb}. Now, the main-beam brightness temperature is defined via

$$T_{\mathrm{mb}} = \frac{T_{\mathrm{A}}^{*}}{\eta_{\mathrm{mb}}} \tag{B.4}$$

Bibliography

N. P. Abel. The H^+ region contribution to [CII] 158-μm emission. MNRAS, 368:1949–1958, June 2006. doi: 10.1111/j.1365-2966.2006.10282.x.

S. Alexander. On the origin of the forms and the present condition of some of the clusters of stars, and several of the nebulae. AJ, 2:97–103, April 1852. doi: 10.1086/100231.

E. J. Alfaro & A. J. Delgado. *The Formation of the Milky Way.* March 2011.

L. J. Allamandola, A. G. G. M. Tielens, & J. R. Barker. Polycyclic aromatic hydrocarbons and the unidentified infrared emission bands - Auto exhaust along the Milky Way. ApJ, 290:L25–L28, March 1985. doi: 10.1086/184435.

N. Altobelli, F. Postberg, K. Fliege, M. Trieloff, H. Kimura, V. J. Sterken, H. W. Hsu, J. Hiller, N. Khawaja, G. Moragas-Klostermeyer, J. Blum, M. Burton, R. Srama, S. Kempf, & E. Gruen. Flux and composition of interstellar dust at Saturn from Cassini ' s Cosmic Dust Analyzer. *Science*, 352:312–318, April 2016.

S. Andree-Labsch, V. Ossenkopf, & M. Röllig. 3D modelling of clumpy PDRs - Understanding the Orion Bar stratification. *ArXiv e-prints*, May 2014.

B. Aschenbach. X-Ray Observations of Hot Thin Plasma in Supernova Remnants. In R. Pallavicini, editor, *NATO Advanced Science Institutes (ASI) Series C*, volume 249 of *NATO Advanced Science Institutes (ASI) Series C*, page 185, 1988.

P. L. Baker & W. B. Burton. Self-absorption and other characteristics of high-angular-resolution emission spectra of galactic H I. A&AS, 35: 129–152, February 1979.

E. L. O. Bakes & A. G. G. M. Tielens. The photoelectric heating mechanism for very small graphitic grains and polycyclic aromatic hydrocarbons. ApJ, 427:822–838, June 1994. doi: 10.1086/174188.

S. P. Balm. The Antarctic submillimetre telescope and remote observatory (AST/RO). PASA, 13:14–16, January 1996.

E. Becklin. The Stratospheric Observatory for Infrared Astronomy (SOFIA). *IAU General Assembly*, 22:46145, August 2015.

E. E. Becklin, A. G. G. M. Tielens, R. D. Gehrz, & H. H. S. Callis. Stratospheric Observatory for Infrared Astronomy (SOFIA). In

Society of Photo-Optical Instrumentation Engineers (SPIE) Conference Series, volume 6678 of *Society of Photo-Optical Instrumentation Engineers (SPIE) Conference Series*, page 0, September 2007. doi: 10.1117/12.735903.

L. R. Bedin, G. Piotto, G. Baume, Y. Momany, G. Carraro, J. Anderson, M. Messineo, & S. Ortolani. Star cluster detection with WFC/ACS in M 33. 33 new clusters and 51 candidates. A&A, 444:831–836, December 2005. doi: 10.1051/0004-6361:20053700.

V. Belokurov, M. J. Irwin, S. E. Koposov, N. W. Evans, E. Gonzalez-Solares, N. Metcalfe, & T. Shanks. ATLAS lifts the Cup: discovery of a new Milky Way satellite in Crater. MNRAS, 441:2124–2133, July 2014. doi: 10.1093/mnras/stu626.

R. A. Benjamin, E. Churchwell, & GLIMPSE Team. A Spitzer/GLIMPSE Investigation of the Stellar Spiral Structure of the Galaxy. In *American Astronomical Society Meeting Abstracts #206*, volume 37 of *Bulletin of the American Astronomical Society*, page 489, May 2005.

E. A. Bergin, L. W. Hartmann, J. C. Raymond, & J. Ballesteros-Paredes. Molecular Cloud Formation behind Shock Waves. ApJ, 612:921–939, September 2004. doi: 10.1086/422578.

H. Beuther, S. E. Ragan, V. Ossenkopf, S. Glover, T. Henning, H. Linz, M. Nielbock, O. Krause, J. Stutzki, P. Schilke, & R. Güsten. Carbon in different phases ([CII], [CI], and CO) in infrared dark clouds: Cloud formation signatures and carbon gas fractions. A&A, 571:A53, November 2014. doi: 10.1051/0004-6361/201424757.

H. Beuther, S. E. Ragan, V. Ossenkopf, S. Glover, T. Henning, H. Linz, M. Nielbock, O. Krause, J. Stutzki, P. Schilke, & R. Güsten. Carbon in different phases ([CII], [CI], and CO) in infrared dark clouds: Cloud formation signatures and carbon gas fractions (Corrigendum). A&A, 574:C2, February 2015. doi: 10.1051/0004-6361/201424757e.

E. Bica, C. Bonatto, B. Barbuy, & S. Ortolani. Globular cluster system and Milky Way properties revisited. A&A, 450:105–115, April 2006. doi: 10.1051/0004-6361:20054351.

T. G. Bisbas, T. A. Bell, S. Viti, J. Yates, & M. J. Barlow. 3D-PDR: a new three-dimensional astrochemistry code for treating photodissociation regions. MNRAS, 427:2100–2118, December 2012. doi: 10.1111/j.1365-2966.2012.22077.x.

L. Blitz & E. Rosolowsky. GMC Formation in M33: the Role of Pressure. In D. Johnstone, F. C. Adams, D. N. C. Lin, D. A. Neufeeld, & E. C. Ostriker, editors, *Star Formation in the Interstellar Medium: In Honor of David Hollenbach*, volume 323 of *Astronomical Society of the Pacific Conference Series*, page 89, December 2004.

L. Blitz & E. Rosolowsky. The Role of Pressure in GMC Formation II: The H_2-Pressure Relation. ApJ, 650:933–944, October 2006. doi: 10.1086/505417.

J. B. G. M. Bloemen, A. W. Strong, H. A. Mayer-Hasselwander, L. Blitz, R. S. Cohen, T. M. Dame, D. A. Grabelsky, P. Thaddeus, W. Hermsen, & F. Lebrun. The radial distribution of galactic gamma rays. III - The distribution of cosmic rays in the Galaxy and the CO-H2 calibration. A&A, 154:25–41, January 1986.

J. Blondel, M. Carter, A. Karpov, B. Lazareff, F. Mattiocco, & J. Lamb. Dual-channel sis receivers for the iram Plateau de Bure Interferometer. *International Journal of Infrared and Millimeter Waves*, 17:2133–2144, December 1996. doi: 10.1007/BF02069489.

R. C. Bohlin. Copernicus observations of interstellar absorption at Lyman alpha. ApJ, 200:402–414, September 1975. doi: 10.1086/153803.

R. C. Bohlin, B. D. Savage, & J. F. Drake. A survey of interstellar H I from L-alpha absorption measurements. II. ApJ, 224:132–142, August 1978. doi: 10.1086/156357.

A. D. Bolatto, M. Wolfire, & A. K. Leroy. The CO-to-H_2 Conversion Factor. ARA&A, 51:207–268, August 2013. doi: 10.1146/annurev-astro-082812-140944.

M. Boquien, D. Calzetti, F. Combes, C. Henkel, F. Israel, C. Kramer, M. Relaño, S. Verley, P. van der Werf, E. M. Xilouris, & HERM33ES Team. Dust Heating Sources in Galaxies: The Case of M33 (HERM33ES). AJ, 142:111, October 2011. doi: 10.1088/0004-6256/142/4/111.

M. Boquien, V. Buat, & V. Perret. Impact of star formation history on the measurement of star formation rates. A&A, 571:A72, November 2014. doi: 10.1051/0004-6361/201424441.

A. Boulares & D. P. Cox. Galactic hydrostatic equilibrium with magnetic tension and cosmic-ray diffusion. ApJ, 365:544–558, December 1990. doi: 10.1086/169509.

I. S. Bowen. The Origin of the Chief Nebular Lines. PASP, 39:295, October 1927a. doi: 10.1086/123745.

I. S. Bowen. The Origin of the Nebulium Spectrum. Nature, 120:473, October 1927b. doi: 10.1038/120473a0.

I. S. Bowen. Forbidden Lines. *Reviews of Modern Physics*, 8:55–81, April 1936. doi: 10.1103/RevModPhys.8.55.

C. Braiding, M. G. Burton, R. Blackwell, C. Glück, J. Hawkes, C. Kulesa, N. Maxted, D. Rebolledo, G. Rowell, A. Stark, N. Tothill, J. S. Urquhart, F. Voisin, A. J. Walsh, P. de Wilt, & G. F. Wong. The Mopra Southern Galactic Plane CO Survey - Data Release 1. PASA, 32:e020, May 2015. doi: 10.1017/pasa.2015.20.

J. Braine, P. Gratier, C. Kramer, E. M. Xilouris, E. Rosolowsky, C. Buchbender, M. Boquien, D. Calzetti, G. Quintana-Lacaci, F. Tabatabaei, S. Verley, F. Israel, F. van der Tak, S. Aalto, F. Combes, S. Garcia-Burillo, M. Gonzalez, C. Henkel, B. Koribalski, B. Mookerjea, M. Roellig, K. F. Schuster, M. Relaño, F. Bertoldi, P. van der Werf, & M. Wiedner. Cool gas and dust in M 33: Results from the HERschel M

33 Extended Survey (HERM33ES). A&A, 518:L69, July 2010. doi: 10.1051/0004-6361/201014551.

J. Braine, P. Gratier, Y. Contreras, K. F. Schuster, & N. Brouillet. A detailed view of a molecular cloud in the far outer disk of M 33. Molecular cloud formation in M 33. A&A, 548:A52, December 2012a. doi: 10.1051/0004-6361/201220093.

J. Braine, P. Gratier, C. Kramer, F. P. Israel, F. van der Tak, B. Mookerjea, M. Boquien, F. Tabatabaei, P. van der Werf, & C. Henkel. Spectrally resolved C II emission in M 33 (HerM33es). Physical conditions and kinematics around BCLMP 691. A&A, 544:A55, August 2012b. doi: 10.1051/0004-6361/201219360.

J. Brand & L. Blitz. The Velocity Field of the Outer Galaxy. A&A, 275: 67, August 1993.

R. Braun & D. Thilker. Tidal Streams and Low Mass Companions of M31. In F. Prada, D. Martinez Delgado, & T. J. Mahoney, editors, *Satellites and Tidal Streams*, volume 327 of *Astronomical Society of the Pacific Conference Series*, page 139, December 2004.

W. Brunswig. Remote Observing with the IRAM 30m Radiotelescope. In D. T. Emerson & R. G. Clowes, editors, *Proceedings of a Workshop on Remote Observing*, page 43, 1993.

C. Buchbender. *The cold and dense interstellar medium of M33, Ph.D. dissertation. Universidad de Granada: Spain. (Publication nbr. GR 873-2014).* 2013.

C. Buchbender, C. Kramer, M. Gonzalez-Garcia, F. P. Israel, S. García-Burillo, P. van der Werf, J. Braine, E. Rosolowsky, B. Mookerjea, S. Aalto, M. Boquien, P. Gratier, C. Henkel, G. Quintana-Lacaci, S. Verley, & F. van der Tak. Dense gas in M 33 (HerM33es). A&A, 549:A17, January 2013. doi: 10.1051/0004-6361/201219436.

E. B. Burgh, K. France, & S. R. McCandliss. Direct Measurement of the Ratio of Carbon Monoxide to Molecular Hydrogen in the Diffuse Interstellar Medium. ApJ, 658:446–454, March 2007. doi: 10.1086/511259.

M. Burton, J. Rathborne, J. L. Pineda Galvez, R. Simon, J. Urquhart, A. A. Stark, G. Rowell, N. Tothill, J. Storey, W. D. Langer, C. Martin, C. Walker, C. Kulesa, J. Stutzki, & D. Hollenbach. The Mopra STO Nanten2 Atomic and Molecular Gas Survey: The Formation of Giant Molecular Clouds. ATNF Proposal, April 2011.

M. Burton, J. Rathborne, J. L. Pineda Galvez, R. Simon, J. Urquhart, A. A. Stark, G. Rowell, N. Tothill, J. Storey, W. D. Langer, C. Martin, C. Walker, C. Kulesa, J. Stutzki, D. Hollenbach, C. Au, & C. Glueck. The Mopra-STO-Nanten2 Atomic and Molecular Gas Survey: The Formation of Giant Molecular Clouds. ATNF Proposal, April 2012.

M. G. Burton, C. Braiding, C. Glueck, P. Goldsmith, J. Hawkes, D. J. Hollenbach, C. Kulesa, C. L. Martin, J. L. Pineda, G. Rowell, R. Simon,

A. A. Stark, J. Stutzki, N. J. H. Tothill, J. S. Urquhart, C. Walker, A. J. Walsh, & M. Wolfire. The Mopra Southern Galactic Plane CO Survey. PASA, 30:e044, August 2013a. doi: 10.1017/pasa.2013.22.

M. G. Burton, C. Braiding, C. Glueck, P. Goldsmith, J. Hawkes, D. J. Hollenbach, C. Kulesa, C. L. Martin, J. L. Pineda, G. Rowell, R. Simon, A. A. Stark, J. Stutzki, N. J. H. Tothill, J. S. Urquhart, C. Walker, A. J. Walsh, & M. Wolfire. The Mopra Southern Galactic Plane CO Survey. PASA, 30:e044, August 2013b. doi: 10.1017/pasa.2013.22.

M. G. Burton, M. C. B. Ashley, C. Braiding, J. W. V. Storey, C. Kulesa, D. J. Hollenbach, M. Wolfire, C. Glück, & G. Rowell. The Carbon Inventory in a Quiescent, Filamentary Molecular Cloud in G328. ApJ, 782:72, February 2014. doi: 10.1088/0004-637X/782/2/72.

W. B. Burton, H. S. Liszt, & P. L. Baker. Atomic hydrogen in galactic molecular clouds. ApJ, 219:L67–L72, January 1978. doi: 10.1086/182608.

D. Calzetti, R. C. Kennicutt, C. W. Engelbracht, C. Leitherer, B. T. Draine, L. Kewley, J. Moustakas, M. Sosey, D. A. Dale, K. D. Gordon, G. X. Helou, D. J. Hollenbach, L. Armus, G. Bendo, C. Bot, B. Buckalew, T. Jarrett, A. Li, M. Meyer, E. J. Murphy, M. Prescott, M. W. Regan, G. H. Rieke, H. Roussel, K. Sheth, J. D. T. Smith, M. D. Thornley, & F. Walter. The Calibration of Mid-Infrared Star Formation Rate Indicators. ApJ, 666:870–895, September 2007. doi: 10.1086/520082.

J. A. Cardelli, D. M. Meyer, M. Jura, & B. D. Savage. The Abundance of Interstellar Carbon. ApJ, 467:334, August 1996. doi: 10.1086/177608.

P. Carlhoff. *Molecular Cloud Structure in the Star-forming Region W43, Ph.D. dissertation. Universität zu Köln.* 2013.

P. Carlhoff, Q. Nguyen Luong, P. Schilke, F. Motte, N. Schneider, H. Beuther, S. Bontemps, F. Heitsch, T. Hill, C. Kramer, V. Ossenkopf, F. Schuller, R. Simon, & F. Wyrowski. Large scale IRAM 30 m CO-observations in the giant molecular cloud complex W43. A&A, 560:A24, December 2013. doi: 10.1051/0004-6361/201321592.

S. Casassus, O. Stahl, & T. L. Wilson. Interstellar ^{12}C/^{13}C ratios through CHˆ+$\lambda\lambda$ 3957,4232 absorption in local clouds: incomplete mixing in the ISM. A&A, 441:181–194, October 2005. doi: 10.1051/0004-6361:20042149.

W. Chen, N. Gehrels, R. Diehl, & D. Hartmann. On the spiral arm interpretation of COMPTEL ˆ26ˆAl map features. A&AS, 120:C315, December 1996.

A. D. Chernin. Spiral patterns with straight arm segments. MNRAS, 308:321–332, September 1999. doi: 10.1046/j.1365-8711.1999.02585.x.

E. Churchwell & W. M. Goss. A High-Resolution VLA and Optical Study of NGC 604. ApJ, 514:188–194, March 1999. doi: 10.1086/306941.

E. Churchwell, B. L. Babler, M. R. Meade, B. A. Whitney, R. Benjamin, R. Indebetouw, C. Cyganowski, T. P. Robitaille, M. Povich, C. Watson, & S. Bracker. The Spitzer/GLIMPSE Surveys: A New View of the Milky Way. PASP, 121:213–230, March 2009. doi: 10.1086/597811.

D. Clayton. *Handbook of Isotopes in the Cosmos*. September 2003.

D. P. Clemens, D. B. Sanders, & N. Z. Scoville. The large-scale distribution of molecular gas in the first Galactic quadrant. ApJ, 327:139–155, April 1988. doi: 10.1086/166177.

A. L. Cooksy, G. A. Blake, & R. J. Saykally. Direct measurement of the fine-structure interval and gJ factors of singly ionized atomic carbon by laser magnetic resonance. ApJ, 305:L89–L92, June 1986. doi: 10.1086/184691.

E. Corbelli. Dark matter and visible baryons in M33. MNRAS, 342:199–207, June 2003. doi: 10.1046/j.1365-8711.2003.06531.x.

E. Corbelli, S. E. Schneider, & E. E. Salpeter. H I mapping of outer disks of galaxies - M33 and NGC 3344. AJ, 97:390–404, February 1989. doi: 10.1086/114989.

M. K. Crawford, R. Genzel, C. H. Townes, & D. M. Watson. Far-infrared spectroscopy of galaxies - The 158 micron C(+) line and the energy balance of molecular clouds. ApJ, 291:755–771, April 1985. doi: 10.1086/163113.

M. Cubick, J. Stutzki, V. Ossenkopf, C. Kramer, & M. Röllig. A clumpy-cloud photon-dominated regions model of the global far-infrared line emission of the Milky Way. A&A, 488:623–634, September 2008. doi: 10.1051/0004-6361:20079270.

A. Dalgarno. Interstellar Chemistry Special Feature: The galactic cosmic ray ionization rate. *Proceedings of the National Academy of Science*, 103:12269–12273, August 2006. doi: 10.1073/pnas.0602117103.

A. Dalgarno & R. A. McCray. Heating and Ionization of HI Regions. ARA&A, 10:375, 1972. doi: 10.1146/annurev.aa.10.090172.002111.

T. M. Dame, H. Ungerechts, R. S. Cohen, E. J. de Geus, I. A. Grenier, J. May, D. C. Murphy, L.-A. Nyman, & P. Thaddeus. A composite CO survey of the entire Milky Way. ApJ, 322:706–720, November 1987. doi: 10.1086/165766.

T. M. Dame, D. Hartmann, & P. Thaddeus. The Milky Way in Molecular Clouds: A New Complete CO Survey. ApJ, 547:792–813, February 2001. doi: 10.1086/318388.

C.-G. Danver. A Morphological Investigation of Some Near Galaxies with Regard to the Lengths and the Form of their Arms, their Inclinations and their Symmetry Properties. *Annals of the Observatory of Lund*, 10: 3–193, 1942.

T. de Graauw, F. P. Helmich, T. G. Phillips, J. Stutzki, E. Caux, N. D. Whyborn, P. Dieleman, P. R. Roelfsema, H. Aarts, R. Assendorp, R. Bachiller, W. Baechtold, A. Barcia, D. A. Beintema, V. Belitsky, A. O. Benz, R. Bieber, A. Boogert, C. Borys, B. Bumble, P. Caïs, M. Caris, P. Cerulli-Irelli, G. Chattopadhyay, S. Cherednichenko, M. Ciechanowicz, O. Coeur-Joly, C. Comito, A. Cros, A. de Jonge, G. de Lange, B. Delforges, Y. Delorme, T. den Boggende, J.-M. Desbat, C. Diez-González, A. M. di Giorgio, L. Dubbeldam, K. Edwards, M. Eggens, N. Erickson, J. Evers, M. Fich, T. Finn, B. Franke, T. Gaier, C. Gal, J. R. Gao, J.-D. Gallego, S. Gauffre, J. J. Gill, S. Glenz, H. Golstein, H. Goulooze, T. Gunsing, R. Güsten, P. Hartogh, W. A. Hatch, R. Higgins, E. C. Honingh, R. Huisman, B. D. Jackson, H. Jacobs, K. Jacobs, C. Jarchow, H. Javadi, W. Jellema, M. Justen, A. Karpov, C. Kasemann, J. Kawamura, G. Keizer, D. Kester, T. M. Klapwijk, T. Klein, E. Kollberg, J. Kooi, P.-P. Kooiman, B. Kopf, M. Krause, J.-M. Krieg, C. Kramer, B. Kruizenga, T. Kuhn, W. Laauwen, R. Lai, B. Larsson, H. G. Leduc, C. Leinz, R. H. Lin, R. Liseau, G. S. Liu, A. Loose, I. López-Fernandez, S. Lord, W. Luinge, A. Marston, J. Martín-Pintado, A. Maestrini, F. W. Maiwald, C. McCoey, I. Mehdi, A. Megej, M. Melchior, L. Meinsma, H. Merkel, M. Michalska, C. Monstein, D. Moratschke, P. Morris, H. Muller, J. A. Murphy, A. Naber, E. Natale, W. Nowosielski, F. Nuzzolo, M. Olberg, M. Olbrich, R. Orfei, P. Orleanski, V. Ossenkopf, T. Peacock, J. C. Pearson, I. Peron, S. Phillip-May, L. Piazzo, P. Planesas, M. Rataj, L. Ravera, C. Risacher, M. Salez, L. A. Samoska, P. Saraceno, R. Schieder, E. Schlecht, F. Schlöder, F. Schmülling, M. Schultz, K. Schuster, O. Siebertz, H. Smit, R. Szczerba, R. Shipman, E. Steinmetz, J. A. Stern, M. Stokroos, R. Teipen, D. Teyssier, T. Tils, N. Trappe, C. van Baaren, B.-J. van Leeuwen, H. van de Stadt, H. Visser, K. J. Wildeman, C. K. Wafelbakker, J. S. Ward, P. Wesselius, W. Wild, S. Wulff, H.-J. Wunsch, X. Tielens, P. Zaal, H. Zirath, J. Zmuidzinas, & F. Zwart. The Herschel-Heterodyne Instrument for the Far-Infrared (HIFI). A&A, 518:L6, July 2010. doi: 10.1051/0004-6361/201014698.

T. de Jong, A. Dalgarno, & W. Boland. Hydrostatic Models of Molecular Clouds. In B. H. Andrew, editor, *Interstellar Molecules*, volume 87 of *IAU Symposium*, page 177, 1980.

G. de Vaucouleurs. Classification and Morphology of External Galaxies. *Handbuch der Physik*, 53:275, 1959.

J. M. Dickey. Fitting the HISA with the CNM: The Distribution of Cool H I Temperatures. In A. R. Taylor, T. L. Landecker, & A. G. Willis, editors, *Seeing Through the Dust: The Detection of HI and the Exploration of the ISM in Galaxies*, volume 276 of *Astronomical Society of the Pacific Conference Series*, page 248, December 2002.

J. M. Dickey & F. J. Lockman. H I in the Galaxy. ARA&A, 28:215–261, 1990. doi: 10.1146/annurev.aa.28.090190.001243.

J. M. Dickey, S. R. Kulkarni, J. H. van Gorkom, & C. E. Heiles. A survey of H I absorption at low latitudes. ApJS, 53:591–621, November 1983. doi: 10.1086/190903.

R. L. Dickman. A survey of carbon monoxide emission in dark clouds. ApJ, 202:50–57, November 1975. doi: 10.1086/153951.

B. T. Draine. Photoelectric heating of interstellar gas. ApJS, 36:595–619, April 1978. doi: 10.1086/190513.

B. T. Draine. *Physics of the Interstellar and Intergalactic Medium*. 2011.

B. T. Draine & N. Katz. Magnetohydrodynamic shocks in diffuse clouds. I - Chemical processes. ApJ, 306:655–666, July 1986. doi: 10.1086/164375.

B. T. Draine & H. M. Lee. Optical properties of interstellar graphite and silicate grains. ApJ, 285:89–108, October 1984. doi: 10.1086/162480.

B. T. Draine & A. Li. Infrared Emission from Interstellar Dust. IV. The Silicate-Graphite-PAH Model in the Post-Spitzer Era. ApJ, 657:810–837, March 2007. doi: 10.1086/511055.

C. Druard, J. Braine, K. F. Schuster, N. Schneider, P. Gratier, S. Bontemps, M. Boquien, F. Combes, E. Corbelli, C. Henkel, F. Herpin, C. Kramer, F. van der Tak, & P. van der Werf. The IRAM M 33 CO(2-1) survey. A complete census of molecular gas out to 7 kpc. A&A, 567: A118, July 2014. doi: 10.1051/0004-6361/201423682.

C. P. Dullemond & C. Dominik. The Global Structure of Protoplanetary Disks. In J. Beaulieu, A. Lecavelier Des Etangs, & C. Terquem, editors, *Extrasolar Planets: Today and Tomorrow*, volume 321 of *Astronomical Society of the Pacific Conference Series*, page 361, December 2004.

A. S. Eddington. The conditions of emission of forbidden lines. MNRAS, 88:134–138, December 1927. doi: 10.1093/mnras/88.2.134.

Y. N. Efremov. On the chains of star complexes and superclouds in spiral arms. MNRAS, 405:1531–1543, July 2010. doi: 10.1111/j.1365-2966.2010.16578.x.

B. Efron. Bootstrap Methods: Another Look at the Jackknife. *The Annals of Statistics*, 7:1–26, 1979. doi: 10.1214/aos/1176344552.

B. Efron & R. J. Tibshirani. *An Introduction to the Bootstrap*. Taylor & Francis Ltd, May 1994.

B. G. Elmegreen. What do we really know about Cloud Formation? In L. Blitz & P. J. Teuben, editors, *Unsolved Problems of the Milky Way*, volume 169 of *IAU Symposium*, page 551, 1996.

B. G. Elmegreen, D. M. Elmegreen, & S. N. Leitner. A Turbulent Origin for Flocculent Spiral Structure in Galaxies. ApJ, 590:271–283, June 2003. doi: 10.1086/374860.

H. I. Ewen & E. M. Purcell. Observation of a Line in the Galactic Radio Spectrum: Radiation from Galactic Hydrogen at 1,420 Mc./sec. Nature, 168:356, September 1951. doi: 10.1038/168356a0.

E. Falgarone, B. Godard, J. Cernicharo, M. de Luca, M. Gerin, T. G. Phillips, J. H. Black, D. C. Lis, T. A. Bell, F. Boulanger, A. Coutens, E. Dartois, P. Encrenaz, T. Giesen, J. R. Goicoechea, P. F. Goldsmith, H. Gupta, C. Gry, P. Hennebelle, E. Herbst, P. Hily-Blant, C. Joblin, M. Kaźmierczak, R. Kołos, J. Krełowski, J. Martin-Pintado, R. Monje, B. Mookerjea, D. A. Neufeld, M. Perault, J. C. Pearson, C. Persson, R. Plume, M. Salez, M. Schmidt, P. Sonnentrucker, J. Stutzki, D. Teyssier, C. Vastel, S. Yu, K. Menten, T. R. Geballe, S. Schlemmer, R. Shipman, A. G. G. M. Tielens, S. Philipp, A. Cros, J. Zmuidzinas, L. A. Samoska, K. Klein, A. Lorenzani, R. Szczerba, I. Péron, P. Cais, P. Gaufre, A. Cros, L. Ravera, P. Morris, S. Lord, & P. Planesas. CH^+(1-0) and $^{13}CH^+$(1-0) absorption lines in the direction of massive star-forming regions. A&A, 521:L15, October 2010a. doi: 10.1051/0004-6361/201015109.

E. Falgarone, V. Ossenkopf, M. Gerin, P. Lesaffre, B. Godard, J. Pearson, S. Cabrit, C. Joblin, A. O. Benz, F. Boulanger, A. Fuente, R. Güsten, A. Harris, T. Klein, C. Kramer, S. Lord, P. Martin, J. Martin-Pintado, D. Neufeld, T. G. Phillips, M. Röllig, R. Simon, J. Stutzki, F. van der Tak, D. Teyssier, H. Yorke, N. Erickson, M. Fich, W. Jellema, A. Marston, C. Risacher, M. Salez, & F. Schmülling. Strong CH^+ J = 1-0 emission and absorption in DR21. A&A, 518:L118, July 2010b. doi: 10.1051/0004-6361/201014671.

K. M. Ferrière. The interstellar environment of our galaxy. *Reviews of Modern Physics*, 73:1031–1066, October 2001. doi: 10.1103/RevModPhys.73.1031.

F. Ferrini, M. Molla, M. C. Pardi, & A. I. Diaz. Evolution of spiral galaxies. 3: Application of the multiphase model to the galactic disk. ApJ, 427: 745–758, June 1994. doi: 10.1086/174181.

G. B. Field, W. B. Somerville, & K. Dressler. Hydrogen Molecules in Astronomy. ARA&A, 4:207, 1966. doi: 10.1146/annurev.aa.04.090166.001231.

P. D. Foote, T. Takamine, & R. L. Chenault. Excitation of Forbidden Spectral Lines. Nature, 115:265, February 1925. doi: 10.1038/115265a0.

A. Fowler. The Origin of the Nebulium Spectrum. Nature, 120:582–583, October 1927. doi: 10.1038/120582a0.

W. L. Freedman, C. D. Wilson, & B. F. Madore. New Cepheid distances to nearby galaxies based on BVRI CCD photometry. II - The local group galaxy M33. ApJ, 372:455–470, May 1991. doi: 10.1086/169991.

K. Freeman & J. Bland-Hawthorn. The New Galaxy: Signatures of Its Formation. ARA&A, 40:487–537, 2002. doi: 10.1146/annurev.astro.40.060401.093840.

B. Fryxell, K. Olson, P. Ricker, F. X. Timmes, M. Zingale, D. Q. Lamb, P. MacNeice, R. Rosner, J. W. Truran, & H. Tufo. FLASH: An Adaptive Mesh Hydrodynamics Code for Modeling Astrophysical Thermonuclear Flashes. ApJS, 131:273–334, November 2000. doi: 10.1086/317361.

Y. Fukui, R. Okamoto, R. Kaji, H. Yamamoto, K. Torii, T. Hayakawa, K. Tachihara, J. M. Dickey, T. Okuda, A. Ohama, Y. Kuroda, & T. Kuwahara. H I, CO, and Planck/IRAS Dust Properties in the High Latitude Cloud Complex, MBM 53, 54, 55 and HLCG 92 - 35. Possible Evidence for an Optically Thick H I Envelope around the CO Clouds. ApJ, 796:59, November 2014. doi: 10.1088/0004-637X/796/1/59.

S. Galleti, M. Bellazzini, & F. R. Ferraro. The distance of M 33 and the stellar population in its outskirts. A&A, 423:925–934, September 2004. doi: 10.1051/0004-6361:20040489.

G. Garay & S. Lizano. Massive Stars: Their Environment and Formation. PASP, 111:1049–1087, September 1999. doi: 10.1086/316416.

P. García, R. Simon, J. Stutzki, M. Requena-Torres, R. Güsten, Y. Fukui, H. Yamamoto, F. Bertoldi, M. Burton, L. Bronfman, & H. Ogawa. The warm ISM in the Sgr A region: mid-J CO, atomic carbon, ionized atomic carbon, and ionized nitrogen line observations with the Herschel/HIFI and NANTEN2/SMART Telescopes. In L. O. Sjouwerman, C. C. Lang, & J. Ott, editors, *IAU Symposium*, volume 303 of *IAU Symposium*, pages 73–74, May 2014. doi: 10.1017/S1743921314000180.

D. R. Garnett, G. A. Shields, M. Peimbert, S. Torres-Peimbert, E. D. Skillman, R. J. Dufour, E. Terlevich, & R. J. Terlevich. Carbon in Spiral Galaxies from Hubble Space Telescope Spectroscopy. ApJ, 513: 168–179, March 1999. doi: 10.1086/306860.

T. R. Geballe, B. J. McCall, K. H. Hinkle, & T. Oka. Detection of ${H^+}_3$ in the Diffuse Interstellar Medium: The Galactic Center and Cygnus OB2 Number 12. ApJ, 510:251–257, January 1999. doi: 10.1086/306580.

T. R. Geballe, N. Indriolo, B. J. McCall, & T. Oka. Abundant ${H_3}^+$ and High Values of ζ: Common Properties of Diffuse Clouds. In *American Astronomical Society Meeting Abstracts*, volume 39 of *Bulletin of the American Astronomical Society*, page 985, December 2007.

R. D. Gehrz, E. E. Becklin, I. de Pater, D. F. Lester, T. L. Roellig, & C. E. Woodward. A new window on the cosmos: The Stratospheric Observatory for Infrared Astronomy (SOFIA). *Advances in Space Research*, 44: 413–432, August 2009. doi: 10.1016/j.asr.2009.04.011.

F. C. Gillett, W. J. Forrest, & K. M. Merrill. 8 - 13-micron spectra of NGC 7027, BD +30 3639, and NGC 6572. ApJ, 183:87–93, July 1973. doi: 10.1086/152211.

P. Girichidis, S. Walch, T. Naab, A. Gatto, R. Wünsch, S. C. O. Glover, R. S. Klessen, P. C. Clark, T. Peters, D. Derigs, & C. Baczynski. The SILCC (SImulating the LifeCycle of molecular Clouds) project - II. Dynamical evolution of the supernova-driven ISM and the launching of outflows. MNRAS, 456:3432–3455, March 2016. doi: 10.1093/mnras/stv2742.

S. C. O. Glover & P. C. Clark. Is atomic carbon a good tracer of molecular gas in metal-poor galaxies? *ArXiv e-prints*, September 2015.

S. C. O. Glover & M.-M. Mac Low. Understanding the physics of the X-factor. In M. Röllig, R. Simon, V. Ossenkopf, & J. Stutzki, editors, *EAS Publications Series*, volume 52 of *EAS Publications Series*, pages 147–150, November 2011. doi: 10.1051/eas/1152023.

S. C. O. Glover, P. C. Clark, M. Micic, & F. Molina. Modelling [C I] emission from turbulent molecular clouds. MNRAS, 448:1607–1627, April 2015. doi: 10.1093/mnras/stu2699.

C. B. Glück, J. Stutzki, M. Röllig, E. T. Chambers, & C. Risacher. SOFIA/GREAT [CII] observations in nearby clouds near the lines of sight towards B0355+508 and B0212+735. A&A, 600:A94, April 2017. doi: 10.1051/0004-6361/201526454.

P. Gnacinski, M. Krogulec, & J. Krelowski. Interstellar CH, CH+ and abundance of atomic species. In *Molecules in Space and Laboratory*, page 23, December 2007.

B. Godard, E. Falgarone, M. Gerin, P. Hily-Blant, & M. de Luca. Molecular absorption lines toward star-forming regions: a comparative study of HCO^+, HNC, HCN, and CN. A&A, 520:A20, September 2010. doi: 10.1051/0004-6361/201014283.

P. Goldreich & J. Kwan. Molecular Clouds. ApJ, 189:441–454, May 1974. doi: 10.1086/152821.

P. F. Goldsmith. Molecular Depletion and Thermal Balance in Dark Cloud Cores. ApJ, 557:736–746, August 2001. doi: 10.1086/322255.

P. F. Goldsmith, W. D. Langer, J. L. Pineda, & T. Velusamy. Collisional Excitation of the [C II] Fine Structure Transition in Interstellar Clouds. ApJS, 203:13, November 2012. doi: 10.1088/0067-0049/203/1/13.

K. D. Gordon, M. M. Hanson, G. C. Clayton, G. H. Rieke, & K. A. Misselt. The Dusty Starburst Nucleus of M33. ApJ, 519:165–176, July 1999a. doi: 10.1086/307350.

S. M. Gordon, N. Duric, R. P. Kirshner, W. M. Goss, & F. Viallefond. A New Sample of Radio-selected and Optically Confirmed Supernova Remnants in M33. ApJS, 120:247–264, February 1999b. doi: 10.1086/313175.

U. U. Graf, S. Heyminck, E. A. Michael, S. Stanko, C. E. Honingh, K. Jacobs, R. Schieder, & J. Stutzki. SMART: The KOSMA Sub-Millimeter Array Receiver for Two frequencies. In *Thirteenth International Symposium on Space Terahertz Technology*, pages 143–152, March 2002.

U. U. Graf, S. Heyminck, R. Güsten, P. Hartogh, H.-W. Hübers, K. Jacobs, M. Philipp, D. Rabanus, H.-P. Röser, J. Stutzki, P. van der Wal, & A. Wagner-Gentner. GREAT: the German first light heterodyne instrument for SOFIA. In *Society of Photo-Optical Instrumentation Engineers (SPIE) Conference Series*, volume 6275 of Proc. SPIE, page 62750K, June 2006. doi: 10.1117/12.673168.

U. U. Graf, C. E. Honingh, K. Jacobs, M. Justen, P. Pütz, M. Schultz, S. Wulff, & J. Stutzki. Upgrade of the SMART Focal Plane Array Receiver for NANTEN2. In W. Wild, editor, *Ninteenth International Symposium on Space Terahertz Technology*, page 488, April 2008.

U. U. Graf, R. Simon, J. Stutzki, S. W. J. Colgan, X. Guan, R. Güsten, P. Hartogh, C. E. Honingh, & H.-W. Hübers. [^{12}Cii] and [^{13}C ii] 158 μm emission from NGC 2024: Large column densities of ionized carbon. A&A, 542:L16, June 2012. doi: 10.1051/0004-6361/201218930.

P. Gratier, J. Braine, N. J. Rodriguez-Fernandez, K. F. Schuster, C. Kramer, E. M. Xilouris, F. S. Tabatabaei, C. Henkel, E. Corbelli, F. Israel, P. P. van der Werf, D. Calzetti, S. Garcia-Burillo, A. Sievers, F. Combes, T. Wiklind, N. Brouillet, F. Herpin, S. Bontemps, S. Aalto, B. Koribalski, F. van der Tak, M. C. Wiedner, M. Röllig, & B. Mookerjea. Molecular and atomic gas in the Local Group galaxy M 33. A&A, 522:A3, November 2010. doi: 10.1051/0004-6361/201014441.

P. Gratier, J. Braine, N. J. Rodriguez-Fernandez, K. F. Schuster, C. Kramer, E. Corbelli, F. Combes, N. Brouillet, P. P. van der Werf, & M. Röllig. Giant molecular clouds in the Local Group galaxy M 33. A&A, 542:A108, June 2012. doi: 10.1051/0004-6361/201116612.

I. A. Grenier, J.-M. Casandjian, & R. Terrier. Unveiling Extensive Clouds of Dark Gas in the Solar Neighborhood. *Science*, 307:1292–1295, February 2005. doi: 10.1126/science.1106924.

M. Griffin, A. Abergel, P. Ade, P. André, J.-P. Baluteau, J. Bock, A. Franceschini, W. Gear, J. Glenn, D. Griffin, K. King, E. Lellouch, D. Naylor, G. Olofsson, I. Perez-Fournon, M. Rowan-Robinson, P. Saraceno, E. Sawyer, A. Smith, B. Swinyard, L. Vigroux, & G. Wright. Herschel-SPIRE: design, performance, and scientific capabilities. In *Society of Photo-Optical Instrumentation Engineers (SPIE) Conference Series*, volume 6265 of Proc. SPIE, page 62650A, June 2006. doi: 10.1117/12.670783.

M. J. Griffin, A. Abergel, A. Abreu, P. A. R. Ade, P. André, J.-L. Augueres, T. Babbedge, Y. Bae, T. Baillie, J.-P. Baluteau, M. J. Barlow, G. Bendo, D. Benielli, J. J. Bock, P. Bonhomme, D. Brisbin, C. Brockley-Blatt, M. Caldwell, C. Cara, N. Castro-Rodriguez, R. Cerulli, P. Chanial, S. Chen, E. Clark, D. L. Clements, L. Clerc, J. Coker, D. Communal, L. Conversi, P. Cox, D. Crumb, C. Cunningham, F. Daly, G. R. Davis, P. de Antoni, J. Delderfield, N. Devin, A. di Giorgio, I. Didschuns, K. Dohlen, M. Donati, A. Dowell, C. D. Dowell, L. Duband, L. Dumaye, R. J. Emery, M. Ferlet, D. Ferrand, J. Fontignie, M. Fox, A. Franceschini, M. Frerking, T. Fulton, J. Garcia, R. Gastaud, W. K. Gear, J. Glenn, A. Goizel, D. K. Griffin, T. Grundy, S. Guest, L. Guillemet, P. C. Hargrave, M. Harwit, P. Hastings, E. Hatziminaoglou, M. Herman, B. Hinde, V. Hristov, M. Huang, P. Imhof, K. J. Isaak, U. Israelsson, R. J. Ivison, D. Jennings, B. Kiernan, K. J. King, A. E. Lange, W. Latter, G. Laurent, P. Laurent, S. J. Leeks, E. Lellouch, L. Levenson, B. Li, J. Li, J. Lilienthal, T. Lim, S. J. Liu, N. Lu, S. Madden, G. Mainetti, P. Marliani, D. McKay, K. Mercier, S. Molinari, H. Morris, H. Moseley, J. Mulder, M. Mur, D. A. Naylor, H. Nguyen, B. O'Halloran, S. Oliver,

G. Olofsson, H.-G. Olofsson, R. Orfei, M. J. Page, I. Pain, P. Panuzzo, A. Papageorgiou, G. Parks, P. Parr-Burman, A. Pearce, C. Pearson, I. Pérez-Fournon, F. Pinsard, G. Pisano, J. Podosek, M. Pohlen, E. T. Polehampton, D. Pouliquen, D. Rigopoulou, D. Rizzo, I. G. Roseboom, H. Roussel, M. Rowan-Robinson, B. Rownd, P. Saraceno, M. Sauvage, R. Savage, G. Savini, E. Sawyer, C. Scharmberg, D. Schmitt, N. Schneider, B. Schulz, A. Schwartz, R. Shafer, D. L. Shupe, B. Sibthorpe, S. Sidher, A. Smith, A. J. Smith, D. Smith, L. Spencer, B. Stobie, R. Sudiwala, K. Sukhatme, C. Surace, J. A. Stevens, B. M. Swinyard, M. Trichas, T. Tourette, H. Triou, S. Tseng, C. Tucker, A. Turner, M. Vaccari, I. Valtchanov, L. Vigroux, E. Virique, G. Voellmer, H. Walker, R. Ward, T. Waskett, M. Weilert, R. Wesson, G. J. White, N. Whitehouse, C. D. Wilson, B. Winter, A. L. Woodcraft, G. S. Wright, C. K. Xu, A. Zavagno, M. Zemcov, L. Zhang, & E. Zonca. The Herschel-SPIRE instrument and its in-flight performance. A&A, 518:L3, July 2010. doi: 10.1051/0004-6361/201014519.

M. A. T. Groenewegen, A. Udalski, & G. Bono. The distance to the Galactic centre based on Population II Cepheids and RR Lyrae stars. A&A, 481:441–448, April 2008. doi: 10.1051/0004-6361:20079101.

X. Guan. *Atmospheric calibration for sub-millimeter radio astronomy , Ph.D. dissertation. Universität zu Köln.* 2013.

X. Guan, J. Stutzki, U. U. Graf, R. Güsten, Y. Okada, M. A. Requena-Torres, R. Simon, & H. Wiesemeyer. GREAT/SOFIA atmospheric calibration. A&A, 542:L4, June 2012. doi: 10.1051/0004-6361/201218925.

A. Gusdorf, S. Cabrit, D. R. Flower, & G. Pineau Des Forêts. SiO line emission from C-type shock waves: interstellar jets and outflows. A&A, 482:809–829, May 2008. doi: 10.1051/0004-6361:20078900.

R. Güsten, L. Å. Nyman, P. Schilke, K. Menten, C. Cesarsky, & R. Booth. The Atacama Pathfinder EXperiment (APEX) - a new submillimeter facility for southern skies -. A&A, 454:L13–L16, August 2006. doi: 10.1051/0004-6361:20065420.

H. J. Habing. The interstellar radiation density between 912 A and 2400 A. Bull. Astron. Inst. Netherlands, 19:421, January 1968.

H. Häsel & W. Neumann. *Physik.* 1995.

P. Hennebelle & M. Pérault. Dynamical condensation in a magnetized and thermally bistable flow. Application to interstellar cirrus. A&A, 359:1124–1138, July 2000.

T. Henning, editor. *Astromineralogy*, volume 815 of *Lecture Notes in Physics, Berlin Springer Verlag*, 2010. doi: 10.1007/978-3-642-13259-9.

I. Hermelo, M. Relaño, U. Lisenfeld, S. Verley, C. Kramer, T. Ruiz-Lara, M. Boquien, E. M. Xilouris, & M. Albrecht. Millimeter and Submillimeter Excess Emission in M33 revealed by Planck and LABOCA. *ArXiv e-prints*, March 2016.

S. Heyminck, U. U. Graf, R. Güsten, J. Stutzki, H. W. Hübers, & P. Hartogh. GREAT: the SOFIA high-frequency heterodyne instrument. A&A, 542:L1, June 2012. doi: 10.1051/0004-6361/201218811.

P. Hodge, editor. *The Spiral Galaxy M33*, volume 379 of *Astrophysics and Space Science Library*, 2012. doi: 10.1007/978-94-007-2025-1.

D. Hollenbach & E. E. Salpeter. Surface Recombination of Hydrogen Molecules. ApJ, 163:155, January 1971. doi: 10.1086/150754.

D. J. Hollenbach & A. G. G. M. Tielens. Photodissociation regions in the interstellar medium of galaxies. *Reviews of Modern Physics*, 71:173–230, January 1999. doi: 10.1103/RevModPhys.71.173.

D. J. Hollenbach, T. Takahashi, & A. G. G. M. Tielens. Low-density photodissociation regions. ApJ, 377:192–209, August 1991. doi: 10.1086/170347.

E. Holmberg. A photographic photometry of extragalactic nebulae. *Meddelanden fran Lunds Astronomiska Observatorium Serie II*, 136:1, 1958.

C. E. Honingh, S. Haas, D. Hottgenroth, K. Jacobs, & J. Stutzki. Determining Input Loss in SIS Receivers. In R. Blundell & E. Tong, editors, *Eighth International Symposium on Space Terahertz Technology*, page 92, 1997.

C. G. Hoopes & R. A. M. Walterbos. The Contribution of Field OB Stars to the Ionization of the Diffuse Ionized Gas in M33. ApJ, 541:597–609, October 2000. doi: 10.1086/309487.

R. M. Humphreys & A. Sandage. On the stellar content and structure of the spiral Galaxy M33. ApJS, 44:319–381, November 1980. doi: 10.1086/190696.

D. A. Hunter, W. A. Baum, E. J. O'Neil, Jr., & R. Lynds. The Intermediate Stellar Mass Population in NGC 604 Determined from Hubble Space Telescope Images. ApJ, 456:174, January 1996. doi: 10.1086/176638.

I. Hunter, P. L. Dufton, S. J. Smartt, R. S. I. Ryans, C. J. Evans, D. J. Lennon, C. Trundle, I. Hubeny, & T. Lanz. The VLT-FLAMES survey of massive stars: surface chemical compositions of B-type stars in the Magellanic Clouds. A&A, 466:277–300, April 2007. doi: 10.1051/0004-6361:20066148.

N. Indriolo, T. R. Geballe, T. Oka, & B. J. McCall. $H^+{}_3$ in Diffuse Interstellar Clouds: A Tracer for the Cosmic-Ray Ionization Rate. ApJ, 671:1736–1747, December 2007. doi: 10.1086/523036.

F. P. Israel. H_2 and its relation to CO in the LMC and other magellanic irregular galaxies. A&A, 328:471–482, December 1997.

Ž. Ivezić, B. Sesar, M. Jurić, N. Bond, J. Dalcanton, C. M. Rockosi, B. Yanny, H. J. Newberg, T. C. Beers, C. Allende Prieto, R. Wilhelm, Y. S. Lee, T. Sivarani, J. E. Norris, C. A. L. Bailer-Jones, P. Re Fiorentin, D. Schlegel, A. Uomoto, R. H. Lupton, G. R. Knapp, J. E. Gunn, K. R. Covey, J. A. Smith, G. Miknaitis, M. Doi, M. Tanaka,

M. Fukugita, S. Kent, D. Finkbeiner, J. A. Munn, J. R. Pier, T. Quinn, S. Hawley, S. Anderson, F. Kiuchi, A. Chen, J. Bushong, H. Sohi, D. Haggard, A. Kimball, J. Barentine, H. Brewington, M. Harvanek, S. Kleinman, J. Krzesinski, D. Long, A. Nitta, S. Snedden, B. Lee, H. Harris, J. Brinkmann, D. P. Schneider, & D. G. York. The Milky Way Tomography with SDSS. II. Stellar Metallicity. ApJ, 684:287–325, September 2008. doi: 10.1086/589678.

J. M. Jackson, J. M. Rathborne, R. Y. Shah, R. Simon, T. M. Bania, D. P. Clemens, E. T. Chambers, A. M. Johnson, M. Dormody, R. Lavoie, & M. H. Heyer. The Boston University-Five College Radio Astronomy Observatory Galactic Ring Survey. ApJS, 163:145–159, March 2006. doi: 10.1086/500091.

K. G. Jansky. Electrical phenomena that apparently are of interstellar origin. *Popular Astronomy*, 41:548, December 1933.

H. L. Johnson & W. W. Morgan. Fundamental stellar photometry for standards of spectral type on the revised system of the Yerkes spectral atlas. ApJ, 117:313, May 1953. doi: 10.1086/145697.

A. P. Jones. The Cycle of Carbon Dust in the ISM. In T. Henning, E. Grün, & J. Steinacker, editors, *Cosmic Dust - Near and Far*, volume 414 of *Astronomical Society of the Pacific Conference Series*, page 473, December 2009.

M. Jura. Interstellar clouds containing optically thin H2. ApJ, 197:575–580, May 1975. doi: 10.1086/153545.

M. Juvela, P. Padoan, & R. Jimenez. Photoelectric Heating and [C II] Cooling in Translucent Clouds: Results for Cloud Models Based on Simulations of Compressible Magnetohydrodynamic Turbulence. ApJ, 591:258–266, July 2003. doi: 10.1086/375344.

P. M. W. Kalberla & J. Kerp. The Hi Distribution of the Milky Way. ARA&A, 47:27–61, September 2009. doi: 10.1146/annurev-astro-082708-101823.

A. Karastergiou & R. Neri. Adapting and expanding the Plateau de Bure interferometer. In N. Solomos, editor, *Recent Advances in Astronomy and Astrophysics*, volume 848 of *American Institute of Physics Conference Series*, pages 857–863, August 2006. doi: 10.1063/1.2348070.

M. J. Kaufman, M. G. Wolfire, D. J. Hollenbach, & M. L. Luhman. Far-Infrared and Submillimeter Emission from Galactic and Extragalactic Photodissociation Regions. ApJ, 527:795–813, December 1999. doi: 10.1086/308102.

M. J. Kaufman, M. G. Wolfire, & D. J. Hollenbach. [Si II], [Fe II], [C II], and H_2 Emission from Massive Star-forming Regions. ApJ, 644:283–299, June 2006. doi: 10.1086/503596.

A. Kawamura, N. Mizuno, Y. Yonekura, T. Onishi, A. Mizuno, & Y. Fukui. NANTEN2: A Submillimeter Telescope for Large Scale Surveys at Atacama. In *IAU Symposium*, volume 235 of *IAU Symposium*, page 275P, 2005.

R. C. Kennicutt, Jr. Multi-wavelength Diagnostics of Star Formation Rates. In R.-R. Chary, H. I. Teplitz, & K. Sheth, editors, *Infrared Diagnostics of Galaxy Evolution*, volume 381 of *Astronomical Society of the Pacific Conference Series*, page 103, March 2008.

B. Klein, S. Hochgürtel, I. Krämer, A. Bell, K. Meyer, & R. Güsten. High-resolution wide-band fast Fourier transform spectrometers. A&A, 542: L3, June 2012. doi: 10.1051/0004-6361/201218864.

H. Klein, F. Lewen, R. Schieder, J. Stutzki, & G. Winnewisser. Precise Laboratory Observation of the $^3P_2 -> {}^3P_1$ Fine-Structure Transitions of ^{12}C and ^{13}C. ApJ, 494:L125–L128, February 1998. doi: 10.1086/311169.

G. R. Knapp. The life cycle of the Interstellar Medium in other galaxies. In M. R. Haas, J. A. Davidson, & E. F. Erickson, editors, *From Gas to Stars to Dust*, volume 73 of *Astronomical Society of the Pacific Conference Series*, 1995.

G. R. Knapp, A. A. Stark, & R. W. Wilson. The global properties of the Galaxy. III - Maps of the (C-12)(O) emission in the first quadrant of the Galaxy. AJ, 90:254–300, February 1985. doi: 10.1086/113729.

J. Koeppen & F. Cuisinier. The vertical abundance variation in the Galaxy as seen with planetary nebulae. In G. Klare, editor, *Astronomische Gesellschaft Abstract Series*, volume 10 of *Astronomische Gesellschaft Abstract Series*, page 101, 1994.

J. W. Kooi. Heterodyne Receiver Development at the Caltech Submillimeter Observatory. In D. C. Lis, J. E. Vaillancourt, P. F. Goldsmith, T. A. Bell, N. Z. Scoville, & J. Zmuidzinas, editors, *Submillimeter Astrophysics and Technology: a Symposium Honoring Thomas G. Phillips*, volume 417 of *Astronomical Society of the Pacific Conference Series*, page 377, December 2009.

J. W. Kooi, M. Chan, T. G. Phillips, B. Bumble, & H. G. Leduc. A Low Noise 230 GHz Heterodyne Receiver Employing .25μm^2 Nb/Al-AlO$_x$/Nb Tunnel Junctions459. In *Second International Symposium on Space Terahertz Technology*, page 459, February 1991.

J. W. Kooi, P. L. Schaffer, B. Bumble, R. Leduc, & T. G. Phillips. Heterodyne instrumentation at the CSO. In T. G. Phillips, editor, *Advanced Technology MMW, Radio, and Terahertz Telescopes*, volume 3357 of Proc. SPIE, pages 22–32, July 1998.

J. W. Kooi, R. R. Monje, B. L. Force, F. Rice, D. Miller, & T. G. Phillips. Measurement Results of the Caltech Submillimeter Observatory 230 GHz and 460 GHz Balanced Receivers. In *Twenty-First International Symposium on Space Terahertz Technology*, page 138, March 2010.

J. Kormendy & R. D. McClure. The nucleus of M33. AJ, 105:1793–1812, May 1993. doi: 10.1086/116555.

C. Kramer, C. Buchbender, G. Quintana-Lacaci, J. Braine, P. Gratier, & E. Rosolowsky. The interplay of dense gas and stars in M33.

Highlights of Astronomy, 15:415–415, November 2010. doi: 10.1017/S1743921310010033.

C. A. Kulesa, C. K. Walker, M. Schein, D. Golish, N. Tothill, P. Siegel, S. Weinreb, G. Jones, J. Bardin, K. Jacobs, C. L. Martin, J. Storey, M. Ashley, J. Lawrence, D. Luong-Van, J. Everett, L. Wang, L. Feng, Z. Zhu, J. Yan, J. Yang, X.-G. Zhang, X. Cui, X. Yuan, J. Hu, Z. Xu, Z. Jiang, H. Yang, Y. Li, B. Sun, W. Qin, & Z. Shang. Pre-HEAT: submillimeter site testing and astronomical spectra from Dome A, Antarctica. In *Ground-based and Airborne Telescopes II*, volume 7012 of Proc. SPIE, page 701249, July 2008. doi: 10.1117/12.789741.

J. Kwan & F. Valdes. The spatial and mass distributions of molecular clouds and spiral structure. ApJ, 315:92–103, April 1987. doi: 10.1086/165116.

K. K. Kwee, C. A. Muller, & G. Westerhout. The rotation of the inner parts of the Galactic System. Bull. Astron. Inst. Netherlands, 12:211, December 1954.

N. Ladd, C. Purcell, T. Wong, & S. Robertson. Beam Size, Shape and Efficiencies for the ATNF Mopra Radio Telescope at 86-115 GHz. PASA, 22:62–72, 2005. doi: 10.1071/AS04068.

K. R. Lang. *Essential Astrophysics*. 2013. doi: 10.1007/978-3-642-35963-7.

W. D. Langer, J. L. Pineda, & T. Velusamy. The scale height of gas traced by [C ii] in the Galactic plane. A&A, 564:A101, April 2014a. doi: 10.1051/0004-6361/201323281.

W. D. Langer, T. Velusamy, J. L. Pineda, K. Willacy, & P. F. Goldsmith. A Herschel [C ii] Galactic plane survey. II. CO-dark H_2 in clouds. A&A, 561:A122, January 2014b. doi: 10.1051/0004-6361/201322406.

T. R. Lauer, S. M. Faber, E. A. Ajhar, C. J. Grillmair, & P. A. Scowen. M32 +/- 1. AJ, 116:2263–2286, November 1998. doi: 10.1086/300617.

A. Leger & J. L. Puget. Identification of the 'unidentified' IR emission features of interstellar dust? A&A, 137:L5–L8, August 1984.

S. Lepp & J. M. Shull. Molecules in the early universe. ApJ, 280:465–469, May 1984. doi: 10.1086/162013.

A. K. Leroy, A. Bolatto, C. Bot, C. W. Engelbracht, K. Gordon, F. P. Israel, M. Rubio, K. Sandstrom, & S. Stanimirović. The Structure of a Low-metallicity Giant Molecular Cloud Complex. ApJ, 702:352–367, September 2009. doi: 10.1088/0004-637X/702/1/352.

A. K. Leroy, A. Bolatto, K. Gordon, K. Sandstrom, P. Gratier, E. Rosolowsky, C. W. Engelbracht, N. Mizuno, E. Corbelli, Y. Fukui, & A. Kawamura. The CO-to-H_2 Conversion Factor from Infrared Dust Emission across the Local Group. ApJ, 737:12, August 2011. doi: 10.1088/0004-637X/737/1/12.

H. Liszt & R. Lucas. Galactic OH absorption and emission toward a sample of compact extragalactic mm-wave continuum sources. A&A, 314:917–926, October 1996.

H. Liszt & R. Lucas. The structure and stability of interstellar molecular absorption line profiles at radio frequencies. A&A, 355:333–346, March 2000.

H. S. Liszt. Conversion from /C-12/O integrated intensity at 2.6 millimeter wavelength to hydrogen column density. ApJ, 262:198–200, November 1982. doi: 10.1086/160410.

H. S. Liszt & R. Lucas. CO in absorption and emission toward compact extragalactic radio continuum sources. A&A, 339:561–574, November 1998.

H. S. Liszt & J. Pety. Imaging diffuse clouds: bright and dark gas mapped in CO. A&A, 541:A58, May 2012. doi: 10.1051/0004-6361/201218771.

H. S. Liszt, J. Pety, & R. Lucas. The CO luminosity and CO-H_2 conversion factor of diffuse ISM: does CO emission trace dense molecular gas? A&A, 518:A45, July 2010. doi: 10.1051/0004-6361/201014510.

N. Lo, M. R. Cunningham, P. A. Jones, L. Bronfman, P. C. Cortes, R. Simon, V. Lowe, L. Fissel, & G. Novak. Tracing H_2 Column Density with Atomic Carbon (C I) and CO Isotopologs. ApJ, 797:L17, December 2014. doi: 10.1088/2041-8205/797/2/L17.

F. J. Lockman. The H I halo in the inner galaxy. ApJ, 283:90–97, August 1984. doi: 10.1086/162277.

R. Lucas & H. Liszt. The Plateau de Bure survey of galactic λ3mm HCOˆ+ˆ absorption toward compact extragalactic continuum sources. A&A, 307:237, March 1996.

W. J. Maciel & R. D. D. Costa. Metallicity gradients in the Milky Way. In K. Cunha, M. Spite, & B. Barbuy, editors, *IAU Symposium*, volume 265 of *IAU Symposium*, pages 317–324, March 2010. doi: 10.1017/S1743921310000803.

S. C. Madden, A. Poglitsch, N. Geis, G. J. Stacey, & C. H. Townes. [C II] 158 Micron Observations of IC 10: Evidence for Hidden Molecular Hydrogen in Irregular Galaxies. ApJ, 483:200–209, July 1997.

S. C. Madden, M. Galametz, D. Cormier, V. Lebouteiller, F. Galliano, S. Hony, M. Sauvage, M. Pohlen, G. Bendo, & B. O'Halloran. The Herschel Space Observatory View of the Gas and Dust Properties of Dwarf Galaxies. In M. Koleva, P. Prugniel, & I. Vauglin, editors, *EAS Publications Series*, volume 48 of *EAS Publications Series*, pages 139–145, July 2011. doi: 10.1051/eas/1148030.

L. Magrini, L. Stanghellini, & E. Villaver. The Planetary Nebula Population of M33 and its Metallicity Gradient: A Look Into the Galaxy's Distant Past. ApJ, 696:729–740, May 2009. doi: 10.1088/0004-637X/696/1/729.

L. Magrini, S. Randich, P. Donati, A. Bragaglia, V. Adibekyan, D. Romano, R. Smiljanic, S. Blanco-Cuaresma, G. Tautvaišienė, E. Friel, J. Overbeek, H. Jacobson, T. Cantat-Gaudin, A. Vallenari, R. Sordo,

E. Pancino, D. Geisler, I. San Roman, S. Villanova, A. Casey, A. Hourihane, C. C. Worley, P. Francois, G. Gilmore, T. Bensby, E. Flaccomio, A. J. Korn, A. Recio-Blanco, G. Carraro, M. T. Costado, E. Franciosini, U. Heiter, P. Jofré, C. Lardo, P. de Laverny, L. Monaco, L. Morbidelli, G. Sacco, S. G. Sousa, & S. Zaggia. The Gaia-ESO Survey: Insights into the inner-disc evolution from open clusters. A&A, 580:A85, August 2015. doi: 10.1051/0004-6361/201526305.

D. Majaess. Concerning the Distance to the Center of the Milky Way and Its Structure. Acta Astron., 60:55–74, March 2010.

S. Makiuti, H. Shibai, T. Nakagawa, H. Okuda, K. Okumura, H. Matsuhara, N. Hiromoto, & Y. Doi. Diffuse far-infrared [C II] line emission from high Galactic latitude. A&A, 382:600–609, February 2002. doi: 10.1051/0004-6361:20011626.

S. Malhotra. High altitude molecular clouds. ApJ, 437:194–203, December 1994a. doi: 10.1086/174988.

S. Malhotra. The vertical equilibrium of molecular gas in the Galactic disk. ApJ, 433:687–704, October 1994b. doi: 10.1086/174677.

S. Malhotra, M. J. Kaufman, D. Hollenbach, G. Helou, R. H. Rubin, J. Brauher, D. Dale, N. Y. Lu, S. Lord, G. Stacey, A. Contursi, D. A. Hunter, & H. Dinerstein. Far-Infrared Spectroscopy of Normal Galaxies: Physical Conditions in the Interstellar Medium. ApJ, 561:766–786, November 2001. doi: 10.1086/323046.

D. C. V. Mallik. Temperature and Emission-Line Structure at the Edges of H II Regions. ApJ, 197:355–364, April 1975. doi: 10.1086/153521.

J. G. Mangum & Y. L. Shirley. How to Calculate Molecular Column Density. PASP, 127:266–298, March 2015. doi: 10.1086/680323.

N. F. Martin, A. W. McConnachie, M. Irwin, L. M. Widrow, A. M. N. Ferguson, R. A. Ibata, J. Dubinski, A. Babul, S. Chapman, M. Fardal, G. F. Lewis, J. Navarro, & R. M. Rich. PAndAS' CUBS: Discovery of Two New Dwarf Galaxies in the Surroundings of the Andromeda and Triangulum Galaxies. ApJ, 705:758–765, November 2009. doi: 10.1088/0004-637X/705/1/758.

J. S. Mathis, W. Rumpl, & K. H. Nordsieck. The size distribution of interstellar grains. ApJ, 217:425–433, October 1977. doi: 10.1086/155591.

R. Mauersberger. Highlights from the IRAM-30m Telescope. In *1^er^ Congreso Nacional de Astrofísica Molecular: Una visión general del potencial de los grupos de química españoles anters los nuevos desafíos de la Astrofísica*, page 13, 2003.

D. McCammon & W. T. Sanders. The soft X-ray background and its origins. ARA&A, 28:657–688, 1990. doi: 10.1146/annurev.aa.28.090190.003301.

N. M. McClure-Griffiths & J. M. Dickey. Milky Way Kinematics. I. Measurements at the Subcentral Point of the Fourth Quadrant. ApJ, 671: 427–438, December 2007. doi: 10.1086/522297.

N. M. McClure-Griffiths, J. M. Dickey, B. M. Gaensler, A. J. Green, M. Haverkorn, & S. Strasser. The Southern Galactic Plane Survey: H I Observations and Analysis. ApJS, 158:178–187, June 2005. doi: 10.1086/430114.

R. McCray & M. Kafatos. Supershells and propagating star formation. ApJ, 317:190–196, June 1987. doi: 10.1086/165267.

S. E. Meidt, E. Schinnerer, S. García-Burillo, A. Hughes, D. Colombo, J. Pety, C. L. Dobbs, K. F. Schuster, C. Kramer, A. K. Leroy, G. Dumas, & T. A. Thompson. Gas Kinematics on Giant Molecular Cloud Scales in M51 with PAWS: Cloud Stabilization through Dynamical Pressure. ApJ, 779:45, December 2013. doi: 10.1088/0004-637X/779/1/45.

K. M. Menten, F. Wyrowski, A. Belloche, R. Güsten, L. Dedes, & H. S. P. Müller. Submillimeter absorption from SH^+, a new widespread interstellar radical, $^{13}CH^+$ and HCl. A&A, 525:A77, January 2011. doi: 10.1051/0004-6361/201014363.

S. N. Milam, C. Savage, M. A. Brewster, L. M. Ziurys, & S. Wyckoff. The $^{12}C/^{13}C$ Isotope Gradient Derived from Millimeter Transitions of CN: The Case for Galactic Chemical Evolution. ApJ, 634:1126–1132, December 2005. doi: 10.1086/497123.

S. Molinari, J. Bally, S. Glover, T. Moore, A. Noreiga-Crespo, R. Plume, L. Testi, E. Vázquez-Semadeni, A. Zavagno, J.-P. Bernard, & P. Martin. The Milky Way as a Star Formation Engine. *Protostars and Planets VI*, pages 125–148, 2014. doi: 10.2458/azu_uapress_9780816531240-ch006.

M. Molla, F. Ferrini, & A. I. Diaz. Evolution of Spiral Galaxies. VII. Time Evolution of the Radial Distributions of Abundances. ApJ, 475:519–533, February 1997.

B. Mookerjea, C. Kramer, C. Buchbender, M. Boquien, S. Verley, M. Relaño, G. Quintana-Lacaci, S. Aalto, J. Braine, D. Calzetti, F. Combes, S. Garcia-Burillo, P. Gratier, C. Henkel, F. Israel, S. Lord, T. Nikola, M. Röllig, G. Stacey, F. S. Tabatabaei, F. van der Tak, & P. van der Werf. The Herschel M 33 extended survey (HerM33es): PACS spectroscopy of the star forming region BCLMP 302 (Corrigendum). A&A, 537:C3, January 2012. doi: 10.1051/0004-6361/201116447e.

B. Mookerjea, F. Israel, C. Kramer, T. Nikola, J. Braine, V. Ossenkopf, M. Röllig, C. Henkel, P. van der Werf, F. van der Tak, & M. C. Wiedner. Velocity resolved [C ii] spectroscopy of the center and the BCLMP 302 region of M 33 (HerM 33es). A&A, 586:A37, February 2016. doi: 10.1051/0004-6361/201527366.

G. G. Moorey, M. W. Sinclair, & J. M. Payne. 3 mm SIS receiver for the Australia Telescope 22 metre Mopra antenna. In W. B. Latter, S. J. E. Radford, P. R. Jewell, J. G. Mangum, & J. Bally, editors, *IAU Symposium*, volume 170 of *IAU Symposium*, page 441, 1997.

C. A. Muller & J. H. Oort. Observation of a Line in the Galactic Radio Spectrum: The Interstellar Hydrogen Line at 1,420 Mc./sec., and an Estimate of Galactic Rotation. Nature, 168:357–358, September 1951. doi: 10.1038/168357a0.

H. S. P. Müller, S. Thorwirth, D. A. Roth, & G. Winnewisser. The Cologne Database for Molecular Spectroscopy, CDMS. A&A, 370:L49–L52, April 2001. doi: 10.1051/0004-6361:20010367.

H. S. P. Müller, F. Schlöder, J. Stutzki, S. Schlemmer, T. Giesen, & P. Schilke. The Cologne Database for Molecular Spectroscopy, CDMS: A Tool for Astrochemists and Astrophysicists. In *IAU Symposium*, volume 235 of *IAU Symposium*, page 62P, 2005.

H. S. P. Müller, S. Schlemmer, & J. Stutzki. The Cologne Database for Molecular Spectroscopy, CDMS. In M. Guainazzi & P. Osuna, editors, *Astronomical Spectroscopy and Virtual Observatory*, page 191, October 2008.

E. J. Murphy, J. J. Condon, E. Schinnerer, R. C. Kennicutt, D. Calzetti, L. Armus, G. Helou, J. L. Turner, G. Aniano, P. Beirão, A. D. Bolatto, B. R. Brandl, K. V. Croxall, D. A. Dale, J. L. Donovan Meyer, B. T. Draine, C. Engelbracht, L. K. Hunt, C.-N. Hao, J. Koda, H. Roussel, R. Skibba, & J.-D. T. Smith. Calibrating Extinction-free Star Formation Rate Diagnostics with 33 GHz Free-free Emission in NGC 6946. ApJ, 737:67, August 2011. doi: 10.1088/0004-637X/737/2/67.

T. Nakagawa, Y. Y. Yui, Y. Doi, H. Okuda, H. Shibai, K. Mochizuki, T. Nishimura, & F. J. Low. Far-Infrared [C II] Line Survey Observations of the Galactic Plane. ApJS, 115:259–269, April 1998. doi: 10.1086/313082.

C. A. Narayan & C. J. Jog. Vertical scaleheights in a gravitationally coupled, three-component Galactic disk. A&A, 394:89–96, October 2002. doi: 10.1051/0004-6361:20021128.

D. Narayanan & P. F. Hopkins. Why is the Milky Way X-factor constant? MNRAS, 433:1223–1229, August 2013. doi: 10.1093/mnras/stt784.

G. Neugebauer, H. J. Habing, R. van Duinen, H. H. Aumann, B. Baud, C. A. Beichman, D. A. Beintema, N. Boggess, P. E. Clegg, T. de Jong, J. P. Emerson, T. N. Gautier, F. C. Gillett, S. Harris, M. G. Hauser, J. R. Houck, R. E. Jennings, F. J. Low, P. L. Marsden, G. Miley, F. M. Olnon, S. R. Pottasch, E. Raimond, M. Rowan-Robinson, B. T. Soifer, R. G. Walker, P. R. Wesselius, & E. Young. The Infrared Astronomical Satellite (IRAS) mission. ApJ, 278:L1–L6, March 1984. doi: 10.1086/184209.

S. Nishiyama, T. Nagata, D. Baba, Y. Haba, R. Kadowaki, D. Kato, M. Kurita, C. Nagashima, T. Nagayama, Y. Murai, Y. Nakajima, M. Tamura, H. Nakaya, K. Sugitani, T. Naoi, N. Matsunaga, T. Tanabé, N. Kusakabe, & S. Sato. A Distinct Structure inside the Galactic Bar. ApJ, 621:L105–L108, March 2005. doi: 10.1086/429291.

T. E. Oberst, S. C. Parshley, G. J. Stacey, T. Nikola, A. Löhr, J. I. Harnett, N. F. H. Tothill, A. P. Lane, A. A. Stark, & C. E. Tucker. Detection of the 205 μm [N II] Line from the Carina Nebula. ApJ, 652:L125–L128, December 2006. doi: 10.1086/510289.

T. E. Oberst, S. C. Parshley, T. Nikola, G. J. Stacey, A. Löhr, A. P. Lane, A. A. Stark, & J. Kamenetzky. A 205 μm [N II] Map of the Carina Nebula. ApJ, 739:100, October 2011. doi: 10.1088/0004-637X/739/2/100.

S. S. R. Offner, T. G. Bisbas, S. Viti, & T. A. Bell. Modeling the Atomic-to-molecular Transition and Chemical Distributions of Turbulent Star-forming Clouds. ApJ, 770:49, June 2013. doi: 10.1088/0004-637X/770/1/49.

S. S. R. Offner, T. G. Bisbas, T. A. Bell, & S. Viti. An alternative accurate tracer of molecular clouds: the 'X_{CI}-factor'. MNRAS, 440: L81–L85, May 2014. doi: 10.1093/mnrasl/slu013.

Y. Okada, M. A. Requena-Torres, R. Güsten, J. Stutzki, H. Wiesemeyer, P. Pütz, & O. Ricken. Velocity resolved [C ii], [C i], and CO observations of the N159 star-forming region in the Large Magellanic Cloud: a complex velocity structure and variation of the column densities. A&A, 580:A54, August 2015. doi: 10.1051/0004-6361/201525630.

V. Ossenkopf, M. Röllig, D. A. Neufeld, P. Pilleri, D. C. Lis, A. Fuente, F. F. S. van der Tak, & E. Bergin. Herschel/HIFI observations of [C II] and [^{13}C II] in photon-dominated regions. A&A, 550:A57, February 2013. doi: 10.1051/0004-6361/201219837.

E. C. Ostriker & W.-T. Kim. Origins of Giant Molecular Clouds. In D. Clemens, R. Shah, & T. Brainerd, editors, *Milky Way Surveys: The Structure and Evolution of our Galaxy*, volume 317 of *Astronomical Society of the Pacific Conference Series*, page 248, December 2004.

B. E. J. Pagel, M. G. Edmunds, R. A. E. Fosbury, & B. L. Webster. A survey of chemical compositions of H II regions in the Magellanic Clouds. MNRAS, 184:569–592, August 1978. doi: 10.1093/mnras/184.3.569.

A. Parikka, M. Juvela, V.-M. Pelkonen, J. Malinen, & J. Harju. The physical state of selected cold clumps. A&A, 577:A69, May 2015. doi: 10.1051/0004-6361/201423428.

T. J. Parkin, C. D. Wilson, K. Foyle, M. Baes, G. J. Bendo, A. Boselli, M. Boquien, A. Cooray, D. Cormier, J. I. Davies, S. A. Eales, M. Galametz, H. L. Gomez, V. Lebouteiller, S. Madden, E. Mentuch, M. J. Page, M. Pohlen, A. Remy, H. Roussel, M. Sauvage, M. W. L. Smith, & L. Spinoglio. The gas-to-dust mass ratio of Centaurus A as seen by Herschel. MNRAS, 422:2291–2301, May 2012. doi: 10.1111/j.1365-2966.2012.20778.x.

E. Peeters, N. L. Martín-Hernández, F. Damour, P. Cox, P. R. Roelfsema, J.-P. Baluteau, A. G. G. M. Tielens, E. Churchwell, M. F. Kessler, J. S. Mathis, C. Morisset, & D. Schaerer. ISO spectroscopy of compact H II regions in the Galaxy. I. The catalogue. A&A, 381:571–605, January 2002. doi: 10.1051/0004-6361:20011516.

A. A. Penzias & R. W. Wilson. A Measurement of Excess Antenna Temperature at 4080 Mc/s. ApJ, 142:419–421, July 1965. doi: 10.1086/148307.

G. Peres, F. Reale, A. Collura, & G. Fabbiano. Time variability of the X-ray sources in M33. ApJ, 336:140–151, January 1989. doi: 10.1086/167001.

J. P. Pérez-Beaupuits, J. Stutzki, V. Ossenkopf, M. Spaans, R. Güsten, & H. Wiesemeyer. Detection of a large fraction of atomic gas not associated with star-forming material in M17 SW. A&A, 575:A9, March 2015. doi: 10.1051/0004-6361/201425020.

J. Pety, R. Lucas, & H. S. Liszt. Imaging galactic diffuse gas: bright, turbulent CO surrounding the line of sight to NRAO150. A&A, 489:217–228, October 2008a. doi: 10.1051/0004-6361:200809803.

J. Pety, R. Lucas, & H. S. Liszt. Imaging galactic diffuse gas: bright, turbulent CO surrounding the line of sight to NRAO150. A&A, 489:217–228, October 2008b. doi: 10.1051/0004-6361:200809803.

J. Pety, H. S. Liszt, & R. Lucas. The CO-H_2 conversion factor of diffuse ISM: Bright ^{12}CO emission also traces diffuse gas. 52:151–155, November 2011. doi: 10.1051/eas/1152024.

J. Pety, E. Schinnerer, A. K. Leroy, A. Hughes, S. E. Meidt, D. Colombo, G. Dumas, S. García-Burillo, K. F. Schuster, C. Kramer, C. L. Dobbs, & T. A. Thompson. The Plateau de Bure + 30 m Arcsecond Whirlpool Survey Reveals a Thick Disk of Diffuse Molecular Gas in the M51 Galaxy. ApJ, 779:43, December 2013. doi: 10.1088/0004-637X/779/1/43.

T. G. Phillips. The Caltech Submillimeter Observatory (CSO). In *American Astronomical Society Meeting Abstracts #188*, volume 28 of *Bulletin of the American Astronomical Society*, page 863, May 1996.

W. Pietsch, B. J. Mochejska, Z. Misanovic, F. Haberl, M. Ehle, & G. Trinchieri. The eclipsing massive X-ray binary M 33 X-7: New X-ray observations and optical identification. A&A, 413:879–887, January 2004. doi: 10.1051/0004-6361:20034081.

G. L. Pilbratt, J. R. Riedinger, T. Passvogel, G. Crone, D. Doyle, U. Gageur, A. M. Heras, C. Jewell, L. Metcalfe, S. Ott, & M. Schmidt. Herschel Space Observatory. An ESA facility for far-infrared and submillimetre astronomy. A&A, 518:L1, July 2010. doi: 10.1051/0004-6361/201014759.

G. Pineau des Forets, E. Roueff, & D. R. Flower. Theoretical studies of interstellar molecular shocks. IV - The sulphur chemistry in diffuse clouds. MNRAS, 223:743–756, December 1986. doi: 10.1093/mnras/223.4.743.

J. L. Pineda, W. D. Langer, T. Velusamy, & P. F. Goldsmith. A Herschel [C ii] Galactic plane survey. I. The global distribution of ISM gas components. A&A, 554:A103, June 2013. doi: 10.1051/0004-6361/201321188.

J. L. Pineda, W. D. Langer, & P. F. Goldsmith. A Herschel [C II] Galactic plane survey. III. [C II] as a tracer of star formation. A&A, 570:A121, October 2014. doi: 10.1051/0004-6361/201424054.

Planck Collaboration, P. A. R. Ade, N. Aghanim, M. I. R. Alves, C. Armitage-Caplan, M. Arnaud, M. Ashdown, F. Atrio-Barandela, J. Aumont, H. Aussel, & et al. Planck 2013 results. I. Overview of products and scientific results. A&A, 571:A1, November 2014a. doi: 10.1051/0004-6361/201321529.

Planck Collaboration, P. A. R. Ade, N. Aghanim, C. Armitage-Caplan, M. Arnaud, M. Ashdown, F. Atrio-Barandela, J. Aumont, C. Baccigalupi, A. J. Banday, & et al. Planck 2013 results. XVI. Cosmological parameters. A&A, 571:A16, November 2014b. doi: 10.1051/0004-6361/201321591.

A. Poglitsch, C. Waelkens, N. Geis, H. Feuchtgruber, B. Vandenbussche, L. Rodriguez, O. Krause, E. Renotte, C. van Hoof, P. Saraceno, J. Cepa, F. Kerschbaum, P. Agnèse, B. Ali, B. Altieri, P. Andreani, J.-L. Augueres, Z. Balog, L. Barl, O. H. Bauer, N. Belbachir, M. Benedettini, N. Billot, O. Boulade, H. Bischof, J. Blommaert, E. Callut, C. Cara, R. Cerulli, D. Cesarsky, A. Contursi, Y. Creten, W. De Meester, V. Doublier, E. Doumayrou, L. Duband, K. Exter, R. Genzel, J.-M. Gillis, U. Grözinger, T. Henning, J. Herreros, R. Huygen, M. Inguscio, G. Jakob, C. Jamar, C. Jean, J. de Jong, R. Katterloher, C. Kiss, U. Klaas, D. Lemke, D. Lutz, S. Madden, B. Marquet, J. Martignac, A. Mazy, P. Merken, F. Montfort, L. Morbidelli, T. Müller, M. Nielbock, K. Okumura, R. Orfei, R. Ottensamer, S. Pezzuto, P. Popesso, J. Putzeys, S. Regibo, V. Reveret, P. Royer, M. Sauvage, J. Schreiber, J. Stegmaier, D. Schmitt, J. Schubert, E. Sturm, M. Thiel, G. Tofani, R. Vavrek, M. Wetzstein, E. Wieprecht, & E. Wiezorrek. The Photodetector Array Camera and Spectrometer (PACS) on the Herschel Space Observatory. A&A, 518:L2, July 2010. doi: 10.1051/0004-6361/201014535.

M. E. Putman, J. E. G. Peek, A. Muratov, O. Y. Gnedin, W. Hsu, K. A. Douglas, C. Heiles, S. Stanimirovic, E. J. Korpela, & S. J. Gibson. The Disruption and Fueling of M33. ApJ, 703:1486–1501, October 2009. doi: 10.1088/0004-637X/703/2/1486.

B. L. Rachford, T. P. Snow, J. D. Destree, T. L. Ross, R. Ferlet, S. D. Friedman, C. Gry, E. B. Jenkins, D. C. Morton, B. D. Savage, J. M. Shull, P. Sonnentrucker, J. Tumlinson, A. Vidal-Madjar, D. E. Welty, & D. G. York. Molecular Hydrogen in the Far Ultraviolet Spectroscopic Explorer Translucent Lines of Sight: The Full Sample. ApJS, 180:125–137, January 2009. doi: 10.1088/0067-0049/180/1/125.

Rayleigh. The Band Spectrum of Mercury from the Excited Vapour. Nature, 119:423, March 1927. doi: 10.1038/119423a0.

M. W. Regan & S. N. Vogel. The near-infrared structure of M33. ApJ, 434:536–545, October 1994. doi: 10.1086/174755.

M. J. Reid. The distance to the center of the Galaxy. ARA&A, 31:345–372, 1993. doi: 10.1146/annurev.aa.31.090193.002021.

M. J. Reid, K. M. Menten, X. W. Zheng, A. Brunthaler, L. Moscadelli, Y. Xu, B. Zhang, M. Sato, M. Honma, T. Hirota, K. Hachisuka, Y. K.

Choi, G. A. Moellenbrock, & A. Bartkiewicz. Trigonometric Parallaxes of Massive Star-Forming Regions. VI. Galactic Structure, Fundamental Parameters, and Noncircular Motions. ApJ, 700:137-148, July 2009. doi: 10.1088/0004-637X/700/1/137.

M. J. Reid, K. M. Menten, A. Brunthaler, X. W. Zheng, T. M. Dame, Y. Xu, Y. Wu, B. Zhang, A. Sanna, M. Sato, K. Hachisuka, Y. K. Choi, K. Immer, L. Moscadelli, K. L. J. Rygl, & A. Bartkiewicz. Trigonometric Parallaxes of High Mass Star Forming Regions: The Structure and Kinematics of the Milky Way. ApJ, 783:130, March 2014. doi: 10.1088/0004-637X/783/2/130.

C. Risacher, R. Guesten, J. Stutzki, H.-W. Huebers, D. Buechel, U. U. Graf, S. Heyminck, C. E. Honingh, K. Jacobs, B. Klein, T. Klein, C. Leinz, P. Puetz, N. Reyes, O. Ricken, H.-J. Wunsch, P. Fusco, & S. Rosner. First supra-THz Heterodyne Array Receivers for Astronomy with the SOFIA Observatory. *ArXiv e-prints*, December 2015.

W. W. Roberts, Jr., M. S. Roberts, & F. H. Shu. Density wave theory and the classification of spiral galaxies. ApJ, 196:381–405, March 1975. doi: 10.1086/153421.

N. J. Rodríguez-Fernández. Gas dynamics in the Milky Way: the nuclear bar and the 3-kpc arms. *Memorie della Societa Astronomica Italiana Supplementi*, 18:195, 2011.

N. J. Rodriguez-Fernandez & F. Combes. Gas flow models in the Milky Way embedded bars. A&A, 489:115–133, October 2008. doi: 10.1051/0004-6361:200809644.

K. Rohlfs & T. L. Wilson. *Tools of radio astronomy.* 2000.

M. Röllig & V. Ossenkopf. Carbon fractionation in photo-dissociation regions. A&A, 550:A56, February 2013. doi: 10.1051/0004-6361/201220130.

M. Röllig, V. Ossenkopf, S. Jeyakumar, J. Stutzki, & A. Sternberg. [CII] 158 μm emission and metallicity in photon dominated regions. A&A, 451:917–924, June 2006. doi: 10.1051/0004-6361:20053845.

M. Röllig, R. Szczerba, V. Ossenkopf, & C. Glück. Full SED fitting with the KOSMA-τ PDR code. I. Dust modelling. A&A, 549:A85, January 2013. doi: 10.1051/0004-6361/201118190.

E. Rosolowsky, E. Keto, S. Matsushita, & S. P. Willner. High-Resolution Molecular Gas Maps of M33. ApJ, 661:830–844, June 2007. doi: 10.1086/516621.

E. Rosolowsky, J. E. Pineda, & Y. Gao. Minimal HCN emission from molecular clouds in M33. MNRAS, 415:1977–1984, August 2011. doi: 10.1111/j.1365-2966.2011.18851.x.

G. W. Rougoor & J. H. Oort. Distribution and Motion of Interstellar Hydrogen in the Galactic System with Particular Reference to the Region within 3 Kiloparsecs of the Center. *Proceedings of the National Academy of Science*, 46:1–13, January 1960. doi: 10.1073/pnas.46.1.1.

R. H. Rubin. Models of H II regions - Heavy element opacity, variation of temperature. ApJS, 57:349–387, February 1985. doi: 10.1086/191007.

R. H. Rubin, J. P. Simpson, S. W. J. Colgan, R. J. Dufour, G. Brunner, I. A. McNabb, A. W. A. Pauldrach, E. F. Erickson, M. R. Haas, & R. I. Citron. Spitzer Observations of M33 and the Hot Star, H II Region Connection. *ArXiv e-prints*, April 2008.

A. L. Rudolph, M. Fich, G. R. Bell, T. Norsen, J. P. Simpson, M. R. Haas, & E. F. Erickson. Abundance Gradients in the Galaxy. ApJS, 162: 346–374, February 2006. doi: 10.1086/498869.

R. W. Russell, G. Melnick, G. E. Gull, & M. Harwit. Detection of the 157 micron /1910 GHz/ /C II/ emission line from the interstellar gas complexes NGC 2024 and M42. ApJ, 240:L99–L103, September 1980. doi: 10.1086/183332.

D. B. Sanders, P. M. Solomon, & N. Z. Scoville. Giant molecular clouds in the Galaxy. I - The axisymmetric distribution of H2. ApJ, 276:182–203, January 1984. doi: 10.1086/161602.

B. D. Savage, R. C. Bohlin, J. F. Drake, & W. Budich. A survey of interstellar molecular hydrogen. I. ApJ, 216:291–307, August 1977. doi: 10.1086/155471.

R. Schieder, V. Tolls, & G. Winnewisser. The Cologne acousto optical spectrometers. *Experimental Astronomy*, 1:101–121, March 1989. doi: 10.1007/BF00457985.

E. Schinnerer, S. E. Meidt, J. Pety, A. Hughes, D. Colombo, S. García-Burillo, K. F. Schuster, G. Dumas, C. L. Dobbs, A. K. Leroy, C. Kramer, T. A. Thompson, & M. W. Regan. The PdBI Arcsecond Whirlpool Survey (PAWS). I. A Cloud-scale/Multi-wavelength View of the Interstellar Medium in a Grand-design Spiral Galaxy. ApJ, 779:42, December 2013. doi: 10.1088/0004-637X/779/1/42.

D. J. Schlegel, D. P. Finkbeiner, & M. Davis. Maps of Dust Infrared Emission for Use in Estimation of Reddening and Cosmic Microwave Background Radiation Foregrounds. ApJ, 500:525–553, June 1998. doi: 10.1086/305772.

K. J. Schlesinger, J. A. Johnson, C. M. Rockosi, Y. S. Lee, H. L. Morrison, R. Schönrich, C. Allende Prieto, T. C. Beers, B. Yanny, P. Harding, D. P. Schneider, C. Chiappini, L. N. da Costa, M. A. G. Maia, I. Minchev, H. Rocha-Pinto, & B. X. Santiago. The Metallicity Distribution Functions of SEGUE G and K Dwarfs: Constraints for Disk Chemical Evolution and Formation. ApJ, 761:160, December 2012. doi: 10.1088/0004-637X/761/2/160.

K. J. Schlesinger, J. A. Johnson, C. M. Rockosi, Y. S. Lee, T. C. Beers, P. Harding, C. Allende Prieto, J. C. Bird, R. Schönrich, B. Yanny, D. P. Schneider, B. A. Weaver, & J. Brinkmann. The Vertical Metallicity Gradient of the Milky Way Disk: Transitions in [α/Fe] Populations. ApJ, 791:112, August 2014. doi: 10.1088/0004-637X/791/2/112.

M. Schmidt. Spiral structure in the inner parts of the Galactic System derived from the hydrogen emission at 21-cm wavelength. Bull. Astron. Inst. Netherlands, 13:247, May 1957.

M. Schmidt. Models of the mass distribution of the Galaxy. In H. van Woerden, R. J. Allen, & W. B. Burton, editors, *The Milky Way Galaxy*, volume 106 of *IAU Symposium*, pages 75–81, 1985.

N. Schneider, R. Simon, C. Kramer, K. Kraemer, J. Stutzki, & B. Mookerjea. A multiwavelength study of the S 106 region. II. Characteristics of the photon dominated region. A&A, 406:915–935, August 2003. doi: 10.1051/0004-6361:20030726.

N. Z. Scoville & D. B. Sanders. H2 in the Galaxy. In D. J. Hollenbach & H. A. Thronson, Jr., editors, *Interstellar Processes*, volume 134 of *Astrophysics and Space Science Library*, pages 21–50, 1987.

P. A. Shaver, R. X. McGee, L. M. Newton, A. C. Danks, & S. R. Pottasch. The galactic abundance gradient. MNRAS, 204:53–112, July 1983.

Y. Sheffer, M. Rogers, S. R. Federman, D. L. Lambert, & R. Gredel. Hubble Space Telescope Survey of Interstellar ^{12}CO/^{13}CO in the Solar Neighborhood. ApJ, 667:1002–1016, October 2007. doi: 10.1086/520875.

Y. Sheffer, M. Rogers, S. R. Federman, N. P. Abel, R. Gredel, D. L. Lambert, & G. Shaw. Ultraviolet Survey of CO and H_2 in Diffuse Molecular Clouds: The Reflection of Two Photochemistry Regimes in Abundance Relationships. ApJ, 687:1075–1106, November 2008. doi: 10.1086/591484.

H. Shibai, H. Okuda, T. Nakagawa, H. Matsuhara, T. Maihara, K. Mizutani, Y. Kobayashi, N. Hiromoto, T. Nishimura, & F. J. Low. Large-scale forbidden C II 158 micron emission from the Galaxy. ApJ, 374: 522–532, June 1991. doi: 10.1086/170141.

J. M. Shull & S. Beckwith. Interstellar molecular hydrogen. ARA&A, 20: 163–190, 1982. doi: 10.1146/annurev.aa.20.090182.001115.

T. P. Snow & B. J. McCall. Diffuse Atomic and Molecular Clouds. ARA&A, 44:367–414, September 2006. doi: 10.1146/annurev.astro.43.072103.150624.

T. P. Snow & A. N. Witt. Interstellar Depletions Updated: Where All the Atoms Went. ApJ, 468:L65, September 1996. doi: 10.1086/310225.

D. Sobral, J. Matthee, B. Darvish, D. Schaerer, B. Mobasher, H. J. A. Röttgering, S. Santos, & S. Hemmati. Evidence for PopIII-like Stellar Populations in the Most Luminous Lyman-α Emitters at the Epoch of Reionization: Spectroscopic Confirmation. ApJ, 808:139, August 2015. doi: 10.1088/0004-637X/808/2/139.

U. J. Sofia, J. A. Cardelli, & B. D. Savage. The abundant elements in interstellar dust. ApJ, 430:650–666, August 1994. doi: 10.1086/174438.

U. J. Sofia, J. A. Cardelli, K. P. Guerin, & D. M. Meyer. Carbon in the Diffuse Interstellar Medium. ApJ, 482:L105–L108, June 1997. doi: 10.1086/310681.

U. J. Sofia, J. T. Lauroesch, D. M. Meyer, & S. I. B. Cartledge. Interstellar Carbon in Translucent Sight Lines. ApJ, 605:272–277, April 2004. doi: 10.1086/382592.

P. M. Solomon, A. R. Rivolo, J. Barrett, & A. Yahil. Mass, luminosity, and line width relations of Galactic molecular clouds. ApJ, 319:730–741, August 1987. doi: 10.1086/165493.

P. Sonnentrucker, D. E. Welty, J. A. Thorburn, & D. G. York. Abundances and Behavior of ^{12}CO, ^{13}CO, and C_2 in Translucent Sight Lines. ApJS, 168:58–99, January 2007. doi: 10.1086/508687.

L. Spitzer, Jr. The Dynamics of the Interstellar Medium. III. Galactic Distribution. ApJ, 95:329, May 1942. doi: 10.1086/144407.

L. Spitzer, Jr. Temperature of interstellar matter. AJ, 52:130, 1947. doi: 10.1086/106008.

R. Srama, E. Grun, & Cassini-Dust-Science Team. The Cosmic Dust Analyzer for the Cassini Mission to Saturn. In B. A. S. Gustafson & M. S. Hanner, editors, *IAU Colloq. 150: Physics, Chemistry, and Dynamics of Interplanetary Dust*, volume 104 of *Astronomical Society of the Pacific Conference Series*, page 227, 1996.

G. J. Stacey, C. H. Townes, N. Geis, S. C. Madden, F. Herrmann, R. Genzel, A. Poglitsch, & J. M. Jackson. The optical depth of the 158 micron forbidden C-12 II line - Detection of the F = 1 - 0 forbidden C-13 II hyperfine-structure component. ApJ, 382:L37–L41, November 1991. doi: 10.1086/186208.

A. A. Stark. AST/RO: A submillimetre-wave telescope for the South Pole. *Highlights of Astronomy*, 9:587, 1992.

A. A. Stark. Submillimeter Astronomy from the South Pole (AST/RO). In M. G. Burton, X. Cui, & N. F. H. Tothill, editors, *Astrophysics from Antarctica*, volume 288 of *IAU Symposium*, pages 146–153, January 2013. doi: 10.1017/S1743921312016808.

A. A. Stark, A. D. Bolatto, R. A. Chamberlin, A. P. Lane, T. M. Bania, J. M. Jackson, & K.-Y. Lo. First Detection of 492 GHz [C I] Emission from the Large Magellanic Cloud. ApJ, 480:L59–L62, May 1997. doi: 10.1086/310618.

A. A. Stark, J. Bally, S. P. Balm, T. M. Bania, A. D. Bolatto, R. A. Chamberlin, G. Engargiola, M. Huang, J. G. Ingalls, K. Jacobs, J. M. Jackson, J. W. Kooi, A. P. Lane, K.-Y. Lo, R. D. Marks, C. L. Martin, D. Mumma, R. Ojha, R. Schieder, J. Staguhn, J. Stutzki, C. K. Walker, R. W. Wilson, G. A. Wright, X. Zhang, P. Zimmermann, & R. Zimmermann. The Antarctic Submillimeter Telescope and Remote Observatory (AST/RO). PASP, 113:567–585, May 2001. doi: 10.1086/320281.

T. Y. Steiman-Cameron, M. Wolfire, & D. Hollenbach. COBE and the Galactic Interstellar Medium: Geometry of the Spiral Arms from FIR Cooling Lines. ApJ, 722:1460–1473, October 2010. doi: 10.1088/0004-637X/722/2/1460.

A. Sternberg & A. Dalgarno. The infrared response of molecular hydrogen gas to ultraviolet radiation - High-density regions. ApJ, 338:197–233, March 1989. doi: 10.1086/167193.

A. Sternberg & A. Dalgarno. Chemistry in Dense Photon-dominated Regions. ApJS, 99:565, August 1995. doi: 10.1086/192198.

H. Stoerzer, J. Stutzki, & A. Sternberg. FUV irradiated molecular clumps: spherical geometry and density gradients. A&A, 310:592–602, June 1996.

H. Stoerzer, J. Stutzki, & A. Sternberg. CI fine-structure emission from non-equilibrium PDRs. A&A, 323:L13–L16, July 1997.

J. W. V. Storey. The Detection of Shocked Co/ Emission from G333.6-0.2. *Proceedings of the Astronomical Society of Australia*, 5:566–569, 1984.

O. Struve & C. T. Elvey. Emission Nebulosities in Cygnus and Cepheus. ApJ, 88:364, October 1938. doi: 10.1086/143992.

J. Stutzki. SOFIA: The Stratospheric Observatory for Infrared Astronomy (With 11 Figures). In S. Roeser, editor, *Reviews in Modern Astronomy*, volume 19 of *Reviews in Modern Astronomy*, page 293, January 2006.

J. Stutzki, U. U. Graf, S. Haas, C. E. Honingh, D. Hottgenroth, K. Jacobs, R. Schieder, R. Simon, J. Staguhn, G. Winnewisser, R. N. Martin, W. L. Peters, & J. P. McMullin. Atomic Carbon in M82: Physical Conditions Derived from Simultaneous Observations of the [C I] Fine-Structure Submillimeter-Wave Transitions. ApJ, 477:L33–L36, March 1997. doi: 10.1086/310514.

J. Stutzki, F. Bensch, A. Heithausen, V. Ossenkopf, & M. Zielinsky. On the fractal structure of molecular clouds. A&A, 336:697–720, August 1998.

J. Stutzki, U. U. Graf, R. Simon, S. W. J. Colgan, X. Guan, R. Güsten, & C. E. Honingh. Large column densities and [^{12}CII] 158 μm self-absorption in Orion B. In T. Wong & J. Ott, editors, *IAU Symposium*, volume 292 of *IAU Symposium*, pages 57–58, March 2013. doi: 10.1017/S1743921313000380.

F. S. Tabatabaei, R. Beck, M. Krause, E. M. Berkhuijsen, R. Gehrz, K. D. Gordon, J. L. Hinz, R. Humphreys, K. McQuinn, E. Polomski, G. H. Rieke, & C. E. Woodward. A multi-scale study of infrared and radio emission from Scd galaxy M 33. A&A, 466:509–519, May 2007. doi: 10.1051/0004-6361:20066731.

T. Takamine & M. Fukuda. On the Mercury Line λ2270 A. Nature, 114: 382, September 1924. doi: 10.1038/114382a0.

M. Takano, K. Mitsuda, Y. Fukazawa, & F. Nagase. Properties of M33 X-8, the nuclear source in the nearby spiral galaxy. ApJ, 436:L47–L50, November 1994. doi: 10.1086/187629.

R. J. Talbot, Jr. & W. D. Arnett. The evolution of galaxies. IV - Highly flattened disks. ApJ, 197:551–570, May 1975. doi: 10.1086/153543.

A. G. G. M. Tielens. The Physics and Chemistry of the Interstellar Medium. August 2010.

A. G. G. M. Tielens & D. Hollenbach. Photodissociation regions. I - Basic model. II - A model for the Orion photodissociation region. ApJ, 291: 722–754, April 1985a. doi: 10.1086/163111.

A. G. G. M. Tielens & D. Hollenbach. Photodissociation Regions - Part Two - a Model for the Orion Photodissociation Region. ApJ, 291:747, April 1985b. doi: 10.1086/163112.

T. Tosaki, N. Kuno, S. M. Onodera, Rie, T. Sawada, K. Muraoka, K. Nakanishi, S. Komugi, H. Nakanishi, H. Kaneko, A. Hirota, K. Kohno, & R. Kawabe. NRO M33 All-Disk Survey of Giant Molecular Clouds (NRO MAGiC). I. H I to H_2 Transition. PASJ, 63:1171–1179, December 2011. doi: 10.1093/pasj/63.6.1171.

J. P. Vallée. New Velocimetry and Revised Cartography of the Spiral Arms in the Milky Way - A Consistent Symbiosis. AJ, 135:1301, April 2008. doi: 10.1088/0004-6256/135/4/1301.

F. Valsecchi, E. Glebbeek, W. M. Farr, T. Fragos, B. Willems, J. A. Orosz, J. Liu, & V. Kalogera. Formation of the black-hole binary M33 X-7 through mass exchange in a tight massive system. Nature, 468:77–79, November 2010. doi: 10.1038/nature09463.

H. C. van de Hulst. Radio waves from space: Origin of radiowaves. *Ned. tijd. natuurkunde*, 11:210–221, 1945.

H. C. van de Hulst, C. A. Muller, & J. H. Oort. The spiral structure of the outer part of the Galactic System derived from the hydrogen emission at 21 cm wavelength. Bull. Astron. Inst. Netherlands, 12:117, May 1954.

S. van den Bergh. Updated Information on the Local Group. PASP, 112: 529–536, April 2000a. doi: 10.1086/316548.

S. van den Bergh. *The Galaxies of the Local Group*. Cambridge, May 2000b.

P. C. van der Kruit & L. Searle. Surface photometry of edge-on spiral galaxies. I - A model for the three-dimensional distribution of light in galactic disks. A&A, 95:105–115, February 1981a.

P. C. van der Kruit & L. Searle. Surface Photometry of Edge-On Spiral Galaxies. II - the Distribution of Light and Colour in the Disk and Spheroid of NGC891. A&A, 95:116, February 1981b.

F. F. S. van der Tak, J. H. Black, F. L. Schöier, D. J. Jansen, & E. F. van Dishoeck. A computer program for fast non-LTE analysis of interstellar line spectra. With diagnostic plots to interpret observed line intensity ratios. A&A, 468:627–635, June 2007. doi: 10.1051/0004-6361:20066820.

E. F. van Dishoeck, F. P. Helmich, W. A. Schutte, P. Ehrenfreund, F. Lahuis, A. C. A. Boogert, A. G. G. M. Tielens, T. de Graauw, P. A. Gerakines, & D. C. B. Whittet. ISO Observations of Gas and Dust Chemistry in Star-Forming Regions. In J. Yun & L. Liseau, editors, *Star Formation with the Infrared Space Observatory*, volume 132 of *Astronomical Society of the Pacific Conference Series*, page 54, 1998.

E. Vanhollebeke, M. A. T. Groenewegen, & L. Girardi. Stellar populations in the Galactic bulge. Modelling the Galactic bulge with TRILEGAL. A&A, 498:95–107, April 2009. doi: 10.1051/0004-6361/20078472.

V. Vassilev, D. Meledin, I. Lapkin, V. Belitsky, O. Nyström, D. Henke, A. Pavolotsky, R. Monje, C. Risacher, M. Olberg, M. Strandberg, E. Sundin, M. Fredrixon, S.-E. Ferm, V. Desmaris, D. Dochev, M. Pantaleev, P. Bergman, & H. Olofsson. A Swedish heterodyne facility instrument for the APEX telescope. A&A, 490:1157–1163, November 2008. doi: 10.1051/0004-6361:200810459.

R. Visser, E. F. van Dishoeck, & J. H. Black. The photodissociation and chemistry of CO isotopologues: applications to interstellar clouds and circumstellar disks. A&A, 503:323–343, August 2009. doi: 10.1051/0004-6361/200912129.

E. von der Pahlen. Über die Gestalten einiger Spiralnebel. *Astronomische Nachrichten*, 188:249, April 1911. doi: 10.1002/asna.19111881502.

S. Walch, P. Girichidis, T. Naab, A. Gatto, S. C. O. Glover, R. Wünsch, R. S. Klessen, P. C. Clark, T. Peters, D. Derigs, & C. Baczynski. The SILCC (SImulating the LifeCycle of molecular Clouds) project - I. Chemical evolution of the supernova-driven ISM. MNRAS, 454:238–268, November 2015. doi: 10.1093/mnras/stv1975.

C. Walker. STO, GUSSTO (Explorer): Recent Activities and Results. In *39th COSPAR Scientific Assembly*, volume 39 of *COSPAR Meeting*, page 2114, July 2012.

C. Walker, C. Kulesa, P. Bernasconi, H. Eaton, N. Rolander, C. Groppi, J. Kloosterman, T. Cottam, D. Lesser, C. Martin, A. Stark, D. Neufeld, C. Lisse, D. Hollenbach, J. Kawamura, P. Goldsmith, W. Langer, H. Yorke, J. Sterne, A. Skalare, I. Mehdi, S. Weinreb, J. Kooi, J. Stutzki, U. Graf, M. Brasse, C. Honingh, R. Simon, M. Akyilmaz, P. Puetz, & M. Wolfire. The Stratospheric THz Observatory (STO). In *Society of Photo-Optical Instrumentation Engineers (SPIE) Conference Series*, volume 7733 of *Society of Photo-Optical Instrumentation Engineers (SPIE) Conference Series*, page 0, July 2010. doi: 10.1117/12.857765.

C. K. Walker, J. W. Kooi, M. Chan, H. G. Leduc, P. L. Schaffer, J. E. Carlstrom, & T. G. Phillips. A low-noise 492 GHz SIS waveguide receiver. In *Third International Symposium on Space Terahertz Technology*, 1992.

C. K. Walker, C. A. Kulesa, C. E. Groppi, E. Young, T. McMahon, P. Bernasconi, C. Lisse, D. Neufeld, D. Hollenbach, J. Kawamura, P. Goldsmith, W. Langer, H. Yorke, J. Sterne, A. Skalare, I. Mehdi, S. Weinreb, J. Kooi, J. Stutzki, U. Graf, C. Honingh, P. Puetz, C. Martin, & M. Wolfire. The Stratospheric TeraHertz Observatory (STO).

In W. Wild, editor, *Ninteenth International Symposium on Space Terahertz Technology*, pages 28–30, April 2008.

C. Wegg, O. Gerhard, & M. Portail. The structure of the Milky Way's bar outside the bulge. MNRAS, 450:4050–4069, July 2015. doi: 10.1093/mnras/stv745.

A. Weiß, N. Neininger, S. Hüttemeister, & U. Klein. The effect of violent star formation on the state of the molecular gas in M 82. A&A, 365: 571–587, January 2001. doi: 10.1051/0004-6361:20000145.

S.-S. Weng, J.-X. Wang, W.-M. Gu, & J.-F. Lu. Spectral Analyses of the Nearest Persistent Ultraluminous X-Ray Source M 33 X-8. PASJ, 61: 1287–, December 2009. doi: 10.1093/pasj/61.6.1287.

A. J. Westphal, R. M. Stroud, H. A. Bechtel, F. E. Brenker, A. L. Butterworth, G. J. Flynn, D. R. Frank, Z. Gainsforth, J. K. Hillier, F. Postberg, A. S. Simionovici, V. J. Sterken, L. R. Nittler, C. Allen, D. Anderson, A. Ansari, S. Bajt, R. K. Bastien, N. Bassim, J. Bridges, D. E. Brownlee, M. Burchell, M. Burghammer, H. Changela, P. Cloetens, A. M. Davis, R. Doll, C. Floss, E. Grün, P. R. Heck, P. Hoppe, B. Hudson, J. Huth, A. Kearsley, A. J. King, B. Lai, J. Leitner, L. Lemelle, A. Leonard, H. Leroux, R. Lettieri, W. Marchant, R. Ogliore, W. J. Ong, M. C. Price, S. A. Sandford, J.-A. S. Tresseras, S. Schmitz, T. Schoonjans, K. Schreiber, G. Silversmit, V. A. Solé, R. Srama, F. Stadermann, T. Stephan, J. Stodolna, S. Sutton, M. Trieloff, P. Tsou, T. Tyliszczak, B. Vekemans, L. Vincze, J. Von Korff, N. Wordsworth, D. Zevin, M. E. Zolensky, & aff14. Evidence for interstellar origin of seven dust particles collected by the Stardust spacecraft. *Science*, 345:786–791, August 2014. doi: 10.1126/science.1252496.

L. Wiesenfeld & P. F. Goldsmith. C^+ in the Interstellar Medium: Collisional Excitation by H_2 Revisited. ApJ, 780:183, January 2014. doi: 10.1088/0004-637X/780/2/183.

C. D. Wilson. The Metallicity Dependence of the CO-to-H 2 Conversion Factor from Observations of Local Group Galaxies. ApJ, 448:L97, August 1995. doi: 10.1086/309615.

C. D. Wilson & N. Scoville. The molecular gas content of the nuclear region of M33. ApJ, 347:743–749, December 1989. doi: 10.1086/168165.

C. D. Wilson & N. Scoville. The molecular interstellar medium in two giant H II regions in M33 - NGC 604 and NGC 595. ApJ, 385:512–521, February 1992. doi: 10.1086/170959.

T. L. Wilson, K. Rohlfs, & S. Hüttemeister. *Tools of Radio Astronomy*. Springer-Verlag, 2009. doi: 10.1007/978-3-540-85122-6.

M. G. Wolfire, A. G. G. M. Tielens, & D. Hollenbach. Physical conditions in photodissociation regions - Application to galactic nuclei. ApJ, 358: 116–131, July 1990. doi: 10.1086/168966.

M. G. Wolfire, C. F. McKee, D. Hollenbach, & A. G. G. M. Tielens. Neutral Atomic Phases of the Interstellar Medium in the Galaxy. ApJ, 587: 278–311, April 2003. doi: 10.1086/368016.

M. G. Wolfire, D. Hollenbach, & C. F. McKee. The Dark Molecular Gas. ApJ, 716:1191–1207, June 2010. doi: 10.1088/0004-637X/716/2/1191.

L. Woltjer, editor. *The Distribution and Motion of Interstellar Matter in Galaxies The Distribution and Motion of Interstellar Matter in Galaxies, Proceedings of a conference held at the Institute for Advanced Study, Princeton, New Jersey, April 10 to 20, 1961. Edited by L. Woltjer. New York, W.A. Benjamin, 1962.*, January 1962.

T. Wong & L. Blitz. The Relationship between Gas Content and Star Formation in Molecule-rich Spiral Galaxies. ApJ, 569:157–183, April 2002. doi: 10.1086/339287.

D. O. S. Wood & E. Churchwell. The morphologies and physical properties of ultracompact H II regions. ApJS, 69:831–895, April 1989. doi: 10.1086/191329.

E. M. Xilouris, F. S. Tabatabaei, M. Boquien, C. Kramer, C. Buchbender, F. Bertoldi, S. Anderl, J. Braine, S. Verley, M. Relaño, G. Quintana-Lacaci, S. Akras, R. Beck, D. Calzetti, F. Combes, M. Gonzalez, P. Gratier, C. Henkel, F. Israel, B. Koribalski, S. Lord, B. Mookerjea, E. Rosolowsky, G. Stacey, R. P. J. Tilanus, F. van der Tak, & P. van der Werf. Cool and warm dust emission from M 33 (HerM33es). A&A, 543:A74, July 2012. doi: 10.1051/0004-6361/201219291.

Y. Xu, H. J. Newberg, J. L. Carlin, C. Liu, L. Deng, J. Li, R. Schönrich, & B. Yanny. Rings and Radial Waves in the Disk of the Milky Way. ApJ, 801:105, March 2015. doi: 10.1088/0004-637X/801/2/105.

S. Yamamoto & S. Saito. Laboratory observation of the 3P1-3P0 transition of the neutral carbon atom by submillimeter-wave absorption spectroscopy. ApJ, 370:L103–L105, April 1991. doi: 10.1086/185987.

E. T. Young, E. E. Becklin, P. M. Marcum, T. L. Roellig, J. M. De Buizer, T. L. Herter, R. Güsten, E. W. Dunham, P. Temi, B.-G. Andersson, D. Backman, M. Burgdorf, L. J. Caroff, S. C. Casey, J. A. Davidson, E. F. Erickson, R. D. Gehrz, D. A. Harper, P. M. Harvey, L. A. Helton, S. D. Horner, C. D. Howard, R. Klein, A. Krabbe, I. S. McLean, A. W. Meyer, J. W. Miles, M. R. Morris, W. T. Reach, J. Rho, M. J. Richter, H.-P. Roeser, G. Sandell, R. Sankrit, M. L. Savage, E. C. Smith, R. Y. Shuping, W. D. Vacca, J. E. Vaillancourt, J. Wolf, & H. Zinnecker. Early Science with SOFIA, the Stratospheric Observatory For Infrared Astronomy. ApJ, 749:L17, April 2012. doi: 10.1088/2041-8205/749/2/L17.

J. S. Young & N. Scoville. The dependence of CO emission on luminosity and the rate of star formation in SC galaxies. ApJ, 260:L11–L17, September 1982. doi: 10.1086/183860.

J. A. Zavala, M. S. Yun, I. Aretxaga, D. H. Hughes, G. W. Wilson, J. E. Geach, E. Egami, M. A. Gurwell, D. J. Wilner, I. Smail, A. W. Blain, S. C. Chapman, K. E. K. Coppin, M. Dessauges-Zavadsky, A. C. Edge, A. Montaña, K. Nakajima, T. D. Rawle, D. Sánchez-Argüelles, A. M. Swinbank, T. M. A. Webb, & M. Zeballos. Early Science with the Large Millimeter Telescope: observations of dust continuum and CO emission lines of cluster-lensed submillimetre galaxies at z=2.0-4.7. MNRAS, 452: 1140–1151, September 2015. doi: 10.1093/mnras/stv1351.

Publications

SOFIA/GREAT [CII] observations in nearby clouds near the lines of sight towards B0355+508 and B0212+735
Glück, C.B., Stutzki, J., Röllig, M., Chambers, E.T. and Risacher, C., 2017, A&A, 600, 94G

The Mopra Southern Galactic Plane CO Survey - Data Release 1
Braiding, C., Burton, M.G., Blackwell, R., Glück, C., Hawkes, J., Kulesa, C., Maxted, N., Rebolledo, D., Rowell, G., Stark, A., Tothill, N., Urquhart, J.s., Voisin, F., Walsh, A.J., de Wilt, P. and Wong, G.F., 2015, PASA, 32, 20B

The Carbon Inventory in a Quiescent, Filamentary Molecular Cloud in G328
Burton, M.G., Ashley, M.C.B., Braiding, C., Storey, J.W.V., Kulesa, C., Hollenbach, D.J., Wolfire, M., Glück, C., Rowell, G., 2014, ApJ, 782, 72

The Mopra Southern Galactic Plane CO Survey
Burton, M.G., Braiding, C., Glueck, C., Goldsmith, P., Hawkes, Hollenbach, D.J., Kulesa, C., Martin, C.L., Pineda, J.L., Rowell, G., Simon, R., Stark, A.A., Stutzki, J., Tithill, N.J.H., Urquhart, J.S., Walker, C. Walsh, A.J., Wolfire, M., 2013, PASA, 30, 44B

Full SED fitting with the KOSMA-τ PDR code. I. Dust modelling
Röllig, M., Szczerba, R., Ossenkopf, V., Glück, C., 2013, A&A, 549, 85R

The Mopra-STO-Nanten2 Atomic and Molecular Gas Survey: The Formation of Giant Molecular Clouds
Burton, M.G., Rathborne, M., Pineda Galvez, J.L., Simon, R., Urquhart, J., Stark, A.A., Rowell, G., Tothill, N., Storey, J., Langer, W.D., Martin, C., Walker, C., Kulesa, C., Stutzki, J., Hollenbach, D., Au, C., Glueck, C.„ 2012, ATNF Proposal, 5014B

List of Figures

List of Tables

Acronyms

ATCA Australia Telescope Compact Array

AOS Acusto-optical spectrometer

APEX Atacama Pathfinder Experiment

AST/RO Antarctic Submillimeter Telescope and Remote Observatory

b galactic latitude

CLASS Continuum and Line Analysis Single-dish Software

CNM cold neutral medium

CSO Caltech Submillimetre Observatory

DFG Deutsche Forschungsgemeinschaft

ESO European Southern Observatory

FFTS Fast Fourier-transform spectrometer

FWHM full width at half maximum

GMC Giant Molecular Cloud

GOT C^+ Galactic Observations of the Terahertz C^+ Line

GREAT German REceiver for Astronomy at Terahertz Frequencies

HERM33ES Herschel M33 extended survey

HIFI Heterodyne Instrument for the Far Infrared

HIM Hot ionized medium

IRAM Institut de Radioastronomie Millimétrique

ISRF interstellar radiation field

JCMT James Clerk Maxwell Telescope

l galactic longitude

LTE local thermal equilibrium

ISM Interstellar Medium

PACS Photodetecting Array Camera and Spectrometer

PAH Polycyclic aromatic hydrocarbon

RMS root mean square

pv position velocity

pwv precipitable water vapour

SED Spectral Energy Distribution

SIS superconductor–insulator–superconductor

S/N signal to noise

SOFIA Stratospheric Observatory For Infrared Astronomy

SPIRE Spectral and Photometric Imaging Receiver

STO Stratospheric Terahertz Observatory

WIM warm ionized medium

WNM warn neutral medium

List of Constants and Units

List of the constants and units used in this thesis.

Constant	Value	Unit (SI)	Description
		Physical constants	
c	2.9979×10^{8}	$\frac{\mathrm{m}}{\mathrm{s}}$	speed of light in vacuum
k_{B}	1.2807×10^{-34}	$\frac{\mathrm{J}}{\mathrm{K}}$	Boltzman Constant
G	6.674×10^{-11}	$\frac{\mathrm{N}}{\mathrm{m}}$	Gravitational constant
h	6.6262×10^{-34}	J s	Planck constantn
		Astonomical constants	
pc	3.086×10^{16}	m	Parsec
$M_{\odot}$	1.989×10^{30}	kg	Mass of the sun
$L_{\odot}$	3.85×10^{26}	$\frac{\mathrm{J}}{\mathrm{s}}$	Luminosity of the sun
$R_{\odot}$	8.5	kpc	Distance Sun–Galactic Centre
T		K	Temperature
λ		m	Wavelength
ν		Hz	Frequency
v		$\frac{\mathrm{m}}{\mathrm{s}}$	Velocity
n_{x}		cm^{-3}	Volume density of x
N_{x}		cm^{-2}	Column density of x
$\circ$			Degree
$\prime$			Arcminute
$\prime\prime$			Arcsecond
eV	6.242×10^{11}	erg	electron Volt

Acknowledgements

First of all, I would like to thank my principal supervisor and first referee of this thesis, Prof. Dr. Jürgen Stutzki, for his support and all the various opportunities he had opened up for me. I also like to thank him for all his useful suggestions and comments.

I like thank Prof. Dr. Joachim Hemberger for being the second referee of this thesis. Also I like to thank Prof. Dr. Uwe Ruschewitz for taking over the chairmanship of the PhD–committee. My thanks go also to Volker Okada–Ossenkopf for being the reporter at the defense.

I also like to thank Prof. Dr. Michael J. Burton for his supervision, suggestions and comments. I like to thank him for the opportunity to support the Mopra Southern Galactic Plane CO Survey in Sydney and from the ATCA side. We also had several very interesting, productive and nice stays in Chile.

My special thanks goes to Jérôme Pety and Harvey Liszt for their dedicated support and their helpful and critical comments concerning the project of the SOFIA [CII] observations in B0355+508 and B0212+735. I also like to give special thanks to Markus Röllig for his support and help.

My special thanks goes to the whole HERM33ES team for the dedicated support and useful comments. In particular I would like to mention Bhaswati Mookerjea for her dedicated help concerning the M33 chapter. I also like to thank Carsten Krammer, Jonathan Braine and Frank Israel for their comments and support.
My special thanks goes also to Marc J. Royster (Northwestern University) and Ed Chambers for their essential help in obtaining the CSO data.

I like to thank Annika Franeck for here comments and the discussions concerning the vertical distribution of carbon in the Milky Way.

My thanks go to the whole working group for their support, comments and the nice atmosphere. Even it is hard to pick out special persons I would like to specially mention Ronan Higgins, Markus Röllig, Yoko Okada, Robert Simon, Christoph Buchbender, Philipp Carlhoff, Anna Parikka, Volker Okada-Ossenkopf, Silke Andree-Labsch, Nikola Schneider and Ed Chambers for their support, help and taking their time for my questions.

Thanks again to Ronan Higgins, Anna Parikka and Yoko Okada for the proof–reading.

Thanks to the operators and teams of the telescopes for carrying out the specific observations.

I also like to thank our secretaries for their support, in particular Bettina Krause and Steffi Krämer.

I want to thank my parents, my brother, and all my family and friends who supported me in all that time. In particular I like to thank Corinna Glück and Nadine Khayat for the proof–reading.

Last but not least my special thanks goes to my beloved wife Theresa. You are my inspiration.

This thesis work is carried out within the Collaborative Research Centre 956, sub-project A3, funded by the Deutsche Forschungsgemeinschaft (DFG).

Erklärung

Ich versichere, dass ich die von mir vorgelegte Dissertation selbstständig angefertigt, die benutzten Quellen und Hilfsmittel vollständig angegeben und die Stellen der Arbeit – einschließlich Tabellen, Karten und Abbildungen –, die anderen Werken im Wortlaut oder dem Sinn nach entnommen sind, in jedem Einzelfall als Entlehnung kenntlich gemacht habe; dass diese Dissertation noch keiner anderen Fakultät oder Universität zur Prüfung vorgelegen hat; dass sie – abgesehen von unten angegebenen Teilpublikationen – noch nicht veröffentlicht worden ist sowie, dass ich eine solche Veröffentlichung vor Abschluss des Promotionsverfahrens nicht vornehmen werde. Die Bestimmungen der Promotionsordnung sind mir bekannt. Die von mir vorgelegte Dissertation ist von Prof. Dr. J. Stutzki betreut worden.

Teilpublikationen:
SOFIA/GREAT [CII] observations in nearby clouds near the lines of sight towards B0355+508 and B0212+735
Glück, C.B., Stutzki, J., Röllig, M., Chambers, E.T. and Risacher, C., 2017, A&A, 600, 94G

Ich versichere, dass ich alle Angaben wahrheitsgemäß nach bestem Wissen und Gewissen gemacht habe und verpflichte mich, jedmögliche, die obigen Angaben betreffenden Veränderungen, dem Dekanat unverzüglich mitzuteilen.

Köln, 3. Mai 2017

Christian Björn Glück